Pancreatic Islet Microphysiology System for Disease Modeling of Type 2 Diabetes

by

Connor Ray Wiegand

B.S. in Chemical Engineering, The Ohio State University, 2016

Submitted to the Graduate Faculty of the

Swanson School of Engineering in partial fulfillment

of the requirements for the degree of

Doctor of Philosophy

University of Pittsburgh

2023

UNIVERSITY OF PITTSBURGH

SWANSON SCHOOL OF ENGINEERING

This dissertation was presented

by

Connor Ray Wiegand

It was defended on

October 20, 2023

and approved by

Harvey S Borovetz, Ph.D., Distinguished Professor, University of Pittsburgh Department of Chemical and Petroleum Engineering

Yong Fan, Ph.D., Adjunct Associate Professor, Carnegie Mellon University Department of Biological Sciences

Tagbo Herman Niepa, Ph.D. Associate Professor, Carnegie Mellon University Department of Chemical Engineering

Ioannis Zervantonakis, Ph.D., Assistant Professor, University of Pittsburgh Department of Bioengineering

Dissertation Advisor: Ipsita Banerjee, Ph.D., Professor, University of Pittsburgh Department of Chemical Petroleum Engineering

Pancreatic Islet Microphysiology System for Disease Modeling of Type 2 Diabetes

Connor Ray Wiegand, PhD

University of Pittsburgh, 2023

Diabetes has become an increasingly prominent global issue afflicting 10% of world's population where type 2 diabetes (T2D) comprises the majority of those diagnosed. T2D correlates with a toxic bioenvironment that leads to the body's inability to properly self-regulate blood glucose due to the dysfunction of insulin producing pancreatic islets. While the outcome of T2D is well recognized, the pathogenesis of the disease still requires greater understanding with most studied mechanisms having a non-human basis. Additionally, current disease models fail to fully replicate disease conditions for drug testing leading to only 10% success in clinical trials. To bridge the gap and more accurately replicate human disease, microphysiological systems (MPS) have risen as a viable alternative since they combine microfluidics and tissue engineering to mimic the in vivo micro-environment.

This dissertation focuses on the development of an islet-MPS that utilizes both primary and stem cell-derive tissue to simulate the pathogenesis and drug testing for T2D. In this pursuit, we developed the pancreatic islet (PANIS) system that was able to sustain a healthy islet environment with glucose sensitive insulin secretion from both primary and stem cell-derived islets for more than two weeks. Disease induction was tested by subjecting the primary islet PANIS to toxic conditions correlated with T2D, such as hyperglycemia and/or high free fatty acids (lipotoxicity). The effects of these combinations were studied thoroughly using viability and functionality assays along with RNA sequencing to determine how each toxic factor affected

islets and what toxic condition would most closely replicate T2D. This toxic conditioned islet MPS was able to test drug efficacy with dose dependent trials using the anti-oxidant drug, Resveratrol. Additionally, innate immune cell interactions were studied by co-culturing the primary and stem cell-derived islets with neutrophils while simulating disease conditions. The result of this dissertation ultimately provides a robust islet MPS that can be used to model islet-specific disease induction and drug treatment with the capabilities for personalized medicine using human stem cells.

Table of Contents

List of Tables

List of Figures

Preface

As I come to the completion my work as a PhD student and am thinking of all those who have helped shape and support me through all these years, I feel as if I am at an award ceremony trying to list off all those who I would like to thank before the "get on with it" music begins to play.

I would like to first and foremost sincerely thank my advisor, Dr. Ipsita Banerjee, whose immense patience, forthcoming guidance, and constant mentorship provided me with the framework to grow as a scientist and build my confidence in my ideas and work. Her pursuit for exploring new avenues of research and thoroughness in evaluating information has been a constant inspiration to me. I'm thankful that she always challenged me to step outside of my comfort zone and to acknowledge the greater impact of my work. I'm thankful for the countless opportunities she provided for me to grow and collaborate as a researcher and engineer. Finally, I'm thankful how she has always been there to lend an ear and provide advice and assurance whenever I've gone through tough times. For all this and more, I will be forever grateful that I have such a kind and inspiring mentor.

I would also like to thank my dissertation committee members Dr. Yong Fan, Dr. Harvey Borovetz, Dr. Tagbo Niepa, and Dr. Ioannis Zervantonakis for their support, guidance, and understanding.

With the work for this dissertation, the companionship and aid from my current lab members Ravi Krishnamurthy, Miranda Poklar, and Daniel Angarita and former members Kevin Pietz, Izzy Carnaval, and Nadine Humphry has been invaluable. I'd like to specifically recognize Ravi, Miranda, and Kevin for their help with my work and for their support during the pandemic

when supplies were sparse, and things were uncertain. Working alongside these researchers has been a pleasure, and I hope to stay in touch.

My time working through the courses and research here at Pitt would not have been as fun without my friends Eli Bostian, Michael Cowan, and Chasz Griego. I'm thankful for all the time we spent together talking about our research, helping each other through the base courses and qualifiers, and the times we blew off steam playing foosball where we all became fairly good players. I will always remember these times fondly along with all the times we headed to Las Palmas before playing I+G. I hope to always stay in touch and remain lifelong friends with you all.

I'd like to thank my family for their unwavering love and support throughout my PhD work. I'd like to thank my Mom and Dad, Melissa and KC Wiegand, especially for instilling in me the importance of science and engineering, and who continuously gave me encouragement and reassurance throughout my time in academia. If it wasn't for them both, I would not have had the confidence to pursue a PhD and be on the path I'm on now.

Finally, I would like to thank my beautiful fiancée, Lauren LaRay Luciani, for the constant love, support, patience, and encouragement she has given me. I'm so lucky to have met her in my time here and that she has brought so much joy to my life. I'm thankful for all the late nights and difficult times she has helped me get through. She has become my hand to hold and shoulder to lean on. I'm so thankful that I get to spend the rest of my life with her.

1.0 Introduction

The content of this dissertation focuses on the goal of understanding and aiding in the treatment of diabetes using microphysiological systems (MPS) and human pluripotent stem cells (hPSCs) with the focus on the role of islets of Langerhans. As such, we first need to establish the prevalence of diabetes and the current understanding and methods present to aid in the treatment of it.

1.1 Pancreatic Islets of Langerhans

Diabetes is most correlated with the functionality of the pancreatic islets of Langerhans, which are spheroid, micro-organs that are dispersed throughout the pancreas. The islets of Langerhans, commonly referred to as islets, are major regulators of blood glucose throughout the body through the hormone sections of their endocrine cell populations. Islets are composed of five major endocrine cell groups: the glucagon producing α-cells, insulin producing β-cells, somatostatin producing δ-cells, pancreatic polypeptide producing PP-cells, and ghrelin producing ε-cells. The most prominent of these cells are the β-cells (28-75%) and α-cells (10-65%), which are dispersed heterogeneously in human islets[1]. The α and β cells work inversely in regulating glucose, with glucagon stimulating glucose release from the liver into the blood and insulin stimulating the uptake of glucose by cells.

1.2 Diabetes

Diabetes mellitus is an increasingly prominent affliction that currently effects 537 million people globally (10.5% of total people) between the ages of 20-79 with a projected number of 783.2 million (12.2%) by 2045[2]. The global health-related expenditures were $966 billion in 2021 and are expected to reach $1.054 trillion by 2045[2]. Diabetes is generally characterized by the dysregulation of the blood glucose homeostasis due to the inability of cells to process glucose properly. The means by which the onset of diabetes occurs differs based on the type of diabetes, where the most common ones are Type 1 (T1D) and Type 2 (T2D).

T1D is the second most common form of diabetes and encompasses 2% of globally diagnosed cases[3]. It is associated with an autoimmune response that results in the destruction of the insulin producing β-cells that reside within pancreatic islets, where insulin allows cells to uptake glucose[4]. The lowered number of β-cells leads to lowered insulin production and increased blood glucose concentrations (hyperglycemia). The prominent means of treating T1D is through long-term exogenous insulin supplementation or cadaveric islet implantation using a method called the Edmonton Protocol, established by Shapiro et al., which requires an immunosuppressive regimen[5-7]. As the means of administering the exogenous insulin is not as accurate as the innate in vivo mechanisms, patients will experience oscillating states of hyperglycemia and hypoglycemia, ultimately causing complications with the cardiovascular system and kidneys[8]. The cadaveric islet implantation presents issues as well, due to the limited availability of viable donors and complications from the required immunosuppression[9, 10].

T2D is the most prevalent instance of diabetes, making up 90% of those diagnosed[11]. T2D is more systemic than T1D with multiple organ systems correlating with its onset[12]. It is correlated

with a decreased insulin sensitivity caused by a toxic bioenvironment within the body linked to age, diet, and genetic factors that ultimately leads to dysfunctional β-cells[2, 13]. The bioenvironment associated with T2D is composed of increased concentration of glucose, increased concentrations of free fatty acids, and increased pro-inflammatory cytokines[14]. Since many organ systems are affected during T2D, the direct effect that the correlated toxic components have on each system is still being heavily investigated. As such, the treatment of T2D matches the complexity of the disease with many options for treatment such as drug treatments along with exogenous insulin supplementation[15]. These treatments are able to mitigate symptoms associated with T2D, with many of them stimulating increased insulin secretion from β-cells or increasing cell sensitivity to insulin. However, many of the mechanisms for treating T2D are limited by the disease models present for initial testing.

1.3 Disease Modeling

Disease modeling serves as a means for both mirroring the pathogenesis of diseases to understand the mechanisms by which they form to develop more accurate targets for future drug treatments, and for testing the developed drugs to test for safety and efficacy. The majority of studies to understand glucose metabolism and diabetes have relied on animal models[16-18]. For T1D, the animal models are formed by either chemically ablating the insulin producing β-cells or are pre-disposed for spontaneous auto-immune reaction to the β-cells[18]. These models work well in demonstrating the effect of T1D, but they are limited in modeling the pathogenesis of the it due to not replicating the heterogeneity of the disease[19]. Additionally, the non-obese diabetic (NOD) mice models are capable of replicating the auto-immune reaction, but since the mouse immune system

differs greatly from human immune systems, they can only provide so much insight into the mechanisms behind the disease. These issues are caried over into the T2D animal models as well. The animal models used to replicate T2D focus on forming obese models, where T2D would develop from the diet and a possible predisposition towards an obese state[20, 21]. While these animal models are able to mirror the anatomy of the human body and replicate some of the disease symptoms, the testing for new T2D treatments only have a 10% success rate after succeeding in animal trials[22]. This is due to the animal models not fully recapitulating the human condition with minute differences in the pathways of disease progression and mechanisms for drug activity. Alternatively, in vitro culturing of cells has been used to model diabetes by testing knock-out effects, culturing conditions, and studying the interplay between organ systems by co-culturing the different tissue types. These models allow for more routine and shorter studies, but they do not accurately recapitulate the in vivo environment.

The rise of microphysiological systems (MPS), also known as organ-on chip, has allowed for a new means of in vitro disease modeling that could help bridge the gap between the current models and human patients. These MPS devices combine microfluidics with tissue engineering to mimic the in vivo environments of specific tissues. Thus far, devices have been developed to accurately replicate organs such as heart, lungs, kidney, liver, and brain under normal healthy conditions [23-28]. Disease modeling of these organs has also been carried out with the study of major diseases such as cancer, non-alcoholic fatty liver disease (NAFLD), Alzheimer's disease, and renal fibrosis[29-31]. Since these models utilize both primary and human pluripotent stem cell (hPSC) derived tissue, they can provide a more accurate insight into the mechanisms by which these diseases form and progress than the corresponding animal models[31]. Specifically for diabetes, islet MPS models are being developed to reproduce the dysfunctional states of pancreatic islets with

the ultimate goal of testing and developing T2D drugs[32]. The current state of islet MPS has shown the limitations islets have with culture under flow due to the damage that shear stress can have on islet viability and functionality[33]. As such, the extent for culturing primary islets on MPS devices has been limited to a 10-14 day span[32, 34]. Additionally, the extent of T2D induction on islet MPS has been limited to short timeframe (2.5 hour) testing with high glucose and free fatty acids[32].

1.4 Human Pluripotent Stem Cells

Human pluripotent stem cells (hPSCs) have the capacity to differentiate into almost all cell types and can intrinsically self-renew indefinitely, making them good candidates for cell therapy-based regenerative medicine and disease modeling[35]. The initial hPSCs were human embryonic stem cells (hESCs) which sparked ethical concerns based on their derivation from human embryos using in vitro fertilization[36], but with the formation of the human induced pluripotent stem cell (iPSC) in 2007, the field was revolutionized[37, 38]. iPSCs are derived from somatic cells, such as fibroblasts[39], renal epithelial cells[40], or peripheral blood mononuclear cells[41], that are reprogrammed to a pluripotent state[42, 43]. In addition to avoiding the ethical concerns of hESCs, iPSCs allow for patient specific pluripotent cell formation, which opens the possibility for personalized medicine. These hPSCs have found use in regenerative medicine clinical trials, disease modeling, and drug development through the formation of organoids[44]. Organoids are in vitro representations of in vivo organ systems through the recapitulation of key anatomical and functional aspects of the organ. To develop these organoids, hPSCs undergo directed differentiation using chemical and mechanical stimuli.

1.4.1 Islet Differentiation

The differentiation of hPSCs into pancreatic islets has become a more thoroughly investigated endeavor with multiple groups studying the chemical stimuli required for in vitro formation of functional islets capable of glucose sensitive insulin secretion[45-49]. To form into islets, the hPSCs are directed through the endoderm germ layer pathway, as seen below in Figure 1.1[50], proceeding through the developmental phases of posterior foregut, pancreatic progenitor, immature islet endocrine, and finalizing with mature islet endocrine cell groups. To direct through these pathways, chemical and mechanical stimuli activate and inhibit various signaling pathways to form the islet β-cells. These differentiation methods require precise timing when introducing the specific stimuli, and islet directed differentiation requires a minimum of 28 days to fully form the initial undifferentiated state[45-49]. Along with the chemical stimuli, mechanical stimuli that aid in islet differentiation have been investigated[51-53]. With the mechanical stimulation, the stiffness and texture of the culture environment of the hPSCs would be customized to direct the differentiation alongside the chemical stimuli. Our group has previously investigated this topic using hESCs to form pancreatic progenitor cells using the hydrogel, alginate, to encapsulate the cells and culture them in 3D with both the alginate and 3D culture aiding in the differentiation[53].

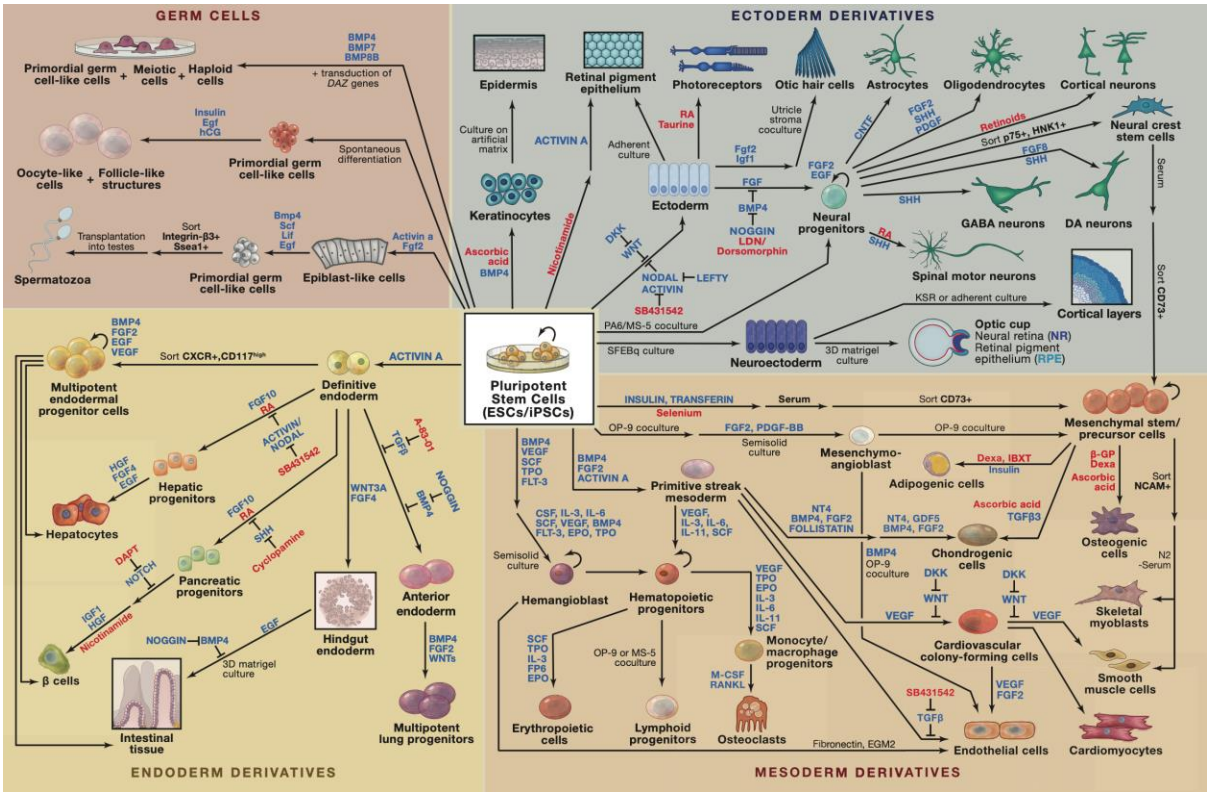

Figure 1.1 Schematic for the different differentiations pathways that hPSCs can undergo to form desired organs/tissues[50]

Alginate is a naturally derived, chemically inert copolymer that can form a 3D network using divalent cations to bind with their polymer chains resulting in a cross-linked polymer network. The mechanical properties of alginate can be fine-tuned based on the type and concentration of divalent cation used for polymerization, where calcium ions will produce weaker bonds than barium due to the greater binding affinity.

1.5 Specific Aims

The innovation with the MPS to allow for in vitro recapitulation of in vivo organs for the modeling of diseases and development of novel, efficient therapeutics has provided a necessary

means of understanding the complexity of diabetes pathogenesis and a means of mitigating its increasing prevalence worldwide. The goal of this work is to develop an islet MPS device using both primary and iPSC-derived islets that is capable of extended healthy culture and T2D induction for the purposes of T2D disease modeling and drug testing. The first aim of this work is to develop the primary islet MPS model, which will serve as the basis for the optimal endpoint capabilities of the device. As the field of islet differentiation from iPSCs continues to progress with the formation of functional islets that closely resemble the capabilities of primary tissue, we hypothesize that the utilization of alginate encapsulation in combination with the chemical stimuli will provide an enhanced differentiation outcome. The aim 2 of this work focuses on the differentiation of iPSCs encapsulated within alginate beads towards endoderm germ layer-based organ. This will encompass furthering the work we have established[53] with differentiating towards pancreatic islets, as well as testing the differentiation into other endoderm-based organs related to diabetes, such as thymus epithelial cells. Aim 3 is the implementation of the iPSC-islets from aim 2 onto the islet MPS device with the goal to test the ability for the device to maintain viability and functionality of the iPSC-islets, as well as test its applicability for disease modeling.

1.5.1 Aim 1: Develop an Islet MPS Model with Primary Human Islets for Disease Pathogenesis Modeling and Drug Testing.

The objective of this aim is to develop a primary islet MPS that would be capable of sustaining the viability and functionality of the islets for long-term culture (>14 days) to model both healthy and T2D conditions. In Chapter 2, we explored a commercially available design that we further optimized for culturing primary islets under healthy conditions where we then tested different T2D-correlated toxic media compositions on the device and conducted thorough analyses

to identify configurations that best match with T2D. Drug testing was also performed under a toxic media culture to determine the device's ability to test drug efficacy.

1.5.2 Aim 2: Develop a Novel Platform for Differentiating Endoderm-Lineage Cell Types from Human Induced Pluripotent Stem Cells (iPSCs).

The objective of this aim is to test the ability of our established alginate encapsulation 3D culture platform to differentiate human iPSCs toward endoderm-lineage cell types. In Chapter 3, we differentiated iPSCs into two different cell types, pancreatic islets and thymus epithelial cells, using established differentiation protocols for both, and tested the alginate encapsulation platform against the original culture configuration. The established islet differentiation utilized a 3D suspension culture platform, and thymus differentiation was conducted under 2D conditions. The resulting differentiations demonstrated the capabilities of the alginate encapsulation, and we sought to further the endpoint differentiation of both cell types by investigating potential procedures that would aid in recapitulating in vivo functionality with the in vitro formed cells.

1.5.3 Aim 3: To Implement Human iPSC-Derived Islets into the Islet MPS Model for Disease Modeling.

The objective of this aim is to build from aims 1 and 2 by implementing the islet differentiated iPSC onto the islet MPS to enhance the developed model by providing a more regenerative cell source. In Chapter 4, we add the iPSC-islets to the islet MPS device and test its ability to maintain the viability and functionality of the iPSC-islets. The cultured iPSC-islets were

further characterized using bioinformatic analysis comparing against statically culture iPSC-islets to determine the effects of flow on the tissue.

2.0 Islet-on-Chip Platform for Sustained Culture and Disease Modelling

2.1 . Introduction

Diabetes mellitus is a chronic metabolic condition characterized by the loss in the ability to regulate blood glucose levels and affects a total of 460 million (9.3%) people globally with a projection of 700 million (10.9%) by the end of 2045 [54]. Type 2 Diabetes (T2D) is caused by β cell dysfunction due to various factors (age, diet, genetic factors) that results in reduced insulin secretion and sensitivity [13]. T2D is complex in its prognosis due to the variety of causes/risk factors and a host of mechanisms that have been proposed for progression of the condition [14]. The development of newer/more efficient therapeutic strategies for T2D has a major hurdle in the lack of appropriate in vitro models that can accurately mimic the physiological conditions of pancreatic islets in their natural (in vivo) environment. Additionally, the animal models that have largely been used for testing new T2D treatments don't fully represent human physiology and disease, leading to only a 10% success rate of drug treatments that enter into clinical trials[22].

To combat this issue, micro-physiological systems (MPS) have gained importance as a versatile platform due to their capability of accurately reproducing physiological microenvironment of several tissue and organ systems in vitro. This platform has been used to replicate the healthy state of organs such as heart, lungs, kidney, liver, and brain [23-28] as well as model major diseases such as cancer, non-alcoholic fatty liver disease (NAFLD), Alzheimer's disease, and renal fibrosis[29-31]. These disease models provide more accurate insight into how diseases form and progress than what can be observed in animal models that do not accurately represent human pathophysiology and enable a more human focused drug testing process rather

than targeting shared mechanisms between the animal models and human patients[31]. With T2D, islet MPS models are being developed to reproduce the dysfunctional states of pancreatic islets under T2D, with the ultimate goal of testing and developing T2D drugs[32].

A major challenge in culturing islets on MPS is sustaining their spheroid structure and major cell groups since both are critical for their ability to remain functional and respond to changes in glucose concentrations. Islets have a complex 3-dimensional (3D) structure with various endocrine cells (β, α, δ, ϵ and PP) interacting through paracrine and autocrine signaling mechanisms in order to maintain their function [55]. The islets are also surrounded by a dense capillary network lined by fenestrated endothelial cells that ensure adequate oxygenation and facilitate insulin release into bloodstream in response to increase in glucose concentration perceived by the β cells from the interstitial flow through the islet [56, 57]. Islet MPS models that focus on islet assaying with short term (<1 day) studies use various islet sources (murine, primary human, and stem cell-derived) hydrodynamic islet traps and real time monitoring of insulin release, mainly based on in situ quantitative fluorescence imaging or miniaturized immunoassays [58-61]. The hydrodynamic traps these designs implement support the islet spheroids while maintaining their positioning using the built-in structures of the device, but islets in these conditions are subjected to a continuous shear stress that would not be conducive for long-term studies (>7 days). Islets cultured under flow have been shown to lose their 3D structure and functionality due to shear stress, which gets compounded over time in culture and is undesirable [33].

Designing a long-term experiment for the purposes of disease modelling has more challenges than prolonged shear stress. Foremost among them is the issue of viability as the majority of islet microvascular network is destroyed during the process of isolation leading to reduced nutrient transport to the core of islets and eventually cell death due to hypoxia, especially

in islets of diameter >150 μm [62]. In this regard, a few islet MPS models have used osmotic perfusion and hydrodynamic traps to preserve islet structure over a longer time scale, reduce shear damage and also simulate interstitial flow in order to mimic the islet in vivo microenvironment [34, 63]. Most commonly in these, islets are placed outside of direct flow by using built-in wells as the hydrodynamic traps, but hydrogel suspension has also been utilized to prevent high levels of shear [32, 34, 64]. These methods allowed the islets to maintain insulin secretion functionality for up to 10 days[32] and 14 days[34] on device using primary human islets and murine islets respectively. Preliminary studies for T2D modelling have been carried out with the long-term MPS designs from Patel et. al.[32], with the limited focus on the combined effect of free fatty acid (palmitic acid) and high glucose.

The main aim of this chapter is to develop an islet MPS model with primary human islets for disease pathogenesis modeling and drug testing. In this chapter, we have used a microfluidic perfusion system along with hydrogel encapsulation of primary human islets in order to recreate the interstitial flow through the islets with the added benefit of the hydrogel capsule reducing the shear damage on the islets. The pancreatic islet (PANIS)-MPS platform presented in this chapter exceeds the current capabilities of supporting long term islet culture for 28 days. This extended span has enabled a thorough characterization of the effect of T2D conditions (hyperglycemia and hyperlipidemia) on human pancreatic islets followed by transcriptomic analysis to determine the alignment of the PANIS-MPS with the clinical phenotype of T2D. Additionally, the platform allows for an in-depth multi-omic characterization of the disease phenotype by enabling a complete recovery of islets from the platform. We also present the feasibility of testing drugs in PANIS model to characterize disease reversal and recovery of islet function.

2.2 Materials and Methods

2.2.1 Pancreatic Islet Description

Human cadaveric pancreatic islets were procured from Prodo labs (San Francisco, USA) and maintained in suspension using the proprietary Prodo islet media for recovery (PIM(R)) with media changes every 2-3 days, which maintains a fasting islet state at 5mM glucose. The details of the donors can be found in supplementary information (Appendix Figure 2). Islets were maintained in a 100mm x 25mm petri dish (Fisher Scientific FB0875711) suspended in 7-10mL PIM(R). Islets were initially cultured for a week in PIM(R) under static suspension conditions before adding them to the fluidic system. A 200uL pipette with SureOne aerosol barrier pipette tips (Fisher Scientific 02-707-430) was used to transfer individual islets with the aid of a dissection microscope.

2.2.2 PANIS Platform Description

The PANIS system is a 2-channel fluidic device consisting of three borosilicate glass layers with the middle layer containing a porous membrane that separates the top and the bottom chambers. The layers are made of borosilicate glass with two punch holes for inlets and outlets, the middle glass layer has an oval cut-out which contains the polyester (PET) membrane. The top and bottom glass layers have gaskets, which form an airtight chamber with a height of 200μm on either side of the middle layer when assembled. The three layers are held together within a metallic clamp which has the openings for inlet and outlet. This system of layers and clamp are the

commercially available “organ-on-chip” system procured Micronit Microtechnologies (OOC 00739, OOC Platform, Enschede, The Netherlands). The system allows for multiple possible fluid flow configurations, with the two chambers perfused independently through their dedicated inlet/ outlet in either a co-flow or counter-flow configuration; or forming a similar looped path through the chip by interconnecting the two chambers and perfusing using a flow through a single pump. We used the latter configuration, using two alternate routes: (i) inlet from the top chamber passing through and exiting the top chamber and looped into the bottom chamber, passing through the bottom chamber and exiting through the bottom chamber (ii) inlet from the top and passing across the membrane to the bottom chamber and exiting the bottom chamber. A schematic of the PANIS system along with the possible flow configurations is shown in Figure 2.1 A, B.

2.2.3 Characterization of PANIS Setup

2.2.3.1 COMSOL Simulations of PANIS Platform

A 3D computational fluid dynamics model of the Islet-on-a-Chip was created using COMSOL Multiphysics, version 6.1 (Comsol Inc., Burlington, MA) based on a previously developed model of the Micronit chip [65]. The geometry of the MPS was arranged based on the experimental setup with the membrane layer that acts as a substrate for islet culture was populated with 20 alginate capsules each containing 8 IEQs (Islets with diameter=150 μm). The inlets and outlets were defined using boundary conditions and a flow of rate of 30 μL/h was used to set the inlet velocity in the model. This model was used to characterize the flow profile, oxygen concentration, of the microphysiological system (MPS). The Navier-Stokes equation was used to model the free flow in the channel, and the Brinkmann equations were used for the porous media (alginate and islets). Fluid flow velocity with streamlines and shear stress were extracted from the

solutions of the model. Interstitial flow inside the alginate capsules was visualized using streamlines exclusively in the vicinity of alginate capsules containing islets. A similar model of the PANIS system without the alginate encapsulation was used to compare the shear stress experienced by islets cultured under flow without alginate encapsulation. The fluid flow model was coupled with a diluted species transport model to simulate oxygen distribution throughout the chip. For the oxygen concentration, the initial condition was set at 0.167 mol/m^3 (ambient oxygen concentration in the culture medium) and the oxygen consumption by the islets was modeled using Michaelis-Menten kinetics using the following equation-

$$\boldsymbol{R_{O2} = V_{max} \times c/(K_m + c)} \qquad (2\text{-}1)$$

where 'R_{O2}' is the total reaction rate for oxygen, 'Vmax' is the maximum islet oxygen consumption rate (0.034 mol/(s*m^3) per IEQ) [66] and 'K_m' is the Michaelis-Menten O_2 constant and 'c' is the oxygen concentration. A smooth Heaviside step-down function was included to arrest the reaction when oxygen concentration falls below a critical value (10^{-4} mol/m^3).[67] The other parameters of relevance in the system were the diffusion co-efficient of oxygen in water ($3.24\times10^{-9}m^2s^{-1}$), porosity of the membrane (0.057), porosity of alginate capsules (0.3) and permeability of alginate ($5\times10^{-15}m^2$).The COMSOL model was solved for a steady state (stationary) solution to determine the oxygen concentration in the device.

2.2.3.2 Flow Characterization

To determine the flow behaviour, the PANIS platform was set up with the three layers and on the middle PET layer, empty alginate capsules were prepared to simulate the conditions of the experiment without using primary human islets. Through this configuration 0.1 mg/ml of Dextran (70 kDa) conjugated with FITC in deionised water was introduced into the platform using a syringe pump at a rate of 30 µL/h. The fluorescence signal on the middle layer of the setup with empty

alginate capsules was monitored under flow using an INCell Analyzer 6000 (GE Health sciences). The entire middle layer was imaged every 15 minutes until the fluorescence signal reached a steady state.

2.2.3.3 Oxygen Concentration Measurement in PANIS

The oxygen concentration in the system was measured using fluorescence ratio imaging of oxygen sensitive beads incorporated into the alginate capsules along with the islets. The measurement was carried out in the platform in situ using an optical oxygen sensor Tris(2,2′-bipyridyl) dichlororuthenium(II) hexahydrate (RTDP), which modulate their fluorescence emission based on the amount of oxygen in the microenvironment. RTDP is loaded onto polystyrene beads which are then encapsulated along with the islets in alginate and polymerized on the membrane layer. In addition to RTDP, an oxygen insensitive dye such as DAPI is also introduced into the polystyrene beads that are loaded along with the islets following the protocol used in a previous study that used a similar platform.[65] The chip assembly is monitored at regular time intervals using an INCell Analyzer 6000 (GE Health sciences) and the ratio of the intensity of oxygen sensitive dye to the oxygen insensitive counterpart is measured at each time. The intensity of oxygen sensitive beads is indirectly proportional to the amount of oxygen present in their environment, by determining the ratio of intensities of the two types of beads at initial condition (0.167 mol/m^3) and at a condition with no oxygen (artificially created in the platform by introducing glucose oxidase which takes away all the oxygen in the system), a standard curve for the intensity ratio and oxygen concentration is determined. Oxygen concentration over the course of culture is then determined by measuring the intensity ratio from the standard curve.

2.2.4 Human Islet Cell Culture

Human cadaveric islets were obtained from Prodo Labs and were cultured both in static and on PANIS with the Prodo islet recovery media (PIM(R)). After receiving and prior to adding the islets to the device, they were cultured under static conditions for 7 d. This allowed the islets to stabilize from the shipping process. The PIM(R) served as the normal fasting state media (NF) and as the base for the toxic condition medias.

2.2.5 Calcium Signaling Measurement on PANIS

Imaging for islet calcium signaling was carried out in situ on chip in order to demonstrate the capability of the device/chip set up in carrying out functional assays on islets in culture without the need for extracting islets from the enclosed system. The islet calcium signaling was probed using a Ca^{2+} sensitive cell permeant dye- Fluo4-AM (Invitrogen, USA) which fluoresces when bound to free Ca^{2+} in the cytosol with an excitation at 488 nm and emission observed at 506 nm. Islets cultured on chip for a week in fasting medium (PIM(R)) were washed by introducing serum free solution (G55) to remove all traces of the culture media. The G55 media is composed of 500 mL Hams F10 (Cytiva SH30025.01) and 500 mL glucose free DMEM (Gibco™ A1443001) supplemented with 600 mg sodium bicarbonate, 110 mg $CaCl_2$, 25 g FAF-BSA and balanced to 7.4 pH. The base G55 has a glucose concentration of 3mM and is used for fasting conditions, and it is supplemented with D-glucose for higher glucose conditions. Fluo4-AM diluted in the serum free to obtain a final concentration of 1μM was introduced into the device with a flow rate of 30 μL/min over a period of 1h, followed by washing with serum free solution to remove excess dye. Islets in the device are then imaged in IN Cell Analyzer 6000 (GE Health sciences) first under

flow with serum free buffer with low glucose to determine the basal Fluo4-AM (Ca^{2+}) intensity. High glucose media was then introduced at a flow rate of 100 μL/min in order to purge the system of low glucose medium over a period of 5 minutes and to ensure that all the islets in system are under high glucose condition. After the 5 min period, the flow was reduced to 30 μL/min and images were taken every 30 min over a period of 2 h to track the response of islets to high glucose in terms of change in the intensity of Fluo4-AM. The data was plotted in terms of the Fluo4-AM intensity for each islet over time normalized to the low glucose intensity and a mean stimulation index over the islets (n=5) was determined.

2.2.6 Experimental Setup/ Device Setup

Islets are encapsulated in alginate droplets patterned on the membrane middle layer prior to loading onto the PANIS platform. This pattern consists of seven droplet columns along the length of the membrane that have shifted rows as seen in Figure 2.2 G. 100-200 IEQs are picked from the suspension culture and re-suspended in 12 μL of 1.1 wt.% alginate (Sigma Aldrich) solution in DMEM/F12 (Gibco™ 11330032). Droplets of this islet-alginate mixture (≈2 μL each) are formed using the described pattern on the middle membrane layer using a 20 μL pipette. The droplets are then polymerized by adding 10 mM $BaCl_2$ solution underneath the membrane and allowed to polymerize for 6 minutes. The $BaCl_2$ solution is then removed and culture media is added to dilute any residual $BaCl_2$. The middle membrane layer with encapsulated islets is then assembled along with the top and bottom glass layers in the PANIS system while taking care to prevent the formation of air bubbles. The media is fed through a syringe pump with a flow rate of 30 μL/h using sterilized tubing attached to the inlets and outlets. The flow starts at the top chamber, passes through the capsules, exits top layer into the bottom layer, flows through the bottom

chamber and out as shown in Figure 2.3 B. The entire system (PANIS device along with the syringe pump) is kept in an incubator with 5% CO_2 at 37ºC. The alginate droplets on the membrane formed as described above were characterized using AFM (Dimension Icon Atomic Force Microscope, Bruker) in fluid mode with a 20 nm tip attached to a cantilever (MLCT Bio A, Bruker) in contact mode to obtain force-indentation curves at multiple points on the capsules. The force-indentation curves were then used to determine Young's modulus by fitting the retraction curve using the JKR model.[68]

2.2.7 Characterization of Islets Cultured on PANIS Platform

At the end of culture in the flow device, the middle layer containing alginate encapsulated islets is extracted from the device and washed with 10 mL of 100 mM of EDTA balanced to a pH of 7.4 for 2-5 min to dissolve the alginate droplets and retrieve the islets for further characterization and analyses.

2.2.7.1 Live/Dead Assay

The viability of islets in the PANIS was tested using live/dead assay at the end of the set culture period. The islets were incubated according to the manufacturer's procedure with 1:4000 Calcein AM and 1:1000 Ethidium homodimer (Invitrogen Life technologies) in DMEM/F12 to selectively stain live and dead cells. Imaging was done using Olympus widefield fluorescence microscope. Viability in islets was determined by calculating the ratio of live cell area to the sum of live and dead cell area using ImageJ. The Ethd1 positive regions (dead cells) in the islets were located using ImageJ and were plotted as a function of distance with respect to the centroid of the islet in order to determine the spatial distribution of dead cell population in all the islets.

2.2.7.2 Immunofluorescence

The endocrine cell markers in islets collected after culture in the PANIS platform were examined by immunostaining for α and β cell markers such as glucagon, PDX1, C-peptide and NKX6.1. Islets collected from the device after 14 and 28 day culture were washed with PBS (×3) and permeabilized with 1% Triton X-100, 5% Donkey serum in PBS for 1 h. The islet markers C-peptide and Glucagon were co-stained using primary mouse C-peptide (R&D systems, USA) and primary rabbit glucagon (Abcam, USA) antibodies with a 1:100 dilution in the permeabilizing solution. The primary antibodies were incubated at 4°C overnight followed by washing with PBS (×3) to remove unbound antibodies. The islets were then incubated at 4°C overnight with secondary antibodies anti-mouse Alexa Fluor 488 and anti-rabbit Alexa Fluor 555 (Invitrogen, USA) in the permeabilizing solution with a dilution of 1:500 and the nuclei were marked using DRAQ5 (1:2000) (Thermofischer, USA). The other group of markers (PDX1 and NKX6.1) were co-stained by incubating primaries mouse NKX6.1 and goat PDX1 (R&D Systems, USA) with a 1:100 dilution in the permeabilizing solution overnight at 4°C followed by PBS washing and incubating with secondaries anti-mouse Alexa Fluor 647 and anti-goat Alexa Fluor 488 (Invitrogen, USA) with a 1:500 dilution at 4°C overnight. In addition to islet markers, the endothelial cell population in islets were stained using a mouse PECAM (Platelet/Endothelial Cell adhesion marker) also known as CD 31 primary antibody (R&D Systems) with a 1:100 dilution in the permeabilizing solution and incubated overnight at 4^{o}C. The primary antibody was then washed with PBS and incubated with the appropriate secondary antibody overnight at 4^{o}C and finally washed with PBS. Before imaging, the islets were whole mounted on depression glass slides using gold anti fade (Invitrogen, USA) and imaged using Fluoview 1000 (Olympus, Japan) Laser scanning confocal microscope with 40x objective with 1.32 NA The images were acquired

with an exposure time of 10 μs/pixel and a line Kalman filter. The images acquired for C-peptide, Glucagon were quantified using a basic machine learning algorithm executed in Qupath to detect the number of C-peptide and Glucagon expressing nuclei.[69] For the images obtained with CD 31 marker, the total volume fraction of CD31+ cells was calculated by measuring the area of CD31+ cells throughout the stack and normalizing it with respect to the total volume of islet.

2.2.7.3 Glucose Stimulated Insulin Secretion

Glucose stimulated insulin secretion is done under static conditions using transwells and G55 solution for both washing steps and glucose levels. For both the static suspended and on chip cultures, 25-30 islets were sampled and added to a 24 well transwell with a pore size of 3-8 μm (Corning™ 3472, Corning™ 3464). The islets were added to the transwells and washed prior to incubating in the G55 solution overnight at 37 C and 5% CO_2. Following the incubation, the islets were washed again and introduced to the low and high glucose G55 solutions for 1 h spans. Insulin was measured using ELISA kits (ALPCO 80-INSHU-E01.1)

2.2.8 Diseased State Islet Culture on PANIS

The islet diseased state is replicated on chip using the PIM(R) supplemented by 14.5 mM D-glucose. The islets are initially maintained in normal fasting (NF) medium before loading onto the chip in alginate capsules. The culture on chip is maintained in the PIM(R) supplemented with glucose (20 mM final) and/or free fatty acids (Palmitic (0.25-0.5 mM) and/or Oleic (0.5 mM) acids) for up to 28 days to observe the effects of long-term disease condition on islet viability and functionality. As a control, corresponding static cultures and on-chip cultures with normal fasting media were maintained in parallel. As in case of culture with NF media, oxygen concentration is

measured in the vicinity of the islets to observe the effect of disease condition on nutrient distribution/consumption on chip. The islets in disease condition are periodically sampled (14 and 28 days) to characterize the effect of high glucose condition on viability, islet markers and its functionality in the form glucose stimulated insulin secretion. The changes gene expression is quantified using bulk RNA sequencing for islet groups cultured on the platform with NF media and high glucose media.

2.2.9 Reactive Oxygen Species (ROS)

10-20 islets cultured in the PANIS platform from each group were decapsulated from alginate capsules by adding 100 mM EDTA and incubating for 2 minutes. They were then washed with 1X DCFDA buffer (3X). DCFDA solution was prepared by diluting 20mM DCFDA (Abcam) to a final concentration of 20 μM in 1X DCFDA buffer and added to the islets and incubated at room temperature for 1 h before a final wash with 1X DCFDA buffer and counterstained using 1 μM of Mitotracker^{TM} Red CMX ROS(Invitrogen) before imaging with Olympus Fluoview laser scanning confocal microscope. For the positive control, islets were preincubated with 50uM of Tert-Butyl hydroperoxide (TBHP) for 1 h before staining with DCFDA and Mitotracker. Islets that were cultured in normal fasting media in static were used as negative control. Islets without the DCFDA dye were imaged at the same conditions to determine the autofluorescence background. Image processing and quantification was carried out using ImageJ. ROS quantification in islets was carried out both in terms of area fraction of ROS signal and area normalized intensity of the ROS signal. For the area fraction. area of the islet showing ROS signal was determined by first subtracting the background and using the ‘threshold’ function in ImageJ to select and measure the ROS area which was then normalized to the total area of the islet. The ROS levels in the islets

were also measured by quantifying the intensity of ROS signal in islets. However, due to the size variability in islets, the ROS signal to noise intensity ratio in larger islets was lower at the core compared to the outer edge of the islet as the dye uptake is a diffusion-controlled process which results in a faulty measurement of ROS intensity. To account for this islet size effect, only the signal from the periphery of the islets was considered. The core was defined to be the region from the center of the islet up to a distance of 2r/3, where 'r' is the radius of the islet, and the remaining region was considered to be the 'periphery'. The intensity from the periphery of islets was corrected for background and mean intensity in the selected region was determined and normalized to the area of the 'periphery' of each islet. The background, threshold parameters and the definition of core and periphery was constant for all groups of islets during the analysis. Normalized ROS intensity for islet groups were represented as a fraction of the corresponding value for the islets treated with TBHP (positive control).

2.2.10 Multiplex Immunoassay

Efflux from the PANIS was collected over the course of the culture time period (14 d) for healthy and disease media conditions and the levels of cytokines were determined using the Human XL Cytokine Discovery (45-plex panel, R&D systems). The assay was carried out using manufacturer's protocol at the University of Pittsburgh Cancer Proteomics Facility Luminex® Core Laboratory. The assay was performed for each treatment condition with three replicates per experiment using the Luminex xMAP platform. The efflux cytokine data from diseased PANIS conditions was normalized with the values from the respective NF condition and represented as a heatmap/ fold change. Statistical analysis was made within the replicates of efflux data from

diseased conditions using one way ANOVA and a p-value of <0.05 was considered statistically significant.

2.2.11 Bulk RNA Sequencing

Acknowledgment: Library generation and sequencing was performed by the University of Pittsburgh Health Sciences Sequencing Core (HSSC), Rangos Research Center, UPMC Children's Hospital of Pittsburgh, Pittsburgh, Pennsylvania, United States of America.

2.2.11.1 RNA Extraction Using Qiagen Kit:

RNeasy Plus Micro Kit was used following the manufacturer's instructions.

2.2.11.2 RNA Sequencing Library Generation

RNA was assessed for quality using an Agilent TapeStation 4150 or Fragment Analyzer 5300 and RNA concentration was quantified on a Qubit FLEX fluorometer. Libraries were generated with the Illumina Stranded Total Library Prep kit (Illumina: 20040529) according to the manufacturer's instructions. Briefly, 50 ng of input RNA was used for each sample. Following adapter ligation, 15 cycles of indexing PCR were completed, using IDT for Illumina RNA UD Indexes (Illumina: 20040553-6). Library quantification and assessment was done using a Qubit FLEX fluorometer and an Agilent TapeStation 4150 or Fragment Analyzer 5300. Libraries were normalized and pooled to 10 nM by calculating the concentration based off the fragment size (base pairs) and the concentration (ng/µl) of the libraries.

2.2.11.3 Library Sequencing

Sequencing was performed on an Illumina NextSeq 2000, using a P3 200 flow cell. The pooled library was loaded at 750 pM and sequencing was carried out with read lengths of 2x101 bp, with a target of ~40 million reads per sample. Sequencing data was demultiplexed by Illumina the on-board DRAGEN FASTQ Generation software v3.8.4.

2.2.11.4 Post-Sequencing Analysis

CLC Genomic Workbench 23 was used to identify gene sequences and create the differentially expressed gene list (DEGs) between the normal fasting and toxic media treatments of the same donors. The feature gene list (gene identifiers, log2 fold change, and p-values) was exported to Ingenuity Pathway Analysis (IPA; Ingenuity Systems, Qiagen) where the data set was further filtered to exclude any differentially expressed genes that did not meet the threshold of $p < 0.05$, and an absolute value Log2 FC >1. Canonical pathway analysis was used to identify any biologically relevant pathways that were significant in comparison between the normal fasting and toxic media treatments. The feature gene list was also imported into BaseSpace Correlation Engine (Illumina) and compared against established data for type 2 diabetes.

2.2.12 PANIS as a Platform for Drug Testing

In order to test the efficacy of the Islet MPS platform for drug testing, Resveratrol (anti-oxidant)[70] was used as a supplement to the HGP toxic media to study the islet response to the drug on the platform. Resveratrol powder (Sigma Aldrich) was reconstituted in DMSO to a working concentration of 100 mM and supplemented to the HGP media at two different concentrations-10 uM and 100 uM. Islets were cultured on the MPS platform with Resveratrol supplemented HGP

media for 14 d. Islets from the same donor cultured in NF and HGP on the platform were used as control groups to gauge the healthy and disease response of the islets without the drug. After the culture period, islets were retrieved from the platform and decapsulated before characterizing for viability, ROS through live imaging, islet markers such as C-peptide and Glucagon through immunofluorescence and GSIS as described in the previous sections.

2.2.13 Statistical Analysis

All values are expressed as the mean ± standard deviation unless otherwise specified. Statistical analysis and comparisons were performed with GraphPad Prism v.8.0 using a two-tailed unpaired Student's t-test (GraphPad Software), unless specified otherwise. The following are the iterations used for p-value significance: *$p < 0.05$, **$p < 0.01$, ***$p < 0.001$, ****$p<0.0001$. All experiments were run with a minimum of $n = 3$ to run statistical significance analysis with a corresponding power analysis having a power >0.8 for all PANIS cultured results and a range of 0.33-1 for static cultured islet GSIS results.

2.3 Results

2.3.1 3D Patterning with Biomaterial Maintains Structural Integrity and Viability of Islets in PANIS

When developing the pancreatic islet (PANIS) microphysiological system, we sought to start with a design that would be highly customizable so that we could further optimize to best sustain primary islets. The commercially available Organ-on-Chip (OOC) system from Micronit Microtechnologies served as a good basis for the PANIS with its two flow chambers partitioned by a porous PET membrane which are formed by utilizing 3 borosilicate glass layers (Figure 2.1 A). To culture on PANIS, cell/ tissue would be added onto the PET membrane, followed by assembly of the device in the holder, which results in the two chambers through which the culture media would be perfused. The two flow chambers have dedicated perfusion channels for external connections, which allows for a range of flow configurations within the PANIS system, allowing for fine tuning the most suitable condition for the islets. The base options for flow (Figure 2.1 B) were found to be direct flow (yellow) over the PET membrane where tissue would be seeded, indirect flow (red) under the membrane, and crossflow (green) flowing from the upper channel to the lower channel through the membrane. In addition to flow customization, the OOC design's metal holder (Figure 2.1 A) maintains the layers' positioning and seals the system, which enables convenient assembly and disassembly of the system for cell/ tissue incorporation and retrieval respectively.

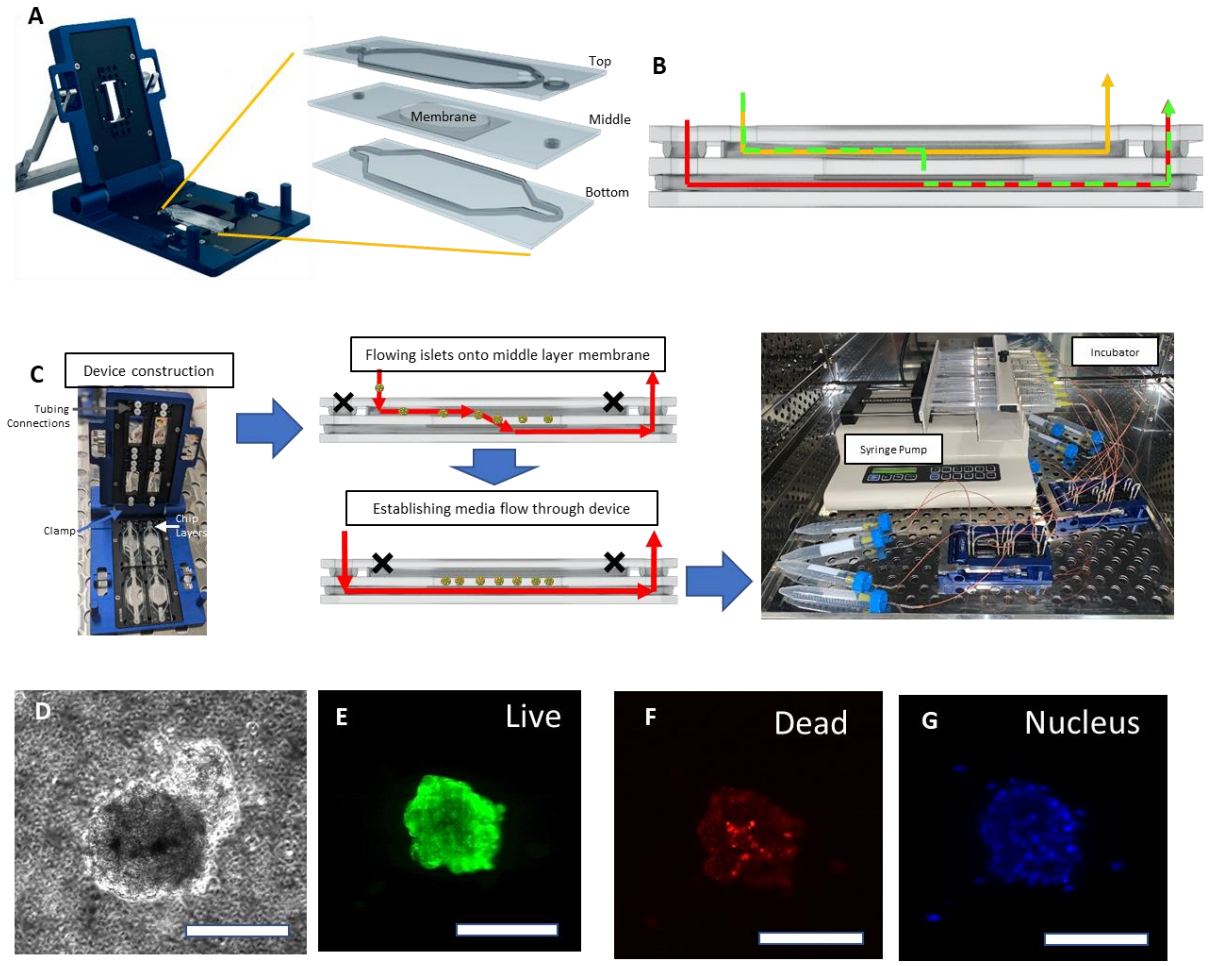

Figure 2.1 Islet MPS initial design and culture settings for 7 day study demonstrate obstacle with culturing 3D islets. (A) The 3-layer Islet-on-chip culture platform from Micronit. (B) Schematic of multiple flow configurations with islets on the membrane in the middle layer shown. (C) device setup with the seeding of islets onto the middle layer by flowing into constructed layers; (D) Primary human islets cultured in Micronit device for 8 days the islets show a loss in structural integrity as seen in the brightfield image. (E-G) The islets remain viable based on Live/dead assay. (Scale bar=50 um)

As an initial study, we wanted to determine the longevity of islets in the base PANIS design. In this, human cadaveric islets were directly loaded on the membrane middle layer by perfusing through the upper chamber using a crossflow configuration (Figure 2.1 C). The islets were maintained for a 7-day span using the indirect flow configuration at a flow rate of 15µL/h. The resulting islets showed degradation of the 3D structure as depicted in the brightfield imaging

(Figure 2.1 D) where the islets' cells began to spread and adhere to the membrane of the device, degenerating into a 2D morphology. Additionally, a viability assay revealed dead cells at the core of the islets indicating compromised cell viability in the base PANIS design (Figure 2.1 E-G). Human pancreatic islets' spheroidal morphology is highly correlated with their function [71, 72]. The degradation in the islets' structure and dead core after 7 days revealed that the islets needed some structural support to maintain their spheroid morphology and more direct flow for more effective nutrient diffusion.

As a means of supporting the islets' 3D structure, alginate hydrogel was incorporated in the device where the islets could be patterned on the membrane based on a droplet-encapsulation technique previously established by our group [73, 74]. Briefly, the islets were suspended in 1.1 wt% alginate that was then patterned in an array of alternating droplets on the middle layer's PET membrane and polymerized by diffusing a 10mM $BaCl_2$ and 10mM HEPES solution from underneath the membrane to form hemi-spherical capsules encapsulating the islets (Figure 2.2 A). The base system design provides the unique framework for forming this alginate array system with the inherent benefits of having both upper and lower flow chambers. The two flow chambers create a greater potential for nutrient diffusion to the islets with flow from each chamber and transverse to the encapsulated islets on the PET membrane. The alginate capsules serve to immobilize the islets on the membrane and protect them from flow induced shear while allowing an interstitial flow through the capsule's pores mimicking the in vivo islet 3D microenvironment. In designing the array, we optimized the capsule volume to accommodate the 0.65mm height of the upper channel and to form a diameter that would provide adequate space to avoid overcrowding the ~0.15mm islets. The three volumes tested were 2μL, 4μL, and 6μL, where each volume was dispensed onto a membrane and imaged laterally (Figure 2.2 B). ImageJ software was used to

quantify the height and diameter of each condition (Figure 2.2 C, D). As seen with the plots, both the 4μL and 6μL capsule heights, 0.78mm and 1.18mm respectively, exceeded the height of the upper channel (0.65mm) and would compress the islets after device setup. Therefore, the optimal volume was determined to be 2uL, which fit within the height limitation of the PANIS (0.59mm) and would give ample diameter (2.31mm) to avoid overcrowding of the ~0.15mm diameter islets. The mechanical properties of these capsules polymerized on the PET membrane was measured using AFM to obtain Force-indentation curves and the Young's modulus measured over multiple indentation among three capsules was found to be 8.26±2.18 kPa (Figure 2.2 E). Since the layers of the system are individually assembled, the middle layer can be then efficiently assembled with islet already embedded onto it, with the PET membrane allowing for the alginate array to properly form as the alginate can be fully polymerized by diffusing the divalent cationic solution from the bottom.

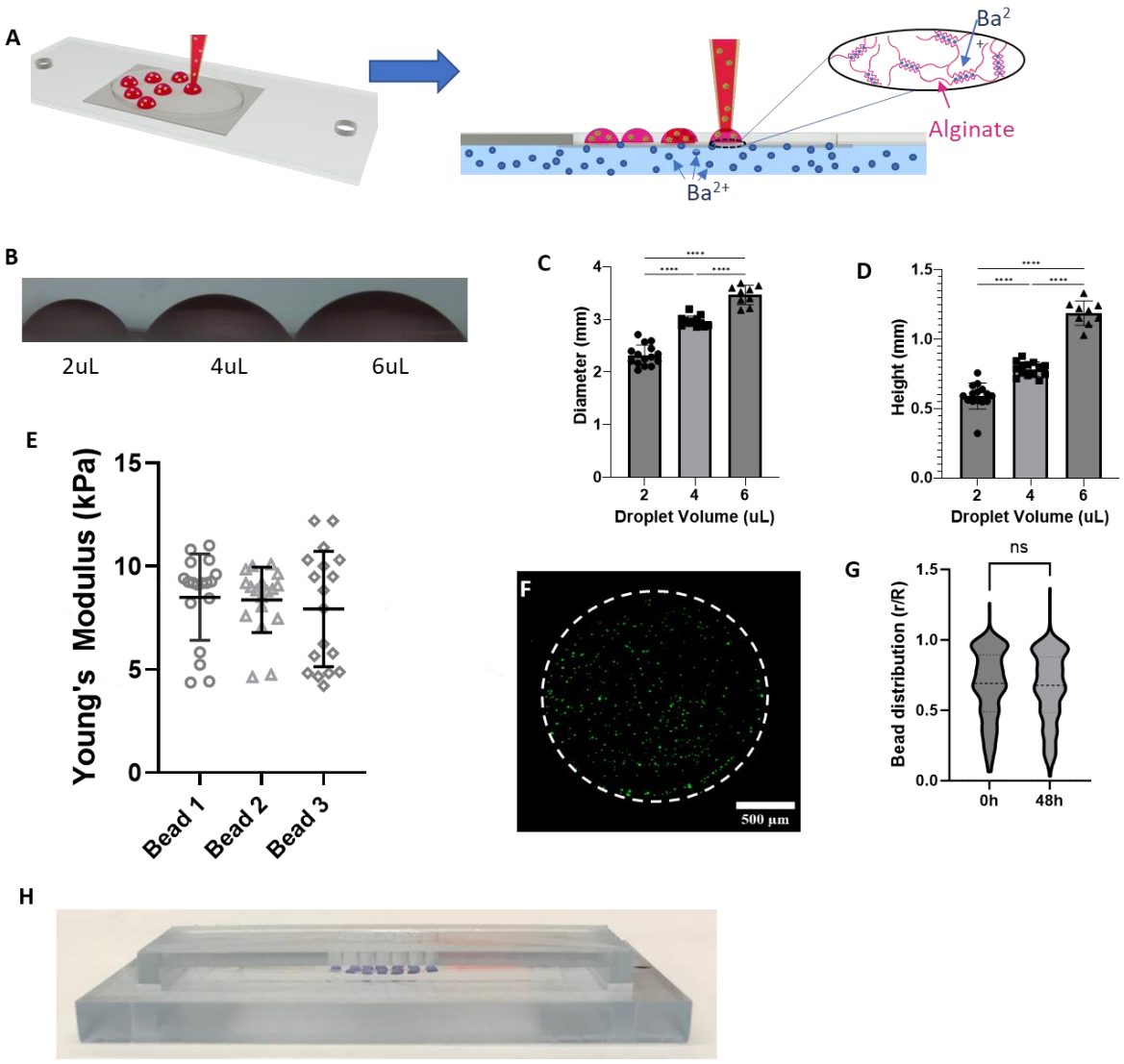

Figure 2.2 Alginate encapsulation of islets on the membrane to ensure retention of islet 3D structure. (A) Schematic of Islets encapsulated in 1.1% alginate polymerized with BaCl2 10mM + HEPES 10mM on the middle membrane layer. (B) Phase images of alginate drops of different volumes with (C, D) showing drop diameter and height (n=9-15) ($p<0.0001$). (E) Young's modulus of capsules polymerized on the membrane as determined by Force-indentation depth curves obtained from AFM, each data point represents one indentation (no statistical significance among the groups). (F, G) Fluorescent beads encapsulated in the alginate capsules subjected to flow over a 2-day span remain inside the capsule indicating that alginate capsules are stable under flow. (H) Oblique view of the template showing the set up used to pattern alginate capsules on the middle membrane layer.

To ensure that the alginate capsule array would be a sustainable platform for maintaining the islets for the duration of the culture, the durability of the capsules was tested against a 30uL/h perfusion flow by monitoring the spatial location of encapsulated fluorescent beads that served to mimic encapsulated islets. After 3 days, the alginate did not show any degradation with the day 3 timepoint having identical fluorescent bead placement as the day 0 timepoint (Figure 2.2 F). This indicates that the alginate will be capable of supporting the islets for the duration of the culture. An additional factor under consideration was the consistency in the formation of the array on the middle layer since the local flow pattern around the capsules will be dictated by the spatial arrangement of the capsules on the membrane. Hence, we designed a stereolithography (SLA) printed stencil (Figure 2.2 H) to control the dispensing of the alginate droplets when forming the capsules, ensuring consistent patterning. This provides an efficient means of dispensing the alginate onto the membrane prior to polymerization.

2.3.2 PANIS Device Flow Characterization Using In silico and In vitro Techniques.

2.3.2.1 Mathematical Modeling of PANIS to Determine Optimal Flow Dynamics and Experimental Validation.

Pancreatic islets are known to have a high oxygen demand, which is met by a majority of the blood flow through pancreas with islets accounting for 23%.[75] Due to their 3D microstructure, the islets are also susceptible to damage from high shear stress[76] under perfusion culture which is generally necessary to provide a microenvironment that mimics human physiology. While hydrogel encapsulation strategy adopted in the present study is expected to protect islets from shear stress, it can also restrict local oxygen concentration leading to hypoxia at the core of the islets. In order to determine the range of fluid flow, which maintains the required O_2 level without causing

shear damage, we developed a mathematical model of flow in the PANIS device. The alginate array layout (Figure 2.3 A) and the internal dimensions of the system (Appendix Table 1) were used to simulate the fluid flow within the system using 3D model in COMSOL. PANIS can be operated in multiple alternate flow configurations; we employed a looped flow model where the outflow from the top chamber is recirculated to the bottom chamber, thereby increasing effective residence time (Figure 2.3 B). The flow velocity predicted by the model is 3μm/s when it first enters the chamber (upstream) and reduces to 1μm/s as it passes the first column of alginate capsules, at the center it is of the order of 0.1μm/s and by the time the flow reaches the far end of the membrane, the flow velocity is ≈ 0.05 μm/s (Figure 2.3 C). The reported interstitial blood flow velocity in the capillaries surrounding the islets is in the range 0.1-2 μm/s [77]. Flow velocity in this range was observed at the interface of alginate capsules in the model as shown in Figure 2.3 D. However, flow velocities inside the alginate capsules are predicted to be in the range of 10^{-3}-10^{-5} μm/s which is orders of magnitude lower than the reported interstitial velocity of blood flow around soft tissues. The flow velocity was also visualized by the fluid flow trajectory predicted by the model (Figure 2.3 C) showing streamlines at the macro-scale across the entire device. It is worth noting that the streamlines change direction midway through the system indicating there is significant crossflow through the middle membrane layer. A closer look at the system does show streamlines crossing the boundary of the alginate capsule (shorter arrows in Figure 2.3 D), but most streamlines are along the surface of the alginate (longer arrows). The magnitude of the velocities in the vicinity of the alginate capsule (≈ 1μm/s) and the change in flow velocities at the boundary of the alginate capsules is a characteristic of interstitial flow. In addition to fluid flow profile, shear stress in the system was also extracted from the model. Shear stress along the membrane and the alginate capsules are visualized in Figure 2.3 E. The variation in shear stress is

similar to the behavior of the flow velocity in the system, it is higher ($\approx 10^{-6}$ Pa) around the capsules closer to the inlet (upstream) and decreases gradually to10^{-7} Pa around the capsules at the downstream end of the membrane. Shear stress on the islets inside the alginate capsules is much lower than around the alginate capsules and is of the order of 10^{-8} Pa inside capsules closer to the inlet and is $\approx 10^{-10}$ Pa inside the capsules at the downstream end of the flow. Alternate views of the flow velocity variation and shear stress distribution are provided in the Supplementary material (Appendix Figure 1). In comparison, islets without alginate encapsulation are predicted to be under a shear stress range of 10^{-5}-10^{-4} Pa for the same flow conditions as shown in Figure 2.3 F.

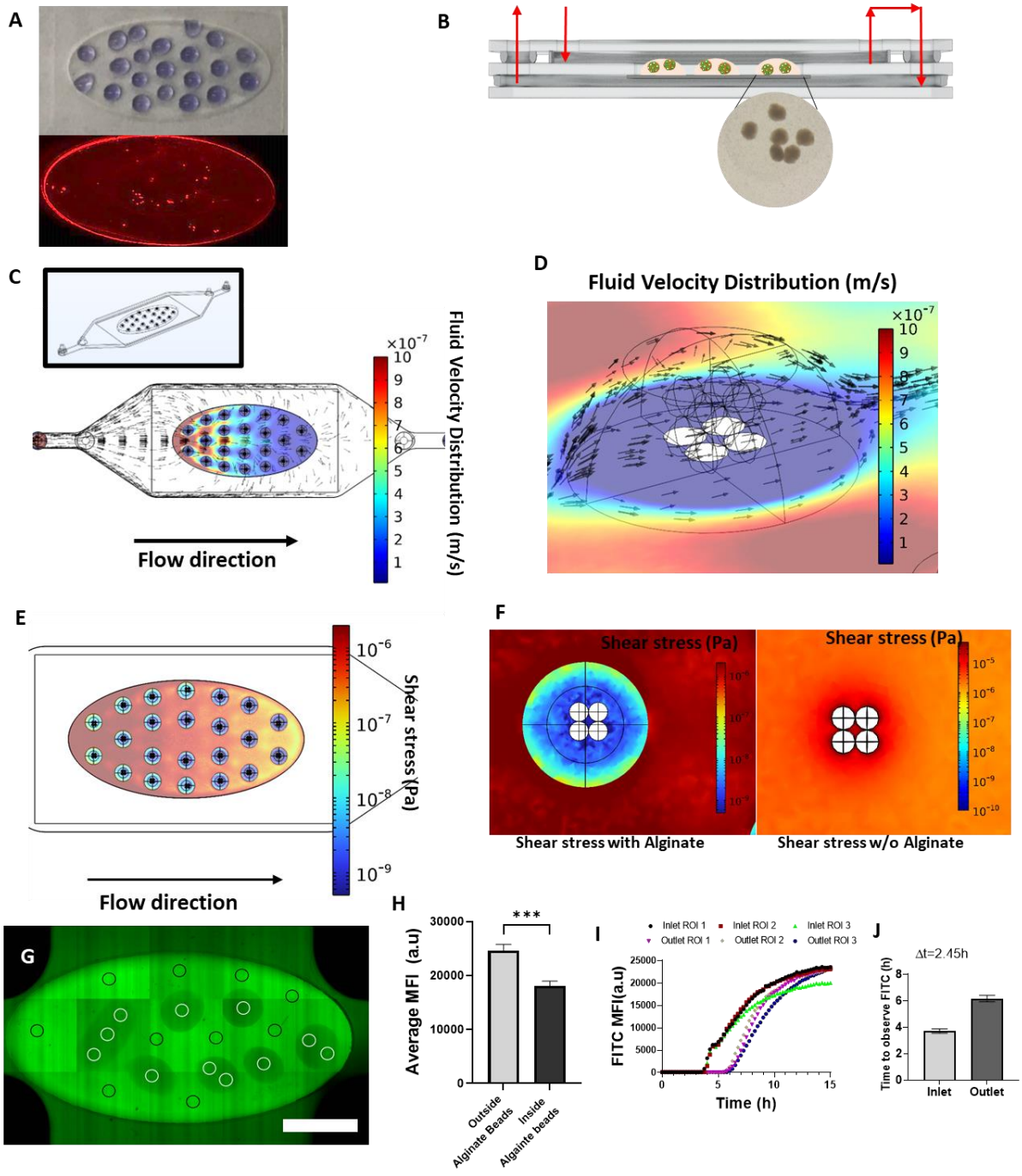

Figure 2.3 Characterization of flow using COMSOL and experimental testing. (A) Top view of the patterned alginate capsule array on the middle membrane layer and fluorescence image of the entire middle layer showing islets distributed over the entire membrane. (B) Media flow configuration with islets suspended in alginate capsules. (C) COMSOL flow model showing the streamlines (black arrows) and fluid velocity distribution in the islet on chip system for the arrangement of the alginate capsules shown in the inset and (D) showing a close-

up of flow streamlines and velocity distribution inside the capsule (close to the inlet) with velocities ranging from 1 um/s outside the capsule and going down to 10^{-6}um/s inside the capsule. (E) Shear stress distribution across the membrane along the alginate capsules with capsules closer to the inlet under a shear stress of 10^{-6}Pa and inside the capsule ranges from 10^{-10} – 10^{-8} Pa. (F) Shows a comparison of shear stress distribution in the vicinity of islets with and without alginate encapsulation in identical location on chip. Shear stress around the islets without alginate encapsulation varies between 10^-5-10^-4 Pa depending on the location in the chip, it is higher closer to the inlet and decreases along the flow direction. (G) Fluorescence image of the entire chip after introducing Dextran conjugated with FITC (Scale bar= 2.5 mm) and the MFI measured in ROIs outside (black circles) and inside (white circles) the alginate capsules in the islet on chip culture platform and the data plotted in (H) shows a statistically significant difference in MFI between the two sets of ROIs ($p<0.001$) at steady state. (I) Variation of intensity with time at the inlet and outlet of the device indicating that it takes 2.45 h (J) for the device to be completely flooded with media at a rate of 30uL/h determined by measuring the difference in time points when FITC is observed at three different ROIs at the inlet and outlet.

The PANIS alginate capsule array was set up without islets and a fluorescent dye (Dextran-FITC) was perfused through the system with the same flow rate used in culture experiments (30μL/h). The dye fluorescence intensity was monitored in situ to observe the dynamic changes in the concentration of dextran over the entire region of the middle layer including the alginate capsules. Imaging was carried out until a steady state in the fluorescence intensity was reached in the middle layer which needed approximately 16-18 h. At the steady state, the mean fluorescence intensity (MFI) in the middle layer at different ROIs are marginally lesser in the alginate capsules as shown in Figure 2.3 G, H (with $p<0.001$). A closer observation of the variation of fluorescence intensity at the inlet and outlet of the fluidic setup allowed us to estimate the total residence time of media passing through the culture platform by determining the lag between the time points where FITC intensity is first observed at the inlet and outlet which was found to be 2.5h (Figure 2.3 I, J). Further, the diffusion co-efficient of Dextran in these alginate capsules has been estimated

by assuming a Fickian diffusion model between the center and circumference of the capsule. If the concentration of dye at the center is represented by MFI 'I_C' and is 'I_O' at the circumference, the diffusion co-efficient is estimated using the equation,

$$\boldsymbol{I_c = I_o erfc\left(\frac{x}{2\sqrt{Dt\pi}}\right)} \qquad (2\text{-}2)$$

where erfc is the error function, x is the distance between center and circumference of the capsule, D is the diffusion co-efficient at different times 't'. The diffusion co-efficient estimated using this model is found to be 2×10^{-10} m^2s^{-1} which agrees within an order of magnitude of the values reported in the literature.[78]

2.3.2.2 Mathematical Modelling and In situ Measurement of Oxygen Concentration in PANIS

Islets have a high metabolic demand and require adequate oxygen and nutrient supply to maintain long-term viability and function, which is a critical constraint to overcome in islet MPS models. Our PANIS design further constraints the system with the encapsulation, by adding another transport barrier between the media in the system and islet micro-environment. Hence, we characterized our PANIS design in detail for oxygen transport, using mathematical modeling and direct measurement using oxygen sensors. the oxygen concentration profile using Michaelis-Menten kinetics by modeling the oxygen consumption rate of the islets. Figure 2.4 A shows the oxygen concentration variation in the system with 22 alginate capsules and 176 IEQ (8 per capsule) arranged symmetrically over the PET membrane at steady state conditions. The model predicts oxygen gradient across the membrane with 0.11 mol/m^3 O_2 at the inlet and 10^{-3} mol/m^3 at the downstream end of the membrane. Oxygen gradient also exists inside the alginate capsules as seen in the inset in Figure 2.4 A and the concentration ranges from 0.07 mol/m^3 at the edge of the

capsule to 3×10^{-3} mol/m^3 at the center of the islet. The critical oxygen concentration (of the order of 10^{-4} mol/m^3) is reached at the core of the islets at the downstream end of the membrane in the last column of alginate capsules (5×10^{-5}mol/m^3). Hence, the model indicates that at a flow rate of 30 uL/h, having 176 IEQs distributed across the membrane in alginate capsule will have necrotic cores in islets at downstream end of the membrane at steady state.

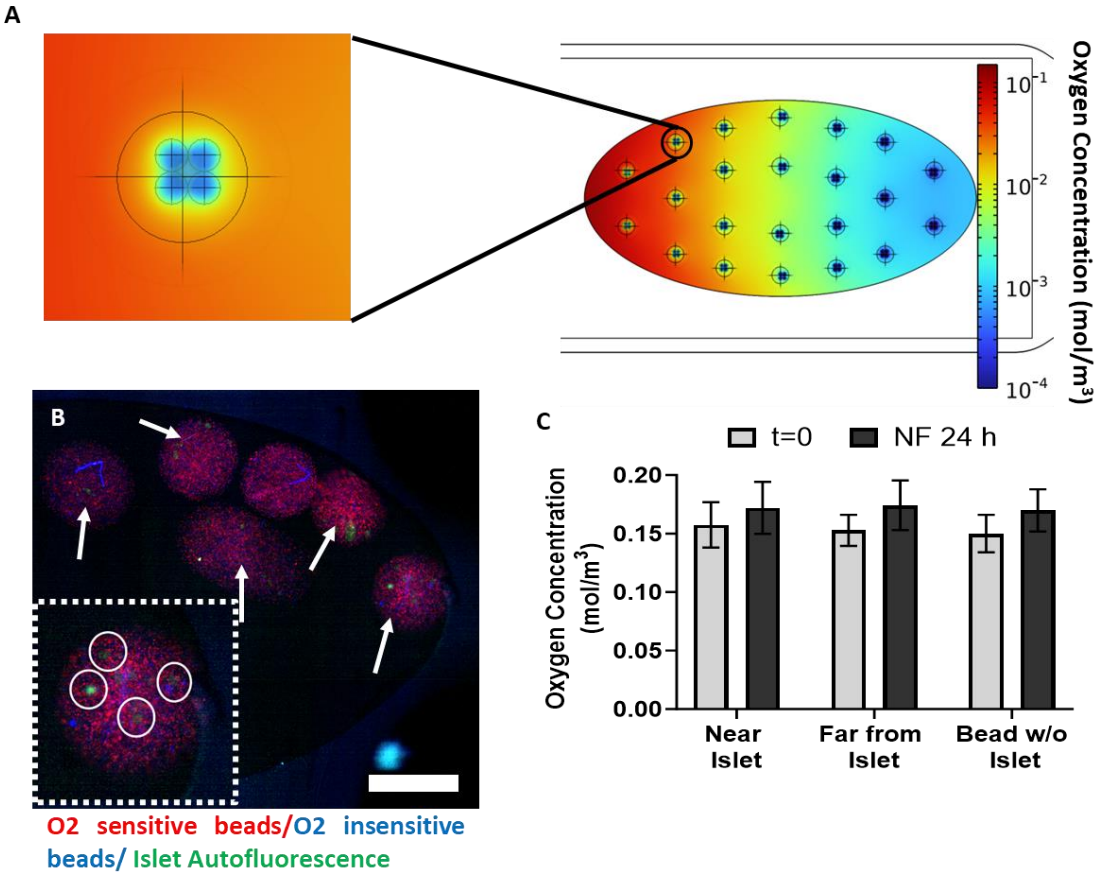

Figure 2.4 Characterization of oxygen concentration using COMSOL and experimental testing. (A) COMSOL model of islet oxygen consumption with 22 alginate capsules distributed across the membrane surface containing 8 islets each showing oxygen gradient across the membrane and inside the alginate at steady state conditions. (B) Islets encapsulated in alginate capsules (white arrows)along with oxygen sensitive (red) and oxygen insensitive (beads) Scale bar= 500 um. The inset shows a single alginate capsule containing islets with white circles designated as regions "near islet" and surrounding regions in the bead "far from islet" and (C) in situ fluorometric quantification of the ratio of the intensity of the two beads show that there is no change in the

oxygen concentration inside the alginate capsules after culture for 24h in NF with 100 IEQs . There is no statistical difference between the groups of data in (C) for $p<0.05$

With the results from the model predicting insufficient oxygen concentration in islet core at the downstream end of PANIS at steady state for 176 IEQs, we reduced the total number of islets loaded on the membrane and specifically targeted the oxygen concentration in the vicinity of the islets in alginate capsules using a fluorometric method by incorporating a mixture of oxygen sensitive and insensitive beads in alginate capsules along with islets. The initial condition (outside the chip) was evaluated by imaging the membrane layer with islets and fluorescent beads in the capsule and measuring the intensity ratio of oxygen sensitive beads to that of the oxygen incentive beads (red to blue). The ratio obtained at the initial condition (1.2±0.05) corresponds to the ambient oxygen concentration which is ≈18% or 0.167 mol/m^3 The membrane layer that was subsequently loaded onto the chip and the measurement was repeated after 24h culture on chip with normal fasting (NF) media flowing into the system at a rate of 30 μL/h. A representative image showing alginate capsules with encapsulated islets (green), oxygen sensitive beads (red) and oxygen insensitive beads (blue) is shown in Figure 2.4 B. The fluorometric ratio was found to be 1.15±0.03 and similar to that of ambient with no statistical significance ($p<0.05$) (Figure 2.4 C). This indicates that the chosen flow rate and arrangement of the capsules is sufficient to maintain the ambient oxygen levels at the proximity of the encapsulated islets within the system.

2.3.3 Islets Retain Viability, Phenotype, and Function in PANIS System

Donor pancreatic islets were patterned on the membrane middle layer, assembled on the PANIS system and perfused for 7 days with PIM(R) media using the looped flow configuration

(Figure 2.3 B) with a flowrate of 30 µL/h as determined by the COMSOL model. The islets were retrieved for post-culture characterization from the PANIS by disassembling the device, collecting the alginate capsules, and dissolving the alginate with 100mM EDTA. The resulting islets showed high viability and characteristic 3D morphology (Figure 2.5 A). Figure 2.5 B depicts a representative fluorescent image of an islet stained for c-peptide (green) positive cells (representing β-cells) and glucagon (red) positive cells (representing α-cells). Based on the high live cell population (Figure 2.5 A) and prominence of α and β-cells (Figure 2.5 B), the encapsulation ensured that both the viability and phenotype of islets were preserved during culture on chip for a 7-day duration.

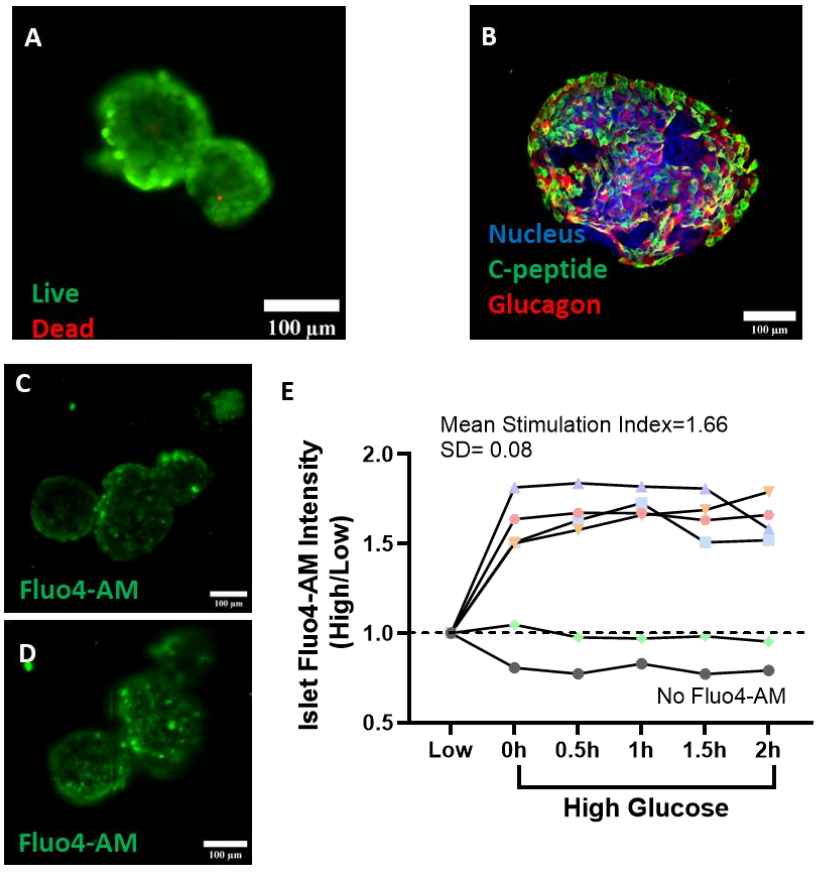

Figure 2.5 Islets retain structure and function under flow in PANIS for 7 days. Representative images showing islet viability (A) and expression of C-peptide and glucagon markers (B). Islets loaded with Fluo4-AM under low (C) and high (D) glucose media and (E) summarizing the time variation of Fluo4-AM intensity under high

glucose medium for multiple islets showing a mean stimulation index of 1.66. The intensity of islets without Fluo4-AM are included for reference.

A key function in islets is the release of insulin in response to increasing levels of glucose, traditionally tested in vitro using a glucose stimulated insulin secretion (GSIS) assay where islets are subjected to varying levels of glucose and insulin levels are measured post-assay. This functionality assay for islets can also be done using fluorescence based Ca^{2+} imaging (Fluo4-AM), which allows a direct correlation between the signal intensity and the activity of calcium ions in the cytosol that directly correlates with the secretion of insulin. One of the advantages of using a glass-based system is that it allows in situ monitoring of the device using fluorescent monitoring, such as with Fluo4-AM. Figure 2.5 C, D shows representative images of islets on PANIS stained with Fluo4-AM dye subjected to low and high glucose media conditions. The change in dye intensity was measured after purging the system of low glucose by introducing high glucose media over a period of 5 min. and was measured over time for individual islets and normalized to their respective low glucose intensity in Figure 2.5 E. All the islets show an increase in fluorescence intensity, and consequently insulin secretion from the increase in glucose. The stimulation index (SI), calculated by the ratio of high to low intensity, remained in the range of 1.5 and 1.8 over the course of 2h of imaging, with a mean value of 1.66 ±0.08 (Mean ±SD). The response of islets without Fluo4-AM loading is also shown for reference.

One of the critical requirements for MPS models to enable disease modeling is to establish long term culture of the organs with retained phenotype and function. Having demonstrated 7-day viable islet culture in our PANIS system with maintained islet phenotype and function (Figure 2.5), we next continued the culture of the islets in the PANIS for more prolonged periods, extending to 28 days. After 14 and 28 days, islets retained high viability, as determined with

live/dead assay conducted post retrieval from the system with representative images shown in Figure 2.6 A, B for a 14-day and 28-day culture respectively. The islets cultured on chip show high viability (>0.8) at both time points with no statistically significant difference between the two groups (Figure 2.6c). Further analysis of the spatial distribution of dead cells within the islets (Figure 2.6 D) indicate that majority of them are in the outer regions of the islets (r/R>0.6) indicating that the observed death is unlikely due to nutrient starvation or lack of oxygen which would result in a death at the islet core. Comparing the dead cell distribution in islets with time indicates that there is no significant difference between the 14-day and 28-day time points for $p<0.05$.

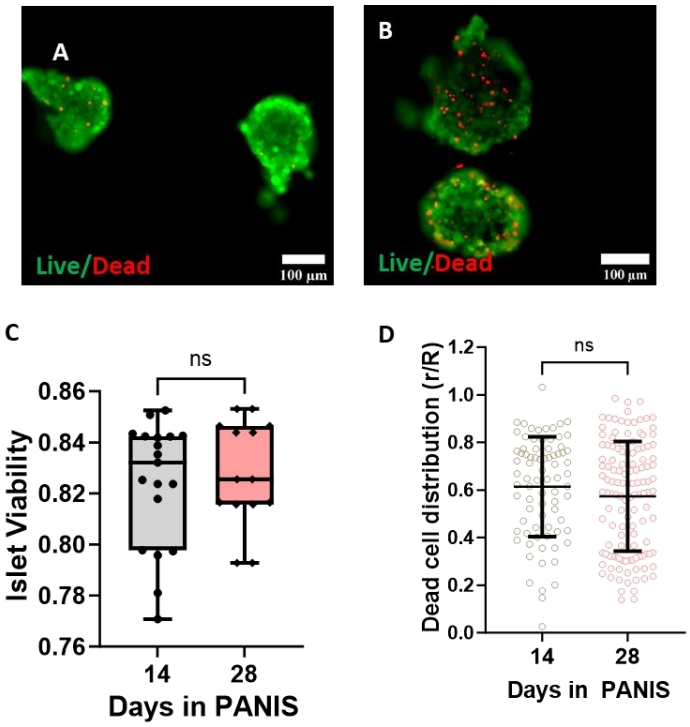

Figure 2.6 Viability of islets over extended periods of culture in the MPS device. (A,B) Representative images showing islet viability under on-chip culture in fasting medium (NF) for 14 days and 28 days respectively. (C) Quantification of islet viability on chip under fasting condition at 14 and 28 days showing no statistical significance between the groups ($p<0.05$). (D) Distribution of dead cells in the islets at both time points

indicating that a majority of the dead cells are located in the regions corresponding to r/R>0.6 without any statistically significant difference in the distribution between the two time points ($p<0.05$).

The phenotype of the cultured islets was characterized by immunostaining for key islet transcription factors PDX1 and NKX6.1, and hormones C-peptide (analogous to insulin) and glucagon. As shown in Figure 2.7a, the islets cultured on PANIS for 28 days retained distinct PDX1(green) and NKX6.1 (red) expression, which were comparable to that of parallel static suspension culture (Figure 2.6 B). Quantification of immunostaining for static and PANIS culture for 28 days (Figure 2.7F) indicates a minor shift in the fractions of PDX1 (decreasing) and NKX6.1 (increasing) positive cells in islets cultured in PANIS, but the difference was not found to be statistically significant ($p<0.05$). Interestingly, immunostaining for C-peptide and Glucagon showed some differences between the static and PANIS culture. The islets cultured on PANIS sustained distinct hormone expression after 28 days of culture (Figure 2.7 C). In contrast, islets at 7 days of static culture showed distinct C-peptide and Glucagon expression levels distributed throughout the islets (Figure 2.7 D), which became progressively localized by 28 days of static culture (Figure 2.7 E).

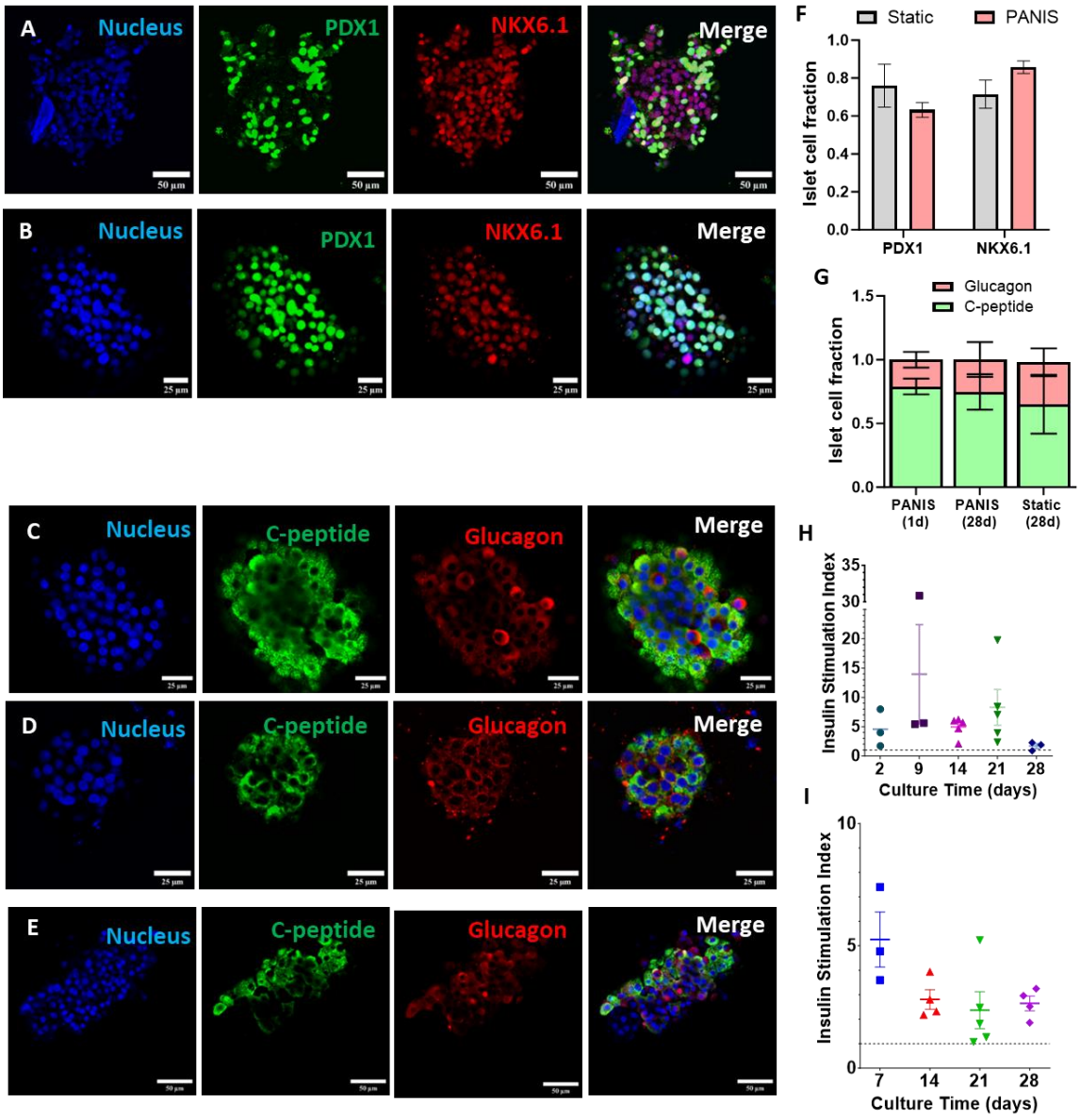

Figure 2.7 Immunostaining for islet markers and Islet insulin response to glucose stimulation. (A-B) PDX1 (green) and NKX6.1 (red) expressions (A) Islets cultured on PANIS for 28 days, (B) Islets cultured in static condition for 28 days and the row. (C-E) C-peptide (green) and Glucagon (red) positive endocrine cells in (C) islets cultured in static condition for 7 days prior to placing on PANIS (day 1 for PANIS), (D) islets cultured on PANIS for 28 days, (E) islets cultured in static for 28 days. (F) Quantified cell fractions of PDX1 and NKX6.1 positive cells for (A,B) 28 day PANIS and static cultured islets. (G) Comparison of cell fraction for C-peptide and Glucagon positive cells for islets cultured in static for 7d and 28d and islets cultured in PANIS for 28d.

(H) GSIS-based insulin stimulation index of islets cultured in static conditions over the course of 28 days (n=3). (I) GSIS-based insulin stimulation index for islet cultured on PANIS over the course of 28 days (n=3-5).

As discussed previously, islet functionality is tested through glucose stimulated insulin secretion (GSIS), which involves measuring the levels of insulin secreted against serial exposure of the islets to alternating low (3 mM) and high (16 mM) levels of glucose. Islets from one donor were tested 2 days after receiving and then weekly for 28 days in static culture, to determine the baseline progression of insulin expression with prolonged culture periods. The focus with this is to assess for proper increased of insulin secretion stimulated by increased concentrations of glucose, which is noted with stimulation index (SI). As shown in Figure 2.7 H, the islets were sensitive to glucose levels even at the first tested time point of 2 days (SI 4.56), but their SI was higher at 9 days of culture (SI 13.95). The SI remained unaltered with SI 4.95 at 14 days and increased with continued culture for up to 21 days (SI 8.30), but further culture to 28 days resulted in a reduction of the SI (1.68). To compare the GSIS test to the static study, PANIS islets were retrieved by disassembling the device and subjected to the static GSIS procedure. Figure 2.7 I presents the SI for PANIS cultured islets after 7 days (SI 5.26), 14 days (SI 2.81), 21 days (SI 3.15) and 28 days (SI 2.65) of culture. Since this required the device to be disassembled, each timepoint for PANIS used islets from different donors. As such, each tested timepoint demonstrated similar SI. Additionally, even at 28 days of culture the islets in PANIS (SI 2.65) retained higher SI compared to static culture (SI 1.68). Overall, these results show the effectiveness of our PANIS system in retaining the viability and phenotype of human islets over long term culture and, most importantly, retain GSIS function over 28 days of culture in PANIS and over 42 days of culture post-isolation.

2.3.4 Endothelial Cell Population in PANIS Islets

Another metric for viewing islet health is in the presence of the native endothelial cell (EC) population since ECs in islets strongly correlates with islet health and insulin secretion[79, 80]. To assess the EC population, we used fluorescent imaging to detect cell positive for the EC surface marker, CD31. Representative images of ECs in islets at the start of PANIS setup, which is equivalent to 7 days in static culture post receiving, are shown in Figure 2.8 A. The dense vascular network that is inherent to islet physiology[81] can clearly be viewed. Islets were sampled from PANIS and static culture after 28 days of culture to check how each culture environment would affect the ECs (Figure 2.8 B, C). Both culture types show a degradation in the vascular network, but the quantity of ECs within the static culture appears lesser than those in PANIS. The prominence of the EC populations for the initial PANIS timepoint and 28-day culture conditions were quantified using image analysis to calculate volume fractions of $CD31^+$ cell population in islets (Figure 2.8d). Based on this quantification, both the 28-day cultures showed a significant decrease in ECs compared to the earlier timepoint, but the islets cultured in PANIS retained a significantly ($p<0.0001$) higher fraction of their CD31+ cells than the static culture (Figure 2.8 B). This is potentially due to the perfusion from the PANIS aiding in EC growth, which has shown to be linked in literature[82, 83], or improved cross-talk between ECs and β-cells may help with EC growth[80, 84].

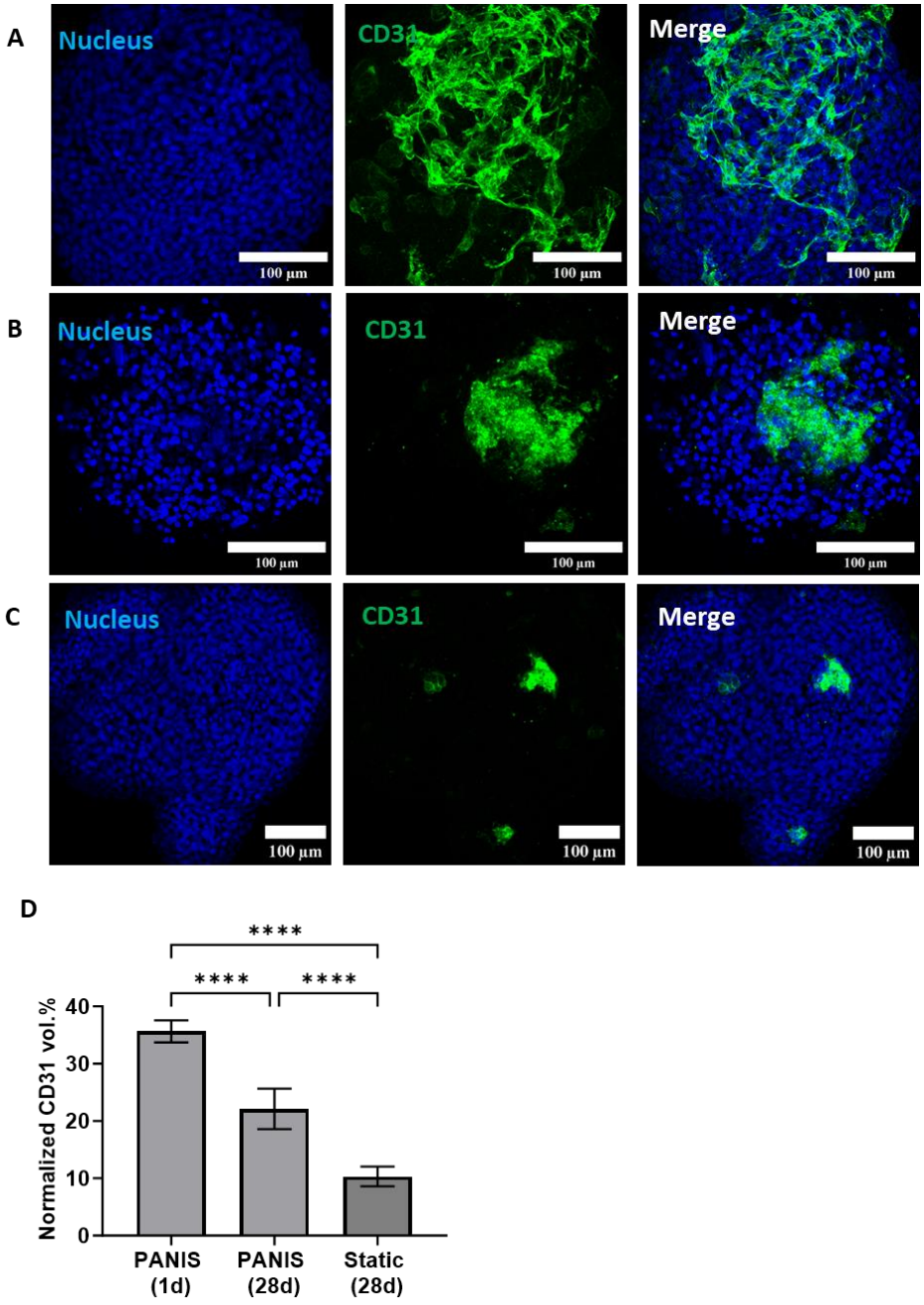

Figure 2.8 Comparison of CD 31 expression in islets in various conditions of culture. (A) islets cultured in PIM(R) in static condition for 7 days in static prior to PANIS setup showing a network of endothelial cells in the islet. (B) Islet cultured under flow in islet on PANIS for 28 days. (C) Islet culture in fasting medium in static condition for 28 days showing a significant loss in endothelial cell population. (D) Quantification of the total vol.% of CD31 population in the islets (n>5). (** indicates p<0.0001)**

2.3.5 T2D Disease Relevant Toxic Treatments in PANIS Platform

2.3.5.1 High Glucose Treatment

Having established the feasibility of long-term culture of the primary human islets in our PANIS system under normal fasting (NF) conditions, we next evaluated the feasibility of simulating a T2D disease condition in PANIS and determine the response of the islets to specific environmental toxicants. With hyperglycemia having the strongest correlation to T2D, our initial toxic treatment for the PANIS was a prolonged culture (14 days) with high levels of glucose (HG) by supplementing the PIM(R) media with glucose to make a 20mM final concentration.

To probe the effect of HG-treated PANIS on cell toxicity, the viability of the islets was characterized by live/dead assay (Figure 2.9 A, B). Overall, the viability was found to be comparable between the HG-treated and that of NF cultured islets, with mean viability >0.8 (Figure 2.9b), and a closer look at the distribution of the dead cells shown in Figure 2.9 C shows that the dead cell distribution under HG-treatment has a similar distribution to NF.

Looking at islet endocrine cell phenotypes, the number C-peptide and Glucagon positive cells in HG-treated PANIS is observed to be similar to the NF control (Figure 2.9 D, E). The resulting functionality of HG-treated PANIS islets was tested with GSIS at the end of 14 days to determine any change in insulin SI compared to NF control (Figure 2.9 F). Islets cultured within the HG-treated PANIS demonstrated a diminished GSIS response with a 1.18 SI with the NF control having a 2.81 SI. We wanted to see if this is a consequence of O_2 deprivation due to altered islet metabolic state under HG condition.

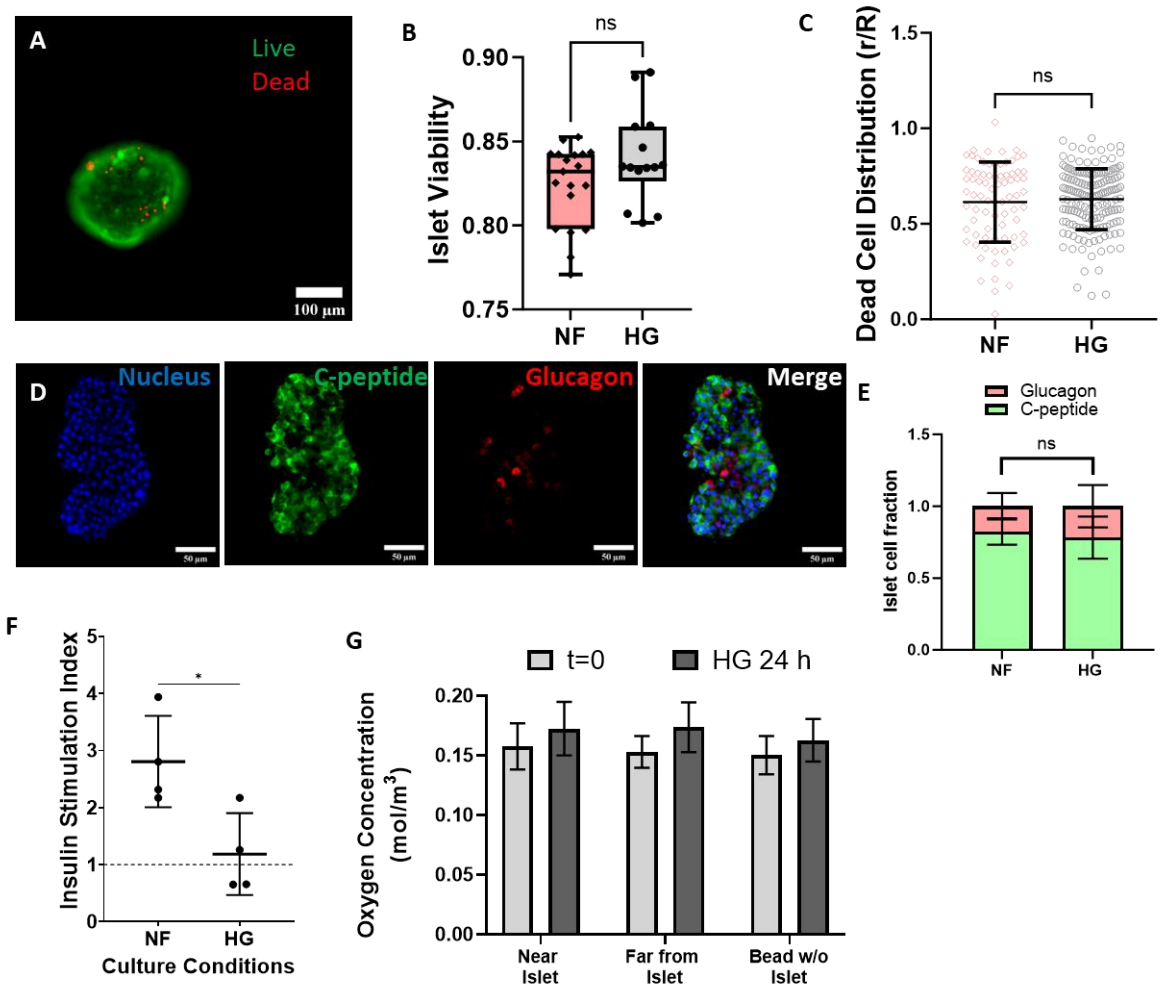

Figure 2.9 Characterization of islet phenotype after 14-day culture with high glucose (HG) treatment. (A) Representative images showing islet viability on PANIS under a 14 day high glucose (HG) media treatment. (B) Quantification of viability of the HG-treated PANIS showing no statistically significant difference in viability ($p>0.05$). (C) Distribution of dead cells in the islets in HG treated PANIS ($p>0.05$). (D) Representative images showing islet endocrine cell markers C-peptide and glucagon for HG-treated PANIS islets. (E) Image analysis calculated fractions of C-peptide and Glucagon positive cells for NF and HG-treated conditions ($p>0.05$). (F) Insulin stimulation index from GSIS of islets cultured on PANIS for both NF and HG-treated conditions ($n=4$) ($p<0.05$). (G) Oxygen concentration measurements show that the islets cultured in PANIS are not oxygen deprived after 24 h of culture with HG media (oxygen concentration is not significantly different among the groups after 24 h in HG media)

We tested the oxygen concentration in the system, in the proximity of the islets, by co-encapsulating the islets with oxygen sensitive and insensitive beads, followed by perfusion with high glucose medium (20 mM). Empty alginate capsules (without any islet) in the same system were used as a control. The fluorescent beads were imaged after 24 h in culture, and the intensity ratio between red and blue beads were recorded both for blank capsules and those with islets. The ratio of the intensities of red to blue beads were observed to be similar to that of fasting condition and there was no significant difference in the oxygen concentration ($p>0.05$) indicating adequate O_2 supply in the system even under the toxic treatment (Figure 2.9 G). Since the nutrient supply was not a factor that would cause damage to the islets with the HG-treated PANIS, the source of the decreased insulin stimulation index would be from the prolonged exposure to high glucose.

We conducted a similar set of analyses for a 28-day study for PANIS subjected to high glucose treatment (HG-28) with a normal fasting control (NF-28), found in Appendix Figure 2. After the more extensive culture in the toxic media, the viability of the islets had a significantly ($p<0.05$) higher viability than NF-28 (Appendix Figure 2 A, B), but there is significantly ($p<0.01$) more death within the core of the HG-28 compared to NF-28 based on the dead cell distribution analysis. Phenotypically, the HG-28 islets don't significantly ($p>0.05$) differ from NF-28 for both islet specific transcription factor (PDX1/NKX6.1) positive cells (Appendix Figure 2 D, F) and islet endocrine (C-peptide/ Glucagon) positive cells. We also looked at how HG-28 PANIS affects ECs compared to NF-28 through CD31 fluorescent imaging and image analysis (Appendix Figure 2 H, I). In this, the HG-28 had significantly fewer CD31+ cells than NF-28 ($p<0.0001$).

2.3.5.2 Lipotoxic Treatments

To further test the capability of the PANIS system to induce a diseased state through toxic culture treatments, we introduced high concentrations of free fatty acids, oleic acid (0.5mM) and

palmitic acid (0.25mM), which correlate with T2D [85-87]. We sought to determine the effects of free fatty as a standalone toxic state (HPO) and in combination with high levels of glucose. Additionally, we wanted to determine the protective effects of the unsaturated oleic acid with the high glucose combination.[88-90] As such, two glucolipotoxicity treatments were tested: high glucose with palmitic and oleic acids (HGPO) and high glucose with only palmitic acid (HGP). Primary islets were cultured with these toxic media treatments on PANIS for 14 days. The islets cultured in high lipid conditions after 14 days showed higher dead cell populations in conditions compared to NF as shown in representative images in Figure 2.10 A-D with the palmitate only condition (HGP) having the lowest viability (<0.8) with a statistically significant difference ($p<0.0001$) compared to NF (Figure 2.10 E). Inclusion of Oleic acid in the cocktail (HGPO) favored the viability, while high oleic and palmitic acids in combination with normal fasting levels of glucose (HPO), interestingly, further compromised viability. The phenotype of the resulting islets, with focus on C-peptide and glucagon positive cell populations, (Figure 2.10 F-I) showed a decrease in C-peptide positive cells with high glucose and free fatty acid supplemented conditions, but no such difference was observed in free fatty acid only condition (HPO). Quantification of C-peptide positive cells (Figure 2.10 J) reveal a statistically significant reduction in the C-peptide positive β-cells from the fasting state for both HGPO (Mean= 0.57, $p<0.01$) and HGP (Mean= 0.53, $p<0.001$) conditions, with no significant difference between NF (Mean=0.82) and HPO (Mean=0.64). It is important to note that though the statistical significance of β-cell fraction in HGPO and HGP compared to NF are at different p levels, there is no significant difference between the groups HGP and HGPO. Glucagon positive α-cells on the other hand, did not have any statistically significant change across conditions, indicating that the insulin secreting β-cells are more susceptible to damage from high glucose and free fatty acid environment.

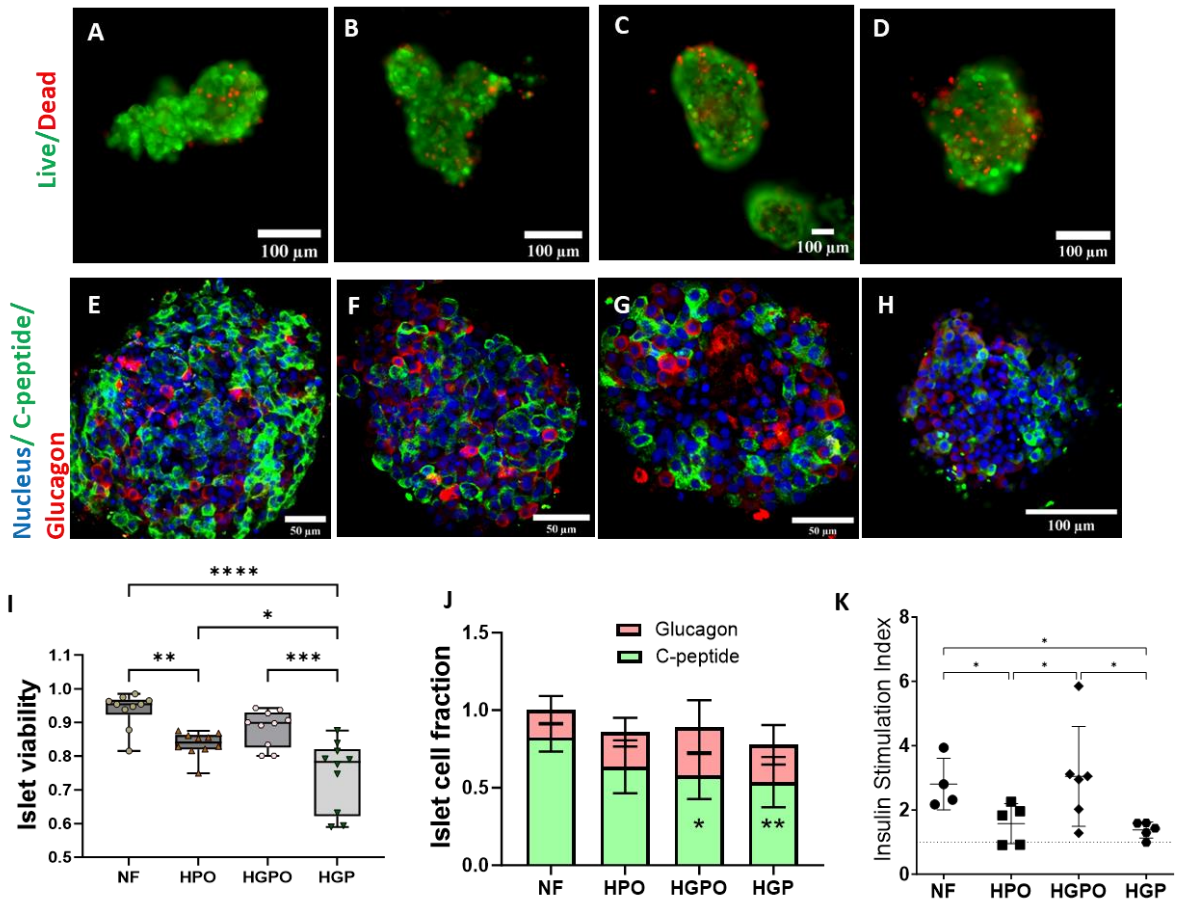

Figure 2.10 Lipotoxic-based treatments for 14 days on PANIS. (A-D) Viability of islets on chip with live (green) and dead (red) cells after 14 days in culture with (A) NF condition, (B) lipotoxic media treatment with high palmitic and oleic acid (HPO), (C) glucolipotox media treatment with high glucose, palmitic and oleic acids (HGPO), (D) glucolipotox media treatment with just high glucose and palmitic acid (HGP). (E-H) Immunofluorescence of C-peptide (green), glucagon (red), and nucleus (blue) for islets cultured for 14 days in (E) NF conditions, (F) HPO, (G) HGPO, and (H) HGP. (I) quantification of live/dead images (and **** represent $p<0.01$ and $p<0.0001$ respectively). (J) quantification of C-peptide and glucagon(* and **represents statistical significance with $p<0.05$ and $p<0.01$ respectively). (K) GSIS-based insulin stimulation index for islets cultured in NF, HPO, HGPO, and HGP conditions.**

The functionality of the islets was tested with GSIS to obtain the insulin stimulation index (SI) (Figure 2.10 K). The most detrimental effect of the toxic media was observed in HGP-treatment, with a significantly ($p<0.05$) lower SI of 1.3. Inclusion of Oleic Acid in the HGPO-

treatment protected the islets' SI to a similar level as the NF state (SI 2.8). Lowering the glucose levels in the HPO condition increased the level of insulin secretion similar to that of the fasting state but compromised the insulin stimulation index (SI 1.4) which was significantly lower ($p<0.05$) compared to the NF state (SI 2.8).

2.3.5.3 Multiplex Immunoassay

Multiplex Immunoassaying provided secreted factors from the islets under the four different toxic media treatments (HG, HPO, HGPO, and HGP) normalized to their corresponding donor NF condition (Figure 2.11 A-E). The heat map depicting the major measured secreted factors (Figure 2.11 A) demonstrates the variation of outcome from each of the toxic treatments. HPO and HGP show an overall increase (red) in cytokines and angiogenic factors compared to NF, while HGPO has an overall lower (blue) or similar (white) secretion profile to the NF condition. The most prominent pro-inflammatory cytokines for all the toxic treatments were CCL2, CCL20, CXCL1, CXCL2, IL-6, G-CSF, and IL-1ra, and the most prominent angiogenic factors were IL-8, TNF-α, VEGF, and PDGF-AA, which are depicted in condition specific plots normalized to NF (Figure 2.11 B-E). The HG, HPO, and HGP conditions had an increase in secretions of these inflammatory factors compared to the NF control (Figure 2.11 B, C, E), while the HGPO condition showed an inverse effect with lower secretions compared to NF. With this stark contrast between the HGP and HGPO treatments, there is an indication that the inclusion of the unsaturated oleic acid in the gluco-lipotoxic condition may provide some anti-inflammatory aid to the islets. The secreted angiogenic factors show a similar trend with the pro-inflammatory factors, where HG, HPO, and HGP demonstrate an overall increase compared to NF, but HG and HPO show a higher fold increase than HGP. HGPO shows no significant fold change from NF, since all angiogenic factors are near one.

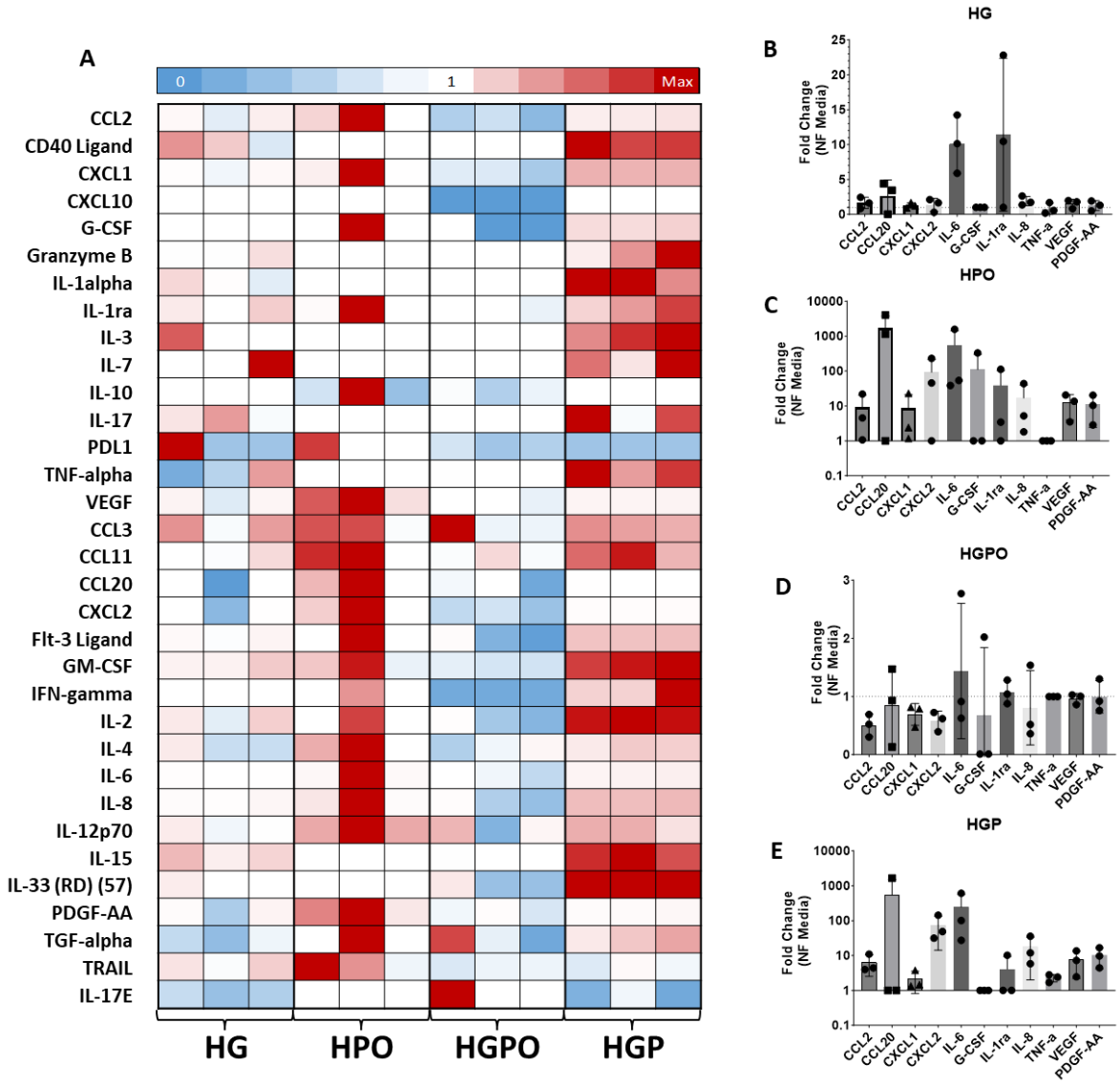

Figure 2.11 Multiplex Immunoassay data for PANIS secretomes under healthy (NF) and toxic conditions (HG, HPO, HGPO, HGP).(A) Heatmap for all prominent secreted factors normalized to the corresponding donor NF values. (B-C) Condition specific plots of prominent inflammatory cytokines (CCL2, CCL20, CXCL1, CXCL2, IL-6, G-CSF, IL-1ra), angiogenic factors (IL-8, TNF-α, VEGF, PDGF-AA) for HG, HPO, HGPO, and HGP respectively.

Based on the cytokine panel, we wanted to see how the inflammatory and angiogenic factors that resulted from each of the toxic treatments may affect the intra-islet endothelial cells (EC) population. As stated previously, the prominence of ECs is strongly correlated with the

functionality of primary islets[79, 80] and can be used for evaluating the condition of islets and determine if they have developed any T2D EC physiology[91]. The presence of CD31+ cells was evaluated in islets cultured on PANIS for 14 days in NF, HG, HPO, HGPO and HGP media conditions. The representative images for the CD31+ cells in islets from these groups are shown in Figure 2.12 F-J, while Figure 2.12 K illustrates the quantitative analysis of CD31+ cells. Consistent with the results in our other metrics for islet health, the most significant reduction of CD31+ cells was observed in the HGP media condition where the ECs were isolated clump without any networks and only 5 vol.% of the islet accounting for CD31+ cells (Figure 2.12 J, K) with a statistically significant difference compared to NF ($p<0.0001$). The addition of Oleic acid with the HGPO treatment showed a significantly higher EC population (12 vol.%) compared to HGP ($p<0.05$). The most dramatic difference was observed with the HPO media treatment, which showed a more prominent retention of the vascular network within the islet; however, the volume fraction of the ECs was not significantly different from the NF or HG conditions ($p>0.05$). Since both HG and HGP showed an increase in secreted angiogenic factors compared to NF (Figure 2.11 B, E) but showed similar if not lower EC population than NF, this indicates there are other factors involved in both the dysfunction to the ECs and to the islets themselves.

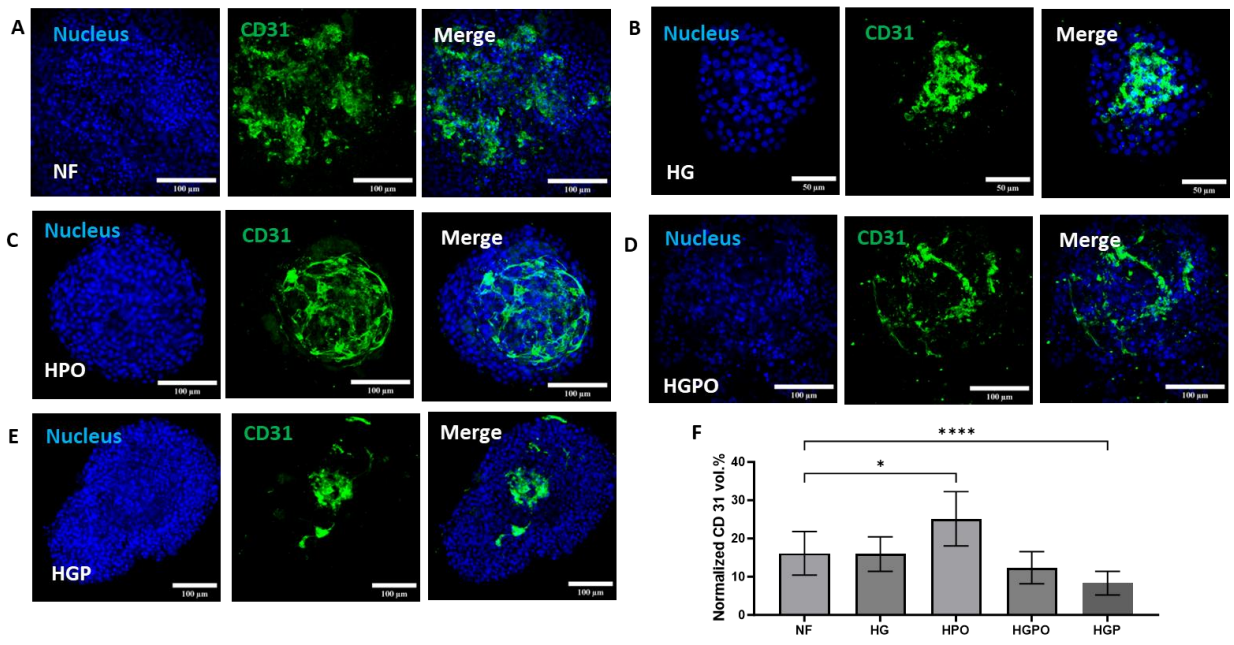

Figure 2.12 Comparison of CD31 expression in islets cultured under toxic conditions for 14 days. Islets cultured in (A) NF, (B) HG (C) HPO, (D) HGPO and (E) HGP media showing CD31+ endothelial cells in healthy and toxic media conditions. (F) Quantification of the amount of CD31+ cells in the islet in these groups with a minimum of 10 islets per group showing significant increase in HPO and a decrease in HGP toxic conditions (** represents p<0.0001 and * represents p<0.05).**

2.3.5.4 RNA Sequencing

Illumina mRNA sequencing provides us a more in-depth analysis into the effects of the toxic media treatments on the PANIS system. With this, we sequenced each of the four toxic treated PANIS conditions (HG, HPO, HGPO, HGP) with each encompassing 3 PANIS replicates and limiting each to one donor to minimize donor-to-donor variance, since the scope of this analysis is with the effect of toxic treatment on PANIS system. The principal component analysis (PCA) plot (Figure 2.13 A) depicts each of the tested conditions (noted by color and label) and each specific donor (noted by symbol). The plot demonstrates the grouping of the NF and toxic treatments regardless of donor, where the majority of NF samples fall below -30 for principal component 2 (PC2) and

all toxic treatments samples are above -10 for PC2, which indicates that the healthy NF condition and toxic treatments have consistent changes across different donors.

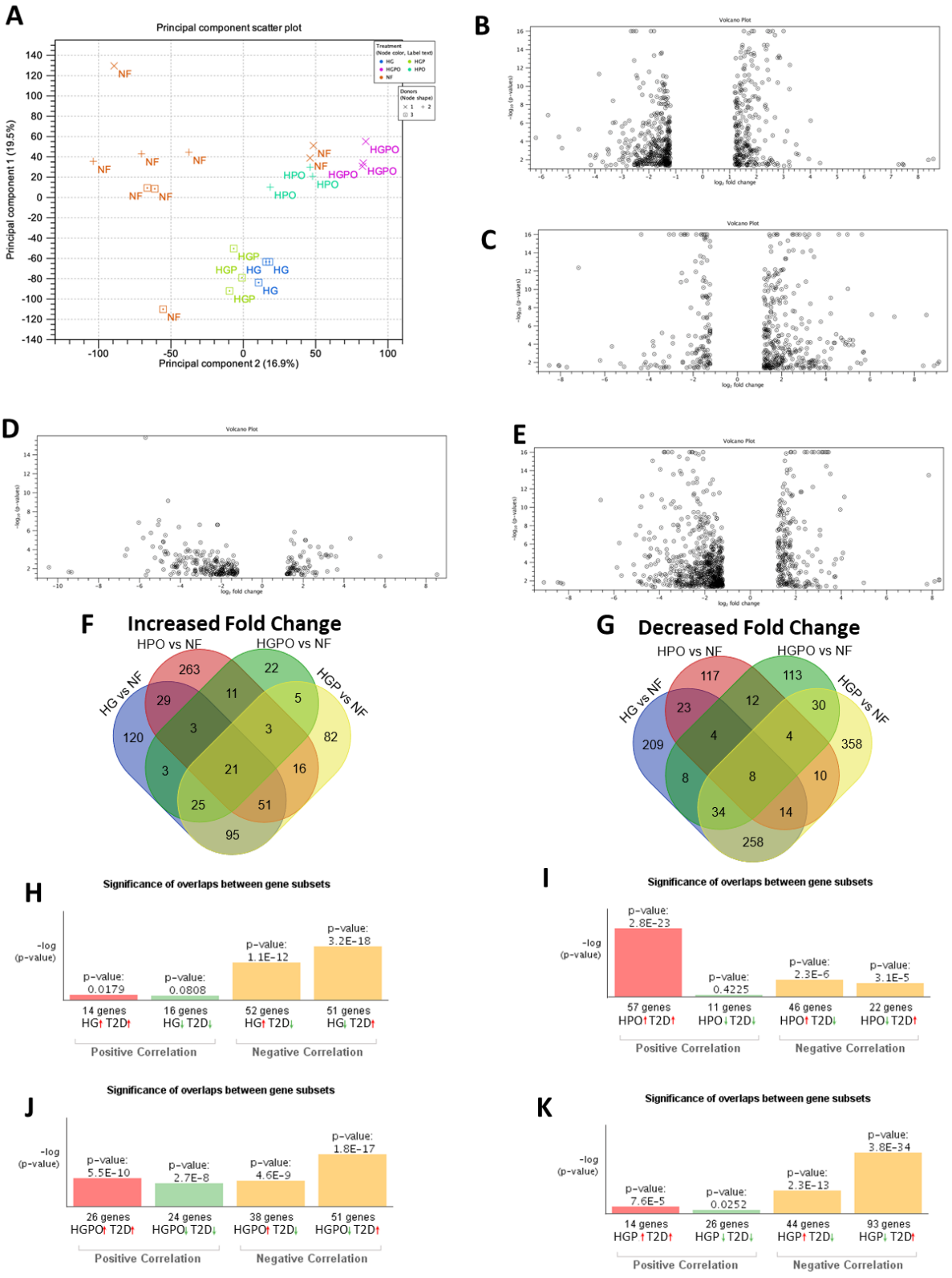
A
Principal component scatter plot
Principal component 1 (19.5%)
Principal component 2 (16.9%)
B
Volcano Plot
C
Volcano Plot
D
Volcano Plot
E
Volcano Plot
F
Increased Fold Change
HPO vs NF
HGPO vs NF
HG vs NF
HGP vs NF
263
22
29
11
5
120
3
3
82
3
21
16
25
51
95
G
Decreased Fold Change
HPO vs NF
HGPO vs NF
HG vs NF
HGP vs NF
117
113
23
12
30
209
4
4
358
8
8
10
34
14
258
H
Significance of overlaps between gene subsets
-log (p-value)
p-value: 0.0179
p-value: 0.0808
p-value: 1.1E-12
p-value: 3.2E-18
14 genes HG↑ T2D↑
16 genes HG↓ T2D↓
52 genes HG↑ T2D↓
51 genes HG↓ T2D↑
Positive Correlation
Negative Correlation
I
Significance of overlaps between gene subsets
-log (p-value)
p-value: 2.8E-23
p-value: 0.4225
p-value: 2.3E-6
p-value: 3.1E-5
57 genes HPO↑T2D↑
11 genes HPO↓T2D↓
46 genes HPO↑T2D↓
22 genes HPO↓T2D↑
Positive Correlation
Negative Correlation
J
Significance of overlaps between gene subsets
-log (p-value)
p-value: 5.5E-10
p-value: 2.7E-8
p-value: 4.6E-9
p-value: 1.8E-17
26 genes HGPO↑ T2D↑
24 genes HGPO↓ T2D↓
38 genes HGPO↑ T2D↓
51 genes HGPO↓ T2D↑
Positive Correlation
Negative Correlation
K
Significance of overlaps between gene subsets
-log (p-value)
p-value: 7.6E-5
p-value: 0.0252
p-value: 2.3E-13
p-value: 3.8E-34
14 genes HGP↑T2D↑
26 genes HGP↓T2D↓
44 genes HGP↑T2D↓
93 genes HGP↓T2D↑
Positive Correlation
Negative Correlation

Figure 2.13 Bulk RNA sequencing comparing toxic treatments (HG, HPO, HGPO, HGP) against NF.(A) Principal component analysis displaying culture conditions (colors and labels) and donors (symbols). (B-E) volcano plots for HG, HPO, HGPO, HGP respectively with points representing differentialy expressed genes (DEGs) with fold change (abs>2) and FDR p>0.05. (F, G) Venn diagram of differential gene expressions with either increased or decreased fold change (abs>2) and FDR p>0.05 for tested treatments vs donor-specific NF. (H-K) BaseSpace Correlation Engine comparison of tested treatments vs donor-based NF (Bs1) and published T2D vs Non-diabetic (ND) data (Bs2).

To determine the transcriptome changes that the toxic treatments had on the PANIS we compared the RNA-sequencing data of the toxic treated PANISs to the donor-specific NF PANIS conditions. The resulting differential expressed genes (DEGs) are visualized as volcano plots (Figure 2.13 B-E) where the displayed points are significantly changed genes (FDR p-value<0.05) with an absolute fold change >2. The toxic treatment with the greatest number of DEGs is HGP vs NF (Figure 2.13 E) with 1,014 genes (298 upregulate and 716 downregulated) all of which are protein coding. The top 20 up/downregulated genes (Appendix Table 3) for HGP vs NF consisted of genes related to inflammation (CXCL10↓, CHIT1↓, IFI44L↓, and TNFSF12-TNFSF13↑), angiogenesis (OLR1↓, MMP9↓, and CALCA↑), ion channels/transporters (P2RX2↑ and SLC5A4↑), lipid metabolism (HBA2↑) and islet functions (IAPP↑). The HG vs NF (Figure 2.13 B) has 905 DEGs (347 upregulated and 558 downregulated) where all are protein coding. Appendix Table 4 shows the top 20 up/downregulated genes which relate to inflammation (CXCL10↓, TREM2↓, and CCL11↓), ion channels/transporters (P2RX2↑ and SLC5A4↑), transcription (E2F2↓, IFI27↓, and RAB4B-EGLN2↓), ECM restructuring (MMP8↓ and COL14A1↓), lipid metabolism (HBA2↑), and islet functions (IAPP↑ and SYT16↑). The HPO vs NF (Figure 2.13 C) has 589 DEGs (397 upregulated and 192 downregulated) with all being protein encoding. The top 20 up/downregulated genes can be found in Appendix Table 5. The pathways

the genes are related to are inflammation (TNFSF12-TNFSF13↓, ITLN1↓, and S100A9↑), lipid metabolism (CEL↑), and islet functions (STMN4↓). The HGPO vs NF (Figure 2.13 D) has 306 DEGs (93 upregulated and 213 downregulated) all of which are protein coding genes. The top 20 up/downregulated genes, found in Appendix Table 6, are related to inflammation (SERPINB3↓, SERPINB4↓, and CXCL9↓), ion channels/transporters (P2RX2↑, RRM2↓, and KCNA4↑), lipid metabolism (HSD17B13↑), transcription (E2F2 ↑), and islet functions (IAPP↑). The different treatments show similarities in the pathways their most up/downregulated DEGs affect, with all showing changes in inflammation and insulin functions (with specific genes of each being similar across each treatment). Their similarities are observed further by comparing the DEGs in Venn diagrams based on increased fold change (Figure 2.13 F) and decreased fold change (Figure 2.13 G). This demonstrates that in different capacities there are 673 shared DEGs (268 upregulated and 405 downregulated). The HPO vs NF has the most unique increased DEGs (263) and the HGP vs NF has the most unique decreased DEGs (358).

BaseSpace Correlation Engine (BSCE) provided direct comparison of published T2D vs non-diabetic (ND) studies [92] to each of the tested DEG datasets (Figure 2.13 H-K), where the output provided positive correlation when direction of the DEGs' fold change matched and negative correlation when the direction of fold change opposed. This BSCE analysis alongside Ingenuity Pathway Analysis (IPA) allowed us to delve into individual pathways associated with T2D, islet functionality, cellular stress, immune signaling, and angiogenesis (Figure 2.14 E-H) to further understand how these T2D related canonical pathways are affected by the different toxic treatments. With the BSCE analysis, the PANIS toxic treatment that showed the most positive correlation with the T2D dataset was the HPO vs NF (Figure 2.13 I) with 68 positively correlated shared DEGs (57 upregulated and 11 downregulated for both) and 68 negatively correlated shared

DEGs (46 upregulated and 22 downregulated for HPO vs NF). Genes that fall within the negative correlation seem to be immune response (CCL22↓, CXCL12↓, IL1RL2↓ for HPO vs NF) and islet specific (SLC2A2↑, IGF2↑, MAFA↑ for HPO vs NF). IPA analysis of the HPO treatment (Figure 2.14 F) showed an increase in insulin secretion signaling (z-score=3, p=0.0139), IL-33 signaling (z-score=2.333, p=0.00273), IL-17 signaling (z-score=2.121, p=0.0248), and T2D signaling (z-score=1, p=0.00827), and a decrease in IL-13 signaling (z-score=-0.0378, p=0.00621) and PPARα activation (z-score=-2.121, p=0.0114). This provides more evidence indicating that the HPO PANIS shows strong similarities to a T2D condition with an increase in the inflammatory pathways (IL-17, IL-33) and T2D signaling correlating to a T2D condition, and the decrease in the PPARα activation correlating with T2D onset[93].

With the HG treatment, the BSCE analysis (Figure 2.13 H) shows an overall negative correlation between the T2D vs ND and the HG vs NF PANIS with 30 positively correlated shared DEGs (14 upregulated and 16 downregulated) and 103 negatively correlated shared DEGs (52 upregulated and 51 downregulated for HG vs NF). The IPA analysis for the HG treatment (Figure 2.14 E) re-affirms this relation with a notable increase in IL-10 signaling (z-score=1.508, p=0.00339) and insulin secretion signaling (z-score=0.832, p=0.0177), and a decrease in T2D signaling (z-score=-0.378, p=0.00322), PDGF signaling (z-score=-1.342, p=0.0316), IL-8 signaling (z-score=-1.387, p=0.00194), interferon signaling (z-score=-2, p=0.0161), and IL-13 signaling (z-score=-2.53, p=0.00129). The decrease in T2D signaling and immune response signaling demonstrates the divergence from a T2D condition. The decrease in immune signaling could originate from the lack in a functioning immune system, since the PANIS is isolated to only pancreatic islets and the patient data in the BSCE analysis would be a systemic view.

Similarly, to HG treatment, the BSCE analysis for HGP vs NF PANIS (Figure 2.13 K) shows an overall negative correlation to the T2D vs ND patient data with 40 positively correlated share DEGs (14 upregulated and 26 downregulated) and 137 negatively correlated shared DEGs (44 upregulated and 93 downregulated for HGP vs NF). The IPA analysis for the HGP treatment (Figure 2.14 H) showed an increase in IL-10 (z-score=2, p=0.000107) and PPAR signaling (z-score=1.414, p=0.0044) and a decrease in IL-17 signaling (z-score=-1.155, p=0.0327), IL-13 signaling (z-score=-1.667, p=0.021), IL-8 signaling (z-score=-1.698, p=0.000462), and IL-4 signaling (z-score=-5.24, p=0.00129). As with the HG treatment, the pathways that would indicate a T2D state are inverted with pro-inflammatory (IL-17, IL-13) and immune (IL-8 and IL-4) signaling showing a decrease and anti-inflammatory signaling (IL-10) increasing.

As with HG and HGP, the BSEC analysis shows a negative correlation for HGPO vs NF PANIS (Figure 2.13 J) compared to T2D vs ND with 50 positively correlated DEGs (26 upregulated and 24 downregulated) and 89 negatively correlated (38 upregulated and 51 downregulated for HGPO vs NF). The IPA analysis for the HGPO treatment (Figure 2.14 G) shows similar outcomes as HGP with an increase in IL-10 signaling (z-score=3, p=0.0000701) and a decrease in IL-33 (z-score= -1.134, p=0.00554) and IL-17 (z-score=-2.333, p=0.000304) signaling.

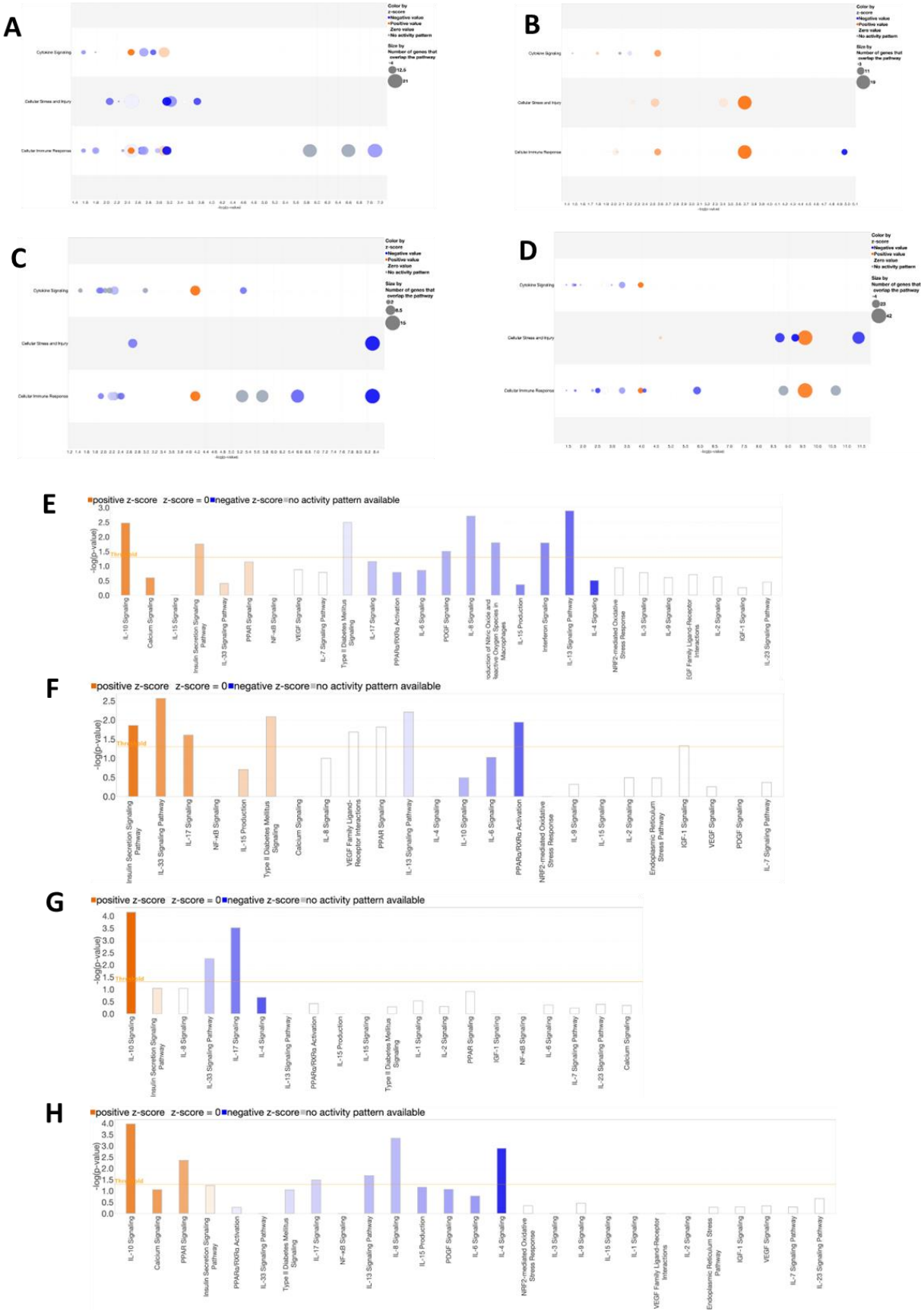
A
B
C
D
E
positive z-score z-score = 0 negative z-score no activity pattern available
-log(p-value)
IL-10 Signaling
Calcium Signaling
IL-15 Signaling
Insulin Secretion Signaling Pathway
IL-33 Signaling Pathway
PPAR Signaling
NF-κB Signaling
VEGF Signaling
IL-7 Signaling Pathway
Type II Diabetes Mellitus Signaling
IL-17 Signaling
PPARα/RXRα Activation
IL-6 Signaling
PDGF Signaling
IL-8 Signaling
Production of Nitric Oxide and Reactive Oxygen Species in Macrophages
IL-15 Production
Interferon Signaling
IL-13 Signaling Pathway
IL-4 Signaling
NRF2-mediated Oxidative Stress Response
IL-3 Signaling
IL-9 Signaling
EGF Family Ligand-Receptor Interactions
IL-2 Signaling
IGF-1 Signaling
IL-23 Signaling Pathway
F
positive z-score z-score = 0 negative z-score no activity pattern available
-log(p-value)
Insulin Secretion Signaling Pathway
IL-33 Signaling Pathway
IL-17 Signaling
NF-κB Signaling
IL-15 Production
Type II Diabetes Mellitus Signaling
Calcium Signaling
IL-8 Signaling
VEGF Family Ligand-Receptor Interactions
PPAR Signaling
IL-13 Signaling Pathway
IL-4 Signaling
IL-10 Signaling
IL-6 Signaling
PPARα/RXRα Activation
NRF2-mediated Oxidative Stress Response
IL-9 Signaling
IL-15 Signaling
IL-2 Signaling
Endoplasmic Reticulum Stress Pathway
IGF-1 Signaling
VEGF Signaling
PDGF Signaling
IL-7 Signaling Pathway
G
positive z-score z-score = 0 negative z-score no activity pattern available
-log(p-value)
IL-10 Signaling
Insulin Secretion Signaling Pathway
IL-8 Signaling
IL-33 Signaling Pathway
IL-17 Signaling
IL-4 Signaling
IL-13 Signaling Pathway
PPARα/RXRα Activation
IL-15 Production
IL-15 Signaling
Type II Diabetes Mellitus Signaling
IL-1 Signaling
IL-2 Signaling
PPAR Signaling
IGF-1 Signaling
NF-κB Signaling
IL-6 Signaling
IL-7 Signaling Pathway
IL-23 Signaling Pathway
Calcium Signaling
H
positive z-score z-score = 0 negative z-score no activity pattern available
-log(p-value)
IL-10 Signaling
Calcium Signaling
PPAR Signaling
Insulin Secretion Signaling Pathway
PPARα/RXRα Activation
IL-33 Signaling Pathway
Type II Diabetes Mellitus Signaling
IL-17 Signaling
NF-κB Signaling
IL-13 Signaling Pathway
IL-8 Signaling
IL-15 Production
PDGF Signaling
IL-6 Signaling
IL-4 Signaling
NRF2-mediated Oxidative Stress Response
IL-3 Signaling
IL-9 Signaling
IL-15 Signaling
IL-1 Signaling
VEGF Family Ligand-Receptor Interactions
IL-2 Signaling
Endoplasmic Reticulum Stress Pathway
IGF-1 Signaling
VEGF Signaling
IL-7 Signaling Pathway
IL-23 Signaling Pathway

Figure 2.14 Ingenuity pathway analysis (IPA) furthers insight in comparison of toxic treatments to NF control. (A) HG, (B) HPO, (C) HGPO, (D) HGP depict bubble graphs of the cytokine signaling, cellular stress and injury, and cellular immune response. (E-H) Bar graph for specific pathways associated with cell stress, immune response, apoptosis, cytokine signaling, islet specific functions, and diabetes pathways for (E) HG, (F) HPO, (G) HGPO, and (H) HGP.

Further analysis using IPA revealed changes in key pathways involved in cytokine signaling, cellular stress and injury, and cellular immune response for each of the four toxic treatments (Figure 2.14 A-D). The PANIS toxic treatments showing an overall downregulation of these processes are HG, HGPO, and HGP (Figure 2.14 A, C, D) where each have a higher number of genes overlapping the pathways with negative z-score (blue). The HPO treatment inversely shows an upregulation of these processes with an overall higher number of genes overlapping with positive z-score (orange) pathways (Figure 2.14 B). This indicates that glucose has a greater effect over cytokine signaling, cellular stress and injury, and cellular immune response pathways over the increased free fatty acids.

2.3.5.5 Islet ROS Quantification

ROS in islets play a vital role in insulin secretion in islets as a response to changes in glucose concentration but chronic higher levels of ROS are reported to cause islet dysfunction.[94] Hence ROS levels were evaluated in the islets exposed to NF and the corresponding toxic conditions. Representative images for ROS along with Mitotracker counterstain are shown in Figure 2.15 (A-E) for NF (normal fasting condition), HPO, HGP and HGPO (toxic treatment) along with TBHP treated positive control. Figure 2.15 F summarizes the mean ROS intensity normalized to area and represented as percentage of positive control, which indicates that the ROS

level is significantly increased relative to NF (28%) only with exposure to HGP (55%) treatment ($p<0.05$) which could be somewhat recovered with the addition of Oleic acid in the HGPO treatment (39%). The remaining toxic treatments did not exhibit significant elevation of ROS levels (HPO (30%) and HGPO (39%)). (In case we use area-based analysis: The quantification of ROS as area fraction of the islet in Figure 2.15g shows that ROS levels in islets cultured in HGP (mean=0.2) and HGPO (mean=0.15) are significantly different from NF (mean=0.08) with $p<0.05$, whereas HG (mean=0.1) and HPO (mean=0.12) media show no significant difference.)

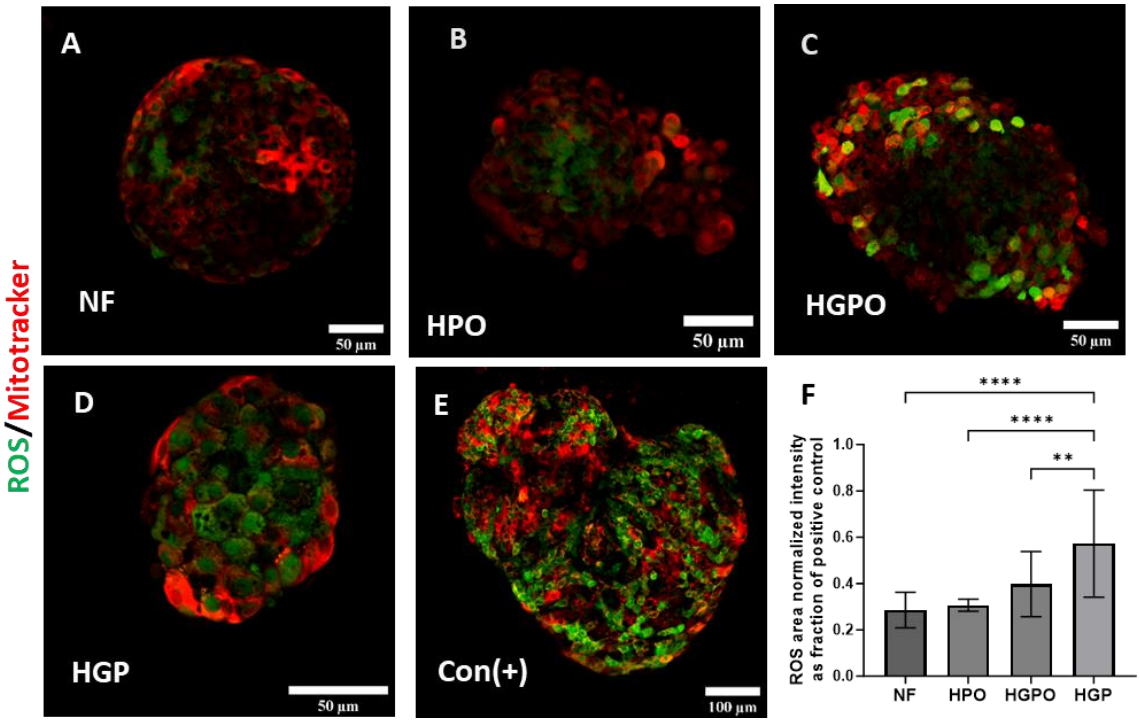

Figure 2.15 Reactive Oxygen Species (ROS) analysis for toxic treatments. Representative images showing ROS and mitotracker expression in islets cultured in (A) NF, (B) HPO, (C) HGPO, (D) HGP media for 14 days and (E) showing ROS in islets treated with Tert-Butyl hydroperoxide for 1 h. (F) ROS mean intensity in the islets in these groups show an increase in total ROS in islets cultured in HGP compared to NF (* represents $p<0.05$ and ** represents $p<0.0001$).**

2.3.6 Islet Response to Resveratrol with Gluco-Lipotoxic Media

Resveratrol (Res), a naturally occurring polyphenol that is commonly found in many plant species is known to have anti-oxidant[95], anticarcinogenic[96], anti-inflammatory[97] and anti-atherosclerotic/vasodilatory effects[98] both in vitro and in vivo. Current research on the mechanism of action of Resveratrol indicates that it regulates the activity of SiRT1, reducing ROS, production and is also known to enhance mitochondrial metabolism and the activity of anti-oxidant enzymes effectively acting as ROS scavenger[99]. In the context of T2D, Res is known to improve insulin sensitivity and has a protective effect on pancreatic β-cells by inhibiting the production of ROS and cytokines[100]. This antioxidant effect of Res on pancreatic islets cultured in HGP (gluco-lipotoxic) media was tested in the current study as the ROS in islets cultured in HGP was observed to be the highest (Figure 2.15). Res was supplemented to HGP media with two different concentrations (10 μM and 100 μM)[101, 102] to study the long term drug response of islets cultured in toxic media on the MPS platform. Islets cultured on the MPS platform for 14 days with toxic media supplemented with Res along with NF and HGP (without drug) as control groups for normal fasting and disease media treatment respectively were characterized for their viability, total ROS, islet markers- C-peptide and Glucagon and their insulin response to changes in glucose concentration (GSIS).

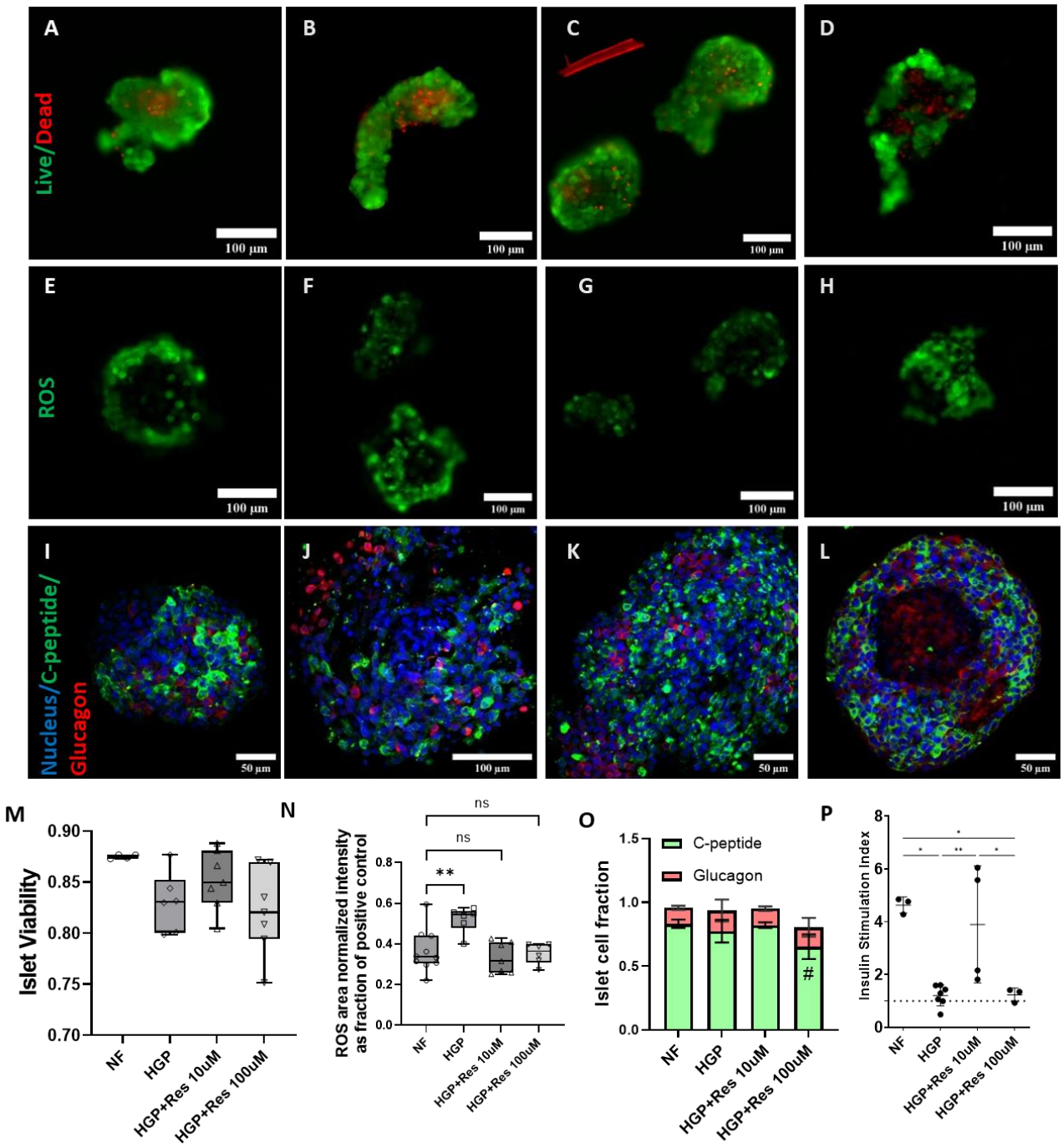

Figure 2.16 PANIS as a platform for testing the response of islets cultured in HGP media to the anti-oxidant drug Resveratrol. (A-D) Representative images from live/dead staining of islets cultured in NF, HGP, HGP with 10 µM Resveratrol and HGP wit 100 µM Resveratrol respectively for 14 days. (E-H) Islet ROS imaged with DCFDA staining in NF, HGP, HGP with 10 µM Resveratrol and HGP with 100 µM Resveratrol respectively for 14 days. (I-L) Immunofluorescence staining for C-peptide and Glucagon for islets cultured

in NF, HGP, HGP with 10 µM Resveratrol and HGP wit 100 µM Resveratrol respectively for 14 days. (M) Islet viability quantification with the boxes representing the interquartile range and whiskers representing the SD showing no significant difference in the viability among the groups. (N) Islet ROS intensity normalized to area (boxes represent interquartile range and whiskers represent SD) showing that mean ROS intensity is higher in islets cultured in HGP and the groups treated with the Reseveratrol show ROS similar to NF (# indicates statistically significant difference w.r.t NF ($p<0.05$)). (O) Quantification of immunofluorescence images for C-peptide and Glucagon showing a loss in C-peptide positive cells in islets treated with 100 µM Resveratrol. (P) GSIS-based insulin stimulation index of the islets among the groups showing islets cultured in HGP with 10 µM Resveratrol maintain good SI similar to that of control (* signifying $p<0.05$ and ** signifying $p<0.005$).

The results from the drug test with islets are summarized in Figure 2.16. Representative images for live/dead staining of islets in groups NF, HGP, HGP+10 µM and 100 µM Res are shown in Figs 16 A-D and quantification of viability shows that islet viability was >80% in all groups (Figure 2.16 M). Although, the group with higher concentration of the drug shows a wider spread in the viability, there was no statistically significant difference among the groups. This was followed by ROS imaged through DCFDA staining, example images for ROS in the islets are presented in Figure 2.16 E-H and the summary of intensity quantification in Figure 2.16 N shows that the amount of ROS in HGP is higher than NF establishing one of the signs of disease condition in islets and in both the groups cultured in HGP with the drug, the ROS levels were similar to that of NF. Islet specific markers that were imaged after 14 d culture for all groups are shown in Figure 2.16i-l and quantification of β and α cell population in Figure 2.16 O indicate that there is a statistically significant reduction in β cell population in islets cultured in HGP with 100 µM Res ($p<0.05$). After testing with a GSIS assay (Figure 2.16 P), the group cultured in HGP showed an expected decrease in insulin stimulation index (SI 1.20) compared to NF (SI 4.63) where the islets

show good glucose responsiveness. The group treated with HGP and 10 μM of Res is observed to retain its glucose responsiveness (SI>>1) similar to that of normal fasting medium (NF) while the higher concentration of the drug (HGP+100 μM Res) results in islets having a reduced glucose responsiveness (SI 1.22). This demonstrates that while the Res functions properly in preventing ROS within the islets, a higher dose can cause toxicity that can lead to insulin stimulation dysfunction.

2.4 Discussion

In this study, we have demonstrated the capabilities of our islet microphysiological system, dubbed PANIS, to remain effective for the prolonged period for over 28 days and serve as a platform capable of developing a diseased metabolic state similar to T2D for modelling and drug testing purposes. PANIS was based on an organ-on-chip device by Micronit that needed to be modified to support the islets' 3D structure using a novel alginate capsule array. We've established the PANIS system as an ample system for maintaining islets by characterizing the flow and nutrient diffusion with COMSOL modelling backed up by experimental testing. With the flow rate of 30μL/h, the system has a residence time of 2.5h for a complete looped flow through the upper and lower chambers. It was observed that with the flow configuration, the majority of the flow from the upper channel to the lower was through the membrane where the islets were located, providing more direct flow to the islets. The flow streamlines and the predicted velocities in the vicinity of alginate capsules in the system is similar to interstitial flow in capillaries around cells.[103] The predicted reduction in shear stress inside the alginate capsules is also favorable as it helps maintain islet 3D microstructure. Oxygen concentration analysis was used as the basis for nutrient diffusion

through the system since islets require adequate oxygen concentrations to meet their high metabolic demand. The system was able to maintain ambient oxygen levels (18%) through the channels and alginate capsules. Although the velocity decreases along the flow trajectory, the stable oxygen concentration predicted by the model indicates that this variation is negligible. Under these conditions, islets were able to maintain high viability, endothelial cell populations ($CD31^{+}$), and functionality up to a 28-day span where functionality was measured through fluorescent staining of key islet markers (C-peptide, glucagon, NKX6.1, PDX1) and glucose stimulated insulin secretion (stimulation index =3 for 14-21 days and 2.2 for 28 days).

In the development of the PANIS system, the design depends on the purpose for the model's development. The major components to an MPS device design are the materials used in constructing and the culture platform used to maintain the cells under flow for the culture duration. The commonly used material for device construction is polydimethylsiloxane (PDMS) due to its high biocompatibility, oxygen permeability, and optical transparency for imaging [34, 104-106]. One such device developed by Jun et al. utilizes PDMS to form a complex microwell culture system for sustaining islets over long term cultures (>7 days) [34]. However, PDMS-devices require specialized photolithography facilities [107] and is susceptible of absorbing small molecules such as drugs, biologics and other reagents due to its hydrophobicity [32, 64, 108]. This poses as a major issue with diabetes pathogenesis and drug testing applications with the need for accurate measurements of the efflux and precise doses administered to the cells. Alternate materials used for islet device construction are polymethyl methacrylate (PMMA), acrylic, and borosilicate glass [32, 64, 108]. The diabetic modelling device developed Patel et al. utilizes PMMA. PMMA has similar benefits of PDMS with biocompatibility, gas permeability, and optical transparency without the drawbacks of small molecule absorption and difficulty in manufacturing, since PMMA can be machined to

form the device [109]. The gas permeability of both PDMS and PMMA can lead to culture media evaporation and oxygen bubble formation over prolonged culturing [110]. Unlike the other long term culture devices, ours utilizes borosilicate glass which has similar positive attributes to PMMA but is gas impermeable, making it resistant to oxygenation and bubble formation. While this makes the oxygen concentration in device media dependent, we have extensively characterized and ensured oxygen concentrations were adequate for sustaining islet health. An additional strength of the material allows for it to be reusable. A disadvantage for using borosilicate glass is the difficulty of in-house manufacturing [111], which is overcome with the commercial availability of the base components of our PANIS system.

Islet MPS devices meant for long term cultures (>7 days) must adhere to the constraints needed to provide a suitable environment for islets. This includes a 3D culture system that maintains the islets' spherical morphology since it directly correlates with function, a surplus of oxygen in the microenvironment to meet the demand of islets, and a flow configuration that minimizes shear forces due to islets' susceptibility to damage [33, 72, 112]. The Jun et al. device maintained the islet 3D morphology in microwell arrays that allowed islet re-aggregation and continue culture under flow, which was capable of maintaining healthy islets under the low flow of 8-25µl/h[34], which corroborates our observation that low flow systems provide enough nutrients for islets. This model minimizes islet morphology variability through the re-aggregation step[34],[113]. Consequently, the islets lose their native extracellular matrix, which have shown to be important in islet function [114]. The device developed by Lenguito et al. also uses the well design where whole islets are added to a well and media flows in an upper channel [64]. This base design was improved to support long term culturing, reported by Patel et al., by suspending islets in a single polymerized alginate droplet within the culture well using a 30µl/min flow rate[32], but this "Acry-chip" design

had issues with oxygen diffusion. They optimized for oxygen diffusion by replacing the bottom of the well with an oxygen-permeable perfluoroalkoxy (PFA) membrane to make the "Oxy-chip" design which improved the viability of the islets, indicating a greater potential for more prolonged culture time and the capability for higher islet loading density[32]. Alternatively, Bauer et al. have demonstrated the feasibility of the Chip2 by TissUse to maintained viability and function of long term cultured re-aggregated islets[115], similar to the islets used by Jun et al.[34]. This is accomplished with their device by using 30uL/hr pulsating flow directly into the islet chamber[115], but since this design has the islets freely floating in the chamber, they are limited to a lower flow rate and to a certain number of islets to avoid overcrowding and islet aggregation. The alginate array implemented with our PANIS system was derived from our previous reports on enhancing throughput of 3D cultures [73, 74] and provided unique integration of biomaterials within a fluidic device. The individual alginate capsules provide the support to the islets similar to the Patel et al. device[32], but the use of the array is a significant improvement over the other designs, since it is a simpler fabrication that allows direct media perfusion all around the capsule. As demonstrated with both our COMSOL models and experimental testing, the alginate provides uniform creeping flow with adequate oxygen concentration across all islets. These system parameters allow for the primary islets to be healthily cultured and maintain function for a greater timeframe than the current state of art, demonstrating how our system as a whole provides significant advancements to the field of islet-on-chip.

The majority of published islet MPS models are designed for screening islet quality through high-throughput assaying [59, 60, 116-119] with others focusing on diabetes pathogenesis and drug testing, which require longer culture times (>7 days). Jun et al., Bauer et al., and Patel et al. demonstrated their islet MPS' capability for long term culture by maintaining islets up to 14 days[32,

[34, 115]. The PANIS system we've developed demonstrates a significant improvement in its ability for extending the culture of islets to 28 days. The ability for the PANIS to maintain islet viability and functionality for prolonged (28 day) cultures under normal fasting (NF) conditions provided the necessary basis to accurately test more extensive culturing (14 days) under toxic treatments with more certainty that any decrease in islet viability and functionality stems from the treatments and not the culture in PANIS.

Islet MPS designs that have studied metabolic toxic treatments (hyperglycemic, lipotoxic, glucolipotoxic) have been limited to short term exposure testing[32] or focused on effect with coupled organ systems[115, 120]. Patel et al. demonstrated the acute effect (2.5hr) of glucolipotoxic treatments (16.7mM glucose+0.5mM palmitic acid) on rodent islets' insulin secretion, calculated using calcium imaging, with treated islets having a significant increase in stimulation compared to basal media control[32] with an additional observation that the treated islets had a greater dead cell population. As seen with the toxic treatment testing in the PANIS, the HGP condition is most related to that tested by Patel et al. [32], and it demonstrated the most detrimental effect on the islets. With the ability to culture for longer periods of time, we can observe the effects of treatments that require chronic exposure to permanently damage the islets, as seen in T2D. An additional advantage this system has is the ability to easily disassemble the device to remove the islets without damaging them for further analysis. This gives us the opportunity to do in-depth analyses to detect any changes in the islets using high resolution imaging, as well as the capability of conducting assays such as RNA sequencing.

The ability to test chronic toxic medias demonstrates the application of our PANIS device in modelling metabolic pathogenesis (ie. T2D). We tested hyperglycemia (HG), lipotoxicity (HPO), and glucolipotoxicity (HGPO, HGP) treatments on PANIS. We demonstrated that the

PANIS oxygen content did not decrease with the introduction of HG media, which would increase the metabolic activity of the islets, and would require more oxygen than NF. This indicates that the observed effects of the toxic treatments was due wholly from the detriment of the media and not a flaw with the PANIS. While this is not due to nutrient deficiency, as depicted in our O_2 detection assay, it is likely that the presence of dead cells closer to the core is due to culture in high glucose media, especially at the end of 28 days in culture. When implementing HG conditions to the system over 14-28 days, the 14-day trial was a sufficient timeframe to decrease GSIS-derived insulin stimulation index compared to normal fasting (NF) state, showcasing islet dysfunction, but it took the 28 days to lower viability compared to 28-day NF. The 14-day timepoint was subsequently used for HPO, HGPO, and HGP. The culture resulted with the HGP treatment displaying the most damage to the islets overall, with a significant decrease in viability, β-cell fraction, insulin stimulation index, and endothelial cell population. We hypothesize that this is due to the combined harmful effects of the high glucose and saturated fatty acid, palmitic acid, through the overproduction of reactive oxygen species, which has shown to correlate with lipotoxicity[121-123]. Since β-cells are very susceptible to oxidative damage due to having few anti-oxidative mechanisms as defense, an overproduction of ROS would lead to the observations made. ROS being a major driver for the dysfunction found in HGP was further supported in the rescue of islet insulin secretion functionality with the inclusion of the antioxidant drug, Resveratrol, which showed normal ROS and GSIS at a 10μM dose. Conversely, the inclusion of the oleic acid with the HGPO treatment mitigated any harmful effects of the high glucose and palmitic acid, with the results of the HGPO treatment not differing significantly from the NF control. This is corroborated by other reports that oleic acid mitigates the harmful effects of the combination of palmitic acid and high glucose[89, 124].

With the HPO treatment, the islets became dysfunctional with a significant decrease in insulin stimulation index and viability, as seen in HGP, but the ROS did not differ from the NF state, which likely resulted from the protective effects of the oleic acid[124]. To determine the reasoning for the loss in function, the RNA sequencing provided a broader view for potential mechanisms. The increase in inflammatory signaling and decrease of the PPARα activation would affect the viability and functionality of the islets by increasing stress on the islets and lower the β-cell replication to maintain proper homeostasis[123, 125]. Additionally, increased T2D signaling and a positive correlation to T2D patient data, as determined through BSCE, indicates that of the toxic treatments tested, the HPO treatment provides the best environment to model T2D in PANIS.

Expanding the applicability of the PANIS, the antioxidant drug, Resveratrol, was tested during the HGP treatment to determine its ability to protect the islets by inhibiting ROS formation by upregulating sirtuin expression[100, 126]. As previously mentioned, the Resveratrol was able to rescue the islets' functionality at a 10mM dose by successfully inhibiting ROS production in the cells, which was confirmed using fluorescent imaging and image analysis. Conversely, the higher dose of 100mM, while inhibiting ROS production, had a detrimental effect on b-cell populations and insulin secretion. This coincides with literature that higher concentrations (>50mM) of Resveratrol can be cytotoxic to cells, leading to apoptosis or arrested cell growth[127-130]. This can be seen in the decreased b-cell fraction for the higher Resveratrol dose, where the cells may have not been able to replenish, leading to the decreased insulin stimulation index. With this contrast between the low and high doses, the PANIS is able to demonstrate its capability of dose sensitive testing.

3.0 Utilizing Alginate Encapsulation Platform for the Directed Differentiation of Human Induced Pluripotent Stem Cells Towards Endoderm Germ Layer-based Organs

3.1 Introduction

Human pluripotent stem cells (hPSCs) have provided an avenue for developing a wide range of cell types for the purposes of regenerative medicine and disease modeling[44]. They have demonstrated robust formation of a wide range of cell types, such as liver[131-134], lung[135-138] and kidney[139, 140], through chemical and mechanical stimuli to direct the differentiation through the developmental phases. In addition to these more common cell types, they have demonstrated the ability to form non-proliferating cells, such as in the pancreas[141-143] or thymus[144]. This provides a means of increasing the availability of these cells that lack an immortal human cell line.

Initial works for these differentiation methods were conducted with 2D tissue cultures[145], but further studies have demonstrated that differentiation in 3D cultures vastly improves the outcome of the differentiation for some cell types as it more closely mimics the development of the tissue in vivo[53]. One such cell type that this has been demonstrated with is the pancreatic islet[53, 146, 147]. The differentiation of hPSCs into functional pancreatic islets has become an increasingly prominent area of study[148], with the current protocols utilizing some form of 3D culturing[45, 46, 149, 150]. The most commonly used 3D platform is a suspension-based culture system, where single cells are seeded and the suspension is maintained using centrifugal forces[45, 46, 147]. While this form of 3D culturing has provided promising results, the suspension culturing exposes the aggregates to continuous hydrodynamic shear forces that can result in increased stress on the aggregates[151]. As an alternative platform, our group has demonstrated the capabilities of alginate encapsulation to

aid in the differentiation towards pancreatic progenitor cells which could be utilized with more modern differentiation techniques for forming functional islets in vitro[53, 146]. The first part of this study compares the two 3D platforms for hPSC-islet differentiation and characterizes induced pluripotent stem cell (iPSC)-islet development with our alginate encapsulation system.

The second part of this study explores the usability of the alginate encapsulation platform to aid in the differentiation towards the endoderm-based thymus cells. The thymus gland does not contain hematopoietic stem cells (HSCs) capable of self-renewal, relying instead on the continuous recruitment of thymus settling/seeding progenitors (TSPs) coming from the bone marrow to maintain long-term thymopoiesis[152]. Once inside the thymus, TSPs undergo a series of differentiation events, including T-lineage specification and positive and negative selection, to become mature T-cells[153-155]. Thymic epithelial cells (TECs), the predominant population of cells in the thymus stroma, play essential regulatory roles throughout thymopoiesis[156]. TECs within the cortical region (cTECs) provide key signals for T-cell fate specification and positively select T cells that can functionally interact with the body's own antigen present cells (APCs)[157-159]. Conversely, TECs within the medullary region (mTECs) possess the unique characteristic of expressing and presenting tissue specific self-antigens (TSAs)[160]. The mTECs are critical for eliminating T cells with high auto-reactivity in the thymus, supporting the development of regulatory T cells and thus maintaining immunologic self-tolerance[161].

Others have shown that functional thymus organoids can be constructed by repopulating decellularized thymus scaffolds with isolated murine TECs[162, 163]. The 3D network of extracellular matrix in the decellularized thymus scaffolds can maintain the long-term survival and function of TECs both in vitro and in vivo. When transplanted under the kidney capsule of athymic nude mice, tissue-engineered murine thymus organoids can support the generation of a diverse and functional

repertoire of T-cells in the recipient mice[164]. Recently, Campinoti and colleagues have shown that functional human thymus can be reconstituted by seeding rat thymus scaffolds with in vitro expanded thymic stromal progenitors isolated from postnatal donors, highlighting the feasibility of the tissue-engineering approach in thymus regeneration[165].

iPSCs have been widely used in regenerative medicine, and have been proposed as a renewable source of TECs for thymus tissue engineering[166]. Since the seminal concurrent reporting from Parent et al.[167] and Sun et al.[168], great progresses have been made in generating TEC progenitor cells (TEPCs) from hPSCs (both embryonic and induced)[169-171].

The aim of this chapter is to develop a novel platform for differentiating endoderm-lineage cell types from human iPSCs. In this chapter, we describe the generation of two functional cell types, pancreatic islets and thymus organoids, derived from the endoderm germ layers through hPSC differentiation in our alginate encapsulation platform. The pancreatic islet differentiation form iPSC-islets that are capable of glucose sensitive insulin secretion and the thymus organoids from iPSCs that can support the development of human T cells from CD34+ hematopoietic progenitor cells (HPCs).

3.2 Materials and Methods

3.2.1 hPSC Culture

Undifferentiated (UD) hESCs and iPSCs were maintained on hESC-qualified Matrigel (BD Biosciences) coated tissue culture plastic for 5-7 days in mTeSR1 (StemCell Technologies) at

37°C and 5% CO2 before passaging. Passaging was done using enzymatic dissociation reagent, Accutase (StemPro).

3.2.2 Stirred Suspension Aggregation

Method for stirred suspension aggregation (SSA) is based on previous published suspension methods[172, 173]. In brief, single-cell hPSCs were formed by pretreating a confluent cell population with 10 μM Y-27632 dihydrochloride (R&D Systems) 2 h before dissociating with Accutase (StemPro). Cells were counted using Trypan Blue (Gibco) and a hemocytometer. The single hPSCs were seeded into a 35mm petri dish (Corning) in 2 mL mTeSR1 (StemCell Technologies) supplemented with 10 μM Y-27632 dihydrochloride (R&D Systems) at a density of 0.5 million cells/mL, and the dish was then placed on an orbital platform shaker, residing in an incubator, and set to 95 RPM.

3.2.3 Single Cell Encapsulation

Alginate encapsulation of iPSCs has been previously described[174]. Single-cell hPSCs were formed by pretreating a confluent cell population with 10 μM Y-27632 dihydrochloride (R&D Systems) 2 h before dissociating with Accutase (StemPro). Cells were counted using Trypan Blue (Gibco) and a hemocytometer. Single cells were suspended in 1.1 w/v% low viscosity alginate (Sigma) at a cell density of 5×105 per ml alginate. The single-cell alginate mixture was polymerized dropwise with a stirred solution of 100 mM CaCl2 (Sigma) with 10 mM HEPES forming spherical capsules. The capsules were washed three times with DMEM/F12 (Gibco)

before culturing in mTeSR1 (StemCell Technologies) supplemented with 10 μM Y-27632 dihydrochloride for 4–6 days before starting differentiation.

3.2.4 Aggregate Retrieval from Alginate

iPSC aggregates differentiated into either islets or TECs in polymerized alginate capsules were decapsulated by incubating with 100 mM EDTA for 2–3 min, which depolymerizes the alginate capsules enabling aggregate retrieval.

3.2.5 Live/Dead Assay

See Chapter 2 methods.

3.2.6 Islet Differentiation

Using a modified version of a previously published protocol [45], islet-like cells were generated using the stagewise differentiation steps as described below. The differentiation base media is composed of 2.44mM D-Glucose (Gibco), 1.23 g/L $NaHCO_3$ (MilliporeSigma), 2% FAF-BSA (Fisher Scientific), 2 mM Glutamax (Gibco), 1% Pen/Strep (Lonza), 490 ml MCDB131 (Corning/Gibco). Media changes were completed as follows with supplements to the differentiation base media. Definitive Endoderm Media (Days 1-3): differentiation base media was supplemented to have 2.46 g/L $NaHCO_3$, 0.25 mM Vitamin C (MilliporeSigma), and 1:50 ITS-X

(MilliporeSigma). Day 1: 100 ng/mL Activin A (R&D Systems) and 1.4 µg/mL Chir99021 (Stemgent). Days 2-3: 100 ng/mL Activin A. Primitive Gut Tube (Days 4 and 6): 50 ng/mL KGF (Peprotech), 0.25 mM Vitamin C, and 1:50 ITS-X. Pancreatic Progenitor 1 (Days 7 and 8): 50 ng/mL KGF, 0.25 µM Sant1 (MilliporeSigma), 2 µM Retinoic Acid (MilliporeSigma), 500 nM PdBU (MilliporeSigma), 0.25 mM Vitamin C, 10 µM Y-27632, and 1:200 ITS-X. Pancreatic Progenitor 2 (Days 9, 11, and 13): 50 ng/mL KGF, 0.25 uM Sant1, 0.1 µM Retinoic Acid, 0.25 mM Vitamin C, 10 µM Y-27632, 5 ng/mL Activin A and 1:200 ITS-X. Endocrine Progenitor (Days 14,16,18, and 20): increase $NaHCO_3$ to 1.75 g/L and increase glucose to 20 mM. Days 14 and 16: 0.25 µM Sant1, 0.1 µM Retinoic Acid, 0.25 mM Vitamin C, 1 µM XXI (MilliporeSigma), 10 µM ALk5i II (Axxora), 1 µM T3 (MilliporeSigma), 20 ng/mL Betacellulin (Fisher Scientific), 10 µg/mL Heparin (MilliporeSigma), 1:200 ITS-X. Days 18 and 20: 0.025 µM Retinoic Acid, 0.25 mM Vitamin C, 1 µM XXI, 10 µM ALk5i II, 1 µM T3, 20 ng/mL Betacellulin, 10 µg/mL Heparin, 1:200 ITS-X. Maturation: 1:200 ITS, and 0.25 mM Vtamin C.

3.2.7 Live-Cell Fluorescent Staining

At the end of the EN phase, the aggregates were retrieved from the alginate and washed in islet differentiation base media 3 times to remove excess dead cell debris. TrypLE Express (Gibco) was added to the aggregates and incubated for 15-20 min where base media was added to dilute the TrypLE Express. The non-dissociated aggregates were disrupted mechanical through pipetting, and the now single cells were spun down at 150 rcf for 3 min and resuspended in fresh maturation media. The single cells were incubated for 30 min with 25µM Newport Green (Thermofisher) and 1:10 anti-mouse DPP4-APC (Miltenyi Biotec) diluted in PBS and washed 3 times before sorting with FACS.

3.2.8 INS-mCherry Reporter Formation

The INS-mCherry plasmid was graciously provided by the lab of Dr. Yong Fan of Allegheny General Hospital, Pittsburgh, PA. Reverse transfection was conducted using TransIT-LT1 (Mirus) transfection reagent following the manufacturer's protocol.

3.2.9 Flow Activated Cell Sorting

Flow activated cell sorting (FACS) was conducted on an Aria-15 5 laser instrument where unstained or undifferentiated transfected cells were used as controls for gating each setup. After collecting the sorted cell populations, the single cells were seeded into a v-bottom ULA plate (Corning) at 3000 cells per well and cultured for up to 4 days to allow for self-organized re-aggregation.

3.2.10 Differentiation of iPSCs into Thymic Epithelial Progenitor Cells (iPSC-TECs)

The stage-wise induction protocol for thymic epithelial progenitor differentiation of hESCs was adopted from a previous study[167]. Stage 1 for definitive endoderm was carried out with Melton beta cell differentiation protocol. Stage 2 for anterior foregut endoderm was carried out in Roswell Park Memorial Institute (RPMI) media supplemented with 0.5% B27 (Gibco). For stage 2 (anterior foregut endoderm), the following factors were used: 100 ng ml−1 Activin A on day 5, 0.25 μM retinoic acid on days 5–7, 50 ng ml−1 BMP4 (Miltenyi Biotec) on days 6–7 and 5 μM LY364947 (MilliporeSigma) on days 6–7. Stages 3 and 4 for VPE and thymic epithelial progenitor were carried out in DMEM/F12 media (Gibco) supplemented with 0.5% B27. For stages 3 (VPE) and 4

(TEP), the following factors were used: 50 ng ml−1 Wnt3A on days 8–11, 0.1 μM retinoic acid on days 8–11, 50 ng ml−1 BMP4 on days 8–11, 5 μM LY364947 on days 8–9, 50 ng ml−1 FGF8b (Miltenyi Biotec) on days 8–11 and 0.5 μM KAAD-cyclopamine (Millipore) on days 8–11.

3.2.11 iPSC-TEC Thymus Organoid Dissociation

To dissociate the thymus organoids cultured in vitro, an enzymatic digestion solution containing 0.4 mg ml−1 collagenase D, 0.6 mg ml−1 dispase II, 0.1 mg ml−1 DNase I, 10 μM rock inhibitor was prepared using DMEM medium. Each thymus organoid was mechanically dissociated in 1 C tube with 2 ml of the digestion solution on gentleMACs Dissociator (Miltenyi Biotec). The dissociation was performed at 37 °C for 6 min under the program 37C-ABDK-02 for two rounds. At the end of the first round, the supernatant of the digestion reaction was collected, filtered and quenched with 4 ml of PBE. The remaining organoid was further dissociated under the same condition with 2 ml of fresh digestion solution. The supernatant was collected the same way and combined with the first round. The dissociated cells were pooled, pelleted and resuspended in 1 ml of culture medium for cell count and downstream analysis. For samples with suboptimal viability, density gradient centrifugation was performed to remove debris and dead cells as described above. Briefly, 1 ml of the cell suspension was laid gently onto 300 μl of Ficoll-Paque in a 1.5-ml Eppendorf tube and centrifuging at 1,600 r.p.m., room temperature for 20 min without brake. Live cells were collected at the medium/Ficoll interface and washed with fresh medium before proceeding to downstream analysis.

3.2.12 Li-COR Imaging

iPSC-TECs and CD34+ HPCs were labeled with Vybrant lipophilic carbocyanine dyes DiD and DiR (ThermoFischer), respectively, following the manufacturer's suggested protocols. The labeled cells were admixed at 1:1 ratio and injected into the decellularized thymus scaffolds. Scaffolds thus recellularized were imaged using Odyssey infrared scanner (LI-COR Biosciences) periodically over a duration of 10 days in culture (days 1, 4, 7 and 10). The images were collected using Odyssey Image Studio with the highest possible sensitivity and resolution (21 μm) in 700 nm (DiD emission) and 800 nm channels (DiR emission). The images were analyzed using Fiji (ImageJ, National Institutes of Health) and the fluorescence intensity is represented as a heatmap of areas in the scaffold with cells. The heatmap was graded into three levels of cell density-low, moderate and high indicated by blue, green and red colors, respectively, based on the fluorescence intensity. Grayscale values in the range (20, 48) were designated with blue (low intensity), (48, 76) as green (moderate intensity) and (76, 101) as red (high intensity) and all levels below 20 are considered as background (black/no signal). The area fractions of images in both TEC and HPC density were extracted from the image data, normalized to total scaffold area from the phase images and compared over time in culture.

3.2.13 Immunofluorescence and Histological Analysis

See Chapter 2 methods for iPSC-islet immunofluorescence staining procedures.

The aggregates were then fixed with 4% PFA for 45 min at room temperature followed by washing in PBS (three times). The aggregates were labeled with primary antibodies for TEC

markers. For mouse antihuman CD45 (Invitrogen MA5-17687, 1:200), mouse antihuman cytokeratin-8 (Cell Signaling Technologies, 4546S, 1:200), mouse antihuman CD205 (Biolegend), mouse antihuman DLL4 (Biolegend) and rabbit antihuman EpCAM (Cell Signaling Technologies) the aggregates were incubated with the primary antibodies diluted in PBS (1:50 unless specified otherwise) containing 10% donkey serum and were incubated overnight at 4 °C. The aggregates were washed with PBS (three times) before adding secondary antibodies diluted (1:500) in the same buffer: AlexaFluor donkey anti-Mouse 488 (Invitrogen) for the mouse primaries and AlexaFluor goat antirabbit 555 (Invitrogen) for rabbit primaries. The aggregates with secondary antibodies were incubated at 4 °C overnight.

For labeling FOXN1, 3D iPSC-TECs were processed as above. Primary rabbit antihuman FoxN1 (Bioss) antibodies were diluted (1:50) in PBS containing 10% donkey serum and 1% Triton X-100 and were incubated overnight at 4 °C followed by washing with PBS (three times) and then incubated with the appropriate secondaries diluted (1:500) in the same buffer as the primary antibodies overnight at 4 °C. After the labeling process, the aggregates were washed with PBS (three times) before mounting onto a glass slide with Gold Antifade (Invitrogen) before imaging using Olympus Fluoview 2 confocal microscope. For FOXN1 labeling of human primary TECs (HTyEpiC, ScienCell Research Laboratories) and human primary lymphatic fibroblasts (ScienCell Research Laboratories), cells were recovered from frozen stock and cultured following the manufacturer's suggested protocol for 2–3 days. Cells were dissociated and fixed in 2.5% PFA solution/PBS at a concentration of 2.5–5 × 105 cells per ml and stored at 4 °C until Cytospin. To prepare the slides for immunofluorescence, the labeled colorfrost plus microscope slides were assembled (Fisherbrand), a cytofunnel (Epredia) added to the slide holder and these were placed in the centrifuge rack in the hood. Each funnel was filled with approximately ten drops of the fixed

cell suspension. The spin was run under program 1 (12,000 r.p.m., 5 min) to obtain the slides with the cell containing spot ready for downstream staining (Thermo Scientific Cytospin Centrifuge). The same protocol was followed for FOXN1 labeling of the slides.

3.2.14 Flow Cytometry and ImageStream

Cells were harvested after 15-20 minutes of TrypLE treatment to obtain a single cell suspension, washed 3 times with PBS, and fixed with 4% formaldehyde (Thermo Scientific) in PBS for 15 minutes. Cells were permeabilized with 0.1% Saponin (Sigma-Aldrich) with 0.5% BSA in PBS for 30 minutes. Samples were incubated in 0.1% Saponin and 5% Donkey serum in PBS for 1 h at room temperature. Primary antibodies were administered overnight at 4C and consisted of mouse anti-NKX6.1 (R&D Systems, 1:100), mouse anti-C-peptide (R&D Systems, 1:100), and rabbit anti-NKX6.1 (Abcam, 1:100). After washing to remove residual primary antibodies, samples were incubated for 1-2hrs at room temperature with secondary antibodies anti-mouse Alexa Fluor 488 and anti-rabbit Alexa Fluor 555 (Invitrogen, 1:500) diluted in the 0.1% Saponin with 0.5% BSA solution. Samples were washed and suspended in PBS before transferring to either flow cytometry tubes or 1.5mL Eppendorf tubes. Accuri C6 © Flow Cytometer or ImageStream Mark II was used to quantify the protein expression. The gate was set beyond cells positive for secondary antibody only to eliminate false positives.

3.2.15 Glucose Stimulated Insulin Secretion

See Chapter 2 methods.

3.2.16 Alignment and Analysis of scRNA-seq Data

Single cells were isolated from both 2D and 3D TEC samples. In brief, 2D TECs were removed from wells via trypsinization. Media was removed from the wells and TrypLE Select dissociation buffer (ThermoFisher) was added. Cells were then incubated at 37 °C for 7 min, after which cells were gently pipetted off the wells and any remaining aggregates were manually broken up. Cells were then placed in DMEM/F12 media supplemented with 1× B-27 (ThermoFisher) and Y-27632 Rock inhibitor (1:1,000, StemCell Technologies) and centrifuged at 250g for 5 min to pellet.

The 3D TECs were decapsulated with 100 mM EDTA and placed in a Ficoll gradient to remove both capsular debris and dead cells as previously noted. The live cell layer was pipetted off the gradient to be dissociated for analysis. Live cellular aggregates were placed in DMEM/F12 media supplemented with 1× B-27 and Y-27632 Rock inhibitor and allowed to settle for 10 min. Media was then gently removed and aggregates were placed in TrypLE Select and incubated for 17 min. On completion, cells were centrifuged at 250g for 5 min to pellet.

Once pelleted, cells were then checked for both viability as well as the presence of any remaining aggregates using the Countess II Automated Cell Counter (ThermoFisher). Single cells were then suspended in PBS supplemented with 20% FBS and sent to the Genomics Research Core at the University of Pittsburgh for quality control, library preparation and droplet sequencing

on the 10X Genomics Chromium controller. Single cells (>70% viability) were washed, strained, and subjected to 10X Genomics single-cell library construction (Chromium single-cell 3′ reagent v.3 kit) and sequencing protocol according to the manufacturer's recommendations. The count files were demultiplexed and aligned using Cell Ranger pipeline.

To cluster the cells in our datasets, we first compute principal component analysis projection for all cells and construct the k-nearest neighbor graph of the cells based on Euclidean distances in principal component analysis space (with k = 20). We then use the Louvain algorithm to cluster our cells[175]. The granularity of the clusters is determined by a user-defined resolution parameter, and for both our 2D and 3D iPSC-TECs, we used a resolution of 0.1. These steps were all completed in R using Seurat.

To align the 2D and 3D iPSC-TEC datasets, scRNA-seq integration was performed following the approach described in Stuart et al. A set of 'anchor' pairs was identified between the two datasets, which are pairs of cells representing the same biological state in the two datasets. Anchors are computed in the reduced dimension space via canonical correlation analysis, which is used to identify pairs of mutual nearest neighbor cells. These anchors were calculated using the Find-Integration-Anchors function in Seurat. After identifying these anchors, a weighted average of vector differences between cells to be integrated and anchors is used to transform the representation of cells and produce a final integrated expression matrix. The integrated expression matrix that combines the 2D and 3D iPSC-TEC datasets was calculated using the Integrate-Data function in Seurat. Cells were clustered again in this aligned dataset using the Louvain algorithm as described above, using the same resolution parameter of 0.1.

3.2.17 RNA Isolation and Gene Expression Analysis

For both differentiation methods, aggregates were retrieved from the alginate capsules and washed 2-3 times with PBS before lysis.

For islets, mRNA was isolated using the NucleoSpin RNA II kit (Macherey-Nagel, Bethlehem, PA). cDNA was obtained using ImpromII Reverse Transcription (Promega, Madison, WI). Each PCR reaction contained 5 µl SYBR Green Master Mix (Agilent, Santa Clara, CA), 2 µl nuclease free H2O, 2 µl primer, and 1µl cDNA. Samples were normalized to the house keeping gene GAPDH and analyzed relative to UD hESCs using the ΔΔCt method. Gene expression was measured with quantitative polymerase chain reaction (qRT-PCR) using an MX3005P system (Agilent).

For TECPs, total RNA was extracted with TRIzol (Invitrogen) and complementary DNA was synthesized using the SuperScript III First-Strand synthesis system for RT–PCR (Invitrogen). Real-time qPCR was performed using the All-in-One qPCR Mix (Genecopoeia) with a Roche LightCycler 480 system (Roche Applied Science). Relative gene expression was normalized to GAPDH.

3.2.18 Statistical Analysis

See Chapter 2 methods.

3.3 Results

3.3.1 Islet Differentiation from hPSCs Using Alginate Encapsulation as 3D Culture Platform

3.3.1.1 3D Culture Platform Comparison

As our group has previously established, islet differentiation is improved with a 3D culture over the traditional 2D culture methods [53, 146, 174]. With the rise of in vitro derived functional islets from human pluripotent stem cells (hPSCs), we sought to utilize our alginate encapsulation system to differentiate human induce pluripotent stem cells (iPSCs) into functional islets. For this, we looked at methods of differentiation that fully differentiated hPSCs into islets in a complete 3D environment. The 30+ day protocols from Pagliuca et al.[147] and the subsequent v8 from Veres et al.[45] stood out to us due to the robust insulin stimulation of the resulting beta cells (sc-β) and the use of suspension aggregation to continuously culture the hPSCs through the differentiation. As such, the differentiation steps we utilized have been adapted from these protocols[45, 147]. For testing our platform with this differentiation, we used a stirred suspension aggregation (SSA) culture as the control to recapitulate the suspension culture systems used. In short, single cells were seeded into a 35mm petri dish in 2 mL media at a density of 0.5 million cells/mL, and the dish was then placed on an orbital platform shaker, residing in an incubator, and set to 95 RPM. The cells would then aggregate due to the centrifugal forces maintaining their suspension in the media. In addition to replicating the published 3D culture platform, the SSA culture provides an appropriate comparison to our alginate-based single-cells-encapsulation (SCE) by both providing support for single cells to form into aggregates and allowing for differentiation of the cells under 3D conditions

from the start. Both culture platforms are depicted in Figure 3.1 with images showing how cells grow in each.

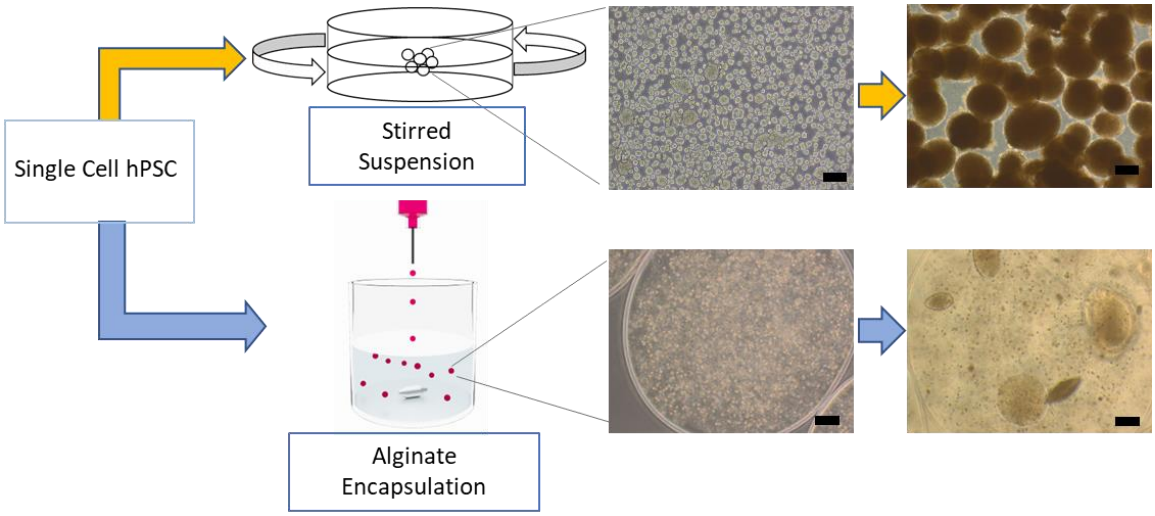

Figure 3.1 Stirred Suspension Aggregation and Single Cell Encapsulation 3D culture platforms that will be compared for differentiating hPSCs into islet-like cells. (scale= 200µm)

Initial testing with SSA on our iPSC lines resulted in a degradation in the aggregates' structure, where only a few irregular-shaped aggregates remained by day 12 (Figure 3.2). As depicted, the cells aggregate well, forming spherical aggregates that remain through the start of the differentiation, but as the differentiation continues, the aggregates start becoming irregular, eventually degrading entirely. This indicated SSA would not be feasible with iPSCs, however, we still wanted to compare our SCE culture platform against the SSA for functional islet differentiation.

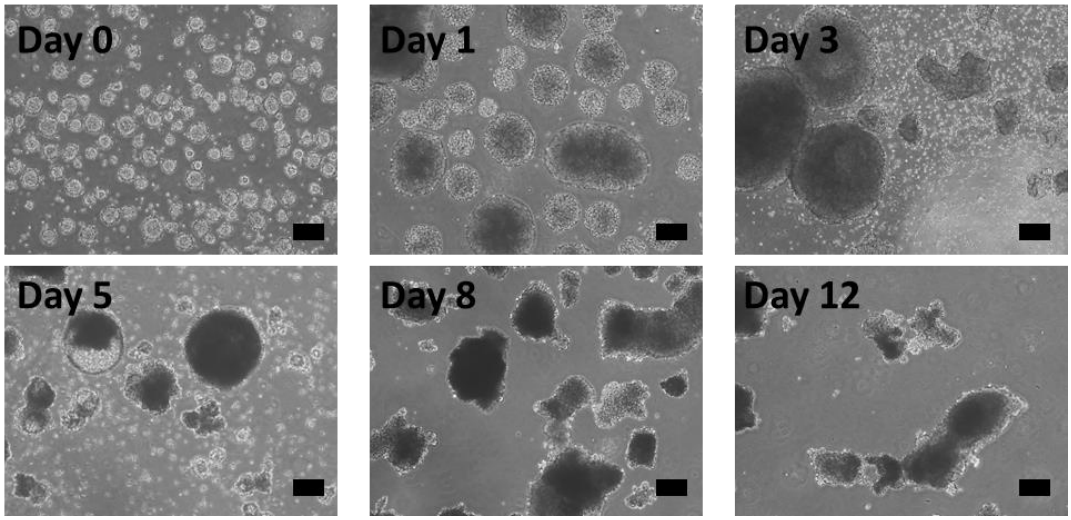

Figure 3.2 iPSC culture in SSA Suspension culture of iPSCs from the intiation of islet differentiation (Day 0) until the aggregates showed degradation (Day 12) (scale=200µm)

In this pursuit, we utilized the human embryonic stem cell (hESC) line, H1, to test SSA and SCE platforms. Having previously demonstrated this hESC line's growth and islet differentiation potential within SCE conditions, we found that it would be an optimal cell line for this test[53]. With initial testing, we wanted to see how SSA would compare to SCE with undifferentiated cell growth, focusing on growth rate and viability for a 1-week span. Since hPSCs grow much faster and require more nutrient diffusion in the undifferentiated state, we could get a glimpse of the extent that the cells could grow while remaining viable and compare the growth rate for each platform. The results of this study can be viewed in Figure 3.3. As parts A, C, and D of Figure 3.3 demonstrate, the growth rate for SSA is much higher than that of SCE with aggregates reaching an average of 145±56µm in radius compared to SCE (63±21µm) by day 7. This signifies that while SCE aggregates would not have issues with oxygen diffusion, the SSA aggregates would risk forming hypoxic cores, since a 100-250µm radius would have issues with oxygen diffusion [176]. In terms of viability (Figure 3.3 B, E), the SSA (0.94±0.08) shows significantly ($p<0.05$) higher

viability than SCE (0.71±0.07). The reduced viability for the SCE stems from the inability to remove dead cells from the alginate capsule without dissolving them. With SCE, dead single cells will remain encapsulated throughout the culture, while the SSA culture allows for dead cell debris to be removed during media changes and during the assay process.

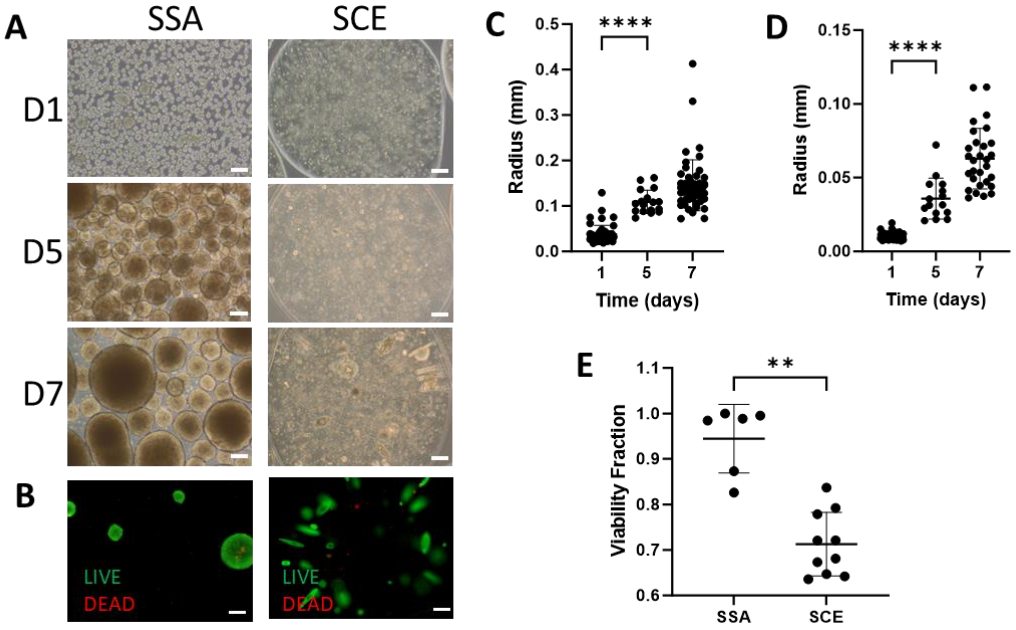

Figure 3.3 hESC SSA vs SCE Undifferentiated Cell Growth (A) Phase images for each culture platform from day 1 to day 7. (B) Representative images for Live/Dead assay for the aggregates on day 7 of growth with live (green) and dead (red). (C, D) Image analysis for growth for SSA and SCE respectively based on the phase images. (E) Image analysis of Live/Dead assay at day 7 of the culture. (scale=200μm)

With the hESC undifferentiated culture characterized, we looked towards the growth during the islet differentiation and endpoint functionality. The differentiation follows a 28–35 day protocol, depicted in Figure 3.4 A, where the main phases for differentiation are the definitive endoderm phase (DE), pancreatic progenitor phase 2 (PP2), endocrine progenitor phase (EN), and hPSC-islets (sc-β), where the cells will mature to gain insulin functionality[147]. To assess the differentiation, we used: phase imaging to see how well the cells maintain their aggregation

through the differentiation; flow cytometry and RT-PCR to determine how well islet-specific markers express as the differentiation progresses; and a glucose stimulated insulin secretion (GSIS) assay to test the insulin functional at the end of differentiation. With the start of the differentiation, the aggregate sizing for the SSA was much higher than the SCE with average radii being 65±33 μm and 36±14 μm respectively (Figure 3.4 B, C). The endpoint morphology for each is very contrasting as well. The day 27 SSA has an irregular, non-spherical shape, while SCE shows a more uniform expansion from the initial shape (Figure 3.4 B, C). The resulting SSA aggregates were unstable and yielded few usable aggregates by the end of the differentiation. In contrast, the endpoint SCE culture provided ample aggregates to conduct multiple assays per well of culture.

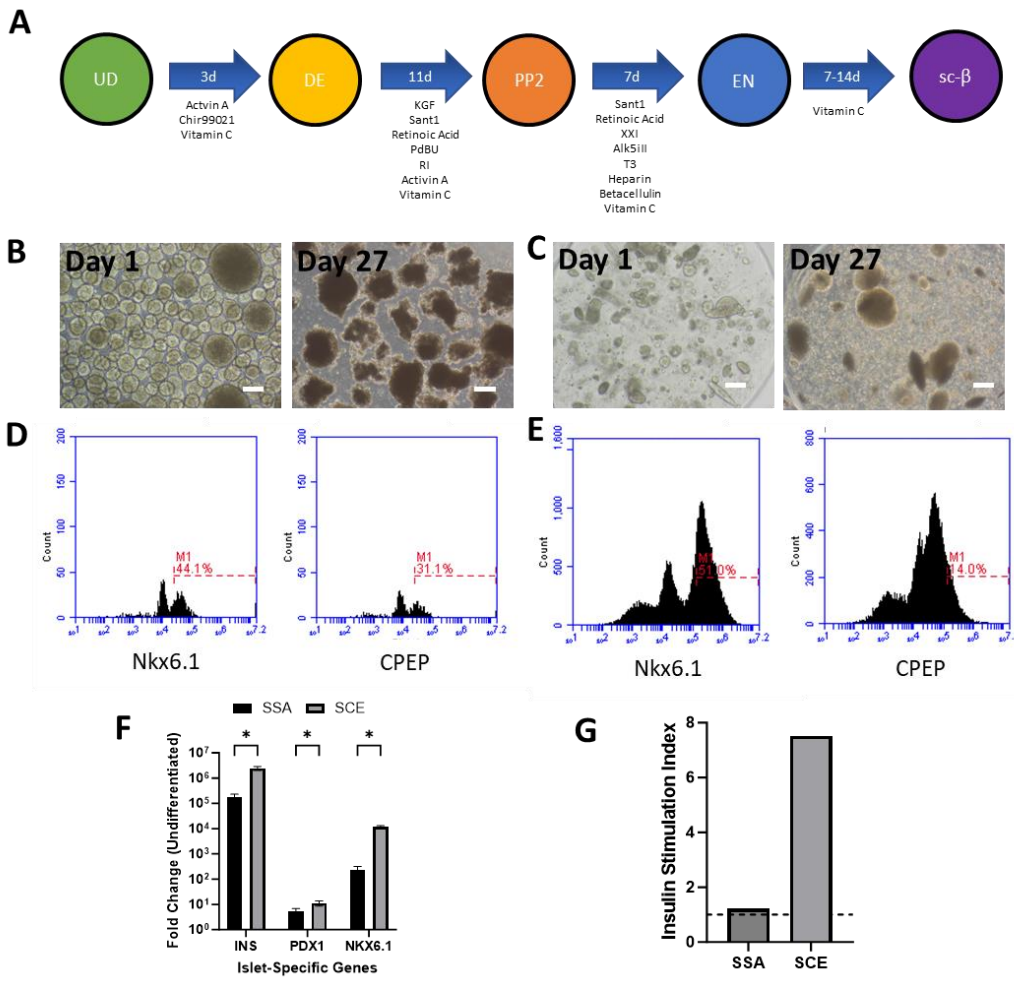

Figure 3.4 hESC SSA vs SCE Islet Differentiation (A) The phases of the islet differentiation with undifferentiated (UD), definitive endoderm (DE), pancreatic progenitor 2 (PP2), endocrine progenitor (EN), and islet-like cells (sc-β) phases. (B) Phase images for days 1 and 27 of differntiation for SSA. (C) Phase images for days 1 and 27 for SCE differentiation. (D) Flow cytometry for NKX6.1 and C-peptide for EN phase SSA cultured cells. (E) Flow cytometry for NKX6.1 and C-peptide for EN phase SCE cultured cells. (F) Gene expression for insulin (INS), PDX1 and NKX6.1 for EN phase SSA and SCE culture cells. (G) Insulin stimulation index derived from GSIS for sc-β phase cells culture with SSA and SCE. (scale=200μm)

The flow cytometry (Figure 3.4 D, E) quantifies the number of cells positive for NKX6.1 and C-peptide, which indicates insulin producing β-cells. The SSA formed a greater number of C-

peptide positive cells (31.1%) and lower NKX6.1 positive cells (44.1%) compared to the SCE, with 14.0% and 51.0% for C-peptide and NKX6.1 respectively. In contrast, the gene expression for key islet factors (INS, PDX1, NKX6.1) is significantly higher in the SCE culture than the SSA culture (Figure 3.4 F). To determine insulin secretion functionality, the aggregates were tested with a GSIS assay where they are subjected to a low glucose concentration (3mM) and subsequent high glucose concentration (16mM), and the secreted insulin is measured. The insulin stimulation index is the fold increase in insulin secretion of the high glucose compared to the low glucose. The resulting stimulation indices for SSA and SCE (Figure 3.4 G) indicate the greater stimulation for SCE over SSA. From this initial study, we found the SCE culture can provide a greater number of aggregates and can provide necessary environment to form insulin functional cells at a similar quality to SSA. With the insight with the hESC differentiation, we had greater confidence in forming iPSC-derived islets using the alginate SCE platform moving forward.

3.3.1.2 iPSC-Islet Development with Alginate Encapsulation Platform

Developing iPSC-islets, instead of utilizing the previously formed hESC-islets, is a necessary step for future application, since iPSCs provide a more sustainable framework. Additionally, the ability to source the cells from a wider range of donors allows for a greater genetic diversity for modeling disease and testing treatments, and the ability to make iPSCs patient specific opens the option for personalize treatment testing and options for immune-suppressant-free implantation that hESCs would not be able to do. As with the hESCs, the initial test for our fibroblast-derived iPSC lines started with the characterizing the growth of the undifferentiated cells within the alginate to best gauge the rate of expansion and viability under optimal growth conditions (Figure 3.5). As seen in Figure 3.5 A, C, the growth of the aggregates increased daily by a statistically significant amount. The growth observed appears similar to the hESC UD growth

(Figure 3.3 D). For comparison, the day 5 aggregates for the iPSC and hESC lines were 30±13μm and 36±14μm radius respectively, showing that growth within the SCE culture platform is uniform across hPSC lines. The viability analysis for the iPSC (Figure 3.5 B, D) was more extensive with daily sampling to best understand the state of the aggregates prior to starting differentiation. The viability overall remains very high (>0.88) from day 1 to 5 with the majority of death from single cells, but a significant decrease occurred on day 6 (0.65 viability fraction) where more aggregate death was observed. From this we set day 5 as the optimal day to initiate differentiation.

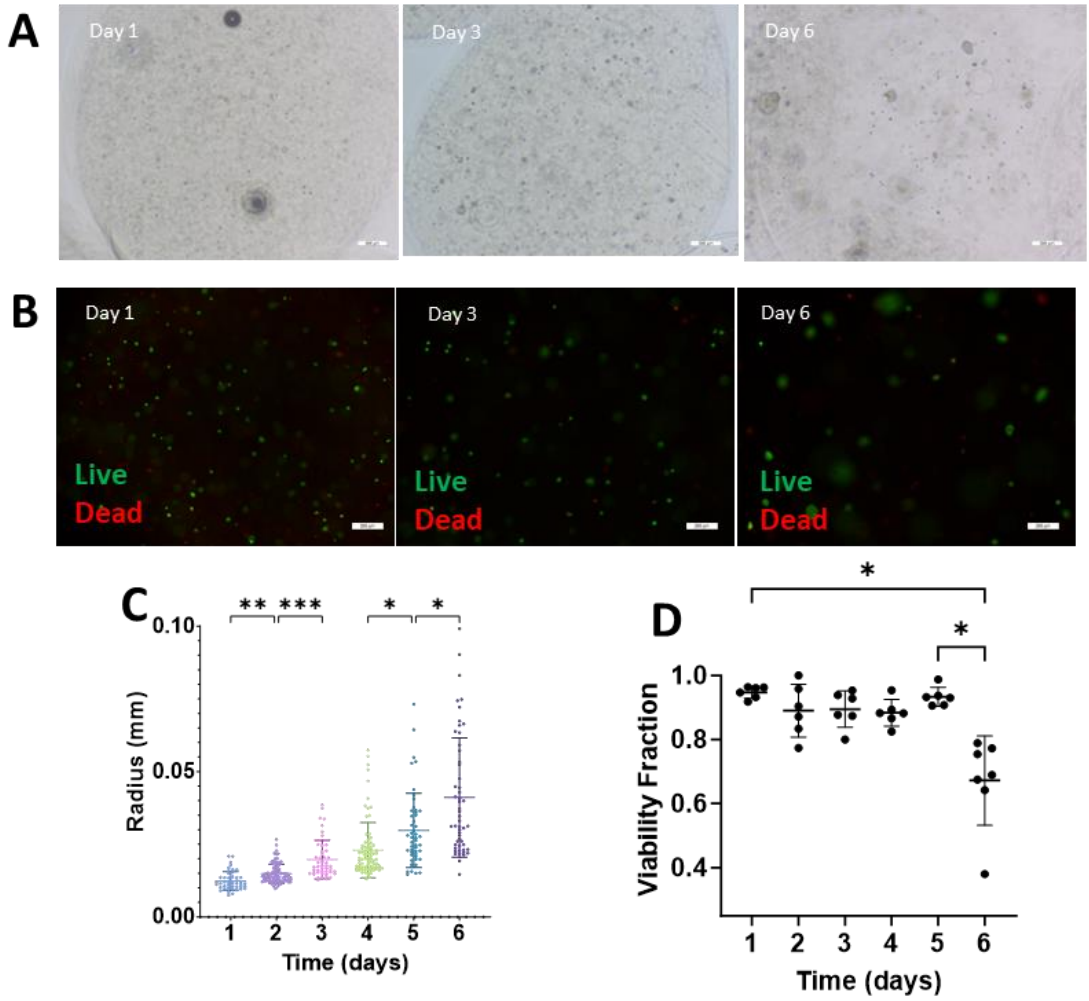

Figure 3.5 Undifferentiated iPSC Culture in Alginate (A) Phase images of SCE for undifferentiated iPSC growth within alginate over 6 day culture. (B) Viability assaying for undifferentiated iPSC growth in alginate over 6 day culture. (C) Image analysis of phase images for iPSC-aggregate expansion over 6 day span. (D) Image analysis of daily viability assay images. (scale=200μm)

The differentiation of the iPSCs toward islets was done using the same steps done with the hESCs. The growth of the iPSC-aggregates was tracked via phase imaging and size distribution analysis provided the growth rate from the initiation of differentiation (day 0) to the end of the EN phase (day 28) (Figure 3.6 A). From the analysis, the initial size of the aggregates was 27±9μm and the most significant ($p<0.05$) changes in aggregate size occurred until day 8, where the

aggregates remained at an average radius of 90µm through the duration of the differentiation (Figure 3.6 B).

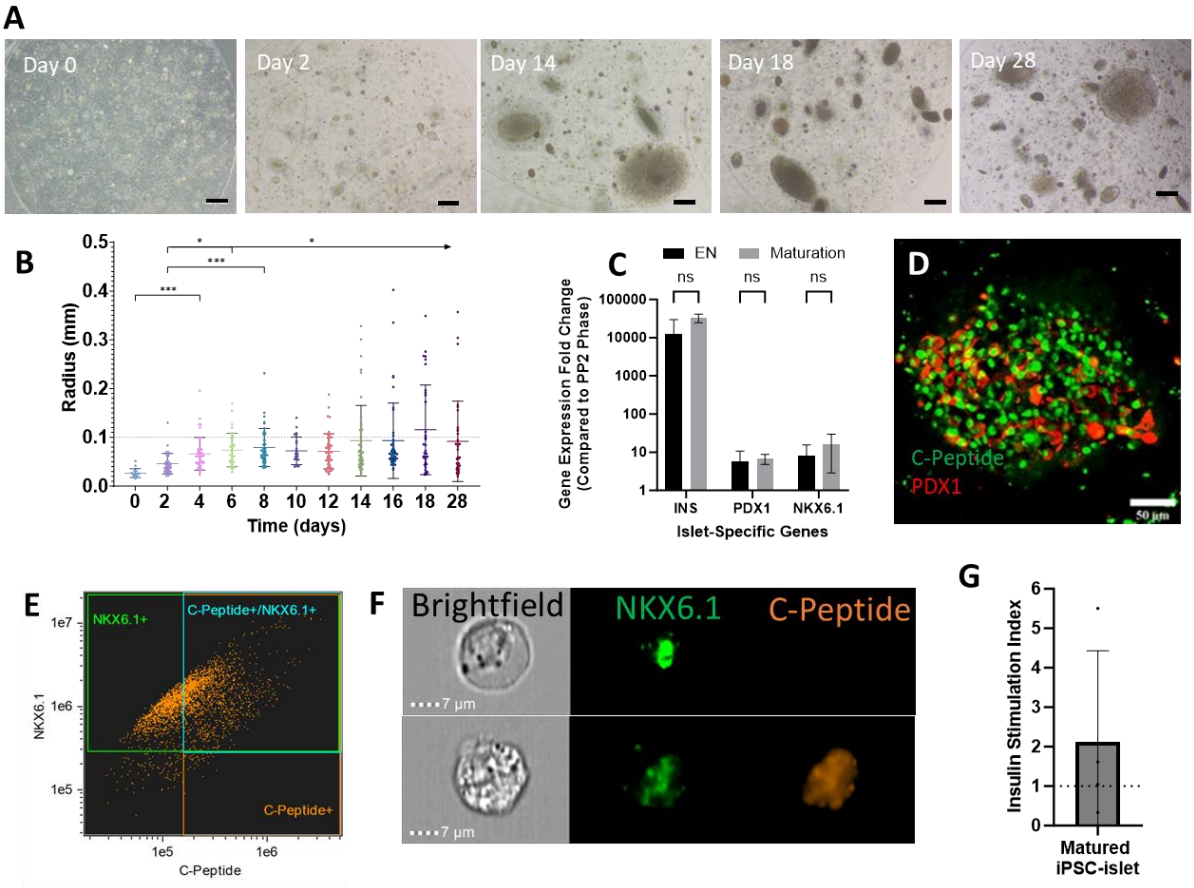

Figure 3.6 iPSC Islet Differentiation (A) Phase images for aggregate growth and differentiation within alginate capsule. (B) Image analysis of phase images for quantifying aggregate growth rate up to end of EN phase. (C) Gene expression from RT-PCR for major islet markers (INS, PDX1, and NKX6.1) for PP2 and EN phases. (D) Representative image for C-peptide/PDX1 co-immunostained aggregate at end of EN phase. (E) Flow cytometry results from ImageStream showing the distribution of cells that are positive for NKX6.1 and/or C-peptide. (F) Representative images from ImageStream analysis for maturation phase cells co-stained for C-peptide and NKX6.1 displaying NKX6.1+/C-peptide- (top) and NKX6.1+/C-peptide+ (bottom) cellss. (G) GSIS-derived insulin stimulation index (SI) for fully matured iPSC-islets where stimulation below the dotted line (SI=1) is not functioning properly.

To characterize the development of the iPSCs into islet-like cells, islet specific markers were examined to confirm their presence and continued to increase as the differentiation progressed. The islet-specific gene expressions, insulin (INS) and transcription factors (PDX1 and NKX6.1), were measured with the progression of the differentiation from PP2 to EN phase (Figure 3.6 C). As seen with the hESC, these factors show an increase from PP2 to EN with INS and NKX6.1 being statistically significant ($p<0.05$). This confirms that SCE supports proper islet differentiation for iPSC. At the end of the EN phase, the aggregates were co-stained for PDX1 and insulin secretion byproduct, C-peptide, to detect the number of immature β-cells present (Figure 3.6 D). As the image shows, there are a large portion of C-peptide producing cells within the formed aggregate as well as cells producing the pancreatic specific transcription factor PDX1 are also prominent within the aggregate.

Further characterization of islet-specific phenotype was conducted at the end of the differentiation. Characterization of the insulin producing cell population at the end of the maturation phase was done using an ImageStream instrument that both functions as a flow cytometer and captures the images of the single cells (Figure 3.6 E, F). The flow cytometry scatter plot from the ImageStream (Figure 3.6 E) provides the composition of insulin producing cells in the culture, where 52.7% are co-positive for NKX6.1 and C-peptide and 42.9% are NKX6.1 positive. Since NKX6.1 is a transcription factor precursor to β-cell development[177], the lack of a C-peptide+ only population shows that there was no non-specific staining of C-peptide. This can be further demonstrated with the images taken for NKX6.1+/C-peptide+ and NKX6.1+/C-peptide- (Figure 3.6 F) where the stains are localized to the correct regions of the cells. To test the functionality of the iPSC-islets, the formed aggregates were subjected to a GSIS test, where the insulin stimulation index (SI) was calculated (Figure 3.6 G). As with the hESC differentiation, the

iPSC-islets were able to demonstrate functional stimulation from glucose (SI>1). However, the produced aggregates were not universal in their functionality, with some samples having SI<1.

3.3.1.3 β-cell Enrichment Using Fluorescent Sorting

To improve the uniformity of the endpoint functionality with the iPSC-islets, we looked to enriching the β-cell population using fluorescence-activated cell sorting (FACS). In this, we would utilize a live cell stain to fluorescently tag the insulin producing β-cell populations and isolate them using FACS. This would enable us to form aggregates with a higher concentration of insulin producing cells which we hypothesize would have improved and more consistent insulin secretion functionality. Promising options for insulin cell stains were zinc targeting intracellular stains, such as Newport Green, which have reportedly been used for detecting and enriching insulin producing cell populations[178-180]. In addition to including the zinc specific stain, the glucagon specific DPP4/CD26 surface stain was utilized to remove any insulin/glucagon-polyhormonal cells within the population. Both stains were used on aggregates (Figure 3.7 A) and single cells (Figure 3.7 B) to visualize the rough number of cells that would stain positive and to confirm that cells would stain properly and remain viable after by reseeding to a well (data not shown). The staining was conducted on differentiated cells at the end of the EN phase, with the objective to use FACS right before maturation to allow the single cells to reform into aggregates during the final stage of differentiation. The FACS results for this staining process can be viewed in Figure 3.7 C, where the number of Zn+/DPP4- cells made up roughly 29.3% of the viable cell population. These cells were isolated, re-aggregated, and re-encapsulated for the duration of the maturation before testing their functionality with GSIS. Comparing the GSIS-based insulin stimulation index (Figure 3.7 D) for the sorted iPSC-islets to the non-sorted, natively formed iPSC-islets from the same differentiation batch, there wasn't a significant ($p>0.05$) improvement with the sorted cell

population in terms of overall stimulation and the uniformity for functioning aggregates remained similar to the native control.

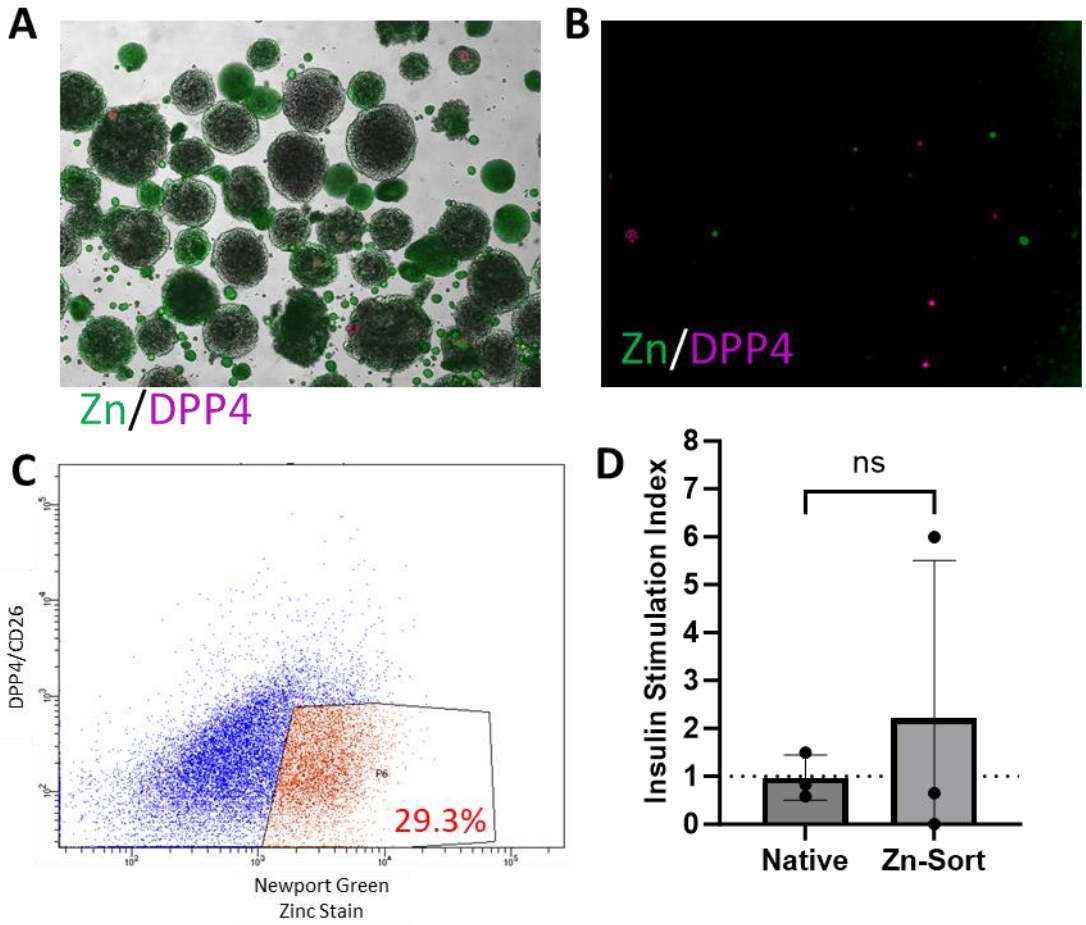

Figure 3.7 Fluroescent Labeling of β-cells with Zinc-specifc Surface Stain (A) Representative image for iPSC-islets stained with Newport Green (Zn) (green) and DPP4 surface marker (purple). (B) iPSC-islets dissociated into single cells and stained with Newport Green (Zn) (green) and DPP4 surface marker (purple). (C) FACS scatter plot for DPP4 (y-axis) and Newport Green (x-axis) with sectioned region being Zn+/DPP4-. (D) The resuling GSIS-based insulin stimulation index (SI) from sorted cells compared to the non-sorted, natively formed iPSC-islets.

To improve the accuracy and efficiency of identifying insulin producing β-cells, we looked towards forming an insulin-reporting iPSC line. In collaboration with Dr. Yong Fan at Allegheny

General Hospital, a plasmid construct for the insulin reporter was created (Figure 3.8 A) where an mCherry fluorescent protein gene sequence would be promoted whenever the insulin gene is promoted, and to maintain the purity of the transfected cells, a puromycin resistance gene was included to allow the transfected cells to survive levels of puromycin that would kill non-transfected cells. To confirm the co-expression of mCherry with insulin, the islet differentiated INS-mCherry reporters were stained for C-peptide at the end of the EN phase when sorting of the cells would occur (Figure 3.8 B). The aggregates showed accurate expression of mCherry in C-peptide producing cells, but regions of the C-peptide+ cells were also mCherry-, meaning not all the differentiated cells retained the reporting gene. Since the mCherry+ cells were correlated with C-peptide producing cells, the reporter would be able to be used as intended. To inform us about the distribution of cells when using FACS, we had also utilized the ImageStream to have a basis for the number of mCherry+ cells and visually confirm the expression within single cells (Figure 3.8 C, D). The flow cytometry data from the ImageStream confirms a good population of mCherry+ cells, and the resulting images show a range of expressed amounts of mCherry within the cells. With the cells analyzed with the ImageStream, we moved forward with utilizing the FACS for isolating the mCherry+ cell populations (Figure 3.8 E), where the resulting positive cells were re-aggregated and matured. The resulting insulin stimulation index from the matured INS-mCherry reporter iPSC-islets showed visibly higher levels of stimulation than the non-sorted matured INS-mCherry reporter iPSC-islets, designated as native culture, but the difference is not statistically significant ($p=0.0542$) (Figure 3.8 F).

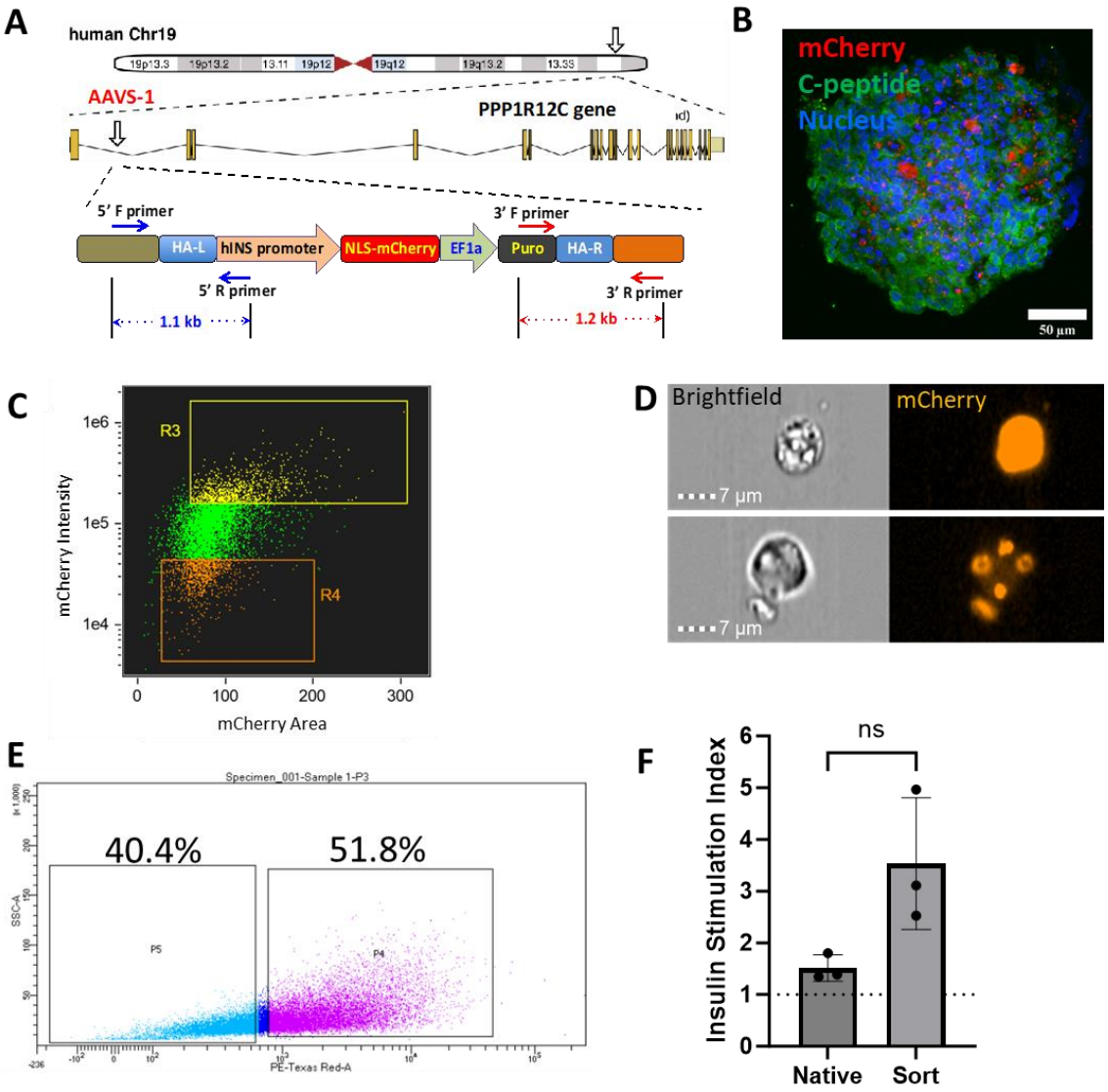

Figure 3.8 INS-mCherry reporter for β-cell enrichment (A) Schematic for the plasmid construct used for developing the INS-mCherry reporter cells. (B) Representative fluorescent image of islet differentiated INS-mCherry reporter aggregate stained for C-peptide comfirming co-expression with mCherry. (C) Scatter plot from ImageStream showing the regions of mCherry+ and mCherry- cells resulting from the islet differentation. (D) Images taken with ImageStream showing the range of mCherry presence within positive expressing cells. (E) FACS scatter plot result for sorting INS-mCherry reporter cell at end of EN phase. (F) Insulin stimulation index comparison of sorted and non-sorted, native INS-mCherry reporter iPSC-islets.

3.3.2 Thymus Epithelial Progenitor Cell (TEPC) Differentiation of iPSCs Using Alginate Encapsulation Platform

The following parts of this chapter are sourced from Zeleniak, A., Wiegand, C., Liu, W. et al. De novo construction of T cell compartment in humanized mice engrafted with iPSC-derived thymus organoids. Nat Methods 19, 1306–1319 (2022). https://doi.org/10.1038/s41592-022-01583-3[181].

3.3.2.1 General Characterization of Differentiation Outcome

We have previously shown that encapsulation of hESCs within 3D alginate capsules not only facilitates their propagation when maintained at the pluripotent state, but also enhances their differentiation into pancreatic islet-like cells on induction, as compared to 2D culture[53]. A similar approach was adopted to promote the differentiation of human iPSCs into TEPCs with a modified four-stage induction protocol[53, 167, 168] (Figure 3.9 A, B). Single iPSCs encapsulated in alginate proliferated at undifferentiated stage into small aggregates of approximately 50 μm in diameter after 4 to 6 days of culture (Figure 3.9 C, D). Initial induction toward definitive endoderm (between days 1–4, D1–D4) resulted in increased mean aggregate sizes (box plot, Figure 3.9 D) and a shift in the distribution toward larger aggregate sizes (Appendix Figure 3 A). The average size of aggregates peaked at D7 and decreased slightly on induction of further differentiation toward TEPC lineage at D10 (Figure 3.9 D). Similar patterns of TEPC aggregate formation were observed in differentiating hESCs (Appendix Figure 3 B-D).

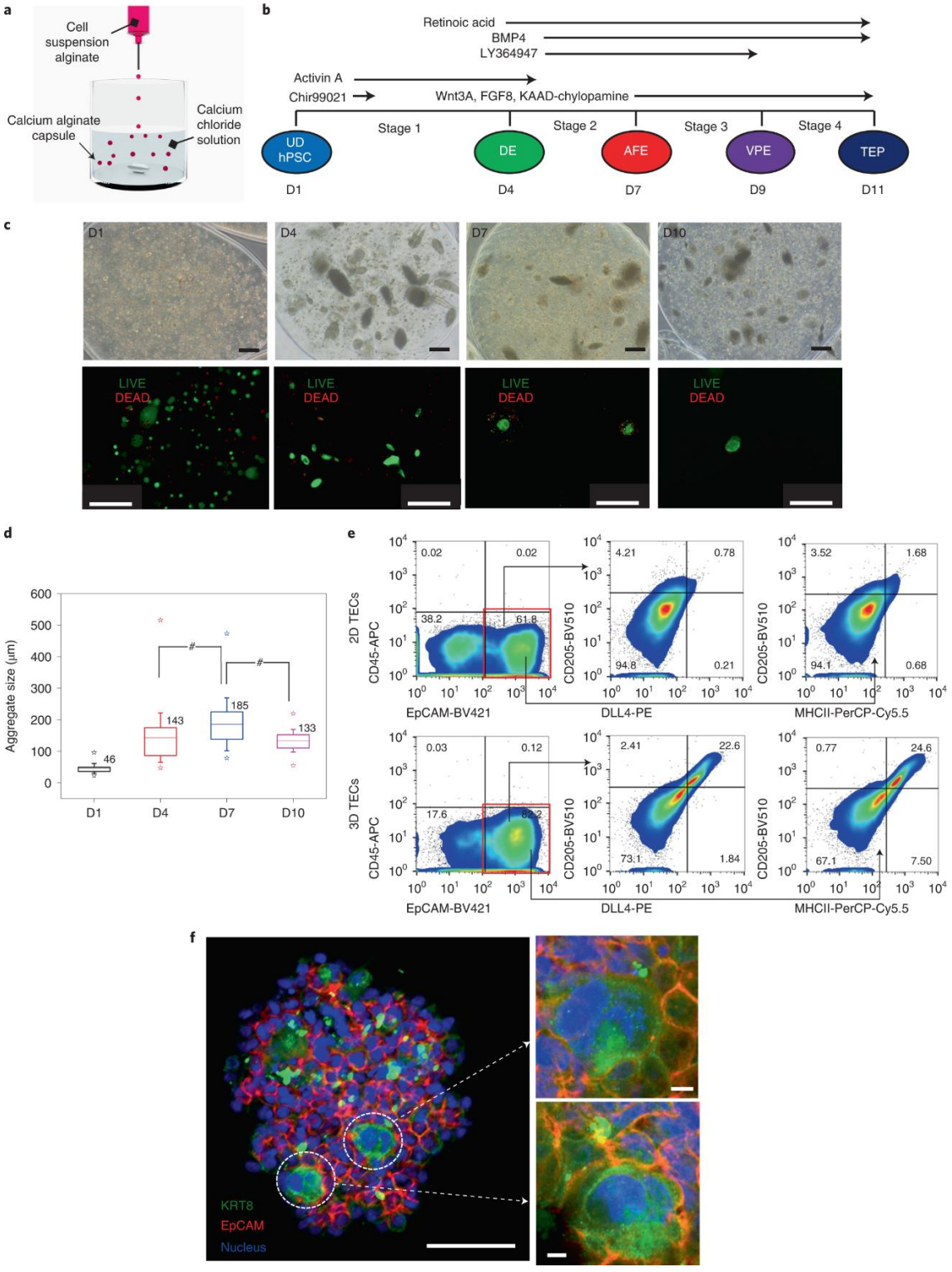

Figure 3.9 Differentiation of iPSC towards TEPC Using Alginate Encapsulation Platform (A) Schematic illustration of iPSC embedding and differentiation in 3D alginate capsule. (B) Differentiation timeline of iPSCs into TEPCs. UD, undifferentiated; DE, definitive endoderm; AFE, anterior foregut endoderm; TEP, thymic

epithelial progenitor. (C) Images of iPSC aggregates at different stages of TEPC differentiation. Top panels, bright field photographic images of iPSC aggregates within the alginate capsules at days 1, 4, 7 and 10 (D1-D10) after initiation of differentiation; blue scale bar, 200 µm. Lower panels, survival of iPSC-derived TEPC aggregates in alginate capsules. Green, live cells with calcein-AM staining; red, dead cells stained with ethidium homodimer-1. Shown are representative images from three independent iPSC-TEC differentiation batches with similar results. Upper scale bars, 200 µm; lower scale bars, 500 µm. (D) Size distribution of iPSC aggregates at different stages of TEPC differentiation. The boxes indicate the interquartile range (25–75th percentile) and the whiskers indicate the standard deviation of the distribution. The mean is denoted by the line across the box and the maximum and minimum is denoted by the 'star' symbol. '#' indicates statistically significant distribution as determined by one way analysis of variance and post hoc Tukey test with a P = 0.05. All groups are statistically significant with respect to D1. (E) Representative FCM analysis of surface expression of TEC lineage markers in 2D- and 3D-cultured iPSC-TECs. All markers were analyzed within the CD45-EpCAM+ gate (red boxes in the left columns). (F) Immunofluorescent images of 3D iPSC-TEC aggregates stained with antibodies against EpCAM (red) and cytokeratin-8 (KRT8, green). White scale bar, 50 µm. Right-hand inserts, high magnification images of the indicated areas; white scale bars, both 5 µm. Shown are representative images from three independent iPSC-TEC differentiations with similar results.

The overall efficiency of iPSC to TEPC differentiation was evaluated by examining the surface expression of EpCAM, a key TEC marker, with flow cytometry (FCM). About 84.6 ± 13% (n = 5) of iPSC-derived TEPCs were EpCAM+ (Figure 3.9 E). Notably, a substantial population of EpCAM+ cells was CD205+DLL4+MHCII+, suggesting that the 3D platform can facilitate the maturation of TEPCs into cTEC subsets (Figure 3.9 E, right panels). In corroboration with the FCM data, immunofluorescence analyses showed the presence of both CD205+ and DLL4+ cells (Appendix Figure 4). In addition, a unique group of EpCAM+ cells coexpressing high levels of KRT8, the cytokeratin gene expressed in both TEC progenitors and cTECs (Figure 3.9 F), was observed. These data highlight the successful progression of iPSC differentiation into TEC subsets.

To further characterize the iPSC-TECs, we analyzed the expression of TEC-specific markers by bulk quantitative PCR with reverse transcription (RT–qPCR) (Appendix Figure 15). In line with previous reports, increased expression of ventral pharyngeal endoderm (VPE), TEPC markers (EYA1 and FOXN1), loss of stem cell (OCT4 and SOX2) and definitive endoderm (SOX17) markers were observed, suggesting successful induction of TEPC lineage specification (Appendix Figure 15 C, D). Marked increases in expression of cytokeratin genes (for example, sixfold for KRT17, fivefold for KRT18) were seen in TEPCs generated in the 3D alginate capsules when compared to those derived from the 2D culture, suggesting their epithelial nature (Appendix Figure 15 A). Moreover, cTEC-specific genes critical for self-antigen processing and positive selection functions (for example, PRSS16, ACKR4 and PSMB11) were expressed at significantly higher levels in 3D TECs (Appendix Figure 15B). DLL4, one of the Notch ligands present on the surface of cTECs that is essential for T-lineage specification is also elevated (Appendix Figure 15 B). Similarly, the expression of AIRE, a key transcriptional regulator for TSA expression in mTECs, was promoted solely in the 3D culture. Consistently, a similar expression pattern was shared by CSN2, a TSA whose expression in mTECs is regulated by AIRE (Appendix Figure 15 E). Such TEC-specific gene expression patterns were also detected in hESC differentiation into TEPCs (Appendix Figure 5), but not observed in iPSC-derived islet aggregates generated from the same 3D platform with islet cell differentiation protocol (Appendix Figure 6), suggesting further the specificity of our protocol to induce TEC differentiation.

FOXN1 is a master regulator for TEC lineage specification during thymus organogenesis and is critical for maintaining TEC function in postnatal thymus[182, 183]. To further evaluate the expression of FOXN1 in 3D iPSC-TECs, we performed immunofluorescence analysis, using in vitro propagated human primary TECs (passage 02 post isolation, P2 hTECs) and lymph node

fibroblastic cells as positive and negative controls, respectively. As shown in Appendix Figure 16, FOXN1 expression was readily detectable in iPSC-TECs, but not in fibroblastic controls. Of note, only a subset of primary P2 hTECs displayed strong FOXN1 staining, presumably due to their exposure to 2D culture in vitro, as it has been shown that TECs cultured under 2D conditions rapidly lose their TEC-specific molecular signature and function (Appendix Figure 16 and Appendix Figure 7)[184]. Indeed, lower levels of FOXN1 transcripts were detected in primary P2 hTECs when compared with freshly isolated human thymus, further suggesting the importance of maintaining 3D configuration for TEC differentiation and culture (Appendix Figure 8). Nevertheless, while much higher than those of 2D iPSC-TECs, FOXN1 expression in 3D iPSC-TECs remained much lower than human thymus, highlighting the need for further protocol optimization to generate mature and functional TECs from human iPSCs (Appendix Figure 15 D and Appendix Figure 8).

3.3.2.2 Phenotypic Characterization of iPSC-TECs with Single-Cell RNA-Sequencing (scRNA-seq)

Expression of markers of non-TEC lineage cells, such as VPE-derived parathyroid epithelial primordium marker GCM2, and mesenchymal/fibroblastic marker PDGFRA, was also detected in 2D and 3D iPSC-TECs by RT–qPCR, suggesting that the iPSC-TECs might not represent a uniformed differentiated product, but rather heterogeneous populations under these conditions (Appendix Figure 15 F). To further characterize the iPSC-TEC populations generated by either 2D or 3D differentiation, scRNA-seq analysis was carried out to profile the transcriptome of individual cells and their relevance to TEC subsets of human thymus was projected. Unsupervised cell clustering analysis showed two and three major cell clusters in the 2D (2D TEC-

0 and −1) and 3D (3D TEC-0, −1 and −2) iPSC-TECs, respectively (Figure 3.10 A). To facilitate the annotation of the iPSC-TEC clusters, we first examined the expression pattern of marker genes specific for published TEC subtypes[165, 185], including common TECs and TEC progenitors (ITGA6, HOX3, EYA1, KRT18), cTECs (PSMB11, LY75, PRSS16, CD274) and mTECs (CD24, CDH1, CLDN3 and CLDN4), as well as markers that are associated with other TEC properties, such as the antigen presenting function (CD74, HLA-DPB1, HLA-DQB1, HLA-DRB1) (Figure 3.10 B and Appendix Figure 17 A). Consistent with the bulk RT–qPCR results, TEC epithelial markers showed increased expression in 3D iPSC-TEC clusters when compared to 2D clusters.

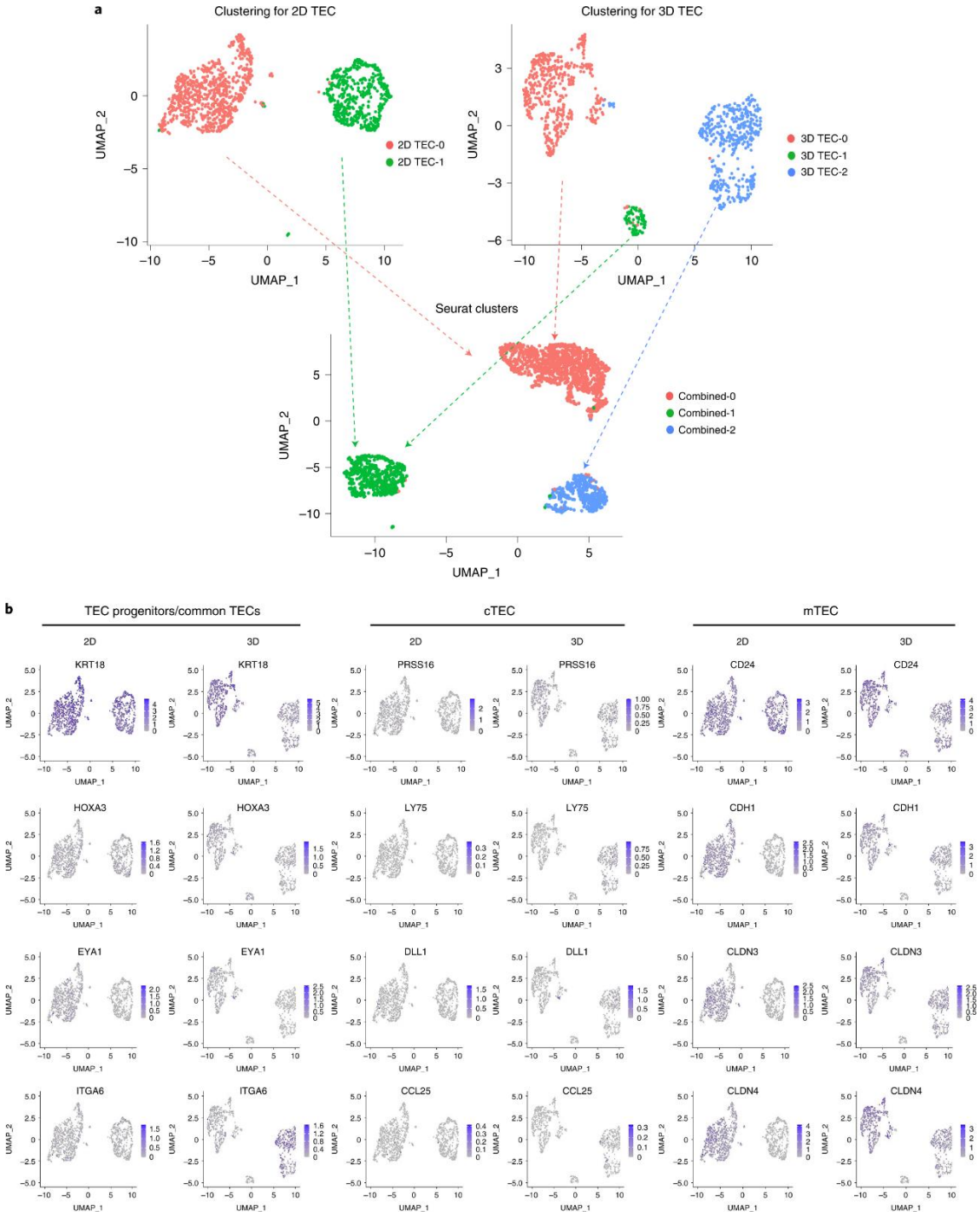

Figure 3.10 Single Cell RNA Sequencing of 2D and 3D differentiated TECs (A) UMAP visualization of 2D and 3D iPSC-TEC datasets. The UMAP graph in the bottom panel represents the clusters of the combined datasets, with the corresponding 2D and 3D clusters connected by the arrows. (B) Annotation of expression of representative TEC progenitor/common TEC (KRT8/KRT18, HOXA3, EYA1 and ITGA6), cTEC (PRSS16,

LY75, DLL1 and CCL25) and mTEC (CD24, CDH1, CLDN3 and CLDN4) specific genes in 2D and 3D clusters. The intensity of purple indicates the levels of gene expression.

To investigate the correlation between the 2D and 3D iPSC-TECs, the two datasets were aligned, and the cells were grouped into three combined clusters (0–2) on the same uniform manifold approximation and projection (UMAP) plot (Figure 3.10 A). The resulting integration of the two datasets suggests that iPSCs followed similar TEC specification/differentiation programs under both the 2D and 3D conditions. Combined cluster 0 represented the largest populations of both 2D and 3D iPSC-TECs (2D TEC-0 and 3D TEC-0, respectively), with a predominant transcriptional signature of epithelial cells, especially those associated with mTECs and progenitors (Figure 3.10 B)[186]. In contrast, cells in combined cluster 1 (corresponding to 2D TEC-1 and 3D TEC-2) express both epithelial and mesenchymal markers, as well as those associated with epithelial-mesenchymal transition, such as SNAI1 and TWIST1. This hybrid epithelial-mesenchymal phenotype is shared by both the in vitro expanded, clonogenic TEC cell lines and the freshly isolated 'common' TEC subsets (comTEC), recently reported by Campinoti and colleagues (Appendix Figure 17 B and Appendix Figure 9)[165]. Finally, cells in combined cluster 2, which only contain cells from the 3D iPSC-TEC, express higher levels of cTEC and its progenitor genes (for example, LY75, ITGA6 and HLA-DPB1), and lower levels of mesenchymal lineage markers (for example, COL1A1 and MMP2), when compared to common cluster 1.

Phenotypic similarities between 2D TEC-0 and 3D TEC-0, as well as 2D TEC-1 and 3D TEC-2 clusters were further demonstrated by Kyoto Encyclopedia of Genes and Genomes (KEGG) pathway enrichment analysis, which showed that they share ten and 11 of the top 20 pathways associated with key cellular and biological functions, respectively (Appendix Figure 10). Moreover, both of the 2D TEC-1 and 3D TEC-2 clusters share five or more of the top 20 (KEGG) pathways with comTEC cells. Taken together, these data indicate that both 2D- and 3D iPSC-

TECs share similar key transcriptional features as those of human TECs and/or TEC cell lines, and that 3D culture encapsulation promotes the development of combined cluster 2, at the expense of combined cluster 1 cells.

3.3.2.3 iPSC-TEC Thymus Can Support T-cell Development In vitro

To examine their ability to program T cell differentiation, we first injected iPSC-TECs with $CD34^+$ HPCs (including HSCs, isolated from human umbilical cord blood) into decellularized mouse thymic scaffolds, to generate the HPC/iPSC-TEC thymus organoids[187] (Figure 3.11 A). The microenvironment of thymic scaffolds would support the survival of injected thymic cells for more than 1 week when cultured in vitro (Appendix Figure 11). To monitor the dynamic spatial distribution of cells within the scaffolds over time, iPSC-TECs and HPCs were labeled with infrared fluorescent dyes DiD and DiR, respectively, coinjected and imaged sequentially with the LI-COR imaging system for 10 days. Broad distribution of both iPSC-TECs and HPCs was observed within the scaffolds, followed by redistribution and expansion after extended culture, suggesting ongoing remodeling of the thymus organoids (Figure3.12 B and Appendix Figure 12). Notably, DiD and DiR signals were largely overlapping throughout the culture, suggesting the colocalization of $CD45^+$ hematopoietic lineage cells with $EpCAM^+$ TEPCs within the scaffold. Close interactions between TEPCs and $CD45^+$ hematopoietic lineage cells were further demonstrated by immunofluorescence analysis, as shown in Figure 3.11 C.

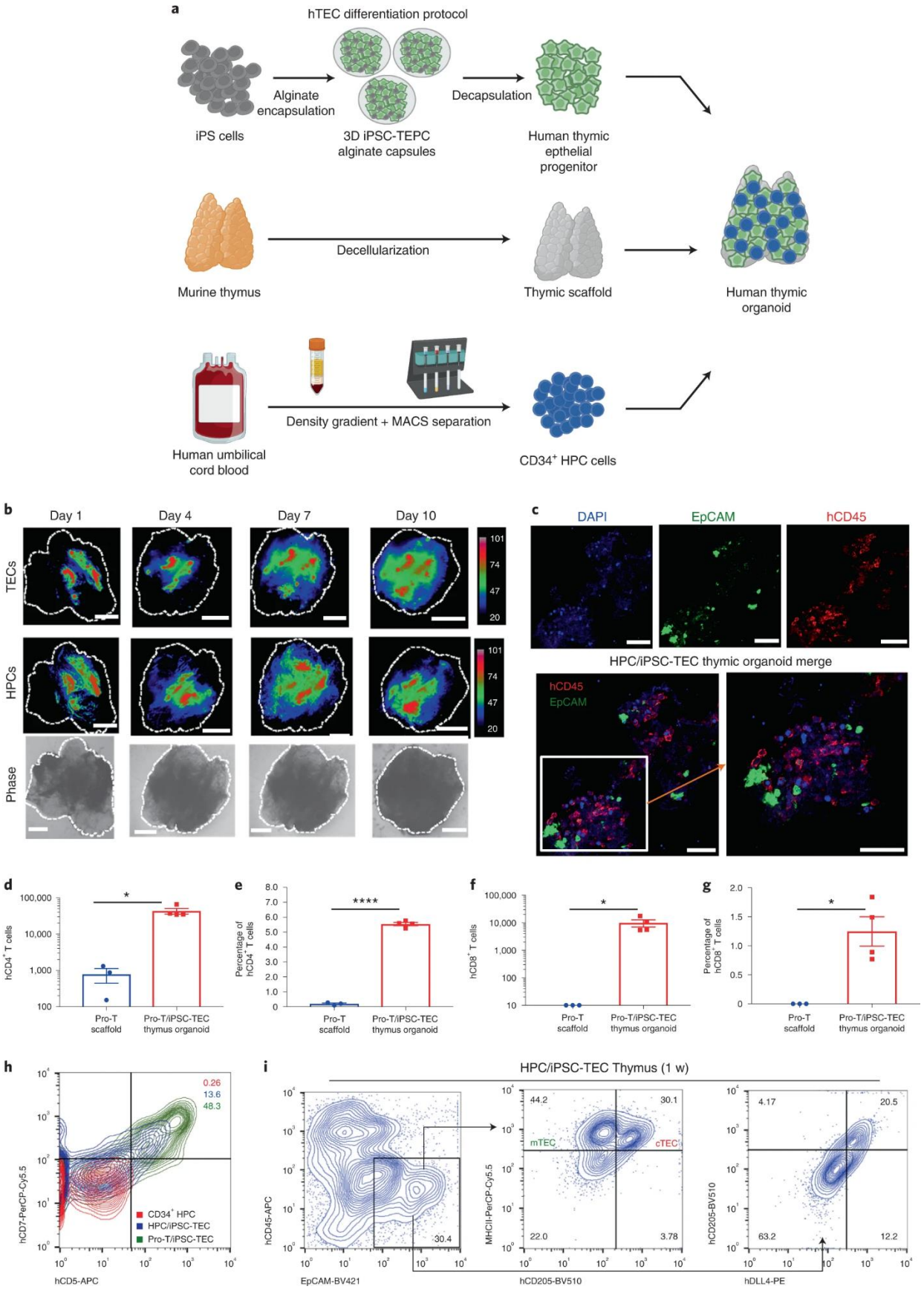
a
hTEC differentiation protocol
iPS cells
Alginate encapsulation
3D iPSC-TEPC alginate capsules
Decapsulation
Human thymic epthelial progenitor
Murine thymus
Decellularization
Thymic scaffold
Human thymic organoid
Human umbilical cord blood
Density gradient + MACS separation
CD34+ HPC cells
b
Day 1
Day 4
Day 7
Day 10
TECs
HPCs
Phase
101
74
47
20
c
DAPI
EpCAM
hCD45
HPC/iPSC-TEC thymic organoid merge
hCD45
EpCAM
d
hCD4+ T cells
Pro-T scaffold
Pro-T/iPSC-TEC thymus organoid
e
Percentage of hCD4+ T cells
f
hCD8+ T cells
g
Percentage of hCD8+ T cells
h
0.26
13.6
48.3
CD34+ HPC
HPC/iPSC-TEC
Pro-T/iPSC-TEC
hCD7-PerCP-Cy5.5
hCD5-APC
i
HPC/iPSC-TEC Thymus (1 w)
hCD45-APC
EpCAM-BV421
30.4
MHCII-PerCP-Cy5.5
hCD205-BV510
44.2
30.1
mTEC
cTEC
22.0
3.78
hDLL4-PE
4.17
20.5
63.2
12.2

Figure 3.11 iPSC-thymus organoids can support the progression of T cell program in vitro.Schematic illustration of human iPSC-thymus organoid construction. iPSC-TECs were coinjected with either CD34+ HPCs or Pro-T cells into decellularized mouse thymus scaffolds to generate HPC/iPSC-TEC or Pro-T/iPSC-TEC thymus organoids, respectively. (B) LI-COR imaging of whole scaffolds showing changes in distribution of iPSC-TECs labeled with DiD (top row) and CD34+ HPCs labeled with DiR (middle row) over 10 days in culture. The boundary of the scaffold is shown as a white dotted line; white scale bar, 2 mm; color bars are a measure of signal intensity. The bottom row shows phase contrast images; scale bars 1 mm. Shown are representative of two independent experiments. (C) Immunofluorescent staining of HPC/iPSC-TEC thymus organoids after 2 weeks of culture. White scale bars, 50 μm. Bottom row shows merged image (lower left panel), with boxed insert displaying higher magnification within the lower right panel. Shown are representative of two independent experiments with similar results. (D-G) Characterization of CD4+ and CD8+ T cell production from Pro-T/iPSC-TEC thymus organoids after 1 week of in vitro culture. 5 × 105 Pro-T cells were used to repopulate the thymus scaffolds either alone or with an equal number of iPSC-TECs. (D, F) Numbers of CD4+ (D, p= 0.0055) and CD8+ T cells (F, p = 0.034) yield per scaffold after 1 week of in vitro culture. (E, G) Percentages of CD4+ (E, p< 0.0001) and CD8+ (G, p = 0.0087) cells in culture. Data are presented as mean values ±s.e.m. using a two-tailed unpaired t-test. (H) Overlay of FCM plots to compare surface expression of T-lineage marker CD7 and CD5: red, CD34+ HPCs; blue, 1 week-cultured HPC/iPSC-TEC thymus organoids and green, 1 week-cultured Pro-T/iPSC-TEC thymus organoids. Shown are representative plots from three independent experiments with similar results. (I) FCM analysis of TEC subset marker expression in 1 week-cultured HPC/iPSC-TEC thymus organoids showing EpCAM+MHCII+CD205− mTECs and EpCAM+MHCII+CD205 + DLL4+ cTECs. Shown are representative FCM graphs from at least three independent isolations with similar results.

It has been shown that crosstalk between TECs and progenitors of T cells (Pro-T, including TSPs and early thymic precursors (ETPs)) within the thymus are critical for T-lineage specification while synergistically promoting their mutual maturation[188-190]. To model thymic crosstalk and to demonstrate that the iPSC-TECs can support the progression of T cell program

within the thymus scaffold microenvironments in vitro, we induced the differentiation of $CD34^+$ HPCs into Pro-T cells (Appendix Figure 13), and co-injected them into the thymus scaffold with the iPSC-TECs to construct the Pro-T/iPSC-TEC thymus organoids. After 1 week of culture, a substantial population of cells progressed into $CD3^+/CD4^+/CD8^+$ double positive, $CD3^+/CD4^+/CD8^-$ and $CD3^+/CD4^-/CD8^+$ single positive stages of T-cell development (Appendix Figure 18 A, lower panels). In contrast, a small population of CD4 single positive cells was observed in thymic scaffolds repopulated with Pro-T cells alone (Pro-T scaffold, Appendix Figure 18 A, upper panels), likely representing the immature single positive (ISP) $CD4^+$ cell population[191]. Characterization of the emigrant population of the Pro-T/iPSC-TEC thymus organoids showed the presence of both $CD3^+/TCR\alpha\beta^+/CD4^+$ and $CD3^+/TCR\alpha\beta^+/CD8^+$ T cells (Figure 3.11 D-G and Appendix Figure 18 B). Significantly higher numbers of $CD4^+$ T cells (over 50 times) were generated from the Pro-T/iPSC-TEC thymus organoids in comparison to the Pro-T scaffold controls (Figure 3.11 D). In comparison to $CD4^+$ T cells, relatively lower amounts of $CD8^+$ T cells were produced in the Pro-T/iPSC-TEC thymus culture and essentially no $CD8^+$ T cells were detected in Pro-T scaffold controls (Figure 3.11 F). These findings suggest that Pro-T/iPSC-TEC thymus organoids can support the development of both $CD4^+$ and $CD8^+$ T cells in vitro.

Similar progression of early T cell program, albeit delayed, was observed in iPSC-TEC thymus organoids constructed with $CD34^+$ HPCs. After 1 week of in vitro culture, a small but prominent population of $CD5^+/CD7^+$ cells was present, suggesting ongoing T-lineage restriction and specification of the $CD34^+$ HPCs (Figure 3.11 H). While delayed in T cell development in comparison to those of Pro-T/iPSC-TEC thymus, continuous culture of HPC/iPSC-TEC thymus organoids after 2 weeks also supported the generation of both double positive and single positive

thymocytes (Appendix Figure 14). These findings suggest that the microenvironments of iPSC-TEC thymus organoids induce the seeded progenitor cells to undergo T cell programming and have the potential to support the generation of $CD4^+$ and $CD8^+$ T cells in vitro.

Further maturation of iPSC-TECs into TEC subsets was also observed. RT–qPCR analyses of HPC/iPSC-TEC thymus organoids show significant increases in expression of both MHCII and CD74, genes that are essential for TECs to present self-antigens to mediate both positive and negative selection of developing T cells (Appendix Figure 19). Characterization of $CD45^-EpCAM^+$ cells with FCM revealed the presence of both the $MHCII^+/CD205^+/DLL4^+$cTEC and $MHCII^+/CD205^-$ mTEC subsets (Figure 3.11 I). These data indicate that successful thymic crosstalk can be established in iPSC-TEC thymus organoids, which synergistically promotes the maturation of iPSC-TECs into functional TEC subsets and the development of human T cells in vitro.

3.4 Discussion

The benefit of alginate encapsulation is in providing a stable 3D environment that shields cells from shear forces allowing the cells to grow and differentiate as they would in vivo. Alginate also provides that benefit of stimulating the differentiating cells with mechanical stimuli that can be fine-tuned depending on the type and concentration of bivalent cation used for polymerization to enhance the directed differentiation. Previous publications, including our own, have demonstrated the ability for alginate encapsulation to aid in the differentiation of hESCs towards

endoderm germ layer cell types through the use of calcium chloride, which we have further analyzed with the two endoderm-based organ differentiations conducted in this study[53, 146, 174, 192].

The first part of this study explored the use of alginate encapsulation as a platform for in vitro differentiating iPSCs into functional islet endocrine cells and comparing this culture method to current suspension 3D differentiation furthering the work we have previously shown comparing our alginate encapsulation to 2D islet differentiation[53]. Several current methods for differentiating iPSCs into functional islets utilize a 3D culture system for the full duration or for at least a portion of the process[45-49, 150, 172]. The predominant method for 3D culturing for the full differentiation has been some form of stirred suspension system, either through spinner flasks[45, 46, 48] or rotational plate[47, 172]. With this work, we have utilized the rotational plate-based stirred suspension culture to reproduce current methods for 3D culturing and directly compare against our alginate encapsulation method in both development of uniform aggregates and functional islet-like cells.

In this, the encapsulated culture provided a distinct advantage over suspension culture with forming smaller aggregates and higher yield by the end of differentiation. The growth in the encapsulated culture was more reliant on cellular expansion rather than aggregation leading to the smaller aggregates, where the suspension culture allows the aggregates to coalesce allowing for faster growth. Along with forming larger aggregates, the suspension culture subjects the aggregates to continuous hydrodynamic shear forces[151] that can cause the unstable, differentiating aggregates to degrade, which was observed with the iPSC culture. For long term culturing required for the islet differentiation, the smaller aggregates formed by SCE are advantageous since they would also avoid the prominent issue with necrotic core formation[193]. This along with the alginate providing structure and protection from shear forces, a greater number of aggregates resulted from the differentiation. In terms of potential for islet differentiation, we demonstrated that the

encapsulated culture provides fewer C-Peptide^{+} cells than suspension culture (Figure 3.4 D, E), but encapsulation enhances islet-specific gene expression (Figure 3.4 F). This indicates that while not as many insulin producing cells form with the encapsulation, the ones that do are more robust than those from the suspension culture. Furthermore, the encapsuled culture overall translated well with the iPSC culture and islet-differentiation where they demonstrated similar growth and islet marker development as hESC, and both types of hPSCs were capable of glucose sensitive insulin secretion (insulin stimulation index> 1) thus showing that alginate encapsulation is a viable and robust platform for forming insulin functional islet cells in vitro with hPSCs.

In addition to differentiating in 3D, an objective for the suspension culture platforms is for developing a scalable system since there is finite growth possible with 2D plates[46, 172]. This advantage is also found within the alginate encapsulation culture platform where we have shown that cells can freely expand throughout undifferentiated culture and during differentiation. Aspects of the SCE platform that aid in its scalability are ease of replacing media and reproducibility across different hPSC lines. Since the aggregates remain within the macro-scale alginate beads throughout the culture, which protects them from hydrodynamic shear, media can be efficiently replaced without issue of unintentionally removing aggregates or damaging them from dispensing fresh media. The reproducible hPSC growth within the alginate capsules has been shown in this chapter, with both the islet and the thymus epithelial cell differentiation[181], where multiple different iPSC lines were successfully cultured. This is not true of suspension culture, as we have shown where testing with the more robust hESCs was required to directly compare our encapsulation culture platform to suspension culture for islet differentiation due to the instability of the suspension-based iPSC-islet differentiation.

A limitation with the encapsulation culture is the heterogenous morphology of the resulting aggregates where elongated aggregates formed along with spherical ones, while the SSA culture provided a unform spherical culture. The elongation may be from the initial high mechanical stiffness of the alginate that then degrades alongside the growth of the aggregates to conform to their growing structure[194]. While this effects the endpoint functionality of the differentiated cells, we have addressed this limitation by exploring enriching the insulin producing cells through FACS, which has shown to improve differentiation outcome[45, 47, 178-180].

We used two methods for purifying the cells: live cell staining and INS-mCherry reporter cell line development. The use of live cell staining has proven an efficient means of isolating insulin producing cells, with both surface marker stains[45] and zinc-specific intracellular stains[178-180]. Between the two methods, Davis et al. found that the zinc-specific staining was more efficient than the surface marker staining since it would have faster binding than the antibody stain[178]. With our work, the live cell staining with zinc-specific stain, Newport Green, was not able to improve the consistency of proper insulin secretion within the formed aggregates. As an alternative approach to enriching the insulin producing cell, we developed and utilized an INS-mCherry reporter cell line that provided a slightly higher insulin stimulation than unsorted aggregates. As this method for identifying insulin producing cells would be more accurate than the zinc-based live stain, this indicates that the sorting and re-aggregation prior to the maturation step does not have a strong impact on the outcome of the differentiation.

With the second part of this study, we reported the successful tissue engineering of thymus organoids from human iPSC-derived TECs that can support the generation of human T cells in vitro. Two and three major clusters were identified by unbiased clustering analysis of scRNA-seq data in the 2D and 3D cultures, respectively, indicating the heterogeneity of the iPSC-TEC

populations generated in vitro. The major cluster in both 2D and 3D samples expressed mTEC markers, suggesting mTEC-oriented specification. A population of iPSC-TECs displaying an epithelial/mesenchymal hybrid phenotype was generated under both the 2D and 3D culture conditions. These cells shared striking molecular signature similarities with 'common TECs', a population of human TEC subsets expressing both cTEC and mTEC markers that was recently identified by Campinoti and colleagues[165]. The authors thought that these progenitor-like cells were the main contributors of the clonogenic TEC lines that can be expanded extensively in vitro and support human T cell development in vivo when engrafted in hu.SRC mice. The unique population of iPSC-TECs identified only in the 3D, but not the 2D culture, displayed decreased mesenchymal markers but increased expression of epithelial markers, especially those of cTECs (for example, PRSS16 and CD205), suggesting that the 3D alginate encapsulation environments might promote the specification of the 'hybrid' TEC progenitors into cTEC lineage. When introduced into the extracellular matrix microenvironment of decellularized thymus scaffolds, together with either $CD34^+$ HPCs or Pro-T cells, 3D iPSC-TECs matured further into $CD205^+/MHCII^+/DLL4^+$ cTEC and $CD205^-/MHCII^+$ mTECs and were able to support the differentiation of hematopoietic progenitors into $CD3^+/CD4^+$ and $CD3^+/CD8^+$ T cells in vitro, highlighting their thymopoiesis function.

4.0 Disease Modeling on hiPSC-Based Islet MPS Model

4.1 Introduction

As we have discussed in previous chapters, the progress with microphysiological systems (MPS) for in vitro modeling healthy and diseased organ systems is providing a promising new avenue for efficiently developing novel therapeutics that would be more effective in treating the targeted disease due to the MPS models more closely recapitulating the disease state in patients. In chapter 2, we demonstrated the ability for our PANIS MPS device to sustain a healthy state over a 28-day span, induce aspects of type 2 diabetes (T2D), test dose dependent outcomes of an antioxidant drug treatment, and co-culture with neutrophils under healthy conditions. The device design, in brief, was composed of 2 flow chambers partitioned by a perfusable membrane, and primary islets were seeded on device by suspending them in alginate capsules that were polymerized on the perfusable membrane in an alternating capsules array. A major limitation of this initial model is the availability and reproducibility of the primary islets. Since donor availability is limited and the process of isolating primary islets is delicate, the ability to consistently source the tissue is difficult. Also, since primary islets are a non-expandable cell type, obtained primary islets originate from different donors, which would have different genetic and environmental factors that would cause heterogeneity in function and response to culture conditions. This limitation ultimately requires larger samplings from one donor to avoid donor variability or a larger sampling of donors to mitigate donor variance effect on analysis. This obstacle can be eliminated with the use of human induced pluripotent stem cell (iPSC) derived islets, which would be a renewable cell source.

Others who have demonstrated iPSC-islet MPS culture[195-197] share a similar 2-chamber design partitioned by a perfusable membrane where one chamber consists of a microwell design where iPSC-islets can be re-aggregated on device, and the second chamber provides fresh flowing media. These designs showcase varying durations of matured, functional iPSC-islet cultures (7 days[197] and 30 days[195, 196]). Additionally, the preparation of iPSC-islets differed between the two device designs. The device developed by Goswami et al.[197] pre-differentiates the iPSC-islets until the start of maturation before seeding onto the device, while the device developed by Tao et al.[195, 196] conducts the whole of the differentiation on device.

In this chapter, we aim to implement human iPSC-derived islets into the islet MPS model for disease modeling. As we demonstrated in chapter 3, we have developed a method for differentiating iPSCs into islets using our alginate encapsulation platform. This device setup is distinct from the published iPSC-islet designs with direct flow interacting with alginate encapsulated iPSC-islets, with flow circulating throughout the 2 chambers of its design. With this device, we will be testing how well the PANIS maintains the iPSC-islets and how well they will mature under flow with endpoint functional testing. Furthermore, we conducted transcriptomic analysis to compare the PANIS culture against iPSC-islets matured under static conditions. As an application to test of the iPSC-islet PANIS model, we introduced neutrophils onto healthy and damaged setups to simulate immune cell interaction with islets.

4.2 Materials and Methods

4.2.1 iPSC Culture and Islet Differentiation

See Chapter 3 methods.

.

4.2.2 Re-aggregation Step

At the end of the EN phase, the aggregates were retrieved from the alginate and washed in islet differentiation base media 3 times to remove excess dead cell debris. TrypLE Express (Gibco) was added to the aggregates and incubated for 15-20 min where base media was added to dilute the TrypLE Express. The non-dissociated aggregates were disrupted mechanical through pipetting, and the now single cells were spun down at 150 rcf for 3 min and resuspended in fresh maturation media. The cells were counted with a Trypan Blue (Gibco) and a hemacytometer. Cells were seeded into a v-bottom ULA plate (Corning) at 3000 cells per well and cultured for up to 4 days to allow for self-organized re-aggregation.

4.2.3 PANIS Assembly

See Chapter 2 methods for general setup. Modifications are that 100mM $CaCl_2$ + 10mM HEPES was used for alginate array formation instead of $BaCl_2$ solution.

4.2.4 Oxygen Concentration Measurement in PANIS

See Chapter 2 methods.

4.2.5 Live/Dead Assay

See Chapter 2 methods for general setup. The on-PANIS viability was carefully flushed with the Live/Dead assay solution created according to the manufacturer's procedure, and imaging was done using InCell Analyzer 6000 (GE Technologies), which is able to capture images of the whole middle layer.

4.2.6 Glucose Stimulated Insulin Secretion

See Chapter 2 method.

4.2.7 Calcium Imaging

See Chapter 2 methods.

4.2.8 Single Cell RNA Sequencing

After 14 days on PANIS or in static, the iPSC-islets were retrieved from the PANIS and alginate using 100mM EDTA, and iPSC-islets were harvested and resuspended in DMEM/F12

(Gibco). To dissociate the aggregates, they were incubated in 2 mL TrypleE Express (Gibco) for 15-20 minutes and mechanically disrupted to single cells. Samples were suspended in PBS+10 μM Y-27632 dihydrochloride (R&D Systems) and sent to the Single Cell Core at the University of Pittsburgh for further quality control. Each sample was verified to meet the >70% viability threshold by using the Countess II Automatic Cell Counter (ThermoFisher). Library preparation and droplet sequencing was done according to the protocol set by 10X Genomics for a 3PrimeV3.1 experiment, using the Chromium NEXT Gem Single Cell 3' Reagent Kit v3.1 (Dual Index). cDNA quality was assessed with the Agilent TapeStation High Sensitivity D5000 ScreenTape and reagents, while final libraries were assessed using Agilent TapeStation High Sensitivity D1000 ScreenTape and reagents.

After sequencing, count files were aligned to a human reference genome (refdata-gex-GRCh38-2020-A) using the 10X Genomics CellRanger pipeline (v7.1.0 including intronic reads). All data was then transferred to Partek Flow (Partek Incorporated) for further analysis. The samples were filtered for high mitochondrial expression and high read counts, in order to eliminate doublets and potential damaged cells from the analysis. The sample counts were then normalized and differential analysis using ANOVA was performed to generate a feature gene list with differential gene expression. The feature gene list (gene identifiers, log2 fold change, and p-values) was exported to Ingenuity Pathway Analysis (IPA; Ingenuity Systems, Qiagen) where the data set was further filtered to exclude any differentially expressed genes that did not meet the threshold of $p < 0.05$, and an absolute value Log2 FC >1. Canonical pathway analysis was used to identify any biologically relevant pathways that were significant in comparison between the PANIS and the control sample. The feature gene list was also imported into BaseSpace Correlation Engine (Illumina) and compared against established data for pancreatic islets.

4.2.9 Immune Cell Interaction with Islets on PANIS

HL-60 cells (ATCC) were differentiated to neutrophil like cells with the addition of 1.3% DMSO in IMEM media supplemented with 20% FBS for 5 days following a previously reported protocol.[198] The neutrophil like cells were labelled with DiI (Invitrogen), a live cell dye for 30 minutes before adding them onto a middle layer containing alginate capsules with and without islets prepared by following the PANIS setup procedure. Damaged islets were formed by preincubating with 50μM of Tert-Butyl hydroperoxide (TBHP) for 1 h. The alginate capsules were distributed on the middle layer so that capsules containing islets and empty capsules (4 each) were symmetrically arranged in 4 columns containing 2 rows of capsules each. The system with encapsulated islets and neutrophil like cells on the middle layer were loaded on to the flow platform and imaged using InCell Analyzer 6000 (GE Technologies) to visualize the labelled neutrophil like cells and then cultured under flow (30 uL/h) for 5 days. At the end of the culture period, Calcein AM (live stain) and EthD1 (dead stain) were introduced into the middle layer through a syringe and incubated for 1 h and then washed by introducing PBS before imaging for live and dead cells. The number of live neutrophil-like cells in all the capsules are then counted using ImageJ and represented as neutrophil density which is the total number of neutrophils per unit area of the capsule. Interestingly, neutrophil-like cells exhibit swarming behavior at the boundary of alginate capsules containing islets, which was not observed around capsules that do not contain any islets suggesting that the infiltration behavior in the two groups of capsules (with and without islets) is distinctly separate.

4.2.10 Statistical Analysis

See Chapter 2 methods.

4.3 Results

4.3.1 Establishing iPSC-Islet on PANIS MPS System

As we previously demonstrated with our work with the primary islet PANIS (Ch 2), our MPS device can sustain primary islets over 28 days maintaining both viability and functionality. The drive of this study is to implement our iPSC-derived islets, which were developed in chapter 4, into the PANIS design. As a brief overview, PANIS is derived from the organ-on-chip (OOC) device from Micronit, which is composed of three borosilicate glass layers that is sealed using an aluminum clamp (Figure 4.1 A). To maintain the spheroid morphology of the islets, the alginate capsule array is incorporated on the middle layer, as previously demonstrated in chapter 2 (Figure 4.1 B). For suspending the iPSC-islets in the alginate capsules, the alginate was polymerized with calcium chloride to recapitulate the alginate encapsulated suspension used for the differentiation. The specifications for the flow match what we have shown with our previously shown primary islet work. In brief, a looped flow at 30μL/hr was utilized for iPSC-islet PANIS to maximize flow around islets (Figure 4.1 C). To ensure that the PANIS can sustain the iPSC-islets, we tested the oxygen availability within the alginate capsules. We tested this using an oxygen-sensitive bead test where red is oxygen sensitive beads and blue is oxygen-insensitive control beads (Figure 4.1 E). Image analysis for the oxygen test confirmed that oxygen supply for iPSC-islets is constant as

there is no change over time and no significant difference from blank alginate capsules (Figure 4.1 F).

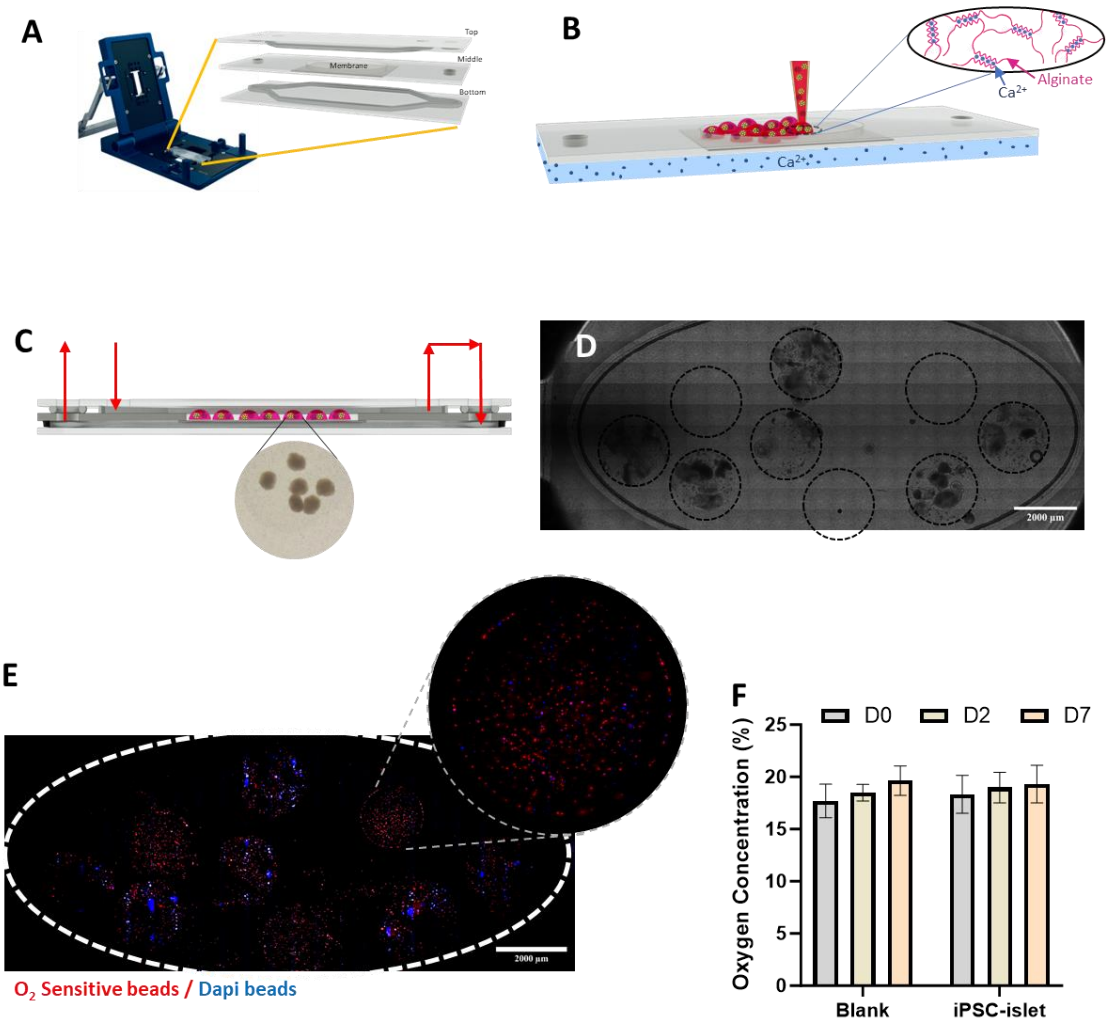

Figure 4.1 PANIS Layout for iPSC-Derived Islets (A) Schematic of re-usable components and layout for assembly of the PANIS device. (B) Schematic of forming the alginate capsule array on the middle layer. (C) Flow pattern used to maintain the iPSC-islets on device where flow initiates in the upper chamber and externally loops to the bottom chamber. (D) Brightfield image showing the layout of the alginate capsule array with a mixture of iPSC-islet containing capsules and empty capsules for the oxygen availability test. (E) Fluorescent bead composition of the oxygen-sensitive beads (red) and oxygen-insensitive DAPI beads (blue).

(F) Image analysis of the fluorescent beads calculating the percent oxygen within the alginate capsule across a 7-day span.

After confirming oxygen availability, we next sought to measure functionality and viability. The alginate capsule array was seeded onto the middle layer with the iPSC-islets prior to the start of the maturation phase to allow the cells to mature under flow (Figure 4.2 A). Before testing for functionality, we wanted to ensure that the aggregates remained viable through the duration of the maturation, which required 14 days. At the endpoint, the live/dead viability assay was conducted in situ to provide an accurate measure of the state of the iPSC-islets within the PANIS device (Figure 4.2 B). The overall viability of the iPSC-islet remained high with 84.6% viable cells. More in depth analysis of capsule-specific viability reveals how the flow affects the iPSC-islets based on the region of the device. As shown in Figure 4.2 C and D, the iPSC-islets within the capsules that are closer to the flow inlet (capsules 1-4 in Figure 4.2 C) have a lower overall viability compared to those at the other end of the membrane (capsule 5-7).

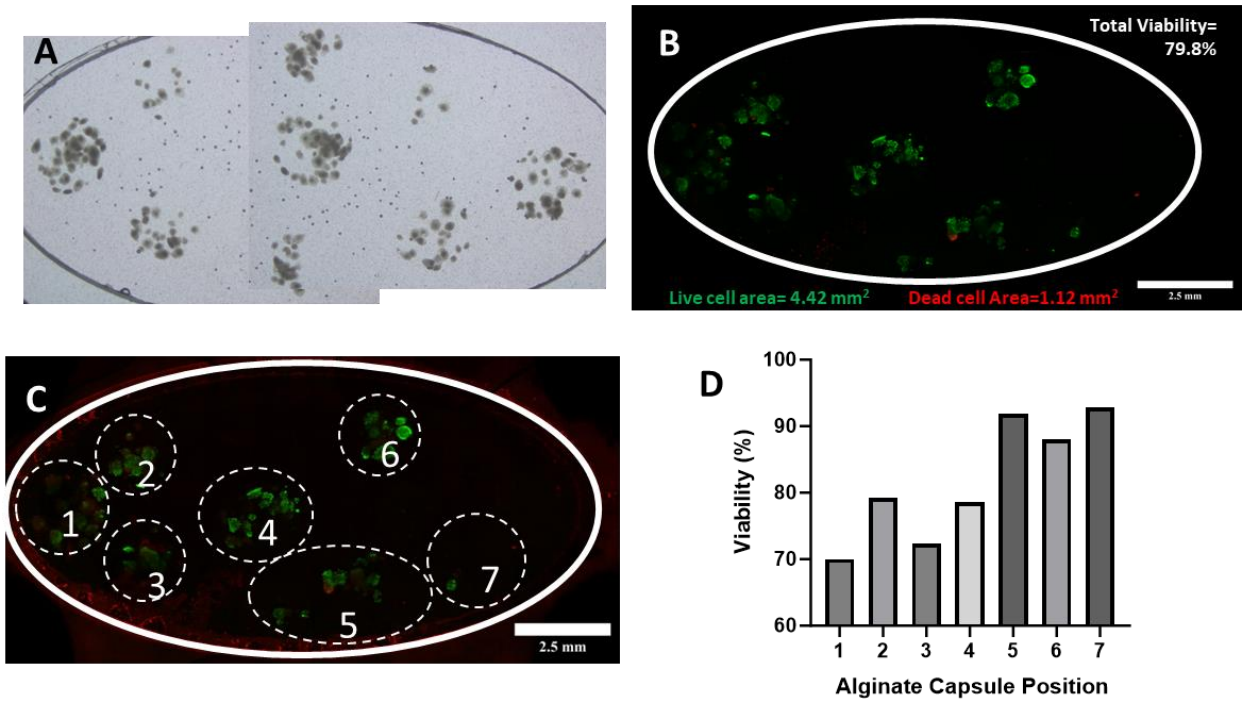

Figure 4.2 iPSC-islet Distribution and Viability on PANIS (A) Phase image of iPSC-islet layout in alginate capsule array on the assembled PANIS. (B) Viability assay for the iPSC-islets on PANIS with results for viability analysis of whole device. (C) Image indicating locations of alginate capsules and designation of each capsule that corresponds to the (D) image analysis for each providing capsule-specific percent viabilty

With the viability confirmed, we sought to analyze the functionality of the system to ensure it would be able to maintain the iPSC-islets' ability to mature into functional insulin secreting aggregates. For this, we utilized glucose stimulated insulin secretion (GSIS) testing to demonstrate the levels of insulin secreted for iPSC-islets post-PANIS culture where two different aggregate types were tested: natively formed aggregates from SCE differentiation and re-aggregated spheroids (Figure 4.3 A). The two aggregate types were tested to determine the optimal method for culturing the iPSC-islets on PANIS. The native aggregates would maintain the organization and extracellular matrix (ECM) developed during the differentiation in alginate that would provide

more structure for the aggregates. However, the re-aggregation would ensure more uniformity between aggregates in terms of size and composition and would allow the cells to self-assemble, which could remove any non-endocrine cell groups[45, 47]. The GSIS test was conducted using the same steps as with the primary islet PANIS, where the iPSC-islets were retrieved from the PANIS device at the end of the 14-day maturation period and then subjected to the static GSIS test. With insulin secretion, the natively formed aggregates demonstrate a significant increase in insulin secretion from low to high glucose, while the re-aggregated iPSC-islets don't show a significant increase (Figure 4.3 B). Both aggregation methods produce statistically similar levels of insulin per aggregate at low glucose, but natively formed aggregates secrete significantly more insulin per aggregate at 16mM glucose (Figure 4.3 B). However, the resulting insulin stimulation indexes for native and re-aggregated show there is no significant difference in stimulation between the two aggregation methods (Figure 4.3 C). Since the improvements for re-aggregation are not significant, the native aggregates were used for further functionality testing and characterization since those aggregates were more easily formed and consistently stable. In addition to GSIS, calcium imaging was conducted on the iPSC-islet PANIS to provide insight into the functionality of the tissue on device (Figure 4.3 D). For this, we utilized statically matured iPSC-islets to allow testing of the calcium chloride stain, Fuo-4AM, on the device with unstained samples as controls. The majority of the PANIS devices tested demonstrated the ability for on-device monitoring of insulin stimulation with a clear increase in the fluorescence intensity with the increase in glucose.

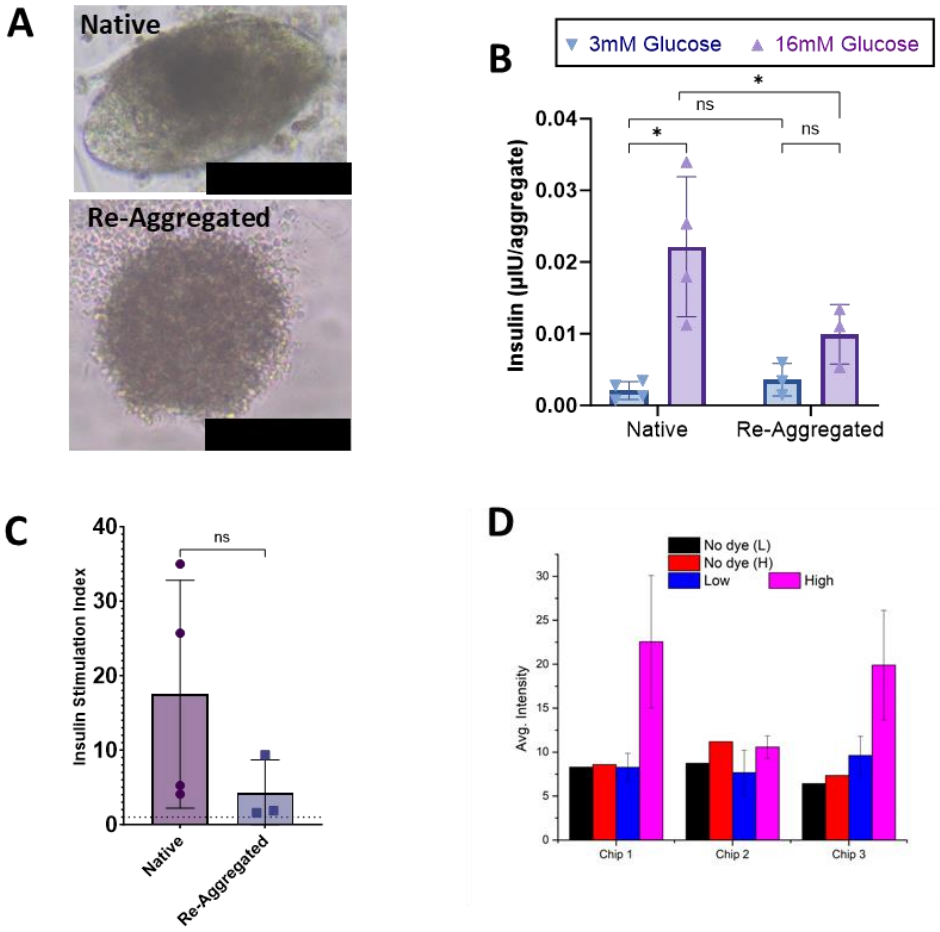

Figure 4.3 Endpoint Functionality of iPSC-islet on PANIS (A) Representative phase images of natively formed (top) and re-aggregated iPSC-islets prior to addition to PANIS. (B) Insulin secreted per aggregate from GSIS test comparing natively formed aggregates with re-aggregated ones. (C) Insulin stimulation index comparison between the two aggregate types. (D) Calcium imaging conducted across three separate iPSC-islet PANIS devices (Chip 1-3) with unstained controls in each device.

Genomic analysis was conducted using RNA sequencing for both statically and PANIS matured iPSC-islets. To directly compare how flow on PANIS affects iPSC-islet maturation, the differentially expressed genes were examined (Figure 4.4 A) with all displayed genes having a significant change ($p<0.05$). With islet endocrine markers, there is an overall increase (fold change>5) in β-cell (INS, ISL1, NKX6.1), α-cell (GCG, IRX2), δ-cell (SST), granule-related

endocrine cell (CHGA), and pancreatic progenitor cell (PDX1) markers. With this analysis, we were also able to see how maturity/age related markers (SIX2[199], SIX3[199], UCN3[200]) were affected with decrease in SIX2 and SIX3 expression (fold change<-4) and increase in UCN3 (fold change=2.55). The lowered SIX2 and SIX3 might indicate that the production of insulin from the PANIS iPSC-islets is not as matured as those in static, as these genes are linked with mature β-cells and correspond to higher insulin production and secretion[199]. Conversely, the increase in UCN3 would indicate that matured β-cells did form more in PANIS over static[200]. The growth of the iPSC-islets can be checked with the cell cycle related genes (CDK2AP1 and TOP2A), which indicate that the PANIS culture has fewer growing cell populations than found in static. Additionally, angiogenic factors (VEGF and PDGFA) are increased in the PANIS culture, which indicates that the flow is stimulating the iPSC-islets to promote vessel growth. The flow also has an effect on the endoplasmic reticulum (ER) stress of the cells, where the ER stress markers (ATF4, DDIT3, and XBP1) showed an overall increase (fold change>2.5) with the PANIS culture.

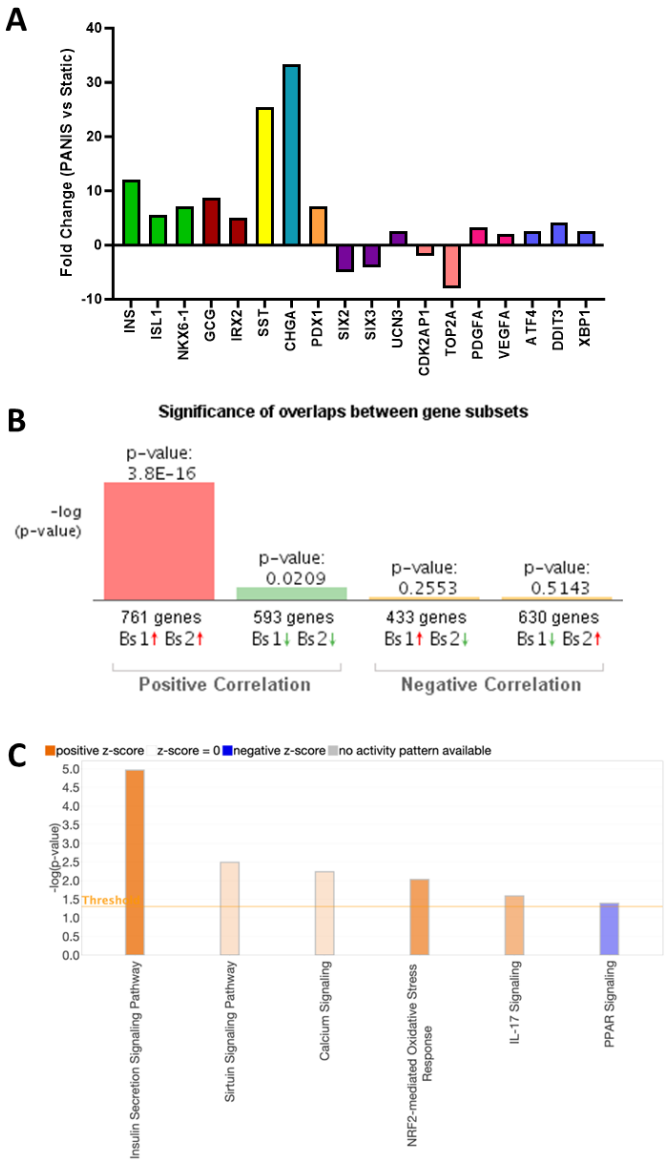

Figure 4.4 iPSC-islet PANIS vs Static Differentially Expressed Genes (DEG) Analysis (A) Gene fold change for key islet endocrine cell markers, cell proliferation markers, angiogenic markers, and ER stress markers. (B) BaseSpace Correlation Engine (BCE) analysis showing the relation of the DEGs to genes associated with pancreatic islets. (C) Ingenuity Pathway Analysis for islet functional pathways and stress pathways.

BaseSpace Correlation Engine (BCE) analysis focused on the comparison of the PANIS vs static analysis (Bs1 in Figure 4.4 B) to published pancreatic islet sequencing data (Bs2 in Figure 4.4 B). The BCE analysis provides a positive correlation between the published sequence for

pancreatic islets and the affected genes from the PANIS culture with no significant negatively correlated genes ($p>0.05$). The strong correlation between the differentially expressed gene list (DEGs) of the PANIS vs static with primary islets indicates that the PANIS culture is improving the islet phenotype of the cells to match more closely to primary tissue compared to static.

Ingenuity pathway analysis (IPA) for native iPSC-islet vs static was used to see how the DEGs correlated with islet and stress-related pathways (Figure 4.4 C). The IPA demonstrated the increased functionality of the iPSC-islets matured under flow compared to static with a significant increase in the insulin secretion signaling pathway (z-score=3.151, p=0.0000109) and calcium signaling (z-score=0.784, p=0.00582), demonstrating an increase in insulin secretion. However, the PANIS showed an increase in stress with the upregulation of the oxidative stress pathway (z-score=2.6, p=0.00936) and IL-17 inflammatory cytokine production (z-score=1.947, p=0.0259) and decrease in PPAR signaling (z-score=-1.528, p=0.0408). Correlating to this increase in stress, the sirtuin pathway (z-score=0.832, p=0.00325) was increased within the PANIS culture, where sirtuin aids in decreasing oxidative stress within the cell.

4.3.2 Islet- Neutrophil Interaction in Primary Islet PANIS

In vivo and clinical studies over the past two decades have clearly shown that islet inflammation is the key contributor to β-cell dysfunction in T2D mainly in the form of pro-inflammatory cytokines recruiting macrophages into islets that eventually lead to β-cell death[201, 202]. The first step in this process is the infiltration of neutrophils in the vicinity of the islets which further encourages downstream processes that include proinflammatory cytokine production and macrophage recruitment[203]. We modelled the neutrophil infiltration in our platform using HL-60

derived neutrophil-like-cells to demonstrate the potential of PANIS platform to study the interactions between alginate encapsulated islets and neutrophils under flow. Figure 4.5 A shows the brightfield image of alginate encapsulated capsules and empty capsules arranged on the middle layer with neutrophil-like-cells in suspension on the membrane before the media flow into the system. Figure 4.5 B shows the initial distribution of the neutrophil-like-cells on the membrane and around the alginate capsules with no neutrophil-like-cells inside the alginate capsules before media flow. After 5 days of flow, live-dead staining in the platform (Figure 4.5 C) shows live neutrophil-like-cells inside alginate capsules with and without islets. Counting the number of neutrophil-like cells inside the capsules indicate that there is no statistical significance ($p>0.05$) of the number of neutrophils inside alginate capsules with and without islets (normalized to alginate capsule area) (Figure 4.5 D) indicating that the alginate capsules allow neutrophil infiltration under flow regardless of the presence of islets.

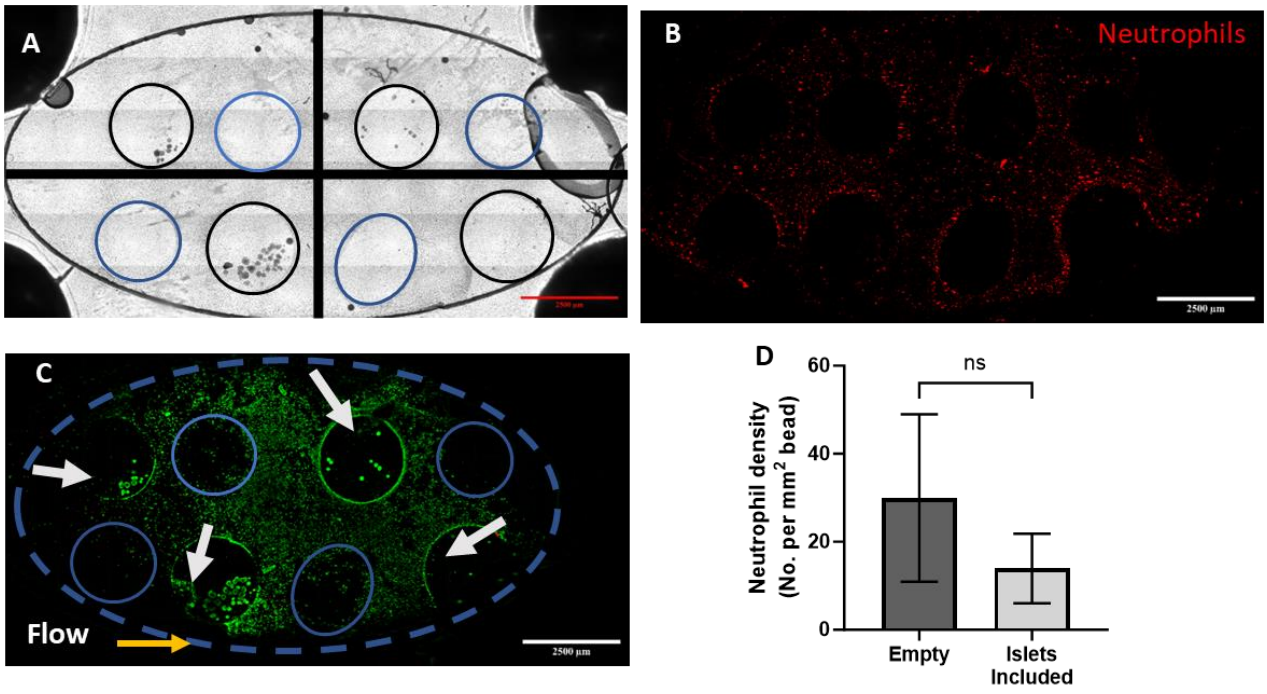

Figure 4.5 Neutrophil infiltration in islet on chip model. (A) Islet on chip set up with 4 alginate capsules containing islets (black circles) and 4 empty alginate capsules (blue circles) distributed symmetrically on the middle layer containing neutrophils. (B) Neutrophils on the middle layer labelled with DiI live stain to facilitate imaging. (C) Calcein AM (green) and Ethd1 (red) staining of the entire chip after 5 days under flow showing live islets and neutrophils inside the capsules (white arrows). The dashed ellipse in blue represents the boundary of the culture area on the membrane and the blue circles mark the boundary of alginate capsules. (D) Quantification of the number of live neutrophils inside the alginate capsules after 5 days of culture under flow showing capsules without islets with higher neutrophils with no statistical significance (p=0.1143).

4.3.3 Immune Interaction with Damaged iPSC-Islet on PANIS

For testing the application of the iPSC-islet PANIS, we wanted to further explore the co-culture with immune cells that we had initially explored with primary islets. With this, we wanted to explore both healthy and damaged iPSC-islet interactions with HL-60 derived neutrophil-like-cells. The damaged condition was formed prior to seeding the iPSC-islets into the alginate capsule

array by subjecting them to 55mM tert-Butyl hydroperoxide (TBHP) for 1hr which subjected the cells to oxidative stress. The iPSC-islets were then washed to remove residual TBHP and added to the PANIS to ensure that any response from the neutrophils was due to the initial damage that the cells experienced. With both the healthy and damaged iPSC-islet setups, some of the alginate capsules were left empty to serve as controls for how the neutrophils would interact with the alginate. Before the final assembly of the layers, the neutrophils were stained with live cell dye and seeded onto the middle layer, settling for a minimum of 30min to avoid loss during assembly.

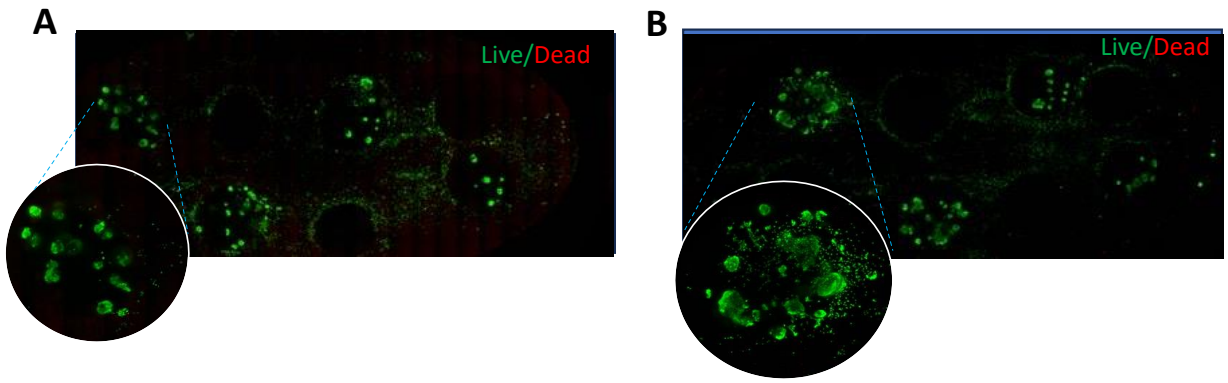

Figure 4.6 On-Device Viability Endpoint for Neutrophil Co-culture with iPSC-islets in PANIS (A) Healthy and (B) damaged iPSC-PANIS devices in situ viability assay images at the end of the 10-day culture span.

The healthy and damaged PANIS setups were cultured for a 10-day span with a viability assay at the end to determine if the viability of the iPSC-islets were affected by the presence of the neutrophil. The healthy condition (Figure 4.6 A) retained the viability of the iPSC-islets, indicating that the presence of neutrophils did not cause apoptosis in the iPSC-islets. Additionally, the high viability of the neutrophil cells seen throughout the membrane surface demonstrates the ability for the iPSC-islet PANIS to provide a sustainable environment for the immune cells. Like the healthy condition, the on-device viability assay for the damaged iPSC-islet condition (Figure 4.6 B) retains high viability both in the aggregates and neutrophil cells.

To see how the neutrophils interacted with and potentially infiltrated the alginate capsule arrays, both with iPSC-islets and empty, the neutrophils were tracked across the 10-day culture using fluorescent labeling to efficiently image and quantify any infiltration of the cells into the alginate capsules. This can be seen in Figure 4.7 A, which depicts one day after the start of the culture, where the neutrophils can be viewed as the white fluorescing points that surround the alginate capsules. The alginate capsules are distinguished using the green outlines for iPSC-islet containing capsules or red outlines for empty capsules and numbered to distinguish the location on the middle layer, where 1 is closer to the initial point of flow and 4 is farther away (Figure 4.7 A, C). The fluorescence within the alginate capsules was analyzed across the 10-day span and quantified in terms of the number of neutrophils per area of each capsule (Figure 4.7 B, D). From the analysis, we see a majority of neutrophils infiltrated the capsules within the first day of culture. As the days progressed, the neutrophil numbers appeared to decrease universally in capsules containing iPSC-islets and increase overall in the empty capsules.

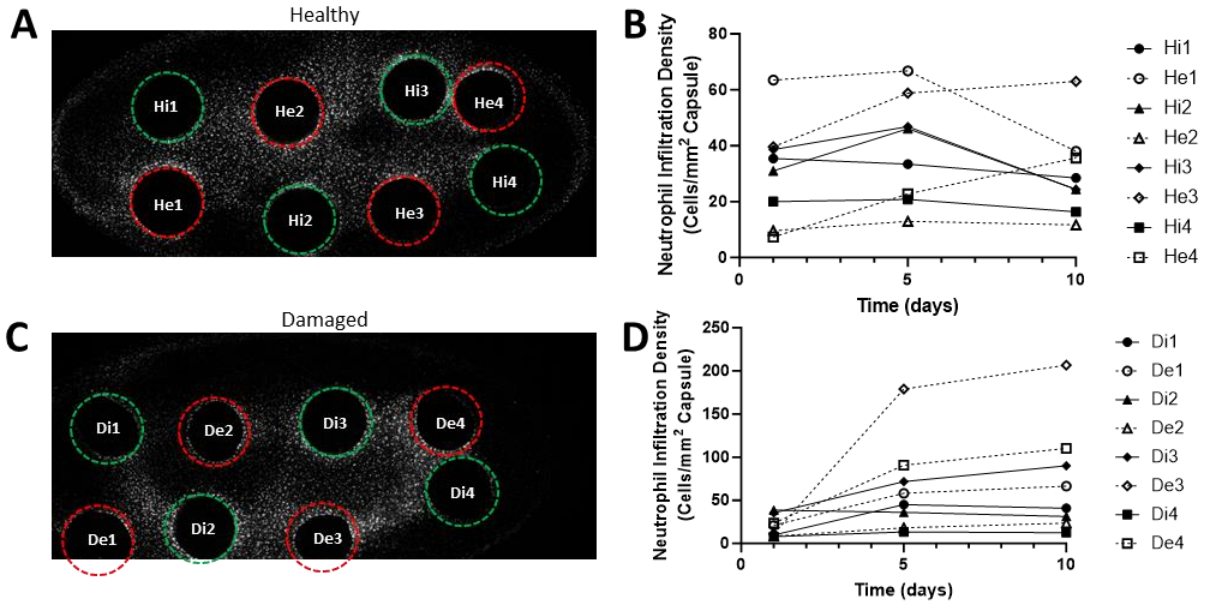

Figure 4.7 Neutrophil Infiltration into Alginate Capsules during 10-day co-culture with iPSC-islets on PANIS (A) On-device image for the healthy iPSC-islet PANIS at the day 1 timepoint. (B) Image analysis for the number of neutrophils in each of the alginate capsules for the healthy condition. (C) On-device image for the damaged iPSC-islet PANIS at the day 1 timepoint. (D) Image analysis for the number of neutrophils in each of the alginate capsules for the damaged condition.

As shown with the healthy condition, the damaged iPSC-islet PANIS was imaged at several timepoints to track the movement of the neutrophils, with the day 1 image shown in Figure 4.7 C and quantification across the 3 timepoints shown in Figure 4.7 D. The initial number of neutrophils that infiltrated the capsules after one day is similar to the healthy condition, but the subsequent timepoints, days 5 and 10, show much greater numbers of neutrophils in capsule. This higher activity of neutrophils is expected with the damaged condition since there would be a higher number of chemo-attractants within the device than the healthy condition. Additionally, the capsules containing the damaged iPSC-islets have significantly higher neutrophils compared to the healthy iPSC-islets. A shared observation across both the healthy and damaged conditions is that

capsules located closer to the source of flow show greater neutrophil activity and infiltration. As shown in Figure 4.2 C, D, the majority of death that occurs within the iPSC-islets is closer to the inlet. While the iPSC-islet viability during this neutrophil co-culture remains high, the higher shear forces may be increasing the cytokine signaling from those cells which would increase mobility of the neutrophils in that area. Since alginate capsules without iPSC-islets also demonstrate the higher neutrophil presence in the inlet regions, another potential reason is possible.

4.4 Discussion

In this chapter, we have furthered our PANIS MPS system, which was first introduced in chapter 2, through the inclusion of iPSC-derived islets. The drive for iPSC inclusion is to provide more reproducibility by removing donor variation and provide a more available, regenerative source, both of which were limitations with the initial setup with primary islets. Additionally, it will provide more customization with the ability for donor specificity. The PANIS maintained the iPSC-islets for 14 days, showcasing both high viability and insulin secretion functionality both in static testing and in situ with fluorescent analysis. Two iPSC-islet aggregation methods were tested on the PANIS, ones formed natively during differentiation and ones re-aggregated. This comparison was made to explore potential improvements to the iPSC-islets, as others have shown[45-47]. When comparing the insulin secretion functionality between the two types of iPSC-islet aggregates cultured on PANIS, both demonstrated similar levels of insulin stimulation, however ones that were formed naturally during the differentiation secreted a greater amount of insulin per aggregate than ones re-aggregated. This aligns with the works of Veres et al., where they showed that the native and re-aggregated iPSC- derived islets had statistically similar insulin

stimulation index (p=0.79)[45]. In terms of usability, the native aggregates were advantageous due to no need for further processing, and they tended to be more stable when seeding and retrieving from the PANIS. As the native aggregates were finalized as the optimal configuration for the iPSC-islet PANIS, we wanted to test the application of this system.

In the current published works for hPSC-derived islet MPS systems, the applications overall consist of serving as a culture platform for iPSC differentiation towards islets[195], drug testing[196, 197], and coupling with other organ systems[196]. The design behind these published systems share some key features where they incorporate microwells to house individual hPSC-islet aggregates that are formed on device from single cell seeding, which is separated from the main media perfusion chamber using a perfusable membrane[195-197]. Goswami et al. utilized this design to re-aggregate sorted hESC-derived islets and culture for up to 1 week with sustained insulin functionality using a media flow rate of 0.83μL/min (~50μL/hr)[197]. This system more closely matches ours in terms of the phase of differentiation when the cells would be added to device, which is at the start of the maturation phase. We have demonstrated a more robust system where our iPSC-islets are able to remain functional in culture over a 14-day span in PANIS using a lower flow rate of 30μL/hr.

The initial design by Tao et al.[195] used their system for fully differentiating iPSCs into islets in situ using a flow rate of 100 μL/hr and cultured up to 60 days on device. They compared the differentiation under flow against a static control and found that directed differentiation towards islets was enhanced with the flow, with universal increase in islet-specific markers (both through immunofluorescent analysis and gene expression)[195]. We also observed this phenomenon with our system through our genomic analysis comparing the PANIS matured iPSC-islets to those matured in static conditions, with increases in markers for all major endocrine cell populations (α,

β, and δ-cells) and increased insulin functional pathways. Tao et al. furthered their design by co-culturing the iPSC-derived islets with iPSC-derived liver aggregates to study the interaction between the organ systems and the effect of hyperglycemic culture and T2D drug inclusion[196].

As we have previously demonstrated PANIS' ability for T2D toxic state induction and drug testing in chapter 2, we sought to further recapitulate in vivo conditions by including neutrophils, which are the most prominent among the leukocytes in the blood[204] and the first response of the immune system. HL-60 derived neutrophils are a well-known model system to study neutrophil behavior such as chemotaxis[205] which is how islet secreted factors attract neutrophils and macrophages causing inflammation and β-cell dysfunction in T2D. We conducted initial testing for this co-culture by using primary islets to see if any differences would occur between primary and iPSC-derived tissue. The introduced HL-60-derived neutrophils infiltrated into the alginate capsules with and without primary islets alike over the course of 5 days under flow by confirming the presence of live primary islets and neutrophils inside the capsules. This demonstrates the feasibility of the PANIS' alginate capsule array to model immune cell infiltration, especially with pre-conditioned islets cultured with high glucose and free fatty acids that induce the production of pro-inflammatory cytokines that attract neutrophils, which further potentiates immune cell interaction with islets during metabolic disease pathogenesis.

With the inclusion of neutrophils with the iPSC-islets, we furthered this analysis by observing the interaction neutrophils had with both healthy and damaged iPSC-islets to simulate a disease state where the neutrophils would be more activated. The neutrophils did not directly damage the iPSC-islets, and they remained viable and mobile under flow. As with the primary islet test, the neutrophils infiltrated the alginate capsules regardless of the presence of iPSC-islets, with empty capsules showing progressive neutrophil infiltration. Additionally, their motility was more

directly correlated with the higher flow closer to the inlet of the device and the health of the iPSC-islets, where iPSC-islets subjected to oxidative stress at the initial timepoint corresponded with greater neutrophil movement.

5.0 Summary and Future Works

The overall goal of this work was to develop an islet MPS device capable of sustaining islets' viability, phenotype, and functionality for long term (>14 days) cultures and would utilize both primary and iPSC-derived islets to ultimately model the pathogenesis and drug treatment of T2D. We established the primary islet based MPS device, dubbed PANIS, in chapter 2, where we could sustain the islets over the course of a 28-day span. We, also, showcased the ability to test multiple T2D related toxic conditions and run dose dependent drug testing on PANIS. To form the iPSC-derived islets, in chapter 3 we utilized an alginate 3D culture platform to fully differentiate the iPSCs into functional islets capable of glucose sensitive insulin secretion in vitro. Additionally, we explored the usability for the alginate culture platform to aid in the differentiation towards thymus epithelial progenitor cells, which are another endocrine germ layer-based cell type, which resulted in the function of T-cell production. This demonstrated the ability of alginate to be used as a more universal platform for differentiating iPSC into endoderm germ layer organ types. The developed iPSC-islets were implemented into the PANIS design in chapter 4, where we demonstrated the ability for PANIS to sustain the iPSC-islets' viability and functionality over a 14-day period. Furthermore, the inclusion of neutrophils along with the iPSC-islets demonstrated the ability for PANIS to sustain co-culturing of disparate cell groups, as well as model immune cell infiltration and interaction with islets under flow. The culmination of this work showcases the ability for our PANIS device to recapitulate in vivo conditions and be utilized as a means for further understanding and treating T2D.

5.1 Aim 1: Develop an Islet MPS Model with Primary Human Islets for Disease Pathogenesis Modeling and Drug Testing.

The establishment of the microphysiological system has revolutionized the field of disease modeling and therapy development, with the ability to efficiently represent organ system in vitro. The development of different organ MPS models provides the ability to study isolated effects on specific organs. With the establishment of our primary islet MPS device, we were able to study the effects of different toxic media compositions on primary islet viability and functionality, which provides insight into what factors can affect islets during T2D. While this insight is helpful in understanding specific effects to isolated organ systems, a more wholistic model would be needed to fully replicate the complexity of diseases such as T2D that encompass crosstalk between multiple organ systems. To add to this complexity, others have coupled multiple organ MPS models together[115, 206, 207]. Future works with this aim would be to couple this with other organ models that have a role in the onset and progression of diabetes, such as liver, intestine, or adipose. Since each tissue type would require a specific media composition to sustain them, studies on forming a common media would be necessary to maintain coupled system. The common media would be based on the requirements of each tissue, but also dependent on the order by which the media would flow, such as less insulin would be needed in the media if the flow initiates with an islet MPS or is re-circulating.

5.2 Aim 2: Develop a Novel Platform for Differentiating Endoderm-Lineage Cell Types from Human Induced Pluripotent Stem Cells (iPSCs).

In aim 2, we developed an INS-mCherry reporter iPSC-line that could be used for enriching the insulin producing cell population where we found that it did not significantly aid in the endpoint functionality of the cells. While the original purpose for the reporter line may not enhance the differentiation, it can be used as an indicator for improving the differentiation steps and alginate composition. Current methods for detecting the success of a differentiating batch of cells or a new protocol for islet differentiation requires lengthy characterization through cell staining or PCR to determine if and how many insulin producing cells are forming. With the use of the INS-mCherry reporter, this detection can be done in situ with only a fluorescent microscope. In addition, the rise of artificial intelligence (AI) image recognition technology and its utilizing to identify the degree of iPSC differentiation[208, 209] would allow for these reporters to be utilized alongside AI to form a predictive model for the quality of a differentiation batch before reaching its endpoint. In this future work, the developed reporter would be used to monitor the progression of islet differentiating aggregates and provide levels of insulin-related fluorescence that the learner could use to initially train with additional input from endpoint characterization and then predict the outcome of the differentiation.

In this aim, the alginate configuration used had been initially optimized for islet differentiation[146], but we were able to still form T-cell producing TECs. Another future work for this aim would be to further optimize the configuration of the alginate to improve the specificity of the differentiation towards either cTECs or mTECS, depending on the desired outcome.

5.3 Aim 3: To Implement Human iPSC-Derived Islet into MPS Model for Disease Modeling.

In this aim, we were able to demonstrate the PANIS' ability for maintaining iPSC-islets for a 14-day span under healthy conditions. The naturally progression of this work would be to use the information gained with testing the T2D-related media compositions on the primary human islet PANIS to form a T2D disease model with the iPSC-islet PANIS, but this can be furthered by also accounting for genetic predisposition. Islet differentiation of iPSCs derived from diabetic donors has been demonstrated as a potential avenue for studying the pathogenesis of diabetes in vitro[210]. Future works for this aim could entail utilizing these iPSCs to form a more detailed diabetic model that accounts for both environment and genetic factors by utilizing diabetic derived iPSCs for islet formation and testing.

Appendix A Chapter 2

Appendix A.1 Tables

Appendix Table 1 PANIS device specifications and infromation.

Distance between channel and top surface	Thickness top layer 1.1 mm
Distance between channel and bottom surface	Thickness bottom layer 0.7 mm
Total chip thickness	2.6 mm (including middle layer)
Chip size	45 mm x15 mm
Channel width	11 mm, 2 channel, 1x on top of membrane, 1x on bottom of membrane
Channel height	~200 µm (per channel)
Number of Inlets	2 (1 inlet for flow channel on top membrane, 1 inlet for flow on bottom of membrane)
Number of outlets	2 (1 outlet for flow channel on top membrane, 1 outlet for flow on bottom of membrane)
Inlet/outlet hole sizes on top of the chip	1.7 mm
Inlet/outlet holes size at channel	0.75 mm

Appendix Table 2 Pancreatic islet donor list

Prodo Labs #	Age	Sex	Ethnicity	Height (in)	Weight (lb)	BMI	HbA1c
HP-19010-01	66	m	Caucasian	67	174	27	4.7
HP-19068-01	20	f	African American	67	238	36.9	5.3
HP-19122-01	57	m	Hispanic	66	160	25.9	5.9
HP-19143-01	45	m	African American	72	235	31.5	5.8
HP-19163-01	24	m	Caucasian	67	155	24.5	5.6
HP-19189-01	37	m	Caucasian	71	231	32.2	5.2
HP-19208-01	35	m	Caucasian	71	155	21.7	4.7
HP-19226-01	51	m	Caucasian	66	195	31.3	5.2
HP-19256-01	64	m	Caucasian	65	151	25.5	5.4
HP-19333-01	38	m	Hispanic	65	150	24.9	5.3
HP-20021-01	52	m	Caucasian	72	218	29.6	5.4
HP-20041-01	30	m	Hispanic	70	159	22.7	5.2
HP-20052-01	34	f	Caucasian	63	195	34.1	5.5
HP-20066-01	60	f	Caucasian	61	139	25.8	5.1
HP-20168-01	26	m	Hispanic	69	163	24.1	5.1
HP-20199-01	21	m	Hispanic	67	174	27.3	5.1
HP-20228-01	36	f	Caucasian	66	160	25.8	5.5

HP-20262-01	67	m	Asian	62	135	24.4	5.8
HP-20341-01	35	m	Hispanic	70	127	18.1	5.3
HP-20346-01	37	f	Indian	65	155	26.1	5
HP-21015-01	56	m	Caucasian	70	230	32.9	5.3
HP-21024-01	51	m	Caucasian	70	150	20.3	5.2
HP-21062-01	41	f	African American	67	178	28	5.3
HP-21079-01	59	m	Caucasian	69	155	22.6	5.2
HP-21213-01	62	f	Caucasian	63	130	23	5
HP-23019/23-01	55	m	Hispanic	69	205	30.4	5.6
HP-23044-01	36	f	Caucasian	69	230	34	4.9
HP-23073-01	55	m	Caucasian	67	166	26.3	5.9
HP-23093-01	63	f	Caucasian	61	117	22.1	5.6

Appendix Table 3 HGP vs NF up/down-regulated DEGs

Name	Log2 fold change	FDR p-value	ENSEMBL
CXCL10	-9.073244703	0.016000053	https://www.ensembl.org/id/ENSG00000169245
CYP26B1	-8.464836294	0.015796485	https://www.ensembl.org/id/ENSG00000003137
ENSG00000283228	-8.33147597	0.018523453	https://www.ensembl.org/id/ENSG00000283228
PSG3	-8.233118199	0.022822025	https://www.ensembl.org/id/ENSG00000221826
CHIT1	-6.566006854	1.82E-11	https://www.ensembl.org/id/ENSG00000133063
IFI44L	-5.852702156	3.77E-04	https://www.ensembl.org/id/ENSG00000137959
OAS2	-5.768417492	8.26E-07	https://www.ensembl.org/id/ENSG00000111335
CD163	-5.658540637	2.74E-03	https://www.ensembl.org/id/ENSG00000177575
CXCL11	-5.11846545	1.91E-04	https://www.ensembl.org/id/ENSG00000169248
ABCB5	-5.086831568	2.06E-03	https://www.ensembl.org/id/ENSG00000004846
FPR3	-5.025085518	1.02E-07	https://www.ensembl.org/id/ENSG00000187474
LILRB4	-4.918060968	0.011962539	https://www.ensembl.org/id/ENSG00000186818

ITGAX	-4.845944252	1.10E-08	https://www.ensembl.org/id/ENSG00000140678
OLR1	-4.828750873	0.016339347	https://www.ensembl.org/id/ENSG00000173391
H2AC17	-4.806814164	0.01266668	https://www.ensembl.org/id/ENSG00000278677
MMP9	-4.797334093	9.83E-11	https://www.ensembl.org/id/ENSG00000100985
CCL3	-4.755216898	0.023563979	https://www.ensembl.org/id/ENSG00000277632
CILP	-4.755134646	7.32E-12	https://www.ensembl.org/id/ENSG00000138615
MYO1F	-4.69484985	2.80E-03	https://www.ensembl.org/id/ENSG00000142347
PLA2G7	-4.669866512	2.79E-07	https://www.ensembl.org/id/ENSG00000146070
CDHR1	3.356443413	3.63E-15	https://www.ensembl.org/id/ENSG00000148600
HAPLN4	3.395453297	4.80E-19	https://www.ensembl.org/id/ENSG00000187664
PCSK9	3.447625697	9.82E-20	https://www.ensembl.org/id/ENSG00000169174
SLC14A2	3.466049973	1.49E-03	https://www.ensembl.org/id/ENSG00000132874
IAPP	3.535500378	2.48E-14	https://www.ensembl.org/id/ENSG00000121351
HBA1	3.68352697	1.73E-04	https://www.ensembl.org/id/ENSG00000206172
WNT2	3.717176436	4.22E-03	https://www.ensembl.org/id/ENSG00000105989
GDPD2	3.749193361	0.049096905	https://www.ensembl.org/id/ENSG00000130055
CALCA	3.757650832	3.63E-03	https://www.ensembl.org/id/ENSG00000110680
P2RX2	3.759070046	4.86E-05	https://www.ensembl.org/id/ENSG00000187848
SLC5A4	3.970574644	1.82E-10	https://www.ensembl.org/id/ENSG00000100191
HSD17B13	4.0199824	3.85E-05	https://www.ensembl.org/id/ENSG00000170509
BORCS7-ASMT	4.08538961	1.03E-05	https://www.ensembl.org/id/ENSG00000270316
HBA2	4.145679125	7.42E-12	https://www.ensembl.org/id/ENSG00000188536
CXorf51A	4.991345253	0.018240361	https://www.ensembl.org/id/ENSG00000224440
TNFSF12-TNFSF13	7.784076706	0.023700852	https://www.ensembl.org/id/ENSG00000248871
PAEP	7.851231639	3.19E-14	https://www.ensembl.org/id/ENSG00000122133
ENSG00000285238	8.122973174	0.011800271	https://www.ensembl.org/id/ENSG00000285238
ENSG00000257767	8.309096314	8.56E-03	https://www.ensembl.org/id/ENSG00000257767
ENSG00000267228	8.321127758	7.84E-03	https://www.ensembl.org/id/ENSG00000267228

Appendix Table 4 HG vs NF up/down-regulated DEGs

Name	Log2 fold change	FDR p-value	ENSEMBL
IFI44L	-6.18338	4.25E-05	https://www.ensembl.org/id/ENSG00000137959
OAS2	-5.74479	1.51E-07	https://www.ensembl.org/id/ENSG00000111335
CXCL11	-5.33956	3.27E-05	https://www.ensembl.org/id/ENSG00000169248
CXCL10	-5.2157	6.15E-04	https://www.ensembl.org/id/ENSG00000169245
MMP8	-4.59648	5.01E-06	https://www.ensembl.org/id/ENSG00000118113
IDO1	-4.1776	3.61E-03	https://www.ensembl.org/id/ENSG00000131203
E2F2	-4.14609	0.040051	https://www.ensembl.org/id/ENSG00000007968
TREM2	-3.99158	6.55E-03	https://www.ensembl.org/id/ENSG00000095970
CCL11	-3.94849	3.17E-03	https://www.ensembl.org/id/ENSG00000172156
COL14A1	-3.83968	4.92E-12	https://www.ensembl.org/id/ENSG00000187955
MS4A6A	-3.70917	0.016926	https://www.ensembl.org/id/ENSG00000110077
KRT5	-3.5692	0.048057	https://www.ensembl.org/id/ENSG00000186081
IFI27	-3.51757	7.29E-04	https://www.ensembl.org/id/ENSG00000165949
ABCB5	-3.49707	2.69E-03	https://www.ensembl.org/id/ENSG00000004846
RAB4B-EGLN2	-3.4885	1.03E-03	https://www.ensembl.org/id/ENSG00000171570
ENSG00000283228	-3.4198	1.14E-05	https://www.ensembl.org/id/ENSG00000283228
VSIG4	-3.41352	0.038449	https://www.ensembl.org/id/ENSG00000155659
CILP	-3.33172	4.12E-09	https://www.ensembl.org/id/ENSG00000138615
DCLK1	-3.32595	1.01E-06	https://www.ensembl.org/id/ENSG00000133083
SPX	2.849838	5.09E-14	https://www.ensembl.org/id/ENSG00000134548
HAPLN4	2.878096	8.11E-14	https://www.ensembl.org/id/ENSG00000187664
SYT16	3.018161	1.57E-26	https://www.ensembl.org/id/ENSG00000139973
GOLGA6C	3.034324	0.049675	https://www.ensembl.org/id/ENSG00000167195
SSTR4	3.054556	1.13E-04	https://www.ensembl.org/id/ENSG00000132671
SLC5A4	3.149915	8.28E-06	https://www.ensembl.org/id/ENSG00000100191
ENSG00000273155	3.208001	0.018355	https://www.ensembl.org/id/ENSG00000273155
GOLGA8G	3.226322	0.04723	https://www.ensembl.org/id/ENSG00000183629
IL5RA	3.230879	2.15E-10	https://www.ensembl.org/id/ENSG00000091181
IAPP	3.246757	5.17E-13	https://www.ensembl.org/id/ENSG00000121351
PI3	3.4744	2.32E-03	https://www.ensembl.org/id/ENSG00000124102
HSD17B13	3.48861	2.27E-04	https://www.ensembl.org/id/ENSG00000170509

NCAN	3.556796	2.77E-03	https://www.ensembl.org/id/ENSG00000130287
ENSG00000259900	3.956471	9.28E-03	https://www.ensembl.org/id/ENSG00000259900
P2RX2	4.016674	5.58E-07	https://www.ensembl.org/id/ENSG00000187848
NXF2	4.374378	0.023825	https://www.ensembl.org/id/ENSG00000269405
ENSG00000267228	7.284969	0.035304	https://www.ensembl.org/id/ENSG00000267228
ENSG00000257767	7.43116	0.032333	https://www.ensembl.org/id/ENSG00000257767
ARL2-SNX15	7.47393	0.040051	https://www.ensembl.org/id/ENSG00000273003
ENSG00000273003	8.398145	0.011588	https://www.ensembl.org/id/ENSG00000285238
ENSG00000261459	8.576269	9.18E-03	https://www.ensembl.org/id/ENSG00000261459

Appendix Table 5 HPO vs NF up/down-regulated DEGs

Name	Log2 fold change	FDR p-value	ENSEMBL
HBA1	-8.49946	0.02080648	https://www.ensembl.org/id/ENSG00000206172
TNFSF12-TNFSF13	-8.06894	0.02321431	https://www.ensembl.org/id/ENSG00000248871
ENSG00000284554	-8.04129	0.02470267	https://www.ensembl.org/id/ENSG00000284554
UGT1A3	-7.69889	0.03416729	https://www.ensembl.org/id/ENSG00000288702
HBA2	-7.17661	4.44E-13	https://www.ensembl.org/id/ENSG00000188536
ITLN1	-6.18911	6.43E-03	https://www.ensembl.org/id/ENSG00000179914
ENSG00000285238	-5.66077	1.79E-04	https://www.ensembl.org/id/ENSG00000285238
ENSG00000259753	-5.27126	0.01394519	https://www.ensembl.org/id/ENSG00000259753
HBG1	-5.12376	0.03196722	https://www.ensembl.org/id/ENSG00000213934
HBB	-4.33934	0.04581909	https://www.ensembl.org/id/ENSG00000244734
RSAD2	-4.33512	1.09E-105	https://www.ensembl.org/id/ENSG00000134321

ENSG00000256861	-4.21639	1.53E-03	https://www.ensembl.org/id/ENSG00000256861
PSG1	-4.19509	0.01715447	https://www.ensembl.org/id/ENSG00000231924
ENSG00000258691	-4.14105	9.63E-03	https://www.ensembl.org/id/ENSG00000258691
GABRR2	-4.03587	0.03774618	https://www.ensembl.org/id/ENSG00000111886
PSG8	-3.91696	0.02242015	https://www.ensembl.org/id/ENSG00000124467
HS3ST5	-3.81424	5.64E-05	https://www.ensembl.org/id/ENSG00000249853
STMN4	-3.78804	1.65E-04	https://www.ensembl.org/id/ENSG00000015592
ENSG00000256349	-3.75362	1.23E-03	https://www.ensembl.org/id/ENSG00000256349
DCC	-3.71533	0.01869445	https://www.ensembl.org/id/ENSG00000187323
IRX3	4.992105	4.86E-19	https://www.ensembl.org/id/ENSG00000177508
CEL	4.996898	9.03E-11	https://www.ensembl.org/id/ENSG00000170835
PLA2G1B	5.038495	1.42E-04	https://www.ensembl.org/id/ENSG00000170890
CPA1	5.076608	3.37E-05	https://www.ensembl.org/id/ENSG00000091704
CELA3B	5.100672	0.04225132	https://www.ensembl.org/id/ENSG00000219073
TFF1	5.234506	4.07E-05	https://www.ensembl.org/id/ENSG00000160182
CRISP3	5.236183	1.31E-04	https://www.ensembl.org/id/ENSG00000096006
WNT6	5.430454	0.01166005	https://www.ensembl.org/id/ENSG00000115596
NOG	5.593487	0.01365667	https://www.ensembl.org/id/ENSG00000183691
RP1L1	5.632965	6.19E-18	https://www.ensembl.org/id/ENSG00000183638
S100A9	5.704731	8.27E-04	https://www.ensembl.org/id/ENSG00000163220
LTF	5.716515	7.68E-04	https://www.ensembl.org/id/ENSG00000012223
LRP2	5.781081	5.49E-03	https://www.ensembl.org/id/ENSG00000081479
PNLIPRP1	6.083369	5.87E-08	https://www.ensembl.org/id/ENSG00000187021
CLPS	7.096323	1.02E-07	https://www.ensembl.org/id/ENSG00000137392
TFF2	8.405316	0.02509405	https://www.ensembl.org/id/ENSG00000160181
BIVM-ERCC5	8.554937	6.59E-08	https://www.ensembl.org/id/ENSG00000270181
KRT6A	8.902948	0.02507094	https://www.ensembl.org/id/ENSG00000205420
AMY2A	9.056036	0.01358097	https://www.ensembl.org/id/ENSG00000243480
P3R3URF-PIK3R3	9.133567	9.39E-03	https://www.ensembl.org/id/ENSG00000278139

Appendix Table 6 HGPO vs NF up/down-regulated DEGs

Name	Log2 fold change	FDR p-value	ENSEMBL
SPRR2A	-10.42403	7.41E-03	https://www.ensembl.org/id/ENSG00000241794
SERPINB3	-9.4443887	0.02254928	https://www.ensembl.org/id/ENSG00000057149
CXCL9	-9.3059463	0.02618056	https://www.ensembl.org/id/ENSG00000138755
ORM1	-6.6955869	4.42E-04	https://www.ensembl.org/id/ENSG00000229314
SERPINB4	-6.5906304	1.01E-04	https://www.ensembl.org/id/ENSG00000206073
RRM2	-6.0272428	1.51E-07	https://www.ensembl.org/id/ENSG00000171848
PI3	-5.8076434	6.19E-06	https://www.ensembl.org/id/ENSG00000124102
FGF19	-5.6925276	1.60E-16	https://www.ensembl.org/id/ENSG00000162344
FCAMR	-5.6778775	0.04796799	https://www.ensembl.org/id/ENSG00000162897
E2F2	-5.5800697	0.01855758	https://www.ensembl.org/id/ENSG00000007968
CXCL6	-5.436487	1.93E-06	https://www.ensembl.org/id/ENSG00000124875
RNASE7	-5.3355613	4.88E-05	https://www.ensembl.org/id/ENSG00000165799
KIF20A	-5.2368919	7.94E-04	https://www.ensembl.org/id/ENSG00000112984
MKI67	-5.0851237	2.44E-07	https://www.ensembl.org/id/ENSG00000148773
LCN2	-5.0311865	8.57E-08	https://www.ensembl.org/id/ENSG00000148346
DTL	-4.9723894	5.91E-05	https://www.ensembl.org/id/ENSG00000143476
NUSAP1	-4.9544388	1.65E-03	https://www.ensembl.org/id/ENSG00000137804
LTF	-4.8781454	2.10E-03	https://www.ensembl.org/id/ENSG00000012223
ASPM	-4.8457196	1.50E-05	https://www.ensembl.org/id/ENSG00000066279
PIP	-4.8043384	0.0132914	https://www.ensembl.org/id/ENSG00000159763
SPX	2.32705667	5.65E-03	https://www.ensembl.org/id/ENSG00000134548
THBD	2.36380265	5.15E-05	https://www.ensembl.org/id/ENSG00000178726
NCAN	2.47889535	0.02847012	https://www.ensembl.org/id/ENSG00000130287
SSTR4	2.57081588	0.02688801	https://www.ensembl.org/id/ENSG00000132671
KCNA4	2.62579079	0.04996415	https://www.ensembl.org/id/ENSG00000182255
ENSG00000284209	2.66267428	0.02768277	https://www.ensembl.org/id/ENSG00000284209
HAPLN4	2.74825503	5.67E-05	https://www.ensembl.org/id/ENSG00000187664
ST8SIA5	2.80752765	3.01E-04	https://www.ensembl.org/id/ENSG00000101638
IAPP	2.9028479	7.18E-04	https://www.ensembl.org/id/ENSG00000121351
CPA1	3.09441489	3.88E-04	https://www.ensembl.org/id/ENSG00000091704
HTR1A	3.15333356	3.75E-04	https://www.ensembl.org/id/ENSG00000178394
ENSG00000268400	3.18529662	0.02069203	https://www.ensembl.org/id/ENSG00000268400

HSD17B13	3.23127605	5.31E-04	https://www.ensembl.org/id/ENSG00000170509
TFF1	3.36870848	3.89E-04	https://www.ensembl.org/id/ENSG00000160182
PCARE	3.39004635	5.45E-05	https://www.ensembl.org/id/ENSG00000179270
SLC5A4	3.61698326	5.41E-04	https://www.ensembl.org/id/ENSG00000100191
ENSG00000255730	3.68221184	0.01352418	https://www.ensembl.org/id/ENSG00000255730
P2RX2	4.32091748	7.18E-06	https://www.ensembl.org/id/ENSG00000187848
TFF2	5.7830283	5.44E-04	https://www.ensembl.org/id/ENSG00000160181
ENSG00000285238	8.55849605	0.04329846	https://www.ensembl.org/id/ENSG00000285238

Appendix A.2 Figures

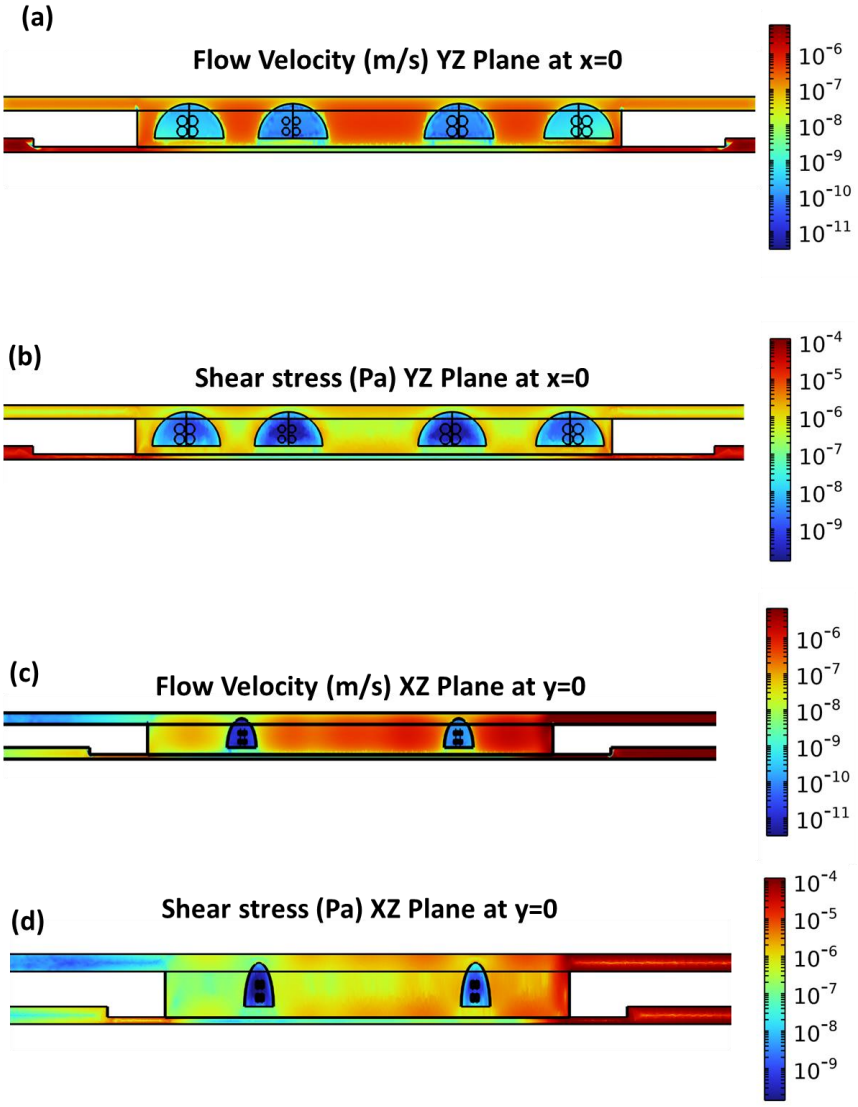

Appendix Figure 1 Alternate views of flow velocity distribution and Shear stress in the islet on chip comsol model.(a,b) Flow velocity and Shear stress distribution on YZ plane passing through x=0 and (c,d) Flow velocity and Shear stress on XZ plane passing through Y=0

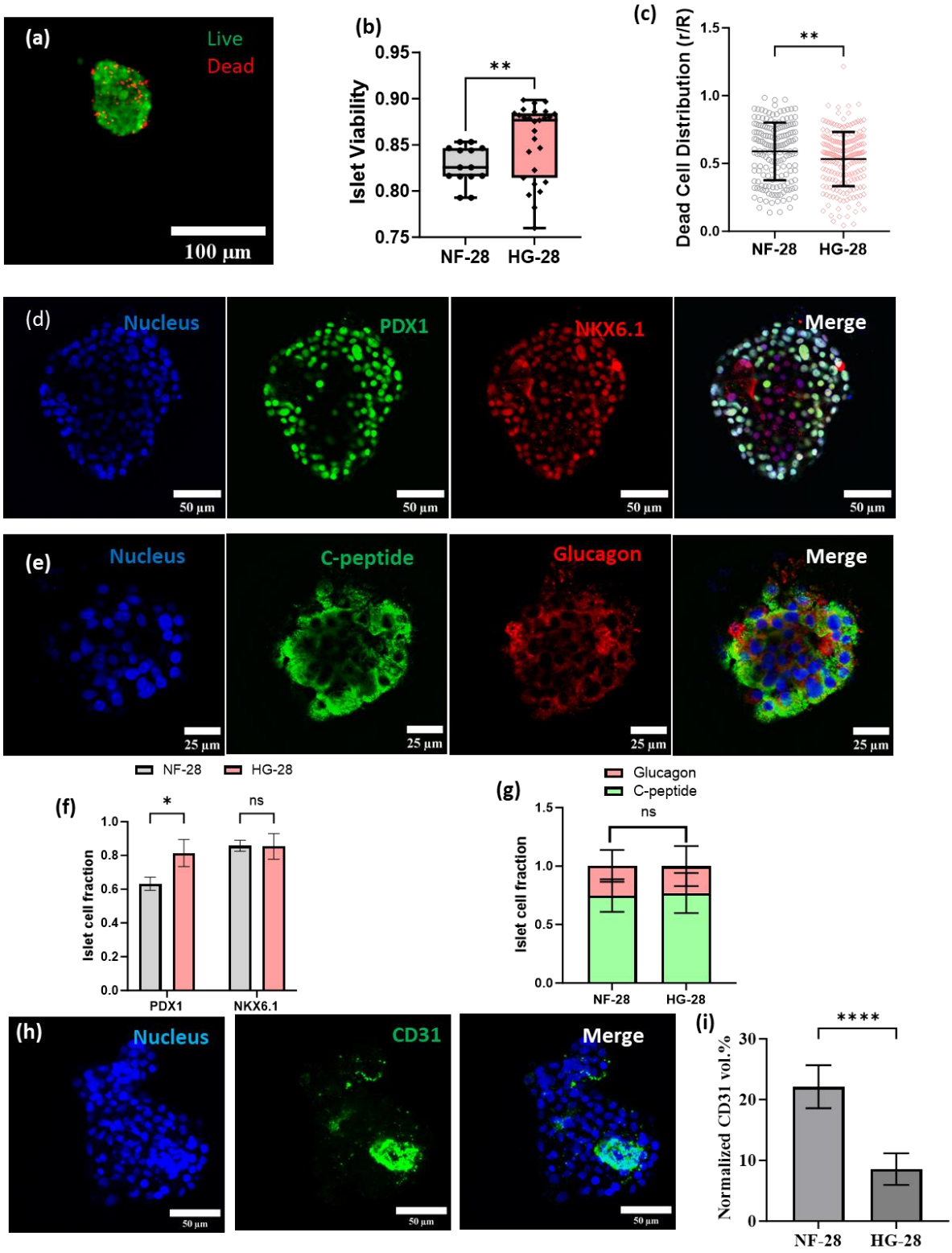

Appendix Figure 2 Islet outcome from 28 days in high glucose (HG-28) treated PANIS(a) Representative image showing PANIS islet viability after 28 days of HG treatment (HG-28); (b) Quantification of islet viability on

PANIS with 28 days normal fasting (NF-28) and HG-28 culture conditions (p<0.01) and (c) shows the distribution of dead cells in the islets (** p<0.01); (d) Representative images showing islet markers PDX1, NKX6.1 and (e) C-peptide and Glucagon for PANIS islets under NF-28 and HG-28 conditions; (g) Image analysis determining the fractions of PDX1 and Nkx 6.1 positive cells in NF-28 and HG-28 conditions; (f) Image analysis determining the fractions of C-peptide and Glucagon positive cells for NF-28 and HG-28 conditions (p>0.05); (h) Representative image for CD31+ cells in HG-28 with (i) image analysis comparing NF-28 and HG-28 (****p<0.0001) (n>7)**

Appendix B Chapter 3 Figures

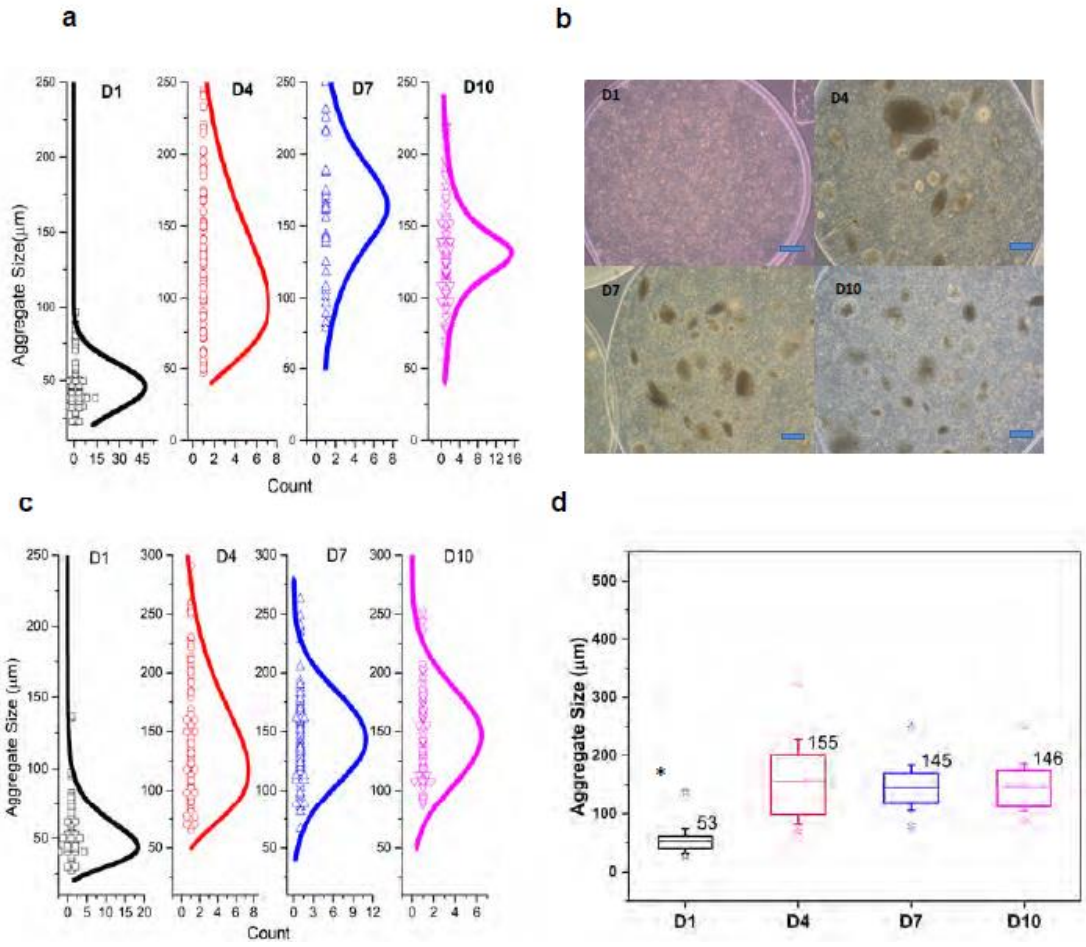

Appendix Figure 3 Differentiation of human hPSCs into TEPCs in 3D alginate hydrogel capsule. Size distribution of iPSC aggregates at different stages of TEPC differentiation. The open shapes in the left panel indicate the size of individual aggregates in the capsule. Solid lines show the overall size distribution of TEPCs aggregates at each stage. b. Images of hESC aggregates at different stages of TEPC differentiation. Bright field photographic images of hESC aggregates within the alginate capsules at days 1, 4, 7 and 10 (D1-D10). Blue scale bar, 200um. Shown are representative images from two independent hESC-TEC differentiation with similar results. c. Size distribution of hESC aggregates at different stages of TEPC differentiation. d. Box plot of size distribution of hESC-derived TEPC aggregates. The boxes indicate the interquartile range (25-75

percentile) and the whiskers indicate the standard deviation of the distribution. The mean is denoted by the line across the box and the maximum and minimum is denoted by the 'star' symbol. All groups are statistically significant with respect to D1 as analyzed by two tailed, unpaired t test with p<0.0001. No change of aggregate size distribution is detected during D4, D7 and D10 differentiation, as analyzed one way ANOVA and post-hoc Tukey test (p=0.3464).

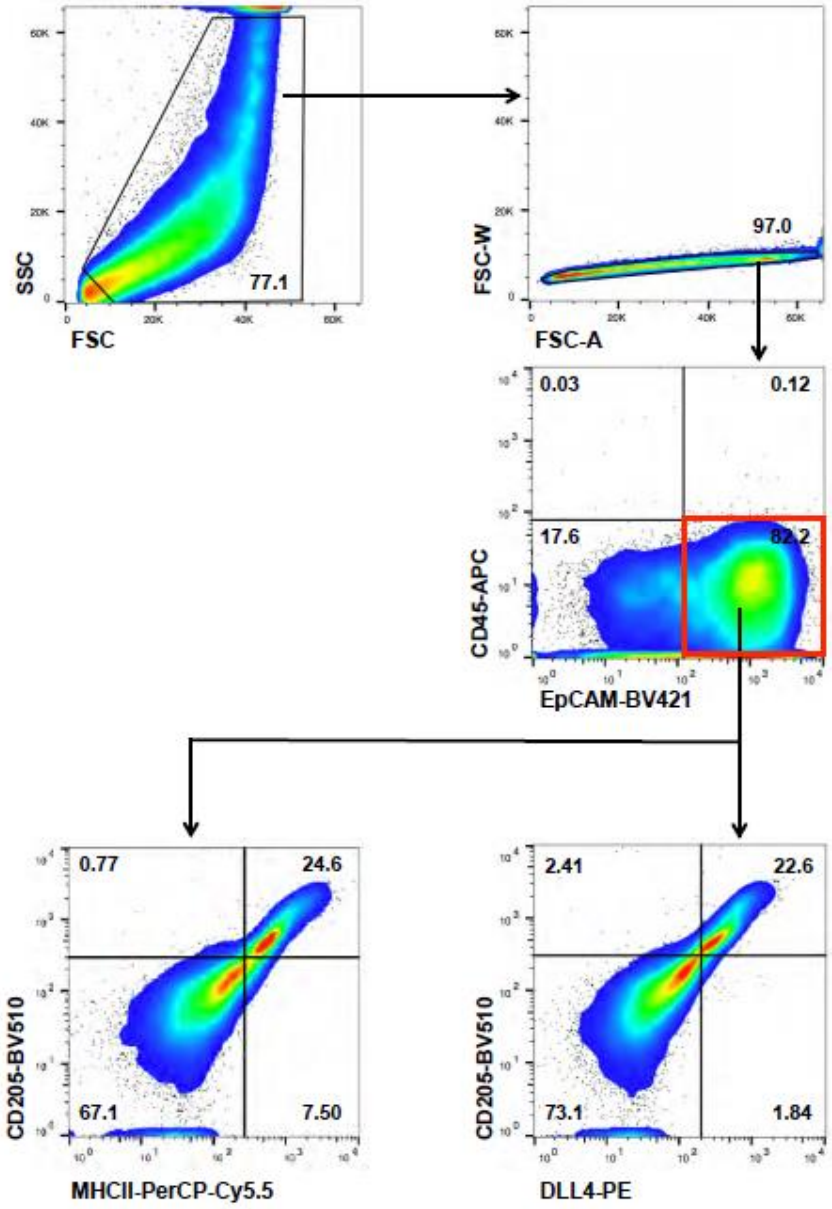

Appendix Figure 4 Gating strategy for FCM analysis of iPSC-derived TEPCs. EpCAM+CD45- cells

(red box) were gated for CD205/MHC-II and CD205/DLL4. Shown are representative FCM images of more than five independent experiments with similar results.

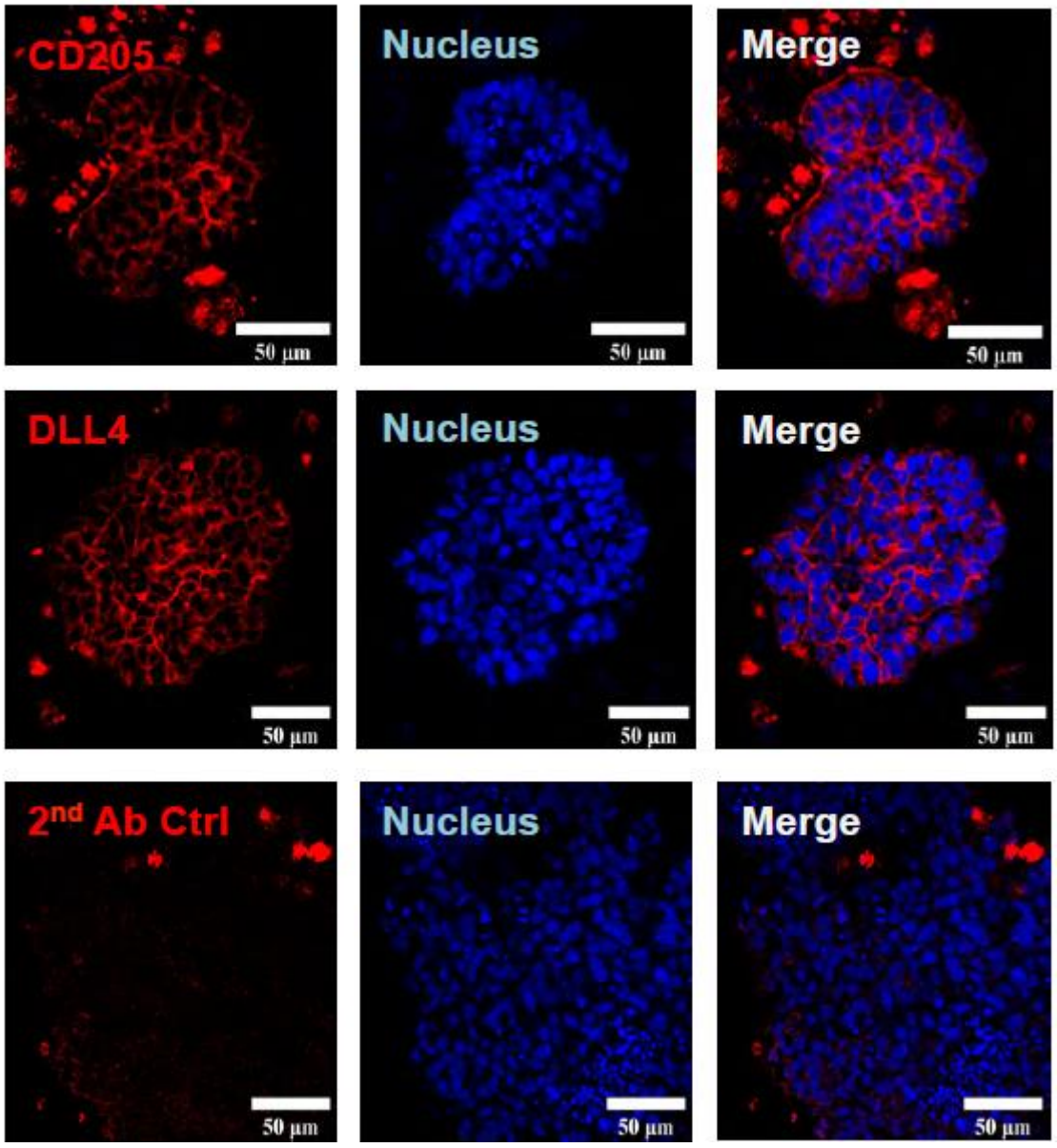

Appendix Figure 5 Immunofluorescent analysis of TEC specific gene expression in iPSC-TEC aggregates.3D iPSC-TEC aggregates were stained with antibodies against DLL4 (red) and CD205 (red). and counter-stained for nucleus (blue). White scale bar, 50um. Shown are representative images from two independent iPSC-TEC differentiations with similar results.

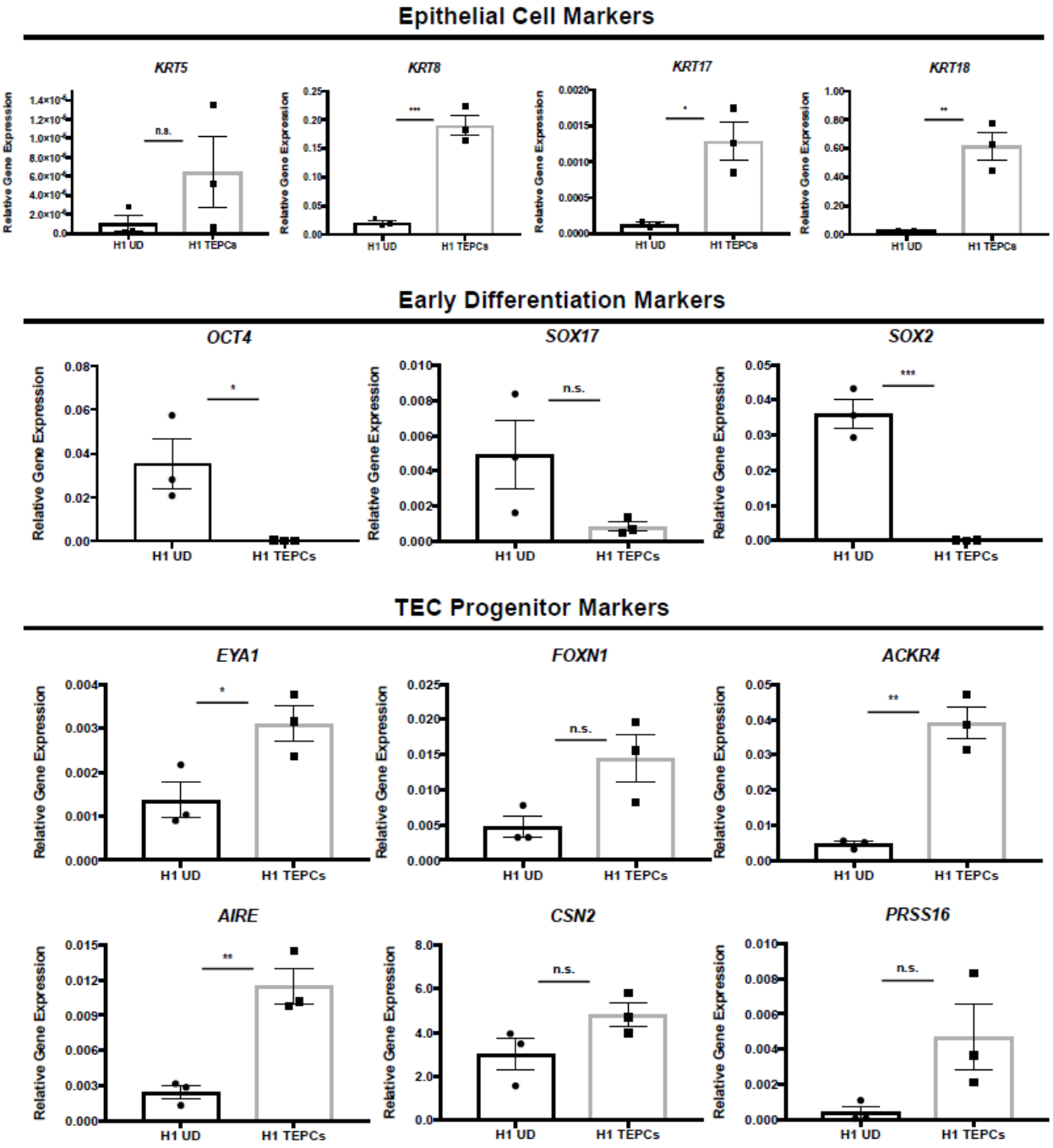

Appendix Figure 6 hESC-derived TEPCs display similar gene expression patterns as iPSCderived TEPCs. H1 hESCs were embedded in alginate capsules and induced to differentiate into TEPCs Expression of genes associated with TEC lineage differentiation was examined by RT-qPCR analysis. H1 UD, undifferentiated H1 hESCs; H1 TEPCs, H1 hESC-derived TEPC aggregates. Shown are results of triplicates from at least two

independent isolations. Data are presented as mean values +/- SEM using a two-tailed unpaired t test. * p<0.05; ** p<0.01; *** p<0.005.

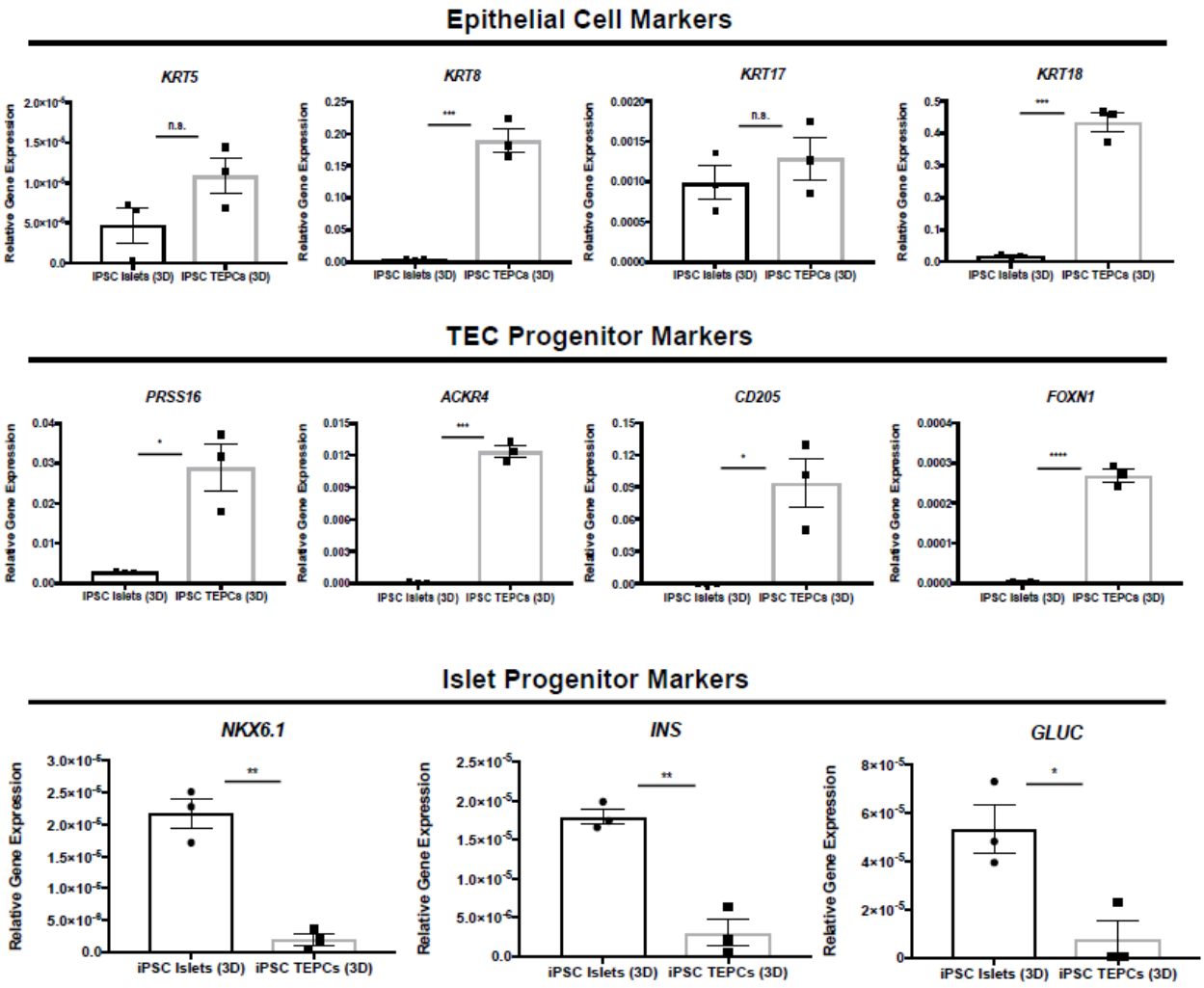

Appendix Figure 7 Differential gene expression profiles between iPSC-derived TECs and iPSCderived islet progenitor cells. TEC progenitors and islet progenitors were generated from Y1 iPSCs, using the same 3D alginate capsule platform but cell type-specific induction protocols. Expression of TEC-expressing epithelial markers, TEC progenitor markers and islet progenitor markers were examined. Levels of gene expression were normalized to hGAPDH. Shown are results of triplicates from three independent isolations. Data are presented as mean values +/- SEM using a two-tailed unpaired t test. * p<0.05; ** p<0.01; ***p<0.005; **** p<0.0001.

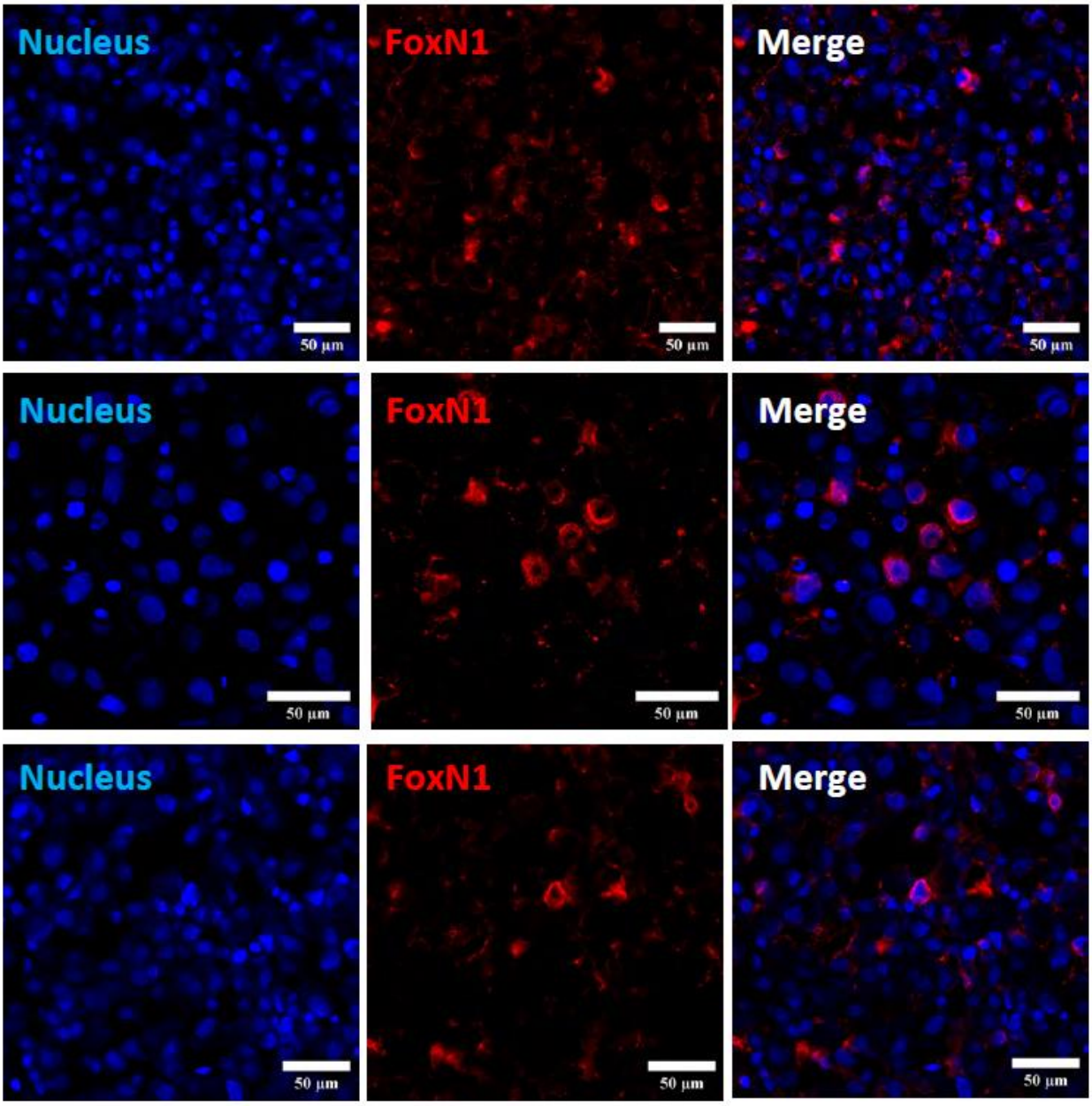

Appendix Figure 8 Immunofluorescence analysis of human FOXN1 expression in primary human TECs.Primary human thymic epithelial cells (Sciencell, CA) were recovered from cryopreservation, cultured for two days in collagen-coated tissue culture dish, cytospan onto slides and stained with antibodies against human FOXN1 (red) and counterstained with Hoechst 33342 for nucleus (blue). White scale bar, 50um. Shown are representative images from three slides of two independent experiments with similar results. Only a small

subset of primary hTECs are positive for FOXN1, and most of the FOXN1-stainings are located at the peri-nucleus region, presumably due to the in vitro 2D culture condition.

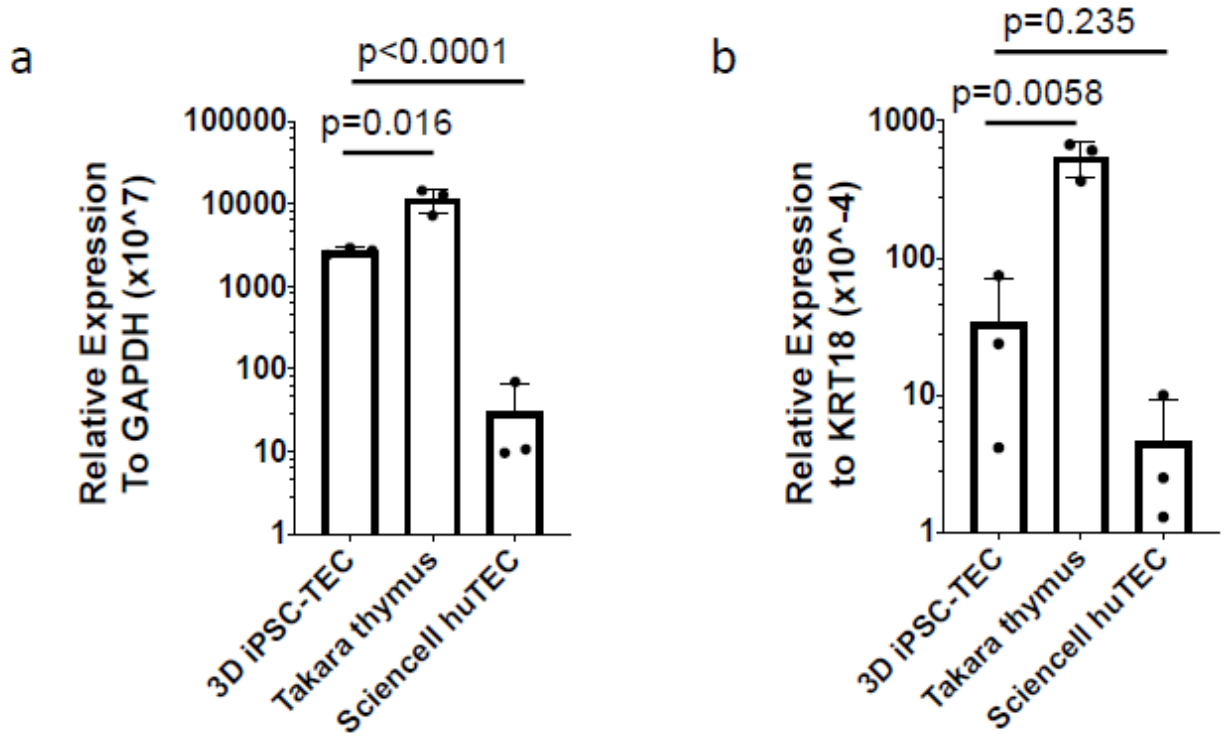

Appendix Figure 9 Comparison of FOXN1 transcription between 3D iPSC-TECs and human TECs. RNAs were extracted from 3D iPSC-TECs and primary human TEC cells (Sciencell huTECs), and reversely transcribed to cDNA. High quality human cDNA was purchased from Takara Bio (Takara thymus). cDNA samples were subjected to qPCR analysis of FOXN1 transcripts, and the levels of expression was normalized to GADPH (a). To limit the influence of hematopoietic cellular components in the whole thymus cDNA sample, FOXN1 expression was also normalized to epitheliumassociated gene, cytokeratin 18 (KRT18) (b). Shown are results from three independent experiments. Data are presented as mean values +/- SEM using a two-tailed unpaired t test.

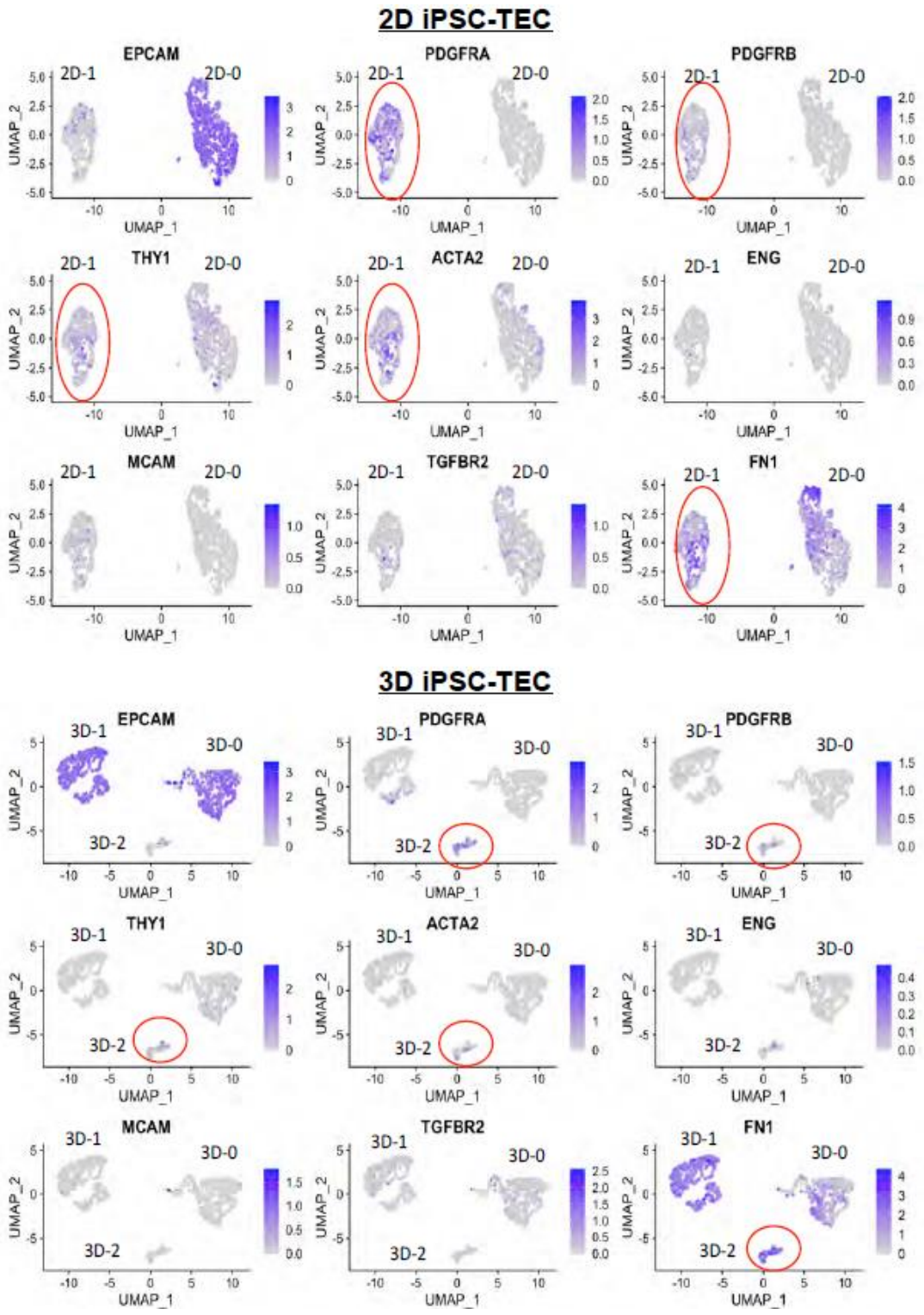

Appendix Figure 10 Annotation of mesenchymal lineage gene expression on 2D and 3D iPSC-TEC Seurat clusters. Red circles highlight the similar elevation of mesenchymal gene expression in 2D-1 and 3D-2 clusters.

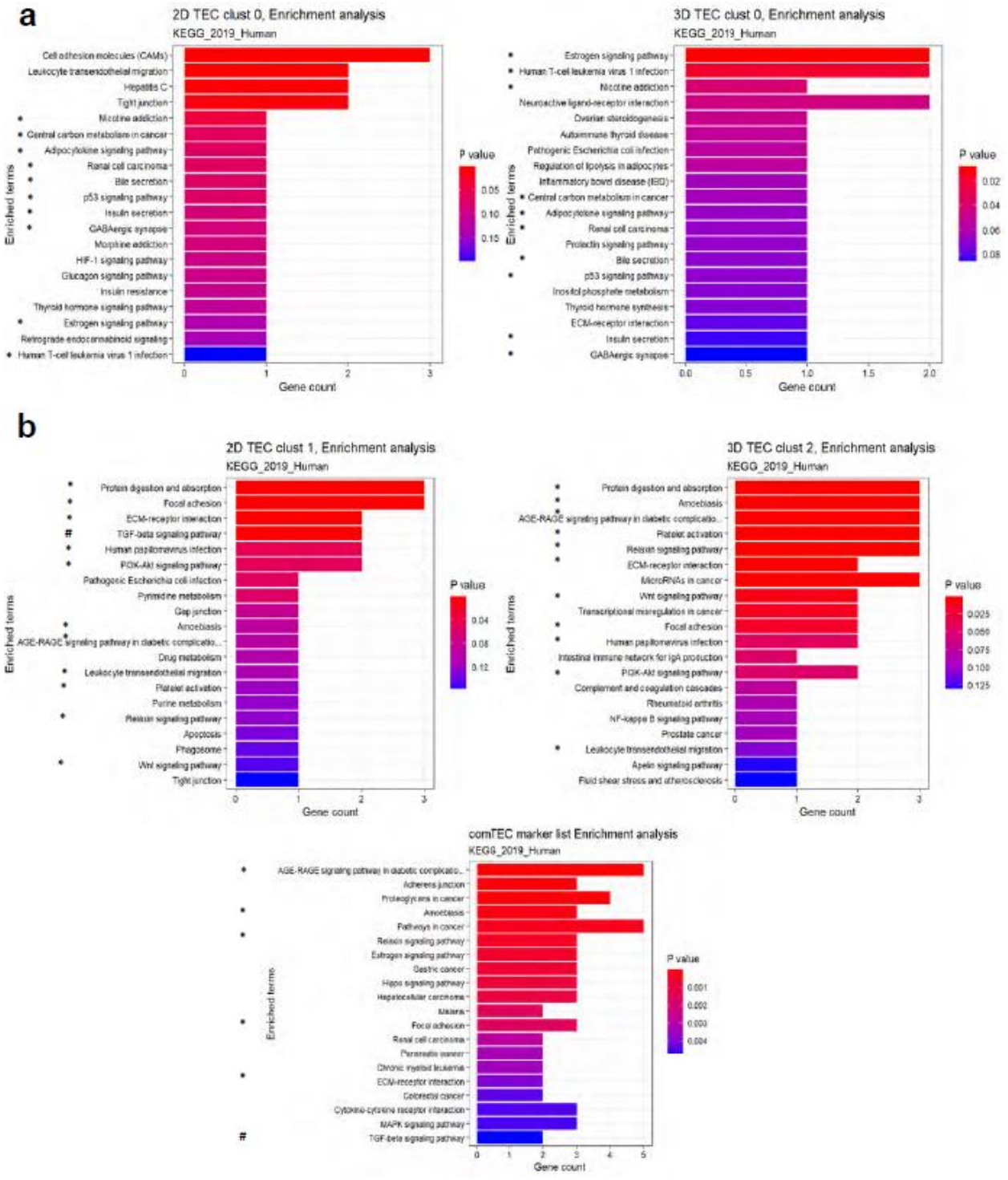

Appendix Figure 11 KEGG pathway enrichment analysis of iPSC-TEC clusters shows significant overlapping of key cellular and organismal function pathways between 2D-0 and 3D-0 clusters. a. 10 out of the top 20), and

between 2D-1 and 3D-2 clusters b. 11 out of the top 20). 2D-1 and 3D-2 clusters share 6 and 5 pathways with the comTEC population identified in human postnatal thymus gland (Campinoti et al., 2020. Nature Comm. 11: 6372), respectively. *, shared pathways between 2D-0 and 3D-0 clusters (a) and 2D-1, 3D-2 and comTECs (b). #, shared between 2D-1 and comTEC.

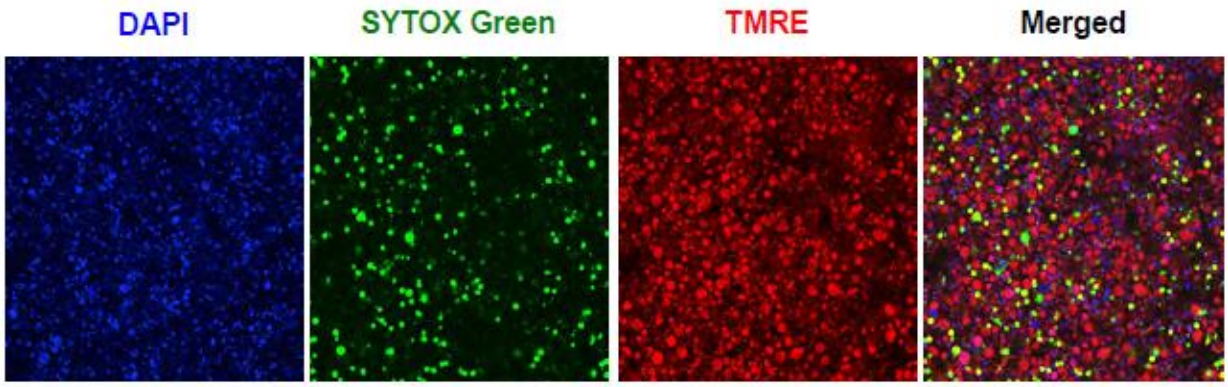

Appendix Figure 12 Thymus organoids can survive long-term in culture. Human thymus organoids were constructed with repopulating decellularized mouse thymus scaffolds with iPSC-derived TECs and CD34+ HPCs, cultured in vitro for one week, stained, and imaged with confocal microscopy (20X). Green, dead cells with nuclei stained with SYTOX Green; Red, live cells whose mitochondria are stained with TMRE (Tetramethylrhodamine ethyl ester); Blue, DAPI staining for nuclei. Shown are images from two independent experiments with similar results.

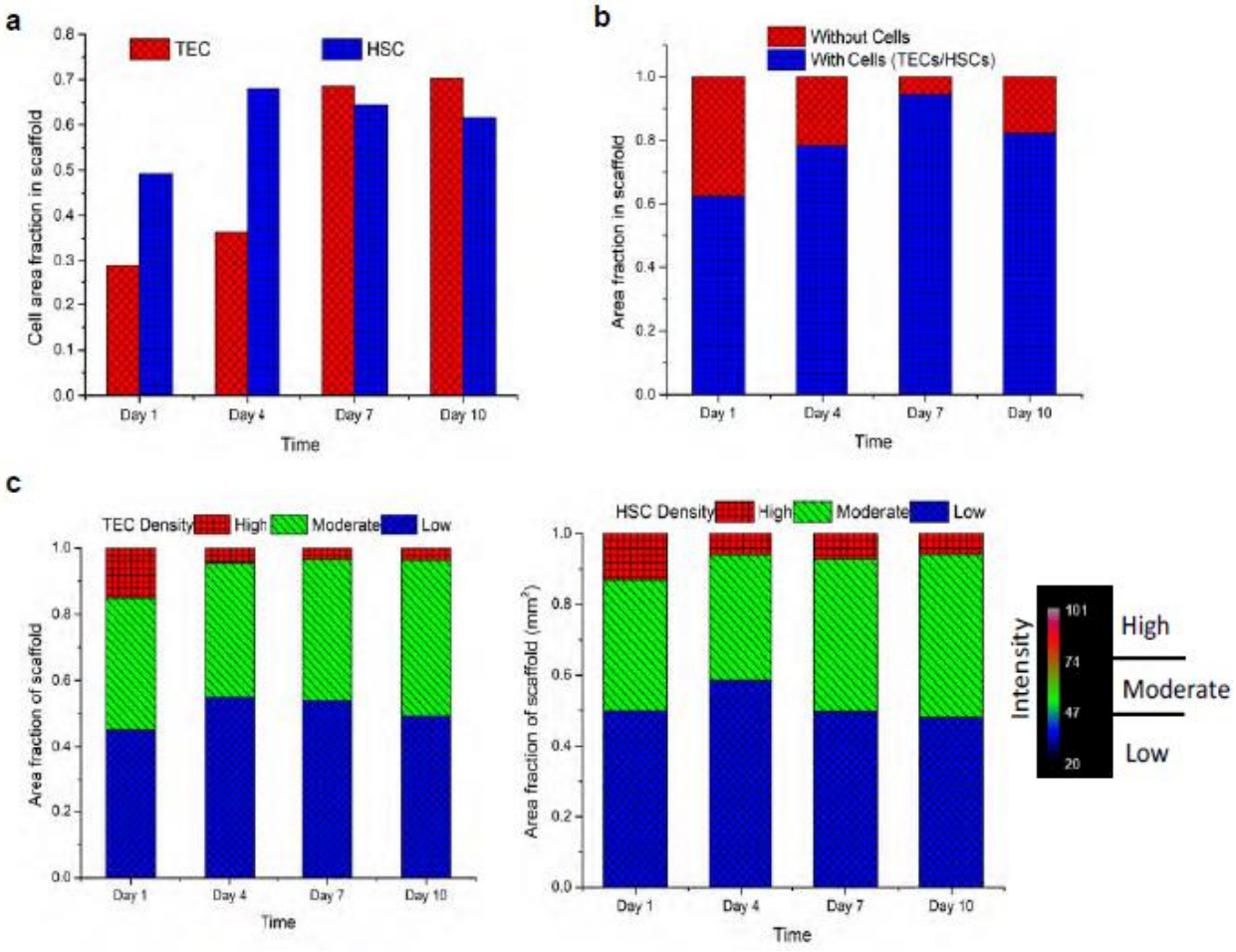

Appendix Figure 13 Both HPC and TEC populations expand within decellularized thymic organoid. a. Comparison of areas in the scaffold with TECs and HPCs (left) and plot showing the variation of areas in the scaffold with TECs/HPCs and without either of the cells over time (b.). The areas have been normalized by the total area of the scaffold. c. Plots showing the distribution of TEC density (left) and HSC density (right) in the scaffold and its variation over time. The scaffold areas are divided into regions of different cell densities based on their grayscale intensity values with high (76-101, red), moderate (48-76, green) and low (20-48, blue) and have been normalized by the total area of the scaffold.

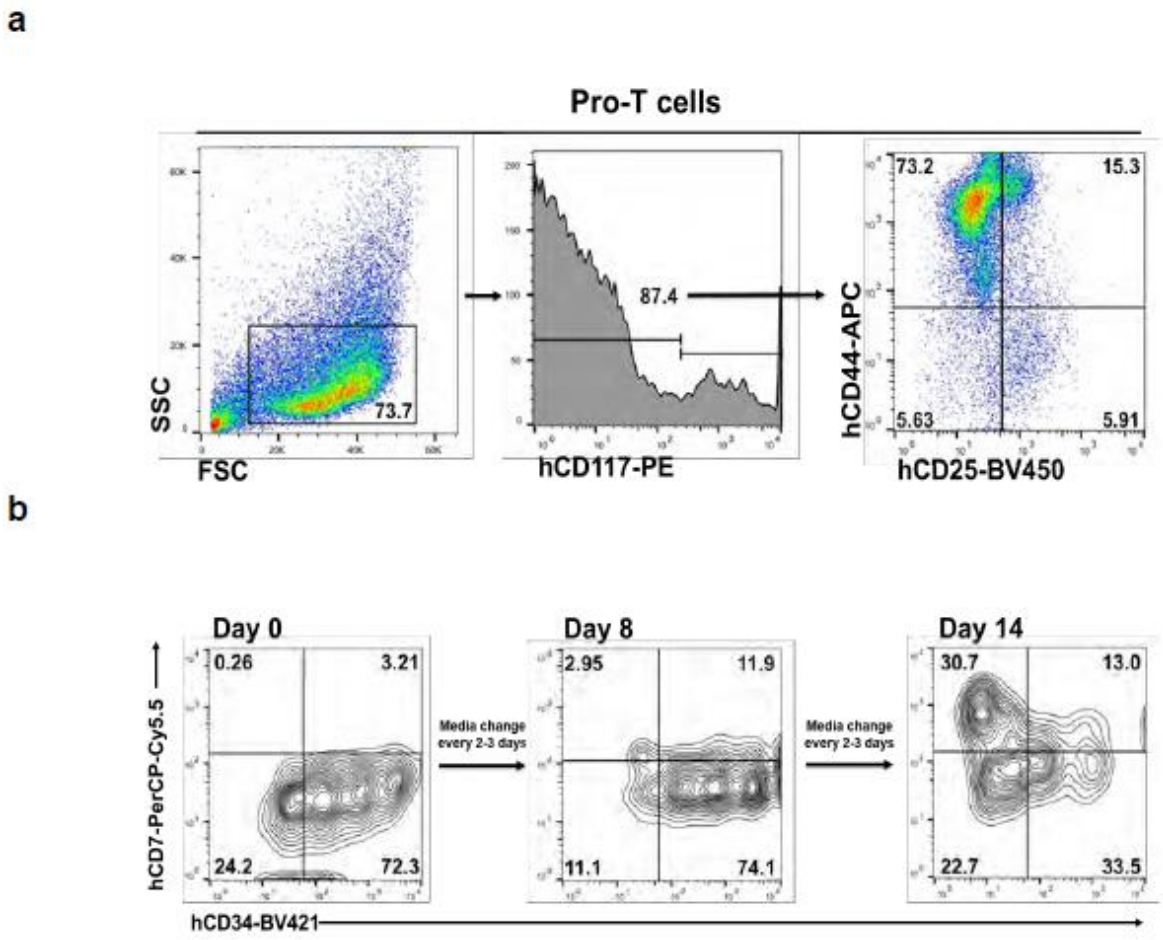

Appendix Figure 14 Differentiation of CD34+ HPCs into Pro-T cells. a. Representative FCM gating strategy to characterize Pro-T cells after 14 of differentiation. Most of the cells are CD117^{-}CD44^{hi}CD25^{low} at this stage. b. Representative FCM plots show progressive changes of key Pro-T surface markers during HPC differentiation, from CD34^{hi}CD7$^{low/-}$ (at day 0) to CD7$^{+/low}$ (at day 8) to predominantly CD34$^{-/low}$CD7$^{hi/+}$ (at day 14). Shown are representatives from two independent experiments with similar results.

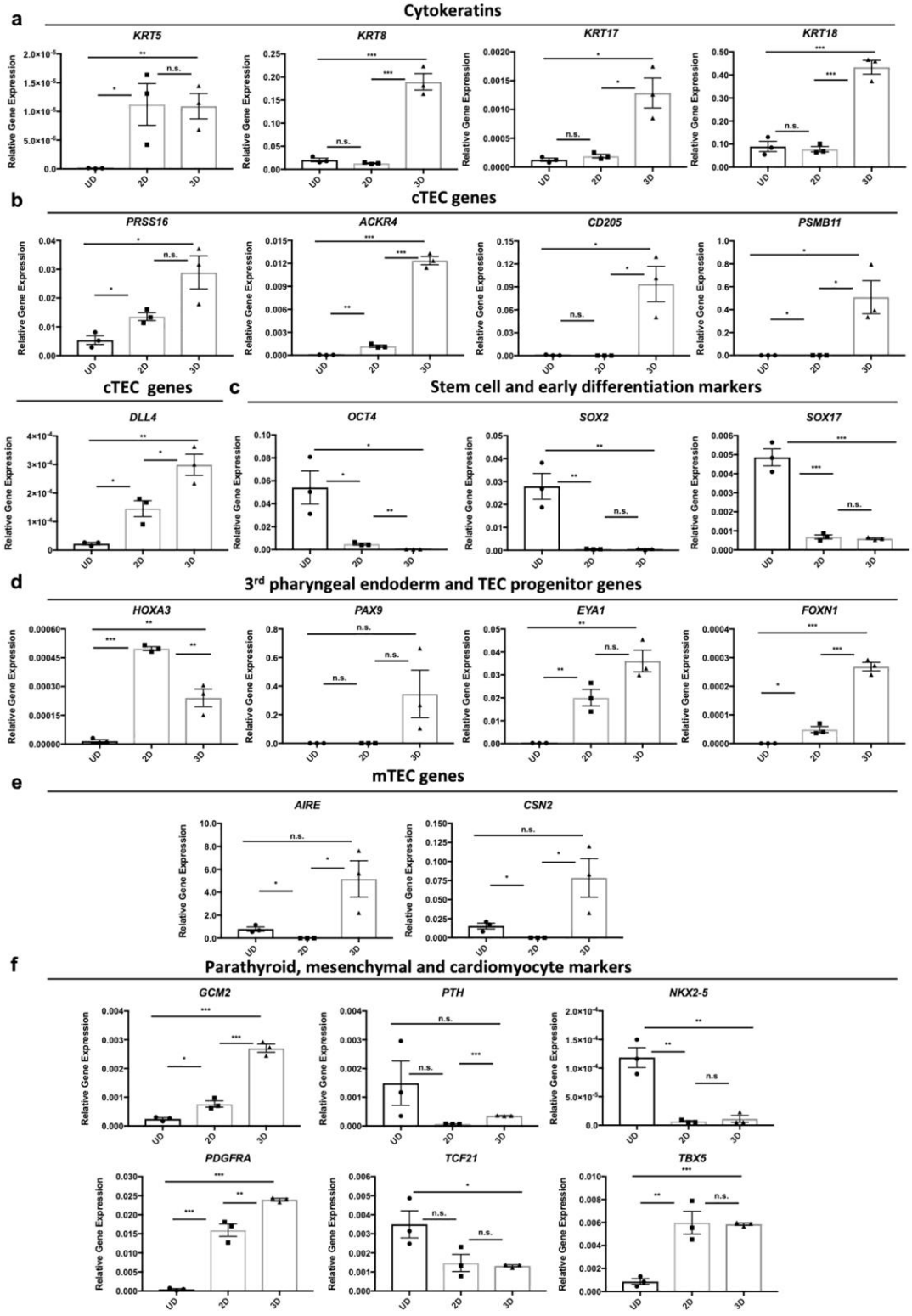

Appendix Figure 15 RT-qPCR analysis of genes associated with TEC differentiation. RNA samples were isolated from undifferentiated iPSCs (UD), 2D TECs (2D), and 3D TECs and were subjected to RT-qPCR

analysis of expression of epithelium-associated cytokeratin genes. (a), cortical TEC (cTEC)-specific genes (b), undifferentiated and early stem cell markers (c), early progenitors of the thymic epithelium (d), mTEC specific markers (e), and markers of the parathyroid (GCM and PTH), mesenchymal (TCF21 and PDGFRA), and cardiomyocyte lineages (NKX2-5 and TBX5) (f). Levels of gene expression were normalized to hGAPDH. Shown are results of triplicates from at least three independent isolations. Data are presented as mean values +/− SEM using a two-tailed unpaired t test. * $p < 0.05$; ** $p < 0.01$; *** $p < 0.005$. Exact p values are listed in the Supporting Information.

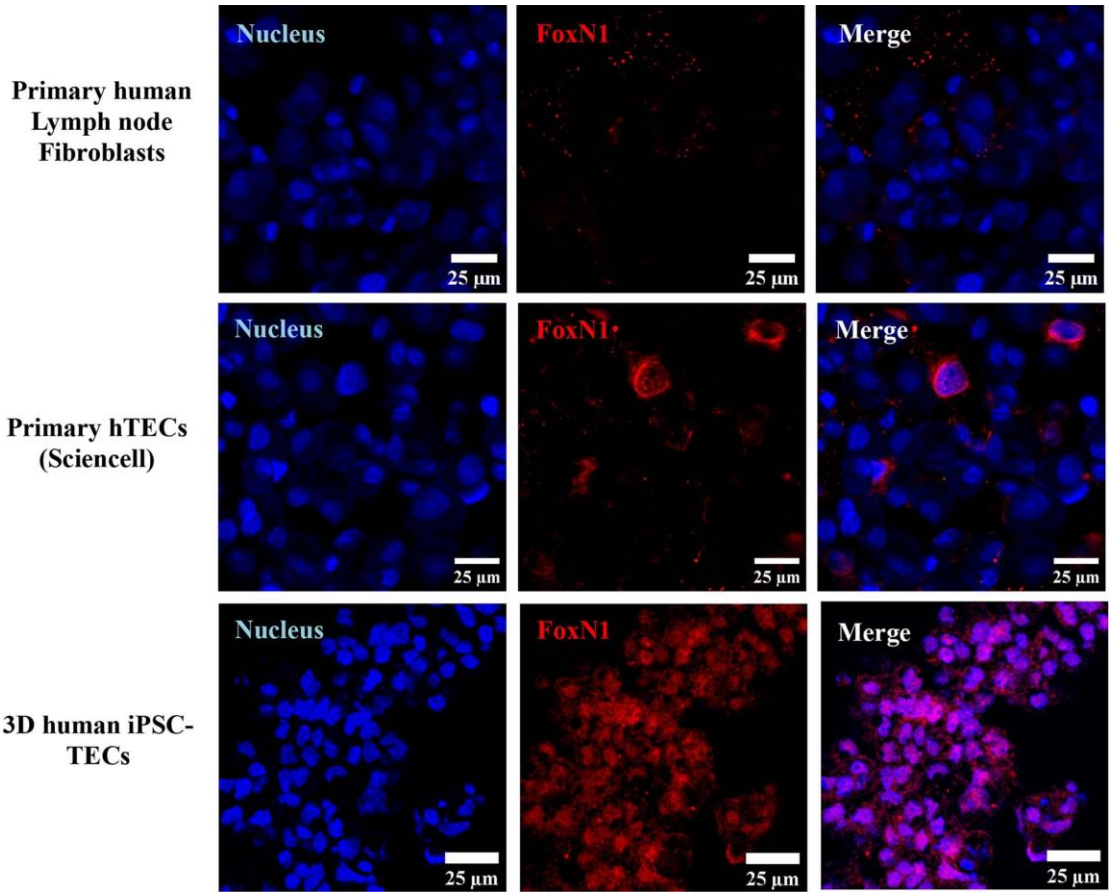

Appendix Figure 16 Immunofluorescence analysis of human FOXN1 expression in 3D iPSC-TECs. Immunofluorescent images of 3D iPSC-TEC aggregates stained with antibodies against human FOXN1 (red) and counterstained with Hoechst 33342 for nucleus (blue). Primary human thymic epithelial cells and lymph node fibroblasts were used as positive and negative controls, respectively. White scale bar, 25um. Shown are representative images from three independent iPSC-TEC differentiations with similar results.

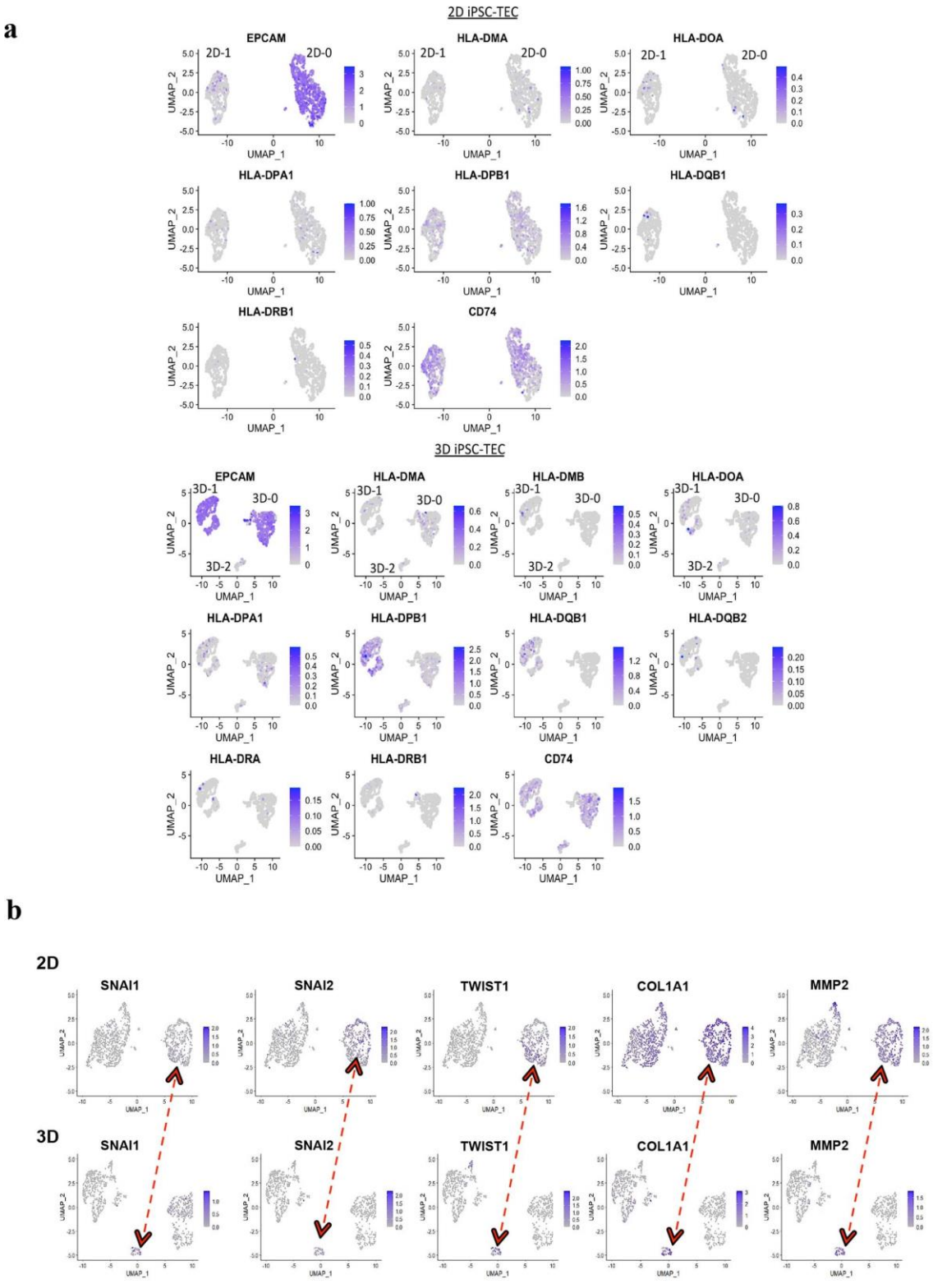

Appendix Figure 17 scRNA-seq analysis of iPSC-TECs. a. Annotation of key human leukocyte antigen (HLA) gene expression on 2D and 3D iPSC-TEC Seurat clusters. 3D iPSC-TECs display higher levels of HLA gene

expression compared with 2D iPSC-TECs. b. c. Annotation of EMT-associated gene expression in 2D and 3D iPSC-TEC clusters, highlighting the phenotypic similarity between 2D-1 and 3D-2 clusters (double arrows).

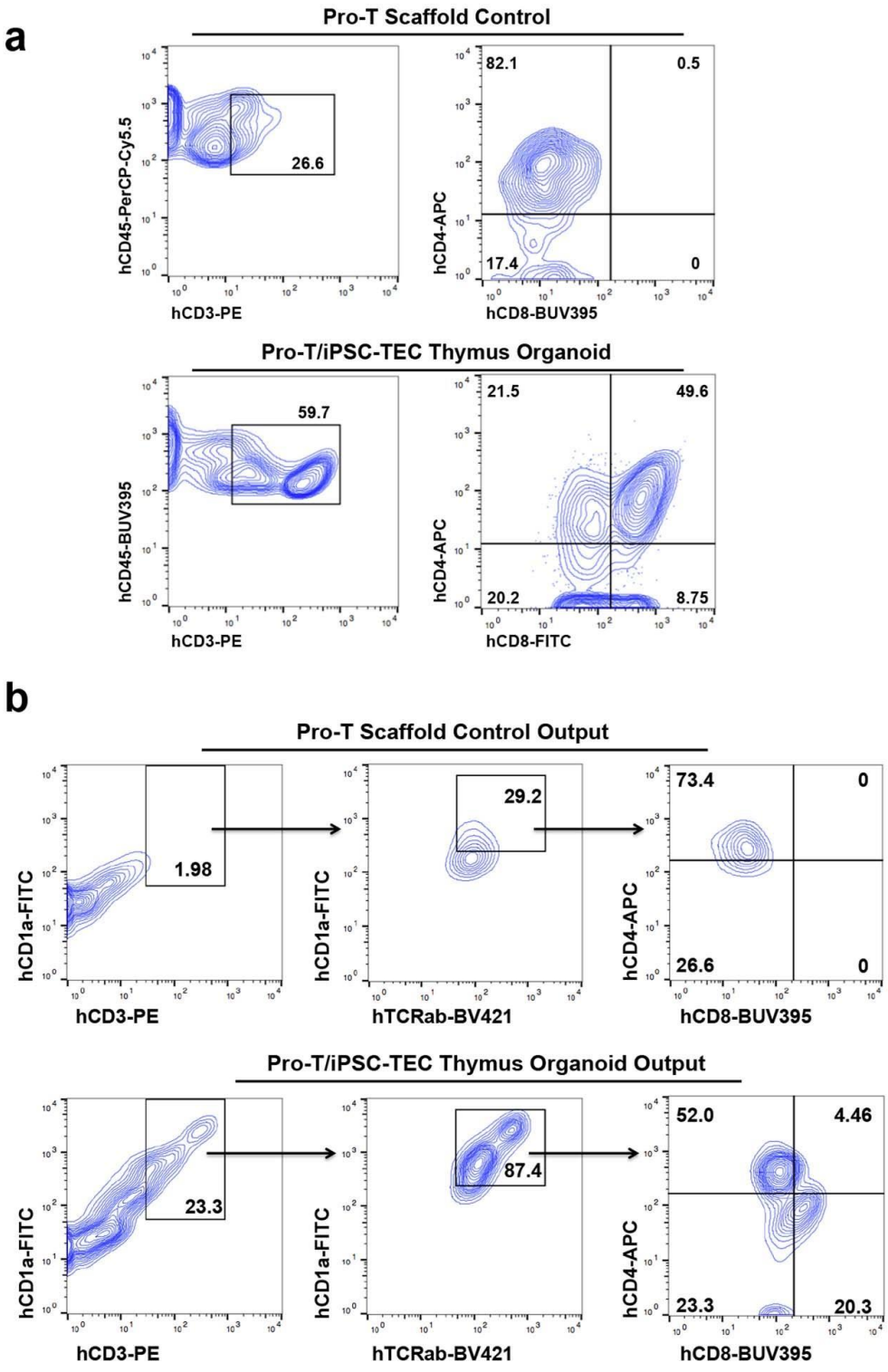

Appendix Figure 18 Pro-T/iPSC-TEC thymus organoids support progression of T cell development in vitro. a. FCM analysis of CD4 and CD8 expression in cells of Pro-T/iPSC-TEC thymus organoids (lower panels) after one week of in vitro culture. Upper panels, cells dissociated from one week cultured decellularized scaffolds

seeded with Pro-T cells alone (Pro-T scaffolds) as controls. Shown are representative FCM graphs from at least three independent experiments with similar results. b. FCM analysis of thymic output from Pro-T/iPSC-TEC thymus organoids (lower panels) and Pro-T scaffold controls (upper panels). hCD45+ cells were examined for key surface markers of T cell development (CD1a + CD3 + , left columns), TCRab (middle columns), and CD4 and CD8 (right columns). Shown are representative graphs of at least two independent experiments for the Pro-T control output and at least five independent experiments for Pro-T/iPSC-TEC thymus organoid output with similar results.

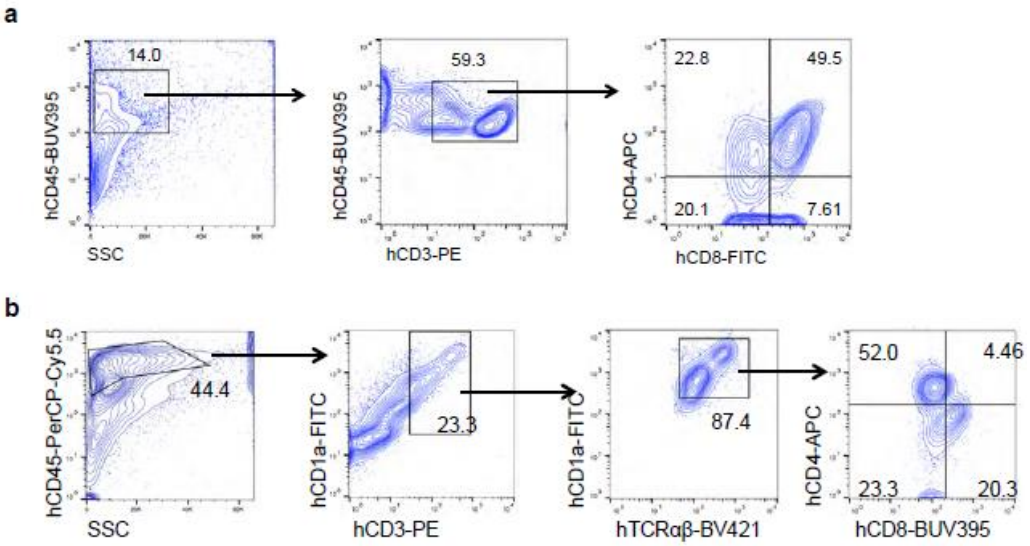

Appendix Figure 19 Gating strategies for FCM analysis of T cell development inside the Pro-T/iPSC-TEC thymus organoids (a) and the CD3+CD4+ and CD3+CD8+ T cells in culture that were generated and emigrated from the thymus organoids (output) (b).

Appendix C Chapter 4 Figures

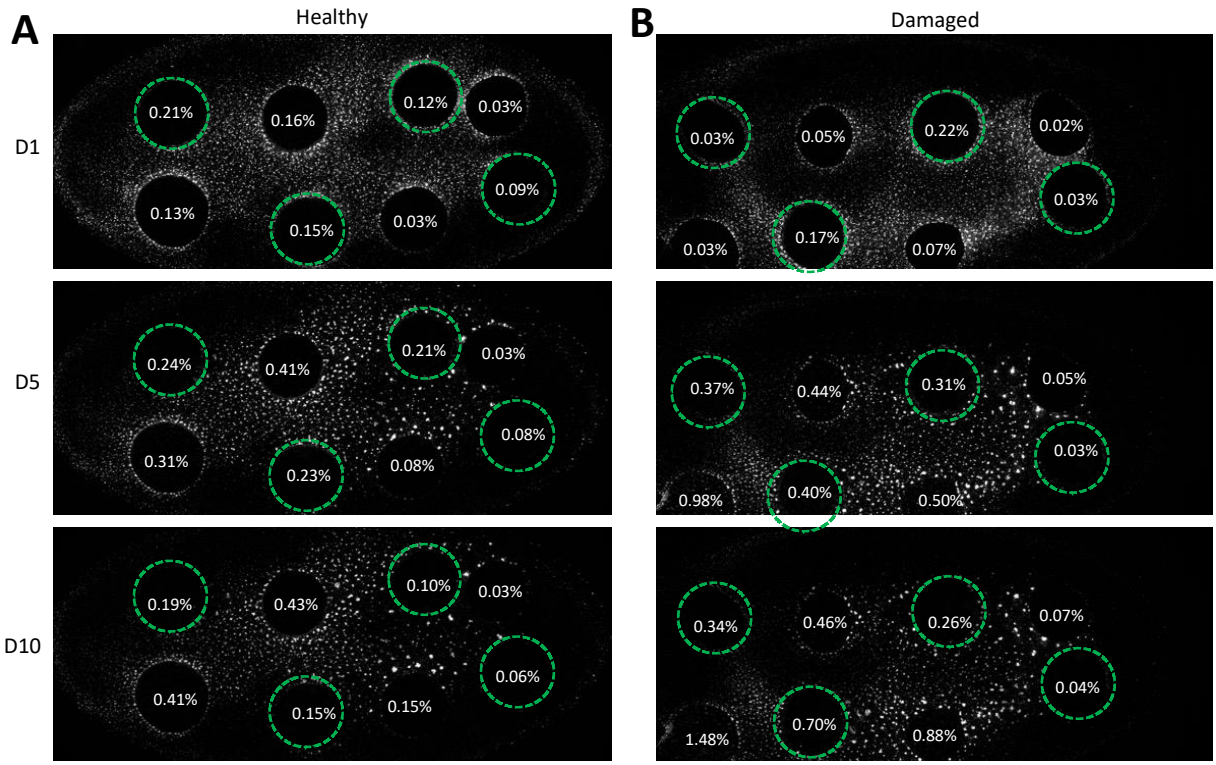

Appendix Figure 20 Neutrophil Infiltration into Alginate Capsules during 10-day co-culture with iPSC-islet on PANIS. Fluorescently tagged neutrophils (white) within the (A) healthy and (B) damaged iPSC-islet conditions over the course of the 10-day culture period with imaged timpoints of day 1 (D1), day 5, (D5) and day 10 (D10) and alginate capsules containing iPSC-islets shown in green.

Bibliography

1. Aamodt, K.I. & Powers, A.C. Signals in the pancreatic islet microenvironment influence β-cell proliferation. *Diabetes Obes Metab* **19 Suppl 1**, 124-136 (2017).

2. Sun, H. et al. IDF Diabetes Atlas: Global, regional and country-level diabetes prevalence estimates for 2021 and projections for 2045. *Diabetes Research and Clinical Practice* **183**, 109119 (2022).

3. Green, A. et al. Type 1 diabetes in 2017: global estimates of incident and prevalent cases in children and adults. *Diabetologia* **64**, 2741-2750 (2021).

4. Mathis, D., Vence, L. & Benoist, C. β-Cell death during progression to diabetes. *Nature* **414**, 792-798 (2001).

5. Meloche, R.M. Transplantation for the treatment of type 1 diabetes. *World Journal of Gastroenterology: WJG* **13**, 6347 (2007).

6. Shapiro, A.J. et al. Islet transplantation in seven patients with type 1 diabetes mellitus using a glucocorticoid-free immunosuppressive regimen. *New England Journal of Medicine* **343**, 230-238 (2000).

7. Kharroubi, A.T. & Darwish, H.M. Diabetes mellitus: The epidemic of the century. *World J Diabetes* **6**, 850-867 (2015).

8. Schwartz, S.S. et al. A unified pathophysiological construct of diabetes and its complications. *Trends in Endocrinology & Metabolism* **28**, 645-655 (2017).

9. Hering, B.J. et al. Phase 3 trial of transplantation of human islets in type 1 diabetes complicated by severe hypoglycemia. *Diabetes care* **39**, 1230-1240 (2016).

10. Ryan, E.A. et al. Five-year follow-up after clinical islet transplantation. *Diabetes* **54**, 2060-2069 (2005).

11. Chatterjee, S., Khunti, K. & Davies, M.J. Type 2 diabetes. *The Lancet* **389**, 2239-2251 (2017).

12. Klein, S., Gastaldelli, A., Yki-Järvinen, H. & Scherer, P.E. Why does obesity cause diabetes? *Cell metabolism* **34**, 11-20 (2022).

13. DeFronzo, R.A. et al. Type 2 diabetes mellitus. *Nature reviews Disease primers* **1**, 1-22 (2015).

14. Stumvoll, M., Goldstein, B.J. & Van Haeften, T.W. Type 2 diabetes: principles of pathogenesis and therapy. *The Lancet* **365**, 1333-1346 (2005).

15. White, J.R., Jr. A Brief History of the Development of Diabetes Medications. *Diabetes Spectr* **27**, 82-86 (2014).

16. Kubota, T., Kubota, N. & Kadowaki, T. Imbalanced insulin actions in obesity and type 2 diabetes: key mouse models of insulin signaling pathway. *Cell metabolism* **25**, 797-810 (2017).

17. Taylor, R. et al. Remission of human type 2 diabetes requires decrease in liver and pancreas fat content but is dependent upon capacity for β cell recovery. *Cell metabolism* **28**, 547-556. e543 (2018).

18. King, A. & Austin, A. in Animal Models for the Study of Human Disease (Second Edition). (ed. P.M. Conn) 245-265 (Academic Press, 2017).

19. von Herrath, M. & Nepom, G.T. Animal models of human type 1 diabetes. *Nature Immunology* **10**, 129-132 (2009).

20. King, A.J.F. The use of animal models in diabetes research. *Br J Pharmacol* **166**, 877-894 (2012).

21. Cefalu, W.T. Animal Models of Type 2 Diabetes: Clinical Presentation and Pathophysiological Relevance to the Human Condition. *ILAR Journal* **47**, 186-198 (2006).

22. Aiyere, E.O., Silverberg, J., Ali, S. & Parker, J.L. Clinical Trial Risk in Type-2 Diabetes: Importance of Patient History. *Journal of Pharmacy & Pharmaceutical Sciences* **17**, 393-400 (2014).

23. Wikswo, J.P. The relevance and potential roles of microphysiological systems in biology and medicine. *Experimental biology and medicine* **239**, 1061-1072 (2014).

24. Chang, S.-Y., Weber, E.J., Ness, K.V., Eaton, D.L. & Kelly, E.J. Liver and kidney on chips: microphysiological models to understand transporter function. *Clinical Pharmacology & Therapeutics* **100**, 464-478 (2016).

25. Low, L. & Tagle, D. Microphysiological systems ("organs-on-chips") for drug efficacy and toxicity testing. *Clinical and translational science* **10**, 237 (2017).

26. Offeddu, G.S., Shin, Y. & Kamm, R.D. Microphysiological models of neurological disorders for drug development. *Current Opinion in Biomedical Engineering* **13**, 119-126 (2020).

27. Miller, C.P., Shin, W., Ahn, E.H., Kim, H.J. & Kim, D.-H. Engineering microphysiological immune system responses on chips. *Trends in Biotechnology* (2020).

28. Fabre, K.M., Livingston, C. & Tagle, D.A. Organs-on-chips (microphysiological systems): tools to expedite efficacy and toxicity testing in human tissue. *Experimental biology and medicine* **239**, 1073-1077 (2014).

29. Irrechukwu, O. et al. Applications of microphysiological systems to disease models in the biopharmaceutical industry: Opportunities and challenges. *ALTEX - Alternatives to animal experimentation* **40**, 485-518 (2023).

30. Holloway, P.M. et al. Advances in microfluidic in vitro systems for neurological disease modeling. *Journal of Neuroscience Research* **99**, 1276-1307 (2021).

31. Saydmohammed, M. et al. Quantifying the progression of non-alcoholic fatty liver disease in human biomimetic liver microphysiology systems with fluorescent protein biosensors. *Experimental biology and medicine (Maywood, N.J.)* **246**, 2420-2441 (2021).

32. Patel, S.N. et al. Organoid microphysiological system preserves pancreatic islet function within 3D matrix. *Science Advances* **7**, eaba5515 (2021).

33. Sankar, K.S. et al. Culturing Pancreatic Islets in Microfluidic Flow Enhances Morphology of the Associated Endothelial Cells. *PloS one* **6**, e24904 (2011).

34. Jun, Y. et al. In vivo–mimicking microfluidic perfusion culture of pancreatic islet spheroids. *Science Advances* **5**, eaax4520 (2019).

35. Robinton, D.A. & Daley, G.Q. The promise of induced pluripotent stem cells in research and therapy. *Nature* **481**, 295-305 (2012).

36. Gearhart, J. & Coutifaris, C. In vitro fertilization, the Nobel Prize, and human embryonic stem cells. *Cell Stem Cell* **8**, 12-15 (2011).

37. Takahashi, K. et al. Induction of pluripotent stem cells from adult human fibroblasts by defined factors. *cell* **131**, 861-872 (2007).

38. Takahashi, K. & Yamanaka, S. Induction of pluripotent stem cells from mouse embryonic and adult fibroblast cultures by defined factors. *cell* **126**, 663-676 (2006).

39. Elitt, M.S., Barbar, L. & Tesar, P.J. Drug screening for human genetic diseases using iPSC models. *Human molecular genetics* **27**, R89-R98 (2018).

40. Xue, Y. et al. Generating a non-integrating human induced pluripotent stem cell bank from urine-derived cells. *PloS one* **8**, e70573 (2013).

41. Staerk, J. et al. Reprogramming of human peripheral blood cells to induced pluripotent stem cells. *Cell stem cell* **7**, 20-24 (2010).

42. Yu, J. et al. Human induced pluripotent stem cells free of vector and transgene sequences. *Science* **324**, 797-801 (2009).

43. Seki, T., Yuasa, S. & Fukuda, K. Generation of induced pluripotent stem cells from a small amount of human peripheral blood using a combination of activated T cells and Sendai virus. *Nature protocols* **7**, 718-728 (2012).

44. Wiegand, C. & Banerjee, I. Recent advances in the applications of iPSC technology. *Current Opinion in Biotechnology* **60**, 250-258 (2019).

45. Veres, A. et al. Charting cellular identity during human in vitro β-cell differentiation. *Nature* **569**, 368-373 (2019).

46. Velazco-Cruz, L. et al. Acquisition of Dynamic Function in Human Stem Cell-Derived β Cells. *Stem Cell Reports* **12**, 351-365 (2019).

47. Nair, G.G. et al. Recapitulating endocrine cell clustering in culture promotes maturation of human stem-cell-derived β cells. *Nature cell biology* **21**, 263-274 (2019).

48. Yabe, S.G. et al. Induction of functional islet-like cells from human iPS cells by suspension culture. *Regenerative Therapy* **10**, 69-76 (2019).

49. Liang, S. et al. Differentiation of stem cell-derived pancreatic progenitors into insulin-secreting islet clusters in a multiwell-based static 3D culture system. *Cell Reports Methods* **3** (2023).

50. Williams, L.A., Davis-Dusenbery, B.N. & Eggan, K.C. SnapShot: directed differentiation of pluripotent stem cells. *Cell* **149**, 1174-1174. e1171 (2012).

51. Kim, J.H. et al. Nanotopographical regulation of pancreatic islet-like cluster formation from human pluripotent stem cells using a gradient-pattern chip. *Acta Biomaterialia* **95**, 337-347 (2019).

52. Rosado-Olivieri, E.A., Anderson, K., Kenty, J.H. & Melton, D.A. YAP inhibition enhances the differentiation of functional stem cell-derived insulin-producing β cells. *Nature Communications* **10**, 1464 (2019).

53. Richardson, T., Kumta, P.N. & Banerjee, I. Alginate Encapsulation of Human Embryonic Stem Cells to Enhance Directed Differentiation to Pancreatic Islet-Like Cells. *Tissue Engineering Part A* **20**, 3198-3211 (2014).

54. Saeedi, P. et al. Global and regional diabetes prevalence estimates for 2019 and projections for 2030 and 2045: Results from the International Diabetes Federation Diabetes Atlas. *Diabetes research and clinical practice* **157**, 107843 (2019).

55. Caicedo, A. in Seminars in cell & developmental biology, Vol. 24 11-21 (Elsevier, 2013).

56. Weir, G.C. & Bonner-Weir, S. Islets of Langerhans: the puzzle of intraislet interactions and their relevance to diabetes. *The Journal of clinical investigation* **85**, 983-987 (1990).

57. Eberhard, D., Kragl, M. & Lammert, E. 'Giving and taking': endothelial and β-cells in the islets of Langerhans. *Trends in Endocrinology & Metabolism* **21**, 457-463 (2010).

58. Dishinger, J.F., Reid, K.R. & Kennedy, R.T. Quantitative monitoring of insulin secretion from single islets of Langerhans in parallel on a microfluidic chip. *Analytical chemistry* **81**, 3119-3127 (2009).

59. Glieberman, A.L. et al. Synchronized stimulation and continuous insulin sensing in a microfluidic human Islet on a Chip designed for scalable manufacturing. *Lab on a Chip* **19**, 2993-3010 (2019).

60. Shackman, J.G., Dahlgren, G.M., Peters, J.L. & Kennedy, R.T. Perfusion and chemical monitoring of living cells on a microfluidic chip. *Lab on a Chip* **5**, 56-63 (2005).

61. Lee, D. et al. Dual microfluidic perifusion networks for concurrent islet perifusion and optical imaging. *Biomedical microdevices* **14**, 7-16 (2012).

62. Ramachandran, K., Williams, S.J., Huang, H.-H., Novikova, L. & Stehno-Bittel, L. Engineering islets for improved performance by optimized reaggregation in a micromold. *Tissue Engineering Part A* **19**, 604-612 (2013).

63. Silva, P.N., Green, B.J., Altamentova, S.M. & Rocheleau, J.V. A microfluidic device designed to induce media flow throughout pancreatic islets while limiting shear-induced damage. *Lab on a chip* **13**, 4374-4384 (2013).

64. Lenguito, G. et al. Resealable, optically accessible, PDMS-free fluidic platform for ex vivo interrogation of pancreatic islets. *Lab on a Chip* **17**, 772-781 (2017).

65. Li, X., George, S.M., Vernetti, L., Gough, A.H. & Taylor, D.L. A glass-based, continuously zonated and vascularized human liver acinus microphysiological system (vLAMPS) designed for experimental modeling of diseases and ADME/TOX. *Lab on a Chip* **18**, 2614-2631 (2018).

66. Kitzmann, J.P. et al. Islet oxygen consumption rate dose predicts insulin independence for first clinical islet allotransplants. *Transplant Proc* **46**, 1985-1988 (2014).

67. Buchwald, P. FEM-based oxygen consumption and cell viability models for avascular pancreatic islets. *Theoretical Biology and Medical Modelling* **6**, 1-13 (2009).

68. J Roa, J., Oncins, G., Diaz, J., Sanz, F. & Segarra, M. Calculation of Young's modulus value by means of AFM. *Recent Patents on Nanotechnology* **5**, 27-36 (2011).

69. Bankhead, P. et al. QuPath: Open source software for digital pathology image analysis. *Scientific reports* **7**, 1-7 (2017).

70. Öztürk, E., Arslan, A.K.K., Yerer, M.B. & Bishayee, A. Resveratrol and diabetes: A critical review of clinical studies. *Biomedicine & pharmacotherapy* **95**, 230-234 (2017).

71. Brereton, M.F., Vergari, E., Zhang, Q. & Clark, A. Alpha-, delta-and PP-cells: are they the architectural cornerstones of islet structure and co-ordination? *Journal of Histochemistry & Cytochemistry* **63**, 575-591 (2015).

72. Kelly, C., McClenaghan, N.H. & Flatt, P.R. Role of islet structure and cellular interactions in the control of insulin secretion. *Islets* **3**, 41-47 (2011).

73. Richardson, T.C. et al. Development of an alginate array platform to decouple the effect of multiparametric perturbations on human pluripotent stem cells during pancreatic differentiation. *Biotechnology journal* **13**, 1700099 (2018).

74. Goh, S.-K. et al. Organ-specific ECM arrays for investigating cell-ECM interactions during stem cell differentiation. **13**, 015015 (2020).

75. Jansson, L. et al. Pancreatic islet blood flow and its measurement. *Upsala journal of medical sciences* **121**, 81-95 (2016).

76. Castiello, F.R., Heileman, K. & Tabrizian, M. Microfluidic perfusion systems for secretion fingerprint analysis of pancreatic islets: applications, challenges and opportunities. *Lab on a Chip* **16**, 409-431 (2016).

77. Swartz, M.A. & Fleury, M.E. Interstitial flow and its effects in soft tissues. *Annu. Rev. Biomed. Eng.* **9**, 229-256 (2007).

78. Schuster, E. et al. Interplay between flow and diffusion in capillary alginate hydrogels. *Soft Matter* **12**, 3897-3907 (2016).

79. Richards, O.C., Raines, S.M. & Attie, A.D. The Role of Blood Vessels, Endothelial Cells, and Vascular Pericytes in Insulin Secretion and Peripheral Insulin Action. *Endocrine Reviews* **31**, 343-363 (2010).

80. Johansson, Å. et al. Endothelial cell signalling supports pancreatic beta cell function in the rat. *Diabetologia* **52**, 2385-2394 (2009).

81. Henderson, J.R. & Moss, M.C. A MORPHOMETRIC STUDY OF THE ENDOCRINE AND EXOCRINE CAPILLARIES OF THE PANCREAS. **70**, 347-356 (1985).

82. Davies, P. How Do Vascular Endothelial Cells Respond to Flow? **4**, 22-25 (1989).

83. Chien, S. Effects of Disturbed Flow on Endothelial Cells. *Annals of Biomedical Engineering* **36**, 554-562 (2008).

84. Narayanan, S. et al. Intra-islet endothelial cell and β-cell crosstalk: Implication for islet cell transplantation. *World journal of transplantation* **7**, 117-128 (2017).

85. Lowell, B.B. & Shulman, G.I. Mitochondrial Dysfunction and Type 2 Diabetes. **307**, 384-387 (2005).

86. Barlow, J., Jensen, Verena H., Jastroch, M. & Affourtit, C. Palmitate-induced impairment of glucose-stimulated insulin secretion precedes mitochondrial dysfunction in mouse pancreatic islets. *Biochemical Journal* **473**, 487-496 (2016).

87. Cunha, D.A. et al. Initiation and execution of lipotoxic ER stress in pancreatic β-cells. *Journal of Cell Science* **121**, 2308-2318 (2008).

88. Maedler, K. et al. Distinct effects of saturated and monounsaturated fatty acids on β-cell turnover and function. *Diabetes* **50**, 69-76 (2001).

89. Maedler, K., Oberholzer, J., Bucher, P., Spinas, G.A. & Donath, M.Y. Monounsaturated fatty acids prevent the deleterious effects of palmitate and high glucose on human pancreatic β-cell turnover and function. *Diabetes* **52**, 726-733 (2003).

90. Eitel, K. et al. Different role of saturated and unsaturated fatty acids in β-cell apoptosis. *Biochemical and biophysical research communications* **299**, 853-856 (2002).

91. Hogan, M.F. & Hull, R.L. The islet endothelial cell: a novel contributor to beta cell secretory dysfunction in diabetes. *Diabetologia* **60**, 952-959 (2017).

92. Taneera, J. et al. A systems genetics approach identifies genes and pathways for type 2 diabetes in human islets. **16**, 122-134 (2012).

93. Lin, Y., Wang, Y. & Li, P.-f. PPARα: An emerging target of metabolic syndrome, neurodegenerative and cardiovascular diseases. **13** (2022).

94. Robertson, R.P. Chronic oxidative stress as a central mechanism for glucose toxicity in pancreatic islet beta cells in diabetes. *Journal of Biological Chemistry* **279**, 42351-42354 (2004).

95. Xia, N., Daiber, A., Förstermann, U. & Li, H. Antioxidant effects of resveratrol in the cardiovascular system. *British journal of pharmacology* **174**, 1633-1646 (2017).

96. Ren, B. et al. Resveratrol for cancer therapy: Challenges and future perspectives. *Cancer letters* **515**, 63-72 (2021).

97. Švajger, U. & Jeras, M. Anti-inflammatory effects of resveratrol and its potential use in therapy of immune-mediated diseases. *International reviews of immunology* **31**, 202-222 (2012).

98. Bonnefont-Rousselot, D. Resveratrol and cardiovascular diseases. *Nutrients* **8**, 250 (2016).

99. Zhang, L.-X. et al. Resveratrol (RV): A pharmacological review and call for further research. *Biomedicine & pharmacotherapy* **143**, 112164 (2021).

100. Palsamy, P. & Subramanian, S. Ameliorative potential of resveratrol on proinflammatory cytokines, hyperglycemia mediated oxidative stress, and pancreatic β-cell dysfunction in streptozotocin-nicotinamide-induced diabetic rats. *Journal of cellular physiology* **224**, 423-432 (2010).

101. Keshtkar, S. et al. Significant reduction of apoptosis induced via hypoxia and oxidative stress in isolated human islet by resveratrol. *Nutrition, Metabolism and Cardiovascular Diseases* **30**, 1216-1226 (2020).

102. Szkudelski, T. Resveratrol inhibits insulin secretion from rat pancreatic islets. *European journal of pharmacology* **552**, 176-181 (2006).

103. Yao, W., Li, Y. & Ding, G. Interstitial fluid flow: the mechanical environment of cells and foundation of meridians. *Evidence-Based Complementary and Alternative Medicine* **2012** (2012).

104. Torino, S., Corrado, B., Iodice, M. & Coppola, G. PDMS-Based Microfluidic Devices for Cell Culture. *Inventions* **3** (2018).

105. Grant, J. et al. Simulating drug concentrations in PDMS microfluidic organ chips. *Lab on a Chip* **21**, 3509-3519 (2021).

106. Wang, Y. et al. Systematic prevention of bubble formation and accumulation for long-term culture of pancreatic islet cells in microfluidic device. *Biomedical microdevices* **14**, 419-426 (2012).

107. Lake, M. et al. Microfluidic device design, fabrication, and testing protocols. *Protocol Exchange* (2015).

108. Schulze, T. et al. A 3D microfluidic perfusion system made from glass for multiparametric analysis of stimulus-secretioncoupling in pancreatic islets. *Biomedical microdevices* **19**, 47 (2017).

109. Campbell, S.B. et al. Beyond Polydimethylsiloxane: Alternative Materials for Fabrication of Organ-on-a-Chip Devices and Microphysiological Systems. *ACS Biomaterials Science & Engineering* **7**, 2880-2899 (2021).

110. Halldorsson, S., Lucumi, E., Gómez-Sjöberg, R. & Fleming, R.M.T. Advantages and challenges of microfluidic cell culture in polydimethylsiloxane devices. *Biosensors and Bioelectronics* **63**, 218-231 (2015).

111. Rodríguez-Comas, J. & Ramón-Azcón, J. Islet-on-a-chip for the study of pancreatic β-cell function. *In vitro models* **1**, 41-57 (2022).

112. Brereton, M.F., Vergari, E., Zhang, Q. & Clark, A. Alpha-, Delta- and PP-cells: Are They the Architectural Cornerstones of Islet Structure and Co-ordination? *Journal of Histochemistry & Cytochemistry* **63**, 575-591 (2015).

113. Buchwald, P. FEM-based oxygen consumption and cell viability models for avascular pancreatic islets. *Theoretical Biology and Medical Modelling* **6**, 5 (2009).

114. Aamodt, K.I. & Powers, A.C. Signals in the pancreatic islet microenvironment influence β-cell proliferation. **19**, 124-136 (2017).

115. Bauer, S. et al. Functional coupling of human pancreatic islets and liver spheroids on-a-chip: Towards a novel human ex vivo type 2 diabetes model. *Scientific Reports* **7**, 14620 (2017).

116. Roper, M.G., Shackman, J.G., Dahlgren, G.M. & Kennedy, R.T. Microfluidic Chip for Continuous Monitoring of Hormone Secretion from Live Cells Using an Electrophoresis-Based Immunoassay. *Analytical chemistry* **75**, 4711-4717 (2003).

117. Dishinger, J.F., Reid, K.R. & Kennedy, R.T. Quantitative monitoring of insulin secretion from single islets of Langerhans in parallel on a microfluidic chip. *Analytical chemistry* **81**, 3119-3127 (2009).

118. Hori, T., Yamane, K., Anazawa, T., Kurosawa, O. & Iwata, H. Compact fluidic system for functional assessment of pancreatic islets. *Biomedical microdevices* **21**, 91 (2019).

119. Misun, P.M. et al. In Vitro Platform for Studying Human Insulin Release Dynamics of Single Pancreatic Islet Microtissues at High Resolution. *Advanced Biosystems* **4**, 1900291 (2020).

120. Casas, B. et al. Integrated experimental-computational analysis of a HepaRG liver-islet microphysiological system for human-centric diabetes research. *PLOS Computational Biology* **18**, e1010587 (2022).

121. Wehinger, S. et al. Phosphorylation of caveolin-1 on tyrosine-14 induced by ROS enhances palmitate-induced death of beta-pancreatic cells. *Biochimica et Biophysica Acta (BBA) - Molecular Basis of Disease* **1852**, 693-708 (2015).

122. Liu, J. et al. Palmitate promotes autophagy and apoptosis through ROS-dependent JNK and p38 MAPK. *Biochemical and biophysical research communications* **463**, 262-267 (2015).

123. Sharma, R.B. & Alonso, L.C. Lipotoxicity in the Pancreatic Beta Cell: Not Just Survival and Function, but Proliferation as Well? *Current Diabetes Reports* **14**, 492 (2014).

124. Nemecz, M. et al. The Distinct Effects of Palmitic and Oleic Acid on Pancreatic Beta Cell Function: The Elucidation of Associated Mechanisms and Effector Molecules. **9** (2019).

125. Hogh, K.-L.N. et al. Overexpression of peroxisome proliferator-activated receptor α in pancreatic β-cells improves glucose tolerance in diet-induced obese mice. **98**, 564-575 (2013).

126. Liang, A. et al. Resveratrol regulates insulin resistance to improve the glycolytic pathway by activating SIRT2 in PCOS granulosa cells. *Front Nutr* **9**, 1019562 (2022).

127. Shaito, A. et al. Potential Adverse Effects of Resveratrol: A Literature Review. *International Journal of Molecular Sciences* **21**, 2084 (2020).

128. Radkar, V., Hardej, D., Lau-Cam, C. & Billack, B. Evaluation of resveratrol and piceatannol cytotoxicity in macrophages, T cells, and skin cells. *Arh Hig Rada Toksikol* **58**, 293-304 (2007).

129. Souza, I.C. et al. Resveratrol inhibits cell growth by inducing cell cycle arrest in activated hepatic stellate cells. *Molecular and Cellular Biochemistry* **315**, 1-7 (2008).

130. Martins, L.A.M. et al. Resveratrol Induces Pro-oxidant Effects and Time-Dependent Resistance to Cytotoxicity in Activated Hepatic Stellate Cells. *Cell Biochemistry and Biophysics* **68**, 247-257 (2014).

131. Takebe, T. et al. Generation of a vascularized and functional human liver from an iPSC-derived organ bud transplant. *Nature protocols* **9**, 396-409 (2014).

132. Sampaziotis, F. et al. Cholangiocytes derived from human induced pluripotent stem cells for disease modeling and drug validation. *Nature biotechnology* **33**, 845-852 (2015).

133. Ogawa, M. et al. Directed differentiation of cholangiocytes from human pluripotent stem cells. *Nature biotechnology* **33**, 853-861 (2015).

134. Takebe, T. et al. Vascularized and functional human liver from an iPSC-derived organ bud transplant. *Nature* **499**, 481-484 (2013).

135. Dye, B.R. et al. In vitro generation of human pluripotent stem cell derived lung organoids. *eLife* **4** (2015).

136. Miller, A.J. et al. Generation of lung organoids from human pluripotent stem cells in vitro. *Nature protocols* **14**, 518-540 (2019).

137. Huang, S.X. et al. Efficient generation of lung and airway epithelial cells from human pluripotent stem cells. *Nature biotechnology* **32**, 84-91 (2014).

138. Firth, A.L. et al. Functional Gene Correction for Cystic Fibrosis in Lung Epithelial Cells Generated from Patient iPSCs. *Cell reports* **12**, 1385-1390 (2015).

139. Takasato, M. et al. Kidney organoids from human iPS cells contain multiple lineages and model human nephrogenesis. *Nature* **526**, 564-568 (2015).

140. Freedman, B.S. et al. Modelling kidney disease with CRISPR-mutant kidney organoids derived from human pluripotent epiblast spheroids. *Nature Communications* **6**, 8715 (2015).

141. Candiello, J. et al. 3D heterogeneous islet organoid generation from human embryonic stem cells using a novel engineered hydrogel platform. *Biomaterials* **177**, 27-39 (2018).

142. Huang, L. et al. Ductal pancreatic cancer modeling and drug screening using human pluripotent stem cell- and patient-derived tumor organoids. *Nat Med* **21**, 1364-1371 (2015).

143. Hohwieler, M. et al. Human pluripotent stem cell-derived acinar/ductal organoids generate human pancreas upon orthotopic transplantation and allow disease modelling. *Gut* **66**, 473-486 (2017).

144. Montel-Hagen, A. et al. Organoid-Induced Differentiation of Conventional T Cells from Human Pluripotent Stem Cells. *Cell stem cell* **24**, 376-389.e378 (2019).

145. D'Amour, K.A. et al. Production of pancreatic hormone–expressing endocrine cells from human embryonic stem cells. *Nature Biotechnology* **24**, 1392-1401 (2006).

146. Richardson, T., Barner, S., Candiello, J., Kumta, P.N. & Banerjee, I. Capsule stiffness regulates the efficiency of pancreatic differentiation of human embryonic stem cells. *Acta biomaterialia* **35**, 153-165 (2016).

147. Pagliuca, Felicia W. et al. Generation of Functional Human Pancreatic β Cells In Vitro. *Cell* **159**, 428-439 (2014).

148. Verhoeff, K. et al. Optimizing Generation of Stem Cell-Derived Islet Cells. *Stem cell reviews and reports* **18**, 2683-2698 (2022).

149. Hogrebe, N.J., Maxwell, K.G., Augsornworawat, P. & Millman, J.R. Generation of insulin-producing pancreatic β cells from multiple human stem cell lines. *Nature protocols* **16**, 4109-4143 (2021).

150. Balboa, D. et al. Functional, metabolic and transcriptional maturation of human pancreatic islets derived from stem cells. *Nature biotechnology* **40**, 1042-1055 (2022).

151. Wang, Y., Cheng, L. & Gerecht, S. Efficient and scalable expansion of human pluripotent stem cells under clinically compliant settings: a view in 2013. *Ann Biomed Eng* **42**, 1357-1372 (2014).

152. Boehm, T. & Bleul, C.C.J.T.i.i. Thymus-homing precursors and the thymic microenvironment. **27**, 477-484 (2006).

153. Hedrick, S.M.J.I. Thymus lineage commitment: a single switch. **28**, 297-299 (2008).

154. Klein, L., Hinterberger, M., Wirnsberger, G. & Kyewski, B.J.N.R.I. Antigen presentation in the thymus for positive selection and central tolerance induction. **9**, 833-844 (2009).

155. Klein, L., Kyewski, B., Allen, P.M. & Hogquist, K.A.J.N.R.I. Positive and negative selection of the T cell repertoire: what thymocytes see (and don't see). **14**, 377-391 (2014).

156. Anderson, G. & Takahama, Y.J.T.i.i. Thymic epithelial cells: working class heroes for T cell development and repertoire selection. **33**, 256-263 (2012).

157. Ohigashi, I., Kozai, M. & Takahama, Y.J.I.r. Development and developmental potential of cortical thymic epithelial cells. **271**, 10-22 (2016).

158. Klug, D.B. et al. Interdependence of cortical thymic epithelial cell differentiation and T-lineage commitment. **95**, 11822-11827 (1998).

159. Mizuochi, T., Kasai, M., Kokuho, T., Kakiuchi, T. & Hirokawa, K.J.T.J.o.e.m. Medullary but not cortical thymic epithelial cells present soluble antigens to helper T cells. **175**, 1601-1605 (1992).

160. Derbinski, J., Schulte, A., Kyewski, B. & Klein, L.J.N.i. Promiscuous gene expression in medullary thymic epithelial cells mirrors the peripheral self. **2**, 1032-1039 (2001).

161. Hinterberger, M. et al. Autonomous role of medullary thymic epithelial cells in central CD4+ T cell tolerance. **11**, 512-519 (2010).

162. Tajima, A. et al. Construction of thymus organoids from decellularized thymus scaffolds. 33-42 (2019).

163. Hun, M. et al. Native thymic extracellular matrix improves in vivo thymic organoid T cell output, and drives in vitro thymic epithelial cell differentiation. **118**, 1-15 (2017).

164. Fan, Y. et al. Bioengineering thymus organoids to restore thymic function and induce donor-specific immune tolerance to allografts. **23**, 1262-1277 (2015).

165. Campinoti, S. et al. Reconstitution of a functional human thymus by postnatal stromal progenitor cells and natural whole-organ scaffolds. **11**, 6372 (2020).

166. Shi, Y., Inoue, H., Wu, J.C. & Yamanaka, S.J.N.r.D.d. Induced pluripotent stem cell technology: a decade of progress. **16**, 115-130 (2017).

167. Parent, A.V. et al. Generation of functional thymic epithelium from human embryonic stem cells that supports host T cell development. **13**, 219-229 (2013).

168. Sun, X. et al. Directed differentiation of human embryonic stem cells into thymic epithelial progenitor-like cells reconstitutes the thymic microenvironment in vivo. **13**, 230-236 (2013).

169. Okabe, M., Ito, S., Nishio, N., Tanaka, Y. & Isobe, K.-I.J.C.R. Thymic epithelial cells induced from pluripotent stem cells by a three-dimensional spheroid culture system regenerates functional T cells in nude mice. **17**, 368-375 (2015).

170. Chhatta, A.R. et al. De novo generation of a functional human thymus from induced pluripotent stem cells. **144**, 1416-1419. e1417 (2019).

171. Ramos, S.A. et al. Generation of functional human thymic cells from induced pluripotent stem cells. *The Journal of allergy and clinical immunology* **149**, 767-781.e766 (2022).

172. Schulz, T.C. et al. A Scalable System for Production of Functional Pancreatic Progenitors from Human Embryonic Stem Cells. *PloS one* **7**, e37004 (2012).

173. Russ, H.A. et al. Controlled induction of human pancreatic progenitors produces functional beta-like cells in vitro. *The EMBO Journal* **34**, 1759-1772 (2015).

174. Richardson, T. et al. Engineering Biophysical Cues for Controlled 3D Differentiation of Endoderm Derivatives. 73-92 (2021).

175. Blondel, V.D., Guillaume, J.-L., Lambiotte, R., Lefebvre, E.J.J.o.s.m.t. & experiment Fast unfolding of communities in large networks. **2008**, P10008 (2008).

176. Hirschhaeuser, F. et al. Multicellular tumor spheroids: an underestimated tool is catching up again. **148**, 3-15 (2010).

177. Aigha, I.I. & Abdelalim, E.M. NKX6.1 transcription factor: a crucial regulator of pancreatic β cell development, identity, and proliferation. *Stem cell research & therapy* **11**, 459 (2020).

178. Davis, J.C. et al. Live Cell Monitoring and Enrichment of Stem Cell-Derived β Cells Using Intracellular Zinc Content as a Population Marker. *Current Protocols in Stem Cell Biology* **51**, e99 (2019).

179. Rasouli, N., Melton, D.A. & Alvarez-Dominguez, J.R. Purification of Live Stem-Cell-Derived Islet Lineage Intermediates. *Current protocols in stem cell biology* **53**, e111 (2020).

180. Hrvatin, S. et al. Differentiated human stem cells resemble fetal, not adult, β cells. *Proceedings of the National Academy of Sciences* **111**, 3038-3043 (2014).

181. Zeleniak, A. et al. De novo construction of T cell compartment in humanized mice engrafted with iPSC-derived thymus organoids. *Nature Methods* **19**, 1306-1319 (2022).

182. Bredenkamp, N. et al. An organized and functional thymus generated from FOXN1-reprogrammed fibroblasts. **16**, 902-908 (2014).

183. Rodewald, H.-R.J.A.R.I. Thymus organogenesis. **26**, 355-388 (2008).

184. Bonfanti, P. et al. Microenvironmental reprogramming of thymic epithelial cells to skin multipotent stem cells. **466**, 978-982 (2010).

185. Park, J.-E. et al. A cell atlas of human thymic development defines T cell repertoire formation. **367**, eaay3224 (2020).

186. Takahama, Y., Ohigashi, I., Baik, S. & Anderson, G.J.N.R.I. Generation of diversity in thymic epithelial cells. **17**, 295-305 (2017).

187. Fan, Y. et al. Bioengineering thymus organoids to restore thymic function and induce donor-specific immune tolerance to allografts. *Molecular Therapy* **23**, 1262-1277 (2015).

188. Park, J.-E. et al. A cell atlas of human thymic development defines T cell repertoire formation. *Science* **367**, eaay3224 (2020).

189. Irla, M. in Thymus Transcriptome and Cell Biology. (ed. G.A. Passos) 149-167 (Springer International Publishing, Cham; 2019).

190. Takahama, Y., Ohigashi, I., Baik, S. & Anderson, G. Generation of diversity in thymic epithelial cells. *Nature Reviews Immunology* **17**, 295-305 (2017).

191. Rothenberg, E.V. Single-cell insights into the hematopoietic generation of T-lymphocyte precursors in mouse and human. *Experimental hematology* **95**, 1-12 (2021).

192. Chayosumrit, M., Tuch, B. & Sidhu, K. Alginate microcapsule for propagation and directed differentiation of hESCs to definitive endoderm. *Biomaterials* **31**, 505-514 (2010).

193. Meng, G., Liu, S., Poon, A. & Rancourt, D.E. Optimizing Human Induced Pluripotent Stem Cell Expansion in Stirred-Suspension Culture. *Stem Cells and Development* **26**, 1804-1817 (2017).

194. Brusatin, G., Panciera, T., Gandin, A., Citron, A. & Piccolo, S. Biomaterials and engineered microenvironments to control YAP/TAZ-dependent cell behaviour. *Nature Materials* **17**, 1063-1075 (2018).

195. Tao, T. et al. Engineering human islet organoids from iPSCs using an organ-on-chip platform. *Lab on a Chip* **19**, 948-958 (2019).

196. Tao, T. et al. Microengineered Multi-Organoid System from hiPSCs to Recapitulate Human Liver-Islet Axis in Normal and Type 2 Diabetes. **9**, 2103495 (2022).

197. Goswami, I., de Klerk, E., Carnese, P., Hebrok, M. & Healy, K.E. Multiplexed microfluidic platform for stem-cell derived pancreatic islet β cells. *Lab on a Chip* **22**, 4430-4442 (2022).

198. Babatunde, K.A. et al. Chemotaxis and swarming in differentiated HL-60 neutrophil-like cells. *Scientific reports* **11**, 1-13 (2021).

199. Arda, H.E. et al. Age-dependent pancreatic gene regulation reveals mechanisms governing human β cell function. *Cell metabolism* **23**, 909-920 (2016).

200. Blum, B. et al. Functional beta-cell maturation is marked by an increased glucose threshold and by expression of urocortin 3. *Nature biotechnology* **30**, 261-264 (2012).

201. Eguchi, K. & Nagai, R. Islet inflammation in type 2 diabetes and physiology. *The Journal of clinical investigation* **127**, 14-23 (2017).

202. Imai, Y., Dobrian, A.D., Morris, M.A. & Nadler, J.L. Islet inflammation: a unifying target for diabetes treatment? *Trends in Endocrinology & Metabolism* **24**, 351-360 (2013).

203. Diana, J. & Lehuen, A. Macrophages and β-cells are responsible for CXCR2-mediated neutrophil infiltration of the pancreas during autoimmune diabetes. *EMBO molecular medicine* **6**, 1090-1104 (2014).

204. Fine, N., Tasevski, N., McCulloch, C.A., Tenenbaum, H.C. & Glogauer, M. The Neutrophil: Constant Defender and First Responder. *Frontiers in immunology* **11**, 571085 (2020).

205. Babatunde, K.A. et al. Chemotaxis and swarming in differentiated HL-60 neutrophil-like cells. *Scientific reports* **11**, 778 (2021).

206. van Berlo, D., van de Steeg, E., Amirabadi, H.E. & Masereeuw, R. The potential of multi-organ-on-chip models for assessment of drug disposition as alternative to animal testing. *Current Opinion in Toxicology* **27**, 8-17 (2021).

207. Ronaldson-Bouchard, K. et al. A multi-organ chip with matured tissue niches linked by vascular flow. *Nature Biomedical Engineering* **6**, 351-371 (2022).

208. Lien, C.-Y. et al. Recognizing the Differentiation Degree of Human Induced Pluripotent Stem Cell-Derived Retinal Pigment Epithelium Cells Using Machine Learning and Deep Learning-Based Approaches. *Cells* **12**, 211 (2023).

209. Issa, J. et al. Artificial-Intelligence-Based Imaging Analysis of Stem Cells: A Systematic Scoping Review. *Biology* **11**, 1412 (2022).

210. Maxwell, K.G. & Millman, J.R. Applications of iPSC-derived beta cells from patients with diabetes. *Cell Reports Medicine* **2** (2021).